Energy modulation of electron bunches using a terahertz-driven dielectric-lined waveguide

Alisa Louise Healy
MPhys (Hons) Physics
A thesis submitted for the degree of Doctor of Philosophy

February 2020
Department of Engineering

Declaration

This thesis has not been submitted in support of an application for another degree at this or any other university. It is the result of my own work and includes nothing that is the outcome of work done in collaboration except where specifically indicated.

Alisa Louise Healy
Lancaster University, UK

Abstract

Alisa Louise Healy, MPhys (Hons) Physics
Doctor of Philosophy
Energy modulation of electron bunches using a terahertz-driven dielectric-lined waveguide
February 2020

In this thesis, the use of a rectangular dielectric-lined waveguide for energy modulation of electron bunches is presented. The choice of waveguide allows for guided THz pulse propagation with phase velocity matched to the electron velocity. The effect of dispersion, in particular group velocity slippage, has been explored and the choice of a narrow bandwidth THz pulse discussed with regards to the increase in interaction length and minimised group velocity dispersion. A coupler was designed for maximising transmission into the accelerating mode of the waveguide. A non-conventional THz source design was required to generate the correct mode.

Modelling of the interaction was performed with different methods and tools so as to investigate the required accuracy of simulations. The use of the Time-Domain (TD) and Particle-in-Cell (PIC) solver in CST Microwave Studio (CST-MWS) was compared with purpose-built simulations in *Mathematica*. It was established that for narrowband THz pulses the interaction as a function of time delay between THz and the bunch is well approximated by a sinusoidal energy modulation. PIC simulations were used to verify the THz bandwidth and centre frequency for which this approximation was valid.

A full structure was designed, manufactured and analysed. THz time domain spectroscopy allowed for measurement of the dispersion relation to compare to the model. Dimensional analysis gave the dimensions of the apertures of the structure. The dimensional analysis showed that, due to a manufacturing error, the waveguide dimensions were larger than designed.

Experimental work performed using the CLARA beam at Daresbury Laboratory demonstrated energy modulation of a long, chirped electron bunch. This has potential

for use as a bunch diagnostic to assess the time-dependent properties. The THz source was of limited energy, showing that only small laser power is required for such a scheme. An energy spread increase of approximately 8 keV was verified, but full bunch acceleration was not observed.

Acknowledgements

Specific persons who have provided or supported the collection of data in this thesis are acknowledged in the relevant chapters.
Firstly I would like to thank my supervisor Professor Graeme Burt for his support, from accepting me for the studentship to the final emails. I also extend thanks to the group leader Professor Steven Jamison. Without our discussions I would not have pursued the research in the way I did. I must also extend my gratitude to other members of the group, in particular Dan, Morgan, and Vasilis, who all made experimental work possible and taught me a lot about terahertz and optics along the way.
These people may have been the ones who made the research possible, but the day-to-day work would have been a lot less interesting without the various members of the Cockcroft Institute who provided company/cake/a shoulder to cry on. My particular appreciation goes first to Emmy, who smoothed out the transition to PhD life, then to Paulo, whose board game nights may have tested friendships at times! Miriam, James, Alex: you made all those terrible films worth watching. Hywel, you're the one who got me into this. I'm still not sure if I should thank you for that.
To my parents, who I could always count on to provide a listening ear and pull me out of the physics bubble. Thanks for the bike rides and the flying visits and reminding me that life wasn't just about the PhD. Finally, to Tom. It may have been tough sometimes, but we've made it through. Without you I wouldn't have been able to achieve the final result, quite literally.

Contents

List of Figures

List of Tables

Chapter 1

Introduction

1.1 Motivation for novel acceleration schemes

The use of radio frequency (RF) driven cavities to accelerate charged particles is well established. However there is always a need to increase the maximum attainable beam energy and improve beam quality. This is at the expense of increasing cost in terms of both capital and space. Research into improving RF technology is being performed, considering both superconducting and normal cavities [1]. At the same time, other avenues are also being explored. For example, the field of plasma-based acceleration is wide ranging [2], starting with demonstration of laser wakefield acceleration in 1979 [3] and followed shortly by plasma wakefield acceleration [4]. Since then, the field has grown significantly and is arguably the most developed novel acceleration scheme, given the scale of research worldwide [5].

There is also interest in acceleration schemes which utilise higher frequency electromagnetic fields. There are two advantages to these schemes. Firstly current RF technology is limited by the breakdown threshold of structures. Scaling studies have shown that this breakdown limit increases with frequency [6], thus increasing the maximum achievable accelerating gradient. The further advantage is that higher frequencies require smaller structures and allow for bunch manipulation on short length scales. There are two well-defined frequency ranges of interest. The first is the use of millimetre waves, which require scaling of conventional RF cavities [7]. The other is the optical regime requiring the use of laser technology which allows for high accelerating gradients in sub-μm structures [8]. However these structures require precise control of the spatial alignment and timing of injected bunches, and whilst GV/m accelerating fields have been achieved, this has been at the expense of low particle transmission [9].

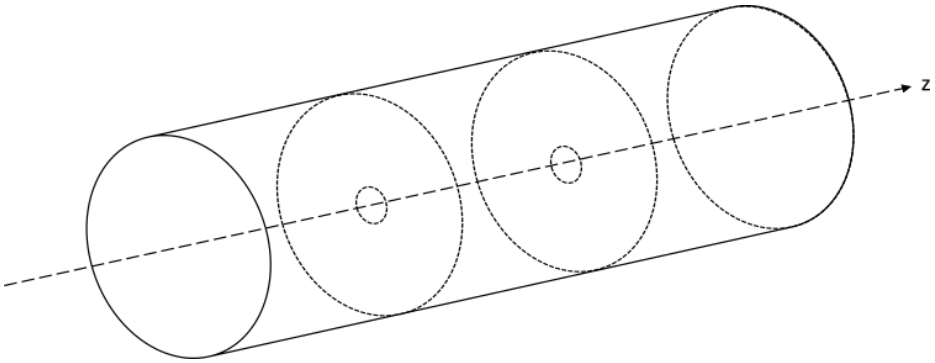

Figure 1.1: A cylindrical waveguide loaded with plates. Each plate has an aperture centred on the z axis. Electrons propagate through the apertures along this axis.

Between millimetre-wave and lasers lies the terahertz (THz) gap, which is served by neither electrical nor laser sources [10]. Advances in high power THz sources have been relatively recent and interest has been driven by a range of fields, from materials research to security scanning [11]. Although the breakdown threshold is lower than when using lasers, the smaller frequency and increased structure size is advantageous for improvement of particle transmission and more relaxed requirements on alignment. The research field is still in its infancy; although electron acceleration has been demonstrated [12, 13], the technology has not been proven as a viable alternative to RF. Therefore the purpose of this thesis is to demonstrate that terahertz-driven dielectric-lined waveguides have use in energy manipulation of relativistic electron bunches.

1.2 Conventional radio frequency cavities

Acceleration of charged particles requires an electric field with a component in the direction of particle propagation. Other forms of particle manipulation use other configurations of fields; examples include deflection, transverse focussing, and longitudinal bunching. The fields must be synchronised with the particles to maximise interaction; if an oscillatory travelling wave propagates at a different velocity, the field experienced by the particle also oscillates. A regular cylindrical waveguide with open boundaries in the longitudinal direction does not satisfy this synchronisation condition. A simple modification is to insert metallic structures into the waveguide, which reduces the phase velocity of the field to below the speed of light. A common accelerating structure is the disk-loaded waveguide, in which metallic plates with iris apertures are added periodically, as shown in Figure 1.1. This alters the boundary conditions, allowing one frequency component to satisfy the synchronism condition [14]. This is an example of a travelling wave linac, which is the closest analogy to the

structure considered in this thesis. The interacting EM wave is launched at the first input cell and propagates along the beam direction. Electron bunches are injected on-axis to be accelerated by the wave. The first disk-loaded waveguide, built in 1948 at Stanford [15], accelerated electrons to 4.5 MeV over 9 feet (∼2.75 m). The maximum achievable accelerating gradient depends on the choice of material; these are typically metal (normal) or niobium (superconducting). Typical accelerating field of normal RF structures is in the range 10-30 MV/m [8], with a maximum demonstrated stable gradient of 100 MV/m [16]. Superconducting cavities have been demonstrated with gradients of up to 45 MV/m [17]. However RF cavities are limited with respect to accelerating gradient due to RF-induced breakdown of the cavity surface. This limit is related to the breakdown rate (BDR), and is dependent on the RF pulse length [18]. Using this as a rough guide suggests that shorter pulses, at higher frequencies, increases the maximum accelerating gradient. For high energy linear accelerators the limit is the size, as long accelerating structures are necessary, which is costly in terms of both the machine and associated construction [19].

Any RF cavity requires an input power source to provide the microwave fields. Producing high RF power is achieved with the use of klystrons. A klystron extracts power from an accelerated electron beam which is then transferred to the accelerating RF cavities. A cathode is used as a source of a continuous electron beam, which is accelerated to high voltage in a DC gun. The beam then enters a cavity which is powered by an external RF source with power of order kilowatts. Because the beam is continuous, interaction with the sinusoidal field causes alternating acceleration and deceleration. Full bunching takes place in the proceeding drift length as the accelerated and decelerated electrons separate longitudinally. This bunching is at a frequency corresponding to the external RF frequency. Passing through a series of cavities the bunched electrons are then decelerated and the power transferred from beam to cavity [20]. This is via beam loading; the electron beam excites electromagnetic fields in the cavity at the resonant frequency of the cavity. An important factor in klystron (and accelerator) design is the wall plug efficiency; the transfer of all electrical power used in the system to the beam [21]. Including all components that require electrical energy, high energy particle accelerators such as the proposed Compact Linear Collider (CLIC) achieve a klystron RF to beam efficiency of 28% [22].

1.3 Millimetre-wave accelerating structures

Millimetre-wave structures, in the frequency range of tens to hundreds gigahertz, have been explored for their potential high accelerating gradient compared to conventional structures. The typical frequency range is the W band region (75-110 GHz).

Such structures were first proposed by Henke *et al* in 1993 [23], in this case using a double-sided 'muffin-top' structure. This prototype used a travelling wave mode due to improved heat dissipation over standing waves. This structure was manufactured using a lithographic process, which allowed for 0.1% accuracy on the dimensions. There was a dedicated W-band program at SLAC in the late 1990s, with research into both travelling wave [24] and standing wave [25] metallic structures. Various manufacturing techniques were explored to achieve sub-micrometre tolerances [26]. Dielectric structures were also explored, including the planar dielectric structure [27]. This achieved a 20 MV/m field gradient. More recent work in 2016 has also considered muffin-top structures, capable of achieving 300 MV/m accelerating gradients [28]. High power testing of such structures is currently underway to test performance [29, 30].

1.4 Laser driven structures

Laser acceleration was first proposed by Shimoda [31] in 1962. Use of a dielectric lining was proposed in order to achieve velocity matching, with the alternative of a gas filled cavity also suggested. Initial studies considered scaling RF structures to the optical regime using gratings [32, 33], employing the inverse Smith-Purcell effect. The Smith-Purcell effect is the generation of radiation when a charged particle propagates close to a periodic structure made of a conducting material, such as a metallic diffraction grating. The inverse Smith-Purcell effect allows for acceleration of charged particles; incident EM radiation excites an evanescent wave on the surface of the grating. This travels with a phase velocity determined by the grating period, allowing for synchronous propagation with a particle [34]. The use of metal is a limiting factor in achieving high accelerating gradient due to the damage threshold. At optical frequencies use of a dielectric is preferred, as the breakdown limit means they can withstand field amplitudes roughly two orders of magnitude higher [35].

A slab-symmetric design was proposed in 1995 [36]. The electron beam propagated between two dielectric masks whose dielectric permittivity varied periodically along the longitudinal direction. These masks were then lined with metallic mirrors, trapping laser power in the cavity. Simulations showed that efficient coupling into the accelerating mode was not achievable due to coupling into deflecting modes, leading to a change of design [37]. The transmission of the metallic mirrors was modulated periodically, which practically meant the use of a uniform mirror with small gaps separated by periodicity equal to the free space wavelength.

The dielectric grating structure was presented in 2006 [38]. A pulsed laser beam is modified by applying a pulse-front tilt so as to illuminate the grating at a rate

corresponding to the electron velocity. Each grating pillar adds a π-phase shift to the fields, so an electron propagating between two gratings experiences a constant accelerating field. Experimental demonstration of an energy gain of 69.3 keV by 60 MeV electrons in 2013 [39] highlighted the key challenges of this acceleration scheme; the bunch was longer than an optical cycle and so the bunch energy was modulated, and only 2.2% of the electron beam entered the structure due to its small dimensions.

Bragg waveguides have also been proposed as accelerating structures. These waveguides consist of a vacuum aperture surrounded by multiple layers of alternating refractive index. The boundaries between the layers result in partial reflection of an EM wave. By controlling the thickness of the layers, these reflections combine with constructive interference, thus acting as an almost 100% reflector. This thickness was found to be optimum when it was equal to a quarter wave [40, 41]. To date there have been no experimental electron acceleration results for such Bragg waveguides.

Considering the most recent achievements, a gradient of 309.8±20.7 MV/m using picosecond pulses was achieved with damage of the grating structure observed [39], but simulations suggested that GV m^{-1} gradients were possible. Future work focussed on the use of femtosecond pulses, as the damage threshold in dielectric structures plateaus for shorter pulses [42]. Most recently, an average accelerating gradient of 850 MV/m was experimentally demonstrated with no observed damage of the structure. This was inferred from the 18.5 keV energy gain of 8 MeV electrons. 1-2% of electrons in a bunch were transmitted through the structure, and the interaction resulted in increase in energy spread. This is still far from the theoretical limit of the incident field which has been given as 13 GV/m for fused silica [43, 44].

The dimensions are a manufacturing challenge as they are too small to be fabricated by conventional means [12]. A range of fabrication techniques have been developed to reduce complexity and improve reproducibility, using techniques that are typical of the semiconductor industry. This allows for an accuracy of nanometres, or on order of a few percent [45, 46, 47].

The wall-plug efficiency of laser-driven accelerators has been estimated to be up to 10% when using solid state lasers [48, 49], assuming the laser wall-plug efficiency is 30% [8].

1.5 Terahertz structures

Considered here are structures that are not driven by an external THz field but have dimensions corresponding to the THz range. Only schemes which accelerate particles through a vacuum are considered; in particular the use of dielectric-lined structures.

A relativistic electron propagating through a dielectric-lined structure excites Cerenkov radiation which propagates behind with phase velocity equal to the electron velocity. The technique was first presented in 1988 [50], with a 21 MeV driving bunch travelling ahead of a 15 MeV witness bunch. The driving bunch generated longitudinal wakefields which imparted energy to the witness bunch. The fundamental wakefield mode was excited at 6 GHz and the maximum observed accelerating gradient was 0.3-0.5 MV/m.

The first experiments involving dielectric-lined slab-symmetric structures were performed in 2012 [51], achieving 150 keV acceleration of the tail of a 60 MeV electron bunch in a 20 mm long quartz-lined structure. The choice of a slab-symmetric structure reduced the effect of transverse wakefields, thus preventing blow-up of the beam. The fundamental wakefield mode was excited at 167 GHz. The current maximum accelerating gradient achieved in experiment is 320±17 MV/m [52], using a 100 mm long quartz-lined cylindrical waveguide, with the fundamental mode excited at 535 GHz. Studies of breakdown of the structures carried out at SLAC in 2006 estimated a decelerating field of 5.5 GV/m, with a surface breakdown threshold of 13.8 GV/m [53, 54]. At this gradient, the aluminium coating of the structure was ablated and microcracks appeared in the dielectric (SiO_2), which became a darker colour. A more recent study has shown peak fields of 2.8 GV/m in cylindrical waveguides, with no deterioration in performance over more than 100,000 pulses [52]. This was demonstrated in the same experimental run as the current maximum accelerating gradient.

Beam driven structures also have uses in bunch manipulation. For example, tunable dechirper structures have been used to remove the energy chirp of an electron bunch [55]. The electrons at the front on the pulse generate wakefields which affect the trailing parts of the bunch. Removing this energy variation across the bunch is of interests in FELs as smaller energy spread results in narrower bandwidths. A dechirper is to be installed on CLARA at Daresbury Laboratory [56] for this reason. A corrugated dechirper has been installed at LCLS [57], and has been used for energy chirp control. Other terahertz scale structures termed passive streakers have been used for generation of multicolour X-rays [58], and time resolved measurements of relativistic electron bunches [59].

1.6 THz-driven structures

A THz-driven scheme was first proposed in 2005 [60], using a slab-symmetric dielectric-lined structure. The THz was coupled in from the side using a metal grating into the dielectric, generating a standing wave in the direction of electron propagation, as shown in Figure 1.2. This simulation work was performed using a THz wavelength

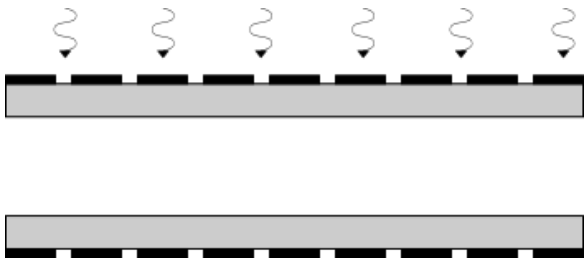

Figure 1.2: Side view of the side-coupled structure from [60]. The electron beam travels across the page, and the laser illuminates the top of the structure. Radiation couples in through the transverse slots in the conductor (black). The dielectric determines the field profile, and a standing wave with periodicity in the electron propagation direction is formed.

$\lambda = 340$ μm, with an accelerating gradient of 100 MV/m. The proposed THz source used difference frequency generation of two CO_2 laser beams in a non-linear crystal [61].

Later simulation work in 2013 considered cylindrical waveguides lined with a layer of chemical vapour deposited (CVD) diamond, which has one of the highest known breakdown limits and thermal conductivities at THz frequencies [62]. The THz pulse was coupled longitudinally into the waveguide in a radially polarised mode, and then propagated through the waveguide. The coupling mechanism itself was not explored. The effect of slippage from a short pulse due to a mismatch between the velocity of phase fronts and the velocity of the pulse envelope was highlighted.

In 2015 THz-driven acceleration of electrons was experimentally verified [12]. 60 keV electrons were accelerated by 7 keV using a THz-driven dielectric-lined cylindrical waveguide, giving an effective accelerating gradient of 2.5 MV/m with a peak of 8.5 MV/m. The low effective gradient was due to mismatch between the electron velocity and the phase velocity on the centre of the THz pulse. The THz was coupled in to the end of the waveguide using a dielectric-loaded horn, then reflected at the entrance using a pinhole aperture before co-propagating with the electron bunch.

This research has been developed further with the development of the segmented THz electron accelerator and manipulator (STEAM) device in 2018 [63]. An average accelerating gradient of 50 MV/m was achieved giving 30 keV acceleration and the device was also suitable for streaking, focussing, and compression. THz pulses with a transverse linear polarisation are launched into both sides of the device; the structure design is shown in Figure 1.3. The interaction region is split into segments, with each containing dielectric of varying thickness and length and isolated by metal sheets. The dielectric slabs serve to delay the THz pulse so that it overlaps with the bunch. The

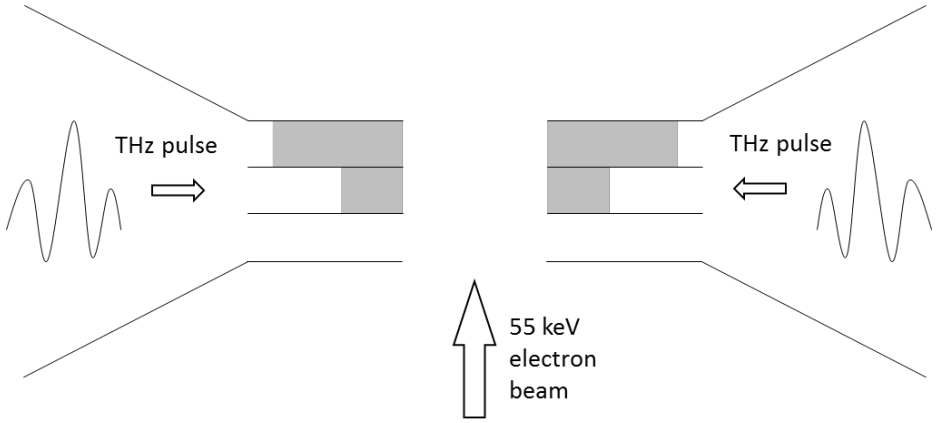

Figure 1.3: Drawing of the cross-section of the STEAM device [63]. Electron bunches propagate through the centre of the device, with THz pulses launched transverse to their propagation. The electric field of the THz pulse is polarised in the same direction as the electron bunches. The device is split into channels which contain dielectric of increasing length.

choice of thickness and length is important, especially for non-relativistic electrons where the velocity changes rapidly with increase in energy. The STEAM device is part of a proposal for an all-THz accelerator; there has also been development of an electron gun [64, 65, 66] and cavity-based linacs [67].

Control of the phase space of an electron bunch using a butterfly resonator has also been demonstrated with 70 keV electrons [68]. This butterfly resonator was a 30 μm thick aluminium foil into which a butterfly shape had been laser machined, as shown in Figure 1.4. This confined and enhanced the THz fields in the centre of the resonator. Tilting the resonator with respect to the electron propagation direction generated a longitudinal field component used for temporal compression.

More recently, an inverse free electron laser (IFEL) scheme [13] was used to modulate the energy of a 4-9 MeV electron beam by up to 150 keV. This scheme used a longitudinally propagating THz pulse through a curved parallel plate waveguide (CPPWG) inside the 300 mm long undulator. The CPPWG is used to match group and phase velocity [69], thus increasing the interaction length. The undulator field causes the electron bunch to oscillate, and a TE_{01} mode accelerates the bunches due to their transverse momentum component.

Efficiency of THz generation is a challenging aspect of use in particle acceleration. In 2013 a conversion efficiency of 3.8% was achieved using cryogenically cooled (to 150 K) lithium niobate [70]. Up to 10% efficiency has been predicted by cooling the lithium niobate to a temperature of 10 K [71]. Narrowband pulse generation is less efficient; the current record is 0.13% with the same setup predicted to reach 1%

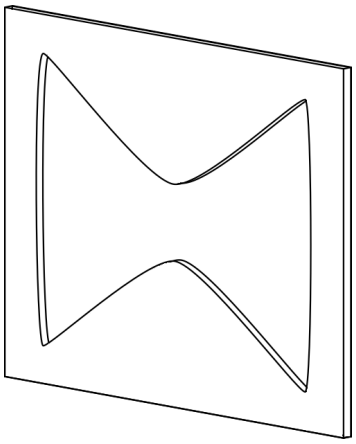

Figure 1.4: A butterfly resonator, as used to demonstrate control of the phase space of an electron bunch [68]. The resonator is made from 30 μm thick aluminium foil, and the structure is approximately 400 μm wide. It is tilted with respect to electron propagation.

efficiency [72]. It is clear that the use of a laser to generate the THz pulses is less efficient than using a laser itself.

1.7 Terahertz sources

The THz regime has been of interest since the 1920s [73], but has been difficult to access due to a lack of sources. The range is not well defined, but covers the range 100 GHz to 30 THz [11], between the microwave and infrared regions of the electromagnetic (EM) spectrum. Generation using electronic or laser sources is limited. Presented here is an overview of current techniques, with a brief discussion of generation using particle accelerators, and a focus on optical generation.

1.7.1 Accelerators

Accelerators are used to generate a wide range of frequencies from the EM spectrum. For example free electron lasers, in which the periodic magnetic field of an undulator leads to generation of a narrow cone of near-monochromatic radiation, are capable of generating high power THz radiation [74, 75]. This radiation is tunable by varying electron energy. However their large footprint means that they do not fit the criteria of a THz source for a 'table-top' accelerator.

An alternative THz source is the coherent transition radiation generated when an electron bunch crosses the boundary between two media with different dielectric properties [76, 77]. This generates a broadband THz pulse, suitable for time-resolved applications. At LCLS the peak electric field has reached 4.4 GV/m [77], for a pulse of $\sim$20 fs RMS length and spectrum 3-30 THz.

Narrowband THz pulses of frequency 367 ± 3 GHz have been generated using sub-ps electron bunches travelling through a dielectric-lined cylindrical structure [78]. This is coherent Cherenkov radiation (CCR). Cherenkov radiation is generated when a charged particle propagates through a dielectric medium at velocity greater than the phase velocity of light in the medium [79], and it is coherent provided that the driving bunch is shorter than a wavelength of the radiation. In this experiment the CCR was emitted using a waveguide taper at the end of the dielectric tube to control the divergence, and a horn antenna then used to direct the radiation to an interferometer for analysis. The CCR energy was dependent on bunch charge; a 10 μJ pulse was generated using a 200 pC bunch.

1.7.2 Optical generation

Optical rectification was first demonstrated in 1962 using a ruby laser illuminating a KDP crystal [80]. An overview of the process, as described in [81], is presented here. An electromagnetic field propagating through a medium exerts a force on the valence electrons. This is a small force, resulting in an electric polarisation of the medium. In a linear isotropic medium this polarisation is parallel and proportional to the EM field;

$$\mathbf{P} = \epsilon_0 \chi \mathbf{E} \ , \tag{1.1}$$

where ϵ_0 is the electric permittivity in vacuum and χ is electric susceptibility, a dimensionless constant. As $\mathbf{P}$ does not increase linearly with $\mathbf{E}$ indefinitely the polarisation must saturate. This non-linearity is accounted for by expressing the polarisation as a series expansion:

$$\mathbf{P} = \epsilon_0 \chi^{(1)} \mathbf{E} + \epsilon_0 \chi^{(2)} \mathbf{E}^2 + \epsilon_0 \chi^{(3)} \mathbf{E}^3 \dots \ . \tag{1.2}$$

$\chi^{(1)}$ is much larger than the higher order non-linear terms, which only contribute at high $\mathbf{E}$. For an incident EM field of the form

$$\mathbf{E} = E_0 \sin\left[\omega t\right] \ , \tag{1.3}$$

the resulting polarisation is given as

$$\mathbf{P} = \epsilon_0 \chi^{(1)} E_0 \sin\left[\omega t\right] + \epsilon_0 \chi^{(2)} E_0^2 \sin^2\left[\omega t\right] + \epsilon_0 \chi^{(3)} E_0^3 \sin^3\left[\omega t\right] \dots \ . \tag{1.4}$$

Rewriting in terms of sine and cosine;

$$\mathbf{P} = \epsilon_0 \chi^{(1)} E_0 \sin\left[\omega t\right] + \frac{\epsilon_0 \chi^{(2)}}{2} E_0^2 \left(1 - \cos\left[2\omega t\right]\right) + \frac{\epsilon_0 \chi^{(3)}}{4} E_0^3 \left(3 \sin\left[\omega t\right] - \sin\left[3\omega t\right]\right) + \dots \ . \tag{1.5}$$

Therefore if only $\chi^{(1)}$ is significant, the polarisation 'wave' corresponds to an oscillatory current. Otherwise, this wave has a different harmonic profile to the incident **E**. The two components of the second order term of Equation (1.5) are of most interest. Firstly, the existence of the time-independent E_0^2 term, which corresponds to a constant polarisation of the medium, is defined as optical rectification. The $\cos[2\omega t]$ term implies variation of the polarisation at twice the frequency of the incident EM field. Light which is re-radiated from the medium therefore contains this second harmonic term. This second harmonic generation (SHG) can be used to generate THz radiation by using an input EM field with multiple frequencies. Using a wave of the form

$$\mathbf{E} = E_1 \sin[\omega_1 t] + E_2 \sin[\omega_2 t] \ , \tag{1.6}$$

and substituting into Equation (1.5), the second term is given as

$$\epsilon_0 \chi^{(2)} \left(E_1^2 \sin^2[\omega_1 t] + E_2^2 \sin^2[\omega_2 t] + E_1 E_2 \left(\cos[(\omega_1 - \omega_2)\, t] - \cos[(\omega_1 + \omega_2)\, t] \right) \right) \ . \tag{1.7}$$

The last term gives both sum and difference terms. Assuming $\omega_1 \approx \omega_2$ and removing all terms which over time periods longer than those associated with ω_1 and ω_2 average to zero, the polarisation is

$$\mathbf{P} = \frac{\epsilon_0 \chi^{(2)}}{2} \left(E_1^2 + E_2^2 + E_1 E_2 \cos[(\omega_1 - \omega_2)\, t] \right) \ . \tag{1.8}$$

The difference term does not average to zero as the corresponding time period is much larger. Therefore there are two constant polarisation terms, and a slowly varying oscillation. This is difference frequency mixing and results in re-radiation from the medium in the THz regime. Due to the small non-linear term, conversion efficiency is small.

THz generation using lithium niobate ($LiNbO_3$) [82] was first demonstrated in 1971. $LiNbO_3$ is a common source, but other crystals are also used. For example, in 2017 [83] a 5 GV/m single-cycle pulse was generated using an organic crystal, whilst a narrowband pulse was also generated with field strength in the 100 MV/m range. The minimum bandwidth achieved was 45 GHz FWHM, centred at 1.8 THz. The narrowband pulse was generated using the same crystal, but with a change in the input laser pulse which was split in two, chirped, and then recombined to create a temporally modulated intensity profile. This is the chirped pulse beating method [84]. An alternative method for narrowband generation is to use periodically poled lithium niobate (PPLN), as demonstrated by Lee *et al* [85]. The length controls the

bandwidth, and the centre frequency is controlled by the periodicity of the alternating poles and the group velocity mismatch between the input laser and generated THz. Much work has focussed on improving efficiency of the process [86, 87, 88].

A longitudinal field has been generated using two identical non-linear crystals mounted together such that their optical axes are reversed. This means that the field generated had a polarity flip in the centre, resulting in a longitudinal field component. This gave a field amplitude of 1.17 MV/m [89].

Photoconductive antennas are semiconductors held under a large electric bias field. The surface is then excited by an optical pump laser. Charge carriers are liberated and accelerate due to the bias field, generating EM radiation. THz generation using such antennas was originally demonstrated in 1984 [90]. Longitudinally polarised field strengths of 220 kV/m have more recently been achieved [91], which was approximately half of the maximum absolute field.

Recent work has produced a maximum longitudinal field gradient of 150 MV/m [92]. Radially polarised THz pulses were first generated were generated via the interaction of a laser and thin metallic foil. An intense laser pulse ionises the foil surface, resulting in a plasma and acceleration of electrons, which escape the surface and result in emission of radiation [93]. Focussing this THz radiation, which has the same polarisation as the input laser, creates a strong longitudinal field. In [92], the ratio of transverse to longitudinal field was 2:1.

The final method of interest is the use of spintronic sources, which emit ultrabroadband (1-30 THz) radiation [94]. These sources consist of layers of metal thin films which are magnetised using external magnets. The local magnetic field dictates the polarisation of emitted THz. A longitudinal field of maximum 17.7 MV/m has been demonstrated with this method [95].

A summary of the methods to generate longitudinal THz fields and the maximum field gradient achieved is presented in Table 1.1. Each of these methods generates an ultrashort THz pulse.

1.8 Outline of this thesis

The thesis is organised as follows. Chapter 2 outlines the underpinning theory of dielectric-lined waveguides (DLWs). In Chapter 3, the dispersive nature of DLWs and the effect on propagating pulse is discussed. Chapter 4 introduces the figures of merit used for characterising accelerating structures, including synchronisation of electrons and radiation, and methods of coupling the radiation into the structure. Chapter 5 outlines the simulation methods used in this thesis to design DLW structures for acceleration and deflection of electrons of different energies. The design

Table 1.1: Summary of experimental generation of longitudinal THz fields, including the method of generation and the field gradient achieved. In each case the THz pulses were single-cycle (broadband).

Field gradient	Peak frequency	Method	Paper	Ref.
1.17 MV/m	0.4 THz	Two crystals with opposite polarisation	Cliffe *et al.* 2016	[89]
220 kV/m	0.2 THz	Photoconductive antenna	Cliffe *et al.* 2014	[91]
150 MV/m	3 THz	Laser-thin metallic foil interaction	Woldegeorgis *et al.* 2018	[92]
17.7 MV/m	1 THz	Magnetic field tailoring of spintronic source	Hibberd *et al.* 2018	[95]

of a dielectric-lined waveguide for acceleration of relativistic electrons is presented in Chapter 6, including optimisation of the waveguide parameters and coupler design. Testing of manufactured structures, including dispersion measurements using THz time-domain spectroscopy and microscopic dimensional analysis, is discussed in Chapter 7. Chapter 8 details the experimental setup and results of demonstration of electron bunch manipulation at the CLARA facility. Finally, conclusions of the work and an evaluation of the current limitations is presented in Chapter 9, with a discussion of the future of THz-driven DLWs and how they can be made more competitive in the field of novel acceleration techniques.

Chapter 2

Underpinning theory of waveguide modes

In this chapter the propagation of electromagnetic fields is discussed, starting with Maxwell's equations to derive the wave equations. The Hertz potentials are used as a method of calculating field components, applied to the specific example of a dielectric-lined waveguide (DLW). Solving the wave equation for the DLW, the dispersion relation is then obtained. Finally the dispersive properties of different waveguide modes are considered. In this chapter two example DLWs are considered. Both were manufactured to be used in electron manipulation experiments; one for deflection of 100 keV electrons, and the other for acceleration of 35 MeV electrons.

2.1 Field propagation in free space

Maxwell's equations are the starting point for classical electromagnetism, and therefore the description of electromagnetic fields. The formalisms used here are the same as in [96] by Jackson.

$$\nabla \cdot \mathbf{D} = \rho \ , \tag{2.1}$$

$$\nabla \cdot \mathbf{B} = 0 \ , \tag{2.2}$$

$$\nabla \times \mathbf{E} = -\frac{\partial \mathbf{B}}{\partial t} \ , \tag{2.3}$$

$$\nabla \times \mathbf{H} = \frac{\partial \mathbf{D}}{\partial t} + \mathbf{J} \tag{2.4}$$

The terms are defined as

$\mathbf{E}$ – electric field intensity,

$\mathbf{D}$ – electric current density,

$\mathbf{H}$ – magnetic field intensity,

$\mathbf{B}$ – magnetic flux density,

$\mathbf{J}$ – electric current density,

ρ – electric charge density,

where for external sources in vacuum

$$\mathbf{D} = \epsilon \mathbf{E} \ , \tag{2.5}$$

$$\mathbf{B} = \mu \mathbf{H} \ , \tag{2.6}$$

where ϵ is the permittivity and μ is the permeability:

$$\epsilon = \epsilon_r \epsilon_0 \ , \tag{2.7}$$

$$\mu = \mu_r \mu_0 \tag{2.8}$$

In general these are complex, frequency dependent, and can be tensors, although these properties are not considered in this work. In particular, the value of ϵ_r is assumed to be independent of frequency. A subscript 0 denotes the values in vacuum, and subscript r denotes the relative value, which depends on the medium. It is assumed that $\mu_r = 1$ throughout this thesis. Maxwell's equations are automatically satisfied if one writes $\mathbf{E}$ and $\mathbf{H}$ in terms of potentials;

$$\mathbf{H} = \frac{1}{\mu} \nabla \times \mathbf{A} \ , \tag{2.9}$$

where $\mathbf{A}$ is a vector potenital. To describe $\mathbf{E}$, one combines Equation (2.9) with Equation (2.3). This yields,

$$\nabla \times \left(\mathbf{E} + \frac{\partial \mathbf{A}}{\partial t} \right) = 0 \ , \tag{2.10}$$

which leads to

$$\mathbf{E} = -\nabla \Phi - \frac{\partial \mathbf{A}}{\partial t} \ , \tag{2.11}$$

where Φ is a scalar potential and thus the curl of $\nabla\Phi$ is zero. Maxwell's equations are now reduced to two equations,

$$\nabla^2\Phi + \frac{\partial}{\partial t}\left(\nabla\cdot\mathbf{A}\right) = -\frac{\rho}{\epsilon}\ , \tag{2.12}$$

$$\nabla^2\mathbf{A} - \mu\epsilon\frac{\partial^2\mathbf{A}}{\partial t^2} - \nabla\left(\nabla\cdot\mathbf{A} + \mu\epsilon\frac{\partial\Phi}{\partial t}\right) = -\mu\mathbf{J}\ . \tag{2.13}$$

The potentials require uncoupling. Under the transform

$$\mathbf{A} \rightarrow \mathbf{A} + \nabla\phi\ , \tag{2.14}$$

$$\Phi \rightarrow \Phi - \frac{\partial\phi}{\partial t}\ , \tag{2.15}$$

the fields $\mathbf{B}$ and $\mathbf{E}$ are unchanged. This means that the potentials can be chosen such that the Lorentz condition is satisfied;

$$\nabla\cdot\mathbf{A} + \mu\epsilon\frac{\partial\Phi}{\partial t} = 0\ . \tag{2.16}$$

Applying this to Equations (2.12) and (2.13) gives the wave equations

$$\nabla^2\Phi - \mu\epsilon\frac{\partial^2\Phi}{\partial t} = -\frac{\rho}{\epsilon}\ , \tag{2.17}$$

$$\nabla^2\mathbf{A} - \mu\epsilon\frac{\partial^2\mathbf{A}}{\partial t} = -\mu\mathbf{J}\ . \tag{2.18}$$

These have solutions in terms of both space and time. $\mathbf{A}$ and Φ can be expressed by a sum of the plane waves of the form $\exp\left[i(\mathbf{k}\cdot\mathbf{r} - \omega t)\right]$, where $\mathbf{k} = (k_x, k_y, k_z)$ is the wavenumber, a currently unknown parameter which can be complex, and $\mathbf{r} = (x, y, z)$. $\mathbf{r}$ is a spatial coordinate vector and ω is an angular frequency which controls the oscillation of the wave. This is the Fourier series, and the wave equation must be valid for a sum of plane waves as it is for a single plane wave. Substituting the Fourier transform,

$$\Phi\left(t\right) = \int_{-\infty}^{+\infty}\tilde{\phi}\left(\omega\right)\exp\left[-i\omega t\right]\mathrm{d}\omega\ , \tag{2.19}$$

into Equation (2.17) in free space we obtain:

$$\frac{\partial^2}{\partial t^2}\int_{-\infty}^{+\infty}\tilde{\phi}(\omega)\exp\left[-i\omega t\right]\mathrm{d}\omega - \nabla^2\int_{-\infty}^{+\infty}\tilde{\phi}(\omega)\exp\left[-i\omega t\right]\mathrm{d}\omega = 0\ , \tag{2.20}$$

$$\int_{-\infty}^{+\infty}\left(-\omega^2-\nabla^2\right)\tilde{\phi}(\omega)\exp\left[-i\omega t\right]\mathrm{d}\omega = 0\ . \tag{2.21}$$

$$\tag{2.22}$$

It is therefore required that

$$-\omega^2\tilde{\phi}(\omega) - \nabla^2\tilde{\phi}(\omega) = 0\ , \tag{2.23}$$

which is true for all frequencies. Therefore the $\exp\left[i(\mathbf{k}\cdot\mathbf{r}-\omega t)\right]$ term can be removed with no loss of generality, provided μ and ϵ are independent of frequency; this is valid in free space.

Assuming a linear isotropic media and adding external sources of polarisation, $\mathbf{P}_{ext}$, and magnetisation, $\mathbf{M}_{ext}$, the macroscopic fields are defined as

$$\mathbf{D} = \epsilon\mathbf{E} + \mathbf{P}_{ext}\ , \tag{2.24}$$

$$\mathbf{B} = \mu\mathbf{H} + \mu_0\mathbf{M}_{ext}\ . \tag{2.25}$$

Inserting Equation (2.24) into Equation (2.11), and Equation (2.25) into Equation (2.9), produces new wave equations;

$$\mu\epsilon\frac{\partial^2\Phi}{\partial t^2} - \nabla^2\Phi = -\frac{1}{\epsilon}\nabla\cdot\mathbf{P}_{ext} \tag{2.26}$$

$$\mu\epsilon\frac{\partial^2\mathbf{A}}{\partial t^2} - \nabla^2\mathbf{A} = \mu\frac{\partial\mathbf{P}_{ext}}{\partial t} + \mu_0\nabla\times\mathbf{M}_{ext}\ . \tag{2.27}$$

2.1.1 Hertz vectors

In a source free region $\nabla\cdot\mathbf{E} = 0$. It is therefore possible to represent the electric field as the curl of a vector potential function. Both $\mathbf{E}$ and $\mathbf{H}$ can be defined in this way. Redefining the potentials in the same form as in [96] gives

$$\Phi = -\frac{1}{\epsilon}\nabla\cdot\mathbf{\Pi}_e\ , \tag{2.28}$$

$$A = \mu\frac{\partial\mathbf{\Pi}_e}{\partial t} + \mu_0\nabla\times\mathbf{\Pi}_m\ , \tag{2.29}$$

where $\mathbf{\Pi_e}$ is the electric Hertz vector and $\mathbf{\Pi_m}$ is the magnetic Hertz vector. The wave equations are still satisfied;

$$\nabla \cdot \left[\nabla^2 \mathbf{\Pi}_e - \mu\epsilon \frac{\partial^2 \mathbf{\Pi}_e}{\partial t} + \mathbf{P}_{ext} \right] = 0 \ , \quad (2.30)$$

$$\mu \frac{\partial}{\partial t} \left[\nabla^2 \mathbf{\Pi}_e - \mu\epsilon \frac{\partial^2 \mathbf{\Pi}_e}{\partial t} + \mathbf{P}_{ext} \right] + \mu_0 \nabla \times \left[\nabla^2 \mathbf{\Pi}_m - \mu\epsilon \frac{\partial^2 \mathbf{\Pi}_m}{\partial t^2} + \mathbf{M}_{ext} \right] = 0 \ . \quad (2.31)$$

The bracketed term in Equation (2.30) must be equal to the curl of some vector, which can be defined as $\frac{\mu_0}{\mu}\mathbf{V}$. The second bracketed term in Equation (2.31) must be equal to the gradient of a scalar, defined here as $\frac{\partial \zeta}{\partial t}$. The final wave equations are given by:

$$\mu\epsilon \frac{\partial^2 \mathbf{\Pi}_e}{\partial t^2} - \nabla^2 \mathbf{\Pi}_e = \mathbf{P}_{ext} - \frac{\mu_0}{\mu} \nabla \times \mathbf{V} \ , \quad (2.32)$$

$$\mu\epsilon \frac{\partial^2 \mathbf{\Pi}_m}{\partial t^2} - \nabla^2 \mathbf{\Pi}_m = \mathbf{M}_{ext} + \frac{\partial \mathbf{V}}{\partial t} + \nabla \frac{\partial \zeta}{\partial t} \ , \quad (2.33)$$

The functions $\mathbf{V}$ and ζ can be removed via gauge transformation of the Hertzian potentials with no loss of generality. The electric and magnetic fields can be expressed in terms of the potentials:

$$\mathbf{E} = \frac{1}{\epsilon} \nabla \left(\nabla \cdot \mathbf{\Pi}_e \right) - \mu \frac{\partial^2 \mathbf{\Pi}_e}{\partial t^2} - \mu_0 \nabla \times \frac{\partial \nabla \mathbf{\Pi}_m}{\partial t} \ , \quad (2.34)$$

$$\mathbf{B} = \mu \nabla \times \frac{\partial \mathbf{\Pi}_e}{\partial t} + \mu_0 \nabla \times \nabla \times \mathbf{\Pi}_m \ , \quad (2.35)$$

where it is assumed that $\mathbf{P}_{ext},\ \mathbf{M}_{ext} = 0$; there are no external sources.

2.2 Waveguide modes

The fields can be constrained by addition of boundary conditions. These conditions can only be satisfied by certain field configurations, termed modes. There are an infinite number of unique configurations which propagate with a given $\mathbf{k}$ for each frequency ω. The fields constrained by the boundary conditions can be made up of any combination of modes, but a feature of the propagation of a single mode is that the form is unchanged with time. The analysis of the modes of any waveguide involves choosing potentials that satisfy the wave equation. The boundary conditions at the vacuum-conductor boundary of a hollow waveguide with conducting walls are:

$$\hat{n} \cdot \mathbf{D} = \rho_s \ , \tag{2.36}$$

$$\hat{n} \times \mathbf{E} = 0 \tag{2.37}$$

$$\hat{n} \cdot \mathbf{B} = 0 \tag{2.38}$$

$$\hat{n} \times \mathbf{H} = \mathbf{J}_s \ , \tag{2.39}$$

where the subscript s denotes the surface, and the unit vector $\hat{n}$ is tangential to the boundary. The field components can be derived using the Hertz potentials:

$$\mathbf{\Pi}_e = \hat{z}\Pi_e(\mathbf{r}) \ , \tag{2.40}$$

$$\mathbf{\Pi}_m = \hat{z}\Pi_m(\mathbf{r}) \ , \tag{2.41}$$

where $\hat{z}$ is the unit vector in the direction of wave propagation. Defining the potentials in the z-direction is necessary to solve for all boundary conditions. A set of modes are obtained by setting $\Pi_m = 0$; in this case the magnetic field only has components in the transverse plane. These modes are subsequently termed transverse magnetic (TM). Conversely setting $\Pi_e = 0$ produces the transverse electric (TE) modes, in which the electric field has components only in the transverse plane.

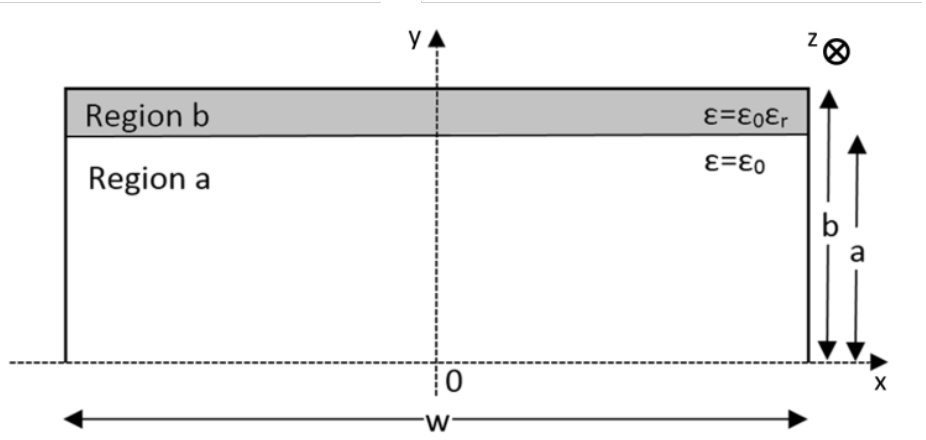

Figure 2.1: Half cross-section of a dielectric-lined waveguide. Region a defines the vacuum component of the DLW, and region b the dielectric component, with relative permittivity ϵ_r. The full parameters of the waveguide are width w, vacuum aperture $2a$, dielectric thickness $b - a$, which will be defined throughout this thesis as δ. The wave propagates in the z direction.

2.3 Dielectric-lined waveguide modes

The addition of two dielectric slabs to the waveguide lining the top and bottom, as shown in Figure 2.1, changes the results in a new set of boundary conditions due to the vacuum-dielectric boundary. These conditions are given as:

$$\hat{n} \cdot \mathbf{D}_a = \hat{n} \cdot \mathbf{D}_b \tag{2.42}$$

$$\hat{n} \cdot \mathbf{B}_a = \hat{n} \cdot \mathbf{B}_b \tag{2.43}$$

$$\hat{n} \times \mathbf{E}_a = \hat{n} \times \mathbf{E}_b \tag{2.44}$$

$$\hat{n} \times \mathbf{H}_a = \hat{n} \times \mathbf{H}_b \ , \tag{2.45}$$

where a denotes the vacuum and b denotes the dielectric, as in Figure 2.1. Using the z-directed Hertz potentials does not produce solutions for these boundary conditions and so TE and TM modes individually are not valid modes. Instead a hybrid mode solution is required; this is obtained by redefining the Hertz potential and using a new mode specification. Unique solutions are then obtained, which are not combinations of multiple modes. This requires directing the potentials along the vacuum-dielectric boundary, in this case the y-direction:

$$\mathbf{\Pi}_e = \hat{y}\psi_e(x, y) \exp\left[-i\beta z\right] \ , \tag{2.46}$$

$$\mathbf{\Pi}_h = \hat{y}\psi_h(x, y) \exp\left[-i\beta z\right] \ , \tag{2.47}$$

where $\beta = k_z$, the propagation constant inside the waveguide. Equations (2.34) and (2.35) are used to obtain all field components. $\psi_e = 0$ gives the field components for the first set of unique solutions;

$$E_x = \omega\mu_0\beta\psi_h \ , \tag{2.48}$$

$$E_y = 0 \ , \tag{2.49}$$

$$E_z = -j\omega\mu_0\frac{\partial\psi_h}{\partial x} \ , \tag{2.50}$$

$$H_x = \frac{\partial^2\psi_h}{\partial x\partial y} \ , \tag{2.51}$$

$$H_y = \frac{\partial^2\psi_h}{\partial y^2} + \epsilon_r k_0^2\psi_h \ , \tag{2.52}$$

$$H_z = -j\beta\frac{\partial\psi_h}{\partial y} \ . \tag{2.53}$$

For the second set of unique solutions, $\psi_h = 0$:

$$E_x = \frac{\partial^2\psi_e}{\partial x\partial y} \ , \tag{2.54}$$

$$E_y = \frac{\partial^2\psi_e}{\partial y^2} + \epsilon_r k_0^2\psi_e \ , \tag{2.55}$$

$$E_z = -j\beta\frac{\partial\psi_e}{\partial y} \ , \tag{2.56}$$

$$H_x = -\omega\epsilon_0\beta\psi_e \ , \tag{2.57}$$

$$H_y = 0 \ , \tag{2.58}$$

$$H_z = -j\omega\epsilon\frac{\partial\psi_e}{\partial x} \ . \tag{2.59}$$

The field components of the modes are found by following the same analysis as in [97]. There are two distinct mode definitions, both of which satisfy the boundary conditions.

2.3.1 Longitudinal Section Magnetic modes

Setting $\psi_h = 0$ results in a group of modes termed Longitudinal Section Magnetic (LSM). Two Hertz scalar potentials are defined, both of which satisfy the wave equation and the boundary conditions. The first set is termed the 'odd' modes:

$$\psi_{emn} = \begin{cases} A_{mn}\sin\left[\frac{m\pi}{w}\left(x+\frac{w}{2}\right)\right]\sin\left(k_y^a y\right) & \text{if } 0 \le y \le a \\ B_{mn}\sin\left[\frac{m\pi}{w}\left(x+\frac{w}{2}\right)\right]\cos\left[k_y^b(b-y)\right] & \text{if } a < y \le b \end{cases} \tag{2.60}$$

The second set is termed the 'even' modes;

$$\psi_{emn} = \begin{cases} A_{mn} \sin\left[\frac{m\pi}{w}\left(x+\frac{w}{2}\right)\right] \cos\left(k_y^a y\right) & \text{if } 0 \le y \le a \\ B_{mn} \sin\left[\frac{m\pi}{w}\left(x+\frac{w}{2}\right)\right] \cos\left[k_y^b (b-y)\right] & \text{if } a < y \le b\ . \end{cases} \tag{2.61}$$

The constants A_{mn} and B_{mn} are dependent on both frequency and DLW parameters. $m,\ n$ are indices which must be integers; they define the number of half-wavelength variations of the field configurations in x and y respectively, corresponding to the mode number. The choice of odd or even modes depends on the boundary condition of the x-axis. A magnetic wall ($H_\perp = 0$) corresponds to the odd modes, and an electric wall corresponds to the even modes. The two sets of potentials contain the y-directed propagation constants; k_y^a in the vacuum and k_y^b in the dielectric. They are defined as:

$$k_{y,mn}^a = \sqrt{k_0^2 - \left(\frac{m\pi}{w}\right)^2 - \beta_{mn}^2}\ , \tag{2.62}$$

$$k_{y,mn}^b = \sqrt{\epsilon_r k_0^2 - \left(\frac{m\pi}{w}\right)^2 - \beta_{mn}^2}\ , \tag{2.63}$$

where ϵ_r is the relative permittivity of the dielectric. The subscript mn is dropped from the wavenumbers for conciseness.

Odd modes

The field components of the 'odd' modes are given by

$$E_x = \begin{cases} A\frac{m\pi}{w} k_y^a \cos\left[\frac{m\pi}{w}\left(x+\frac{w}{2}\right)\right] \cos\left[k_y^a y\right], & 0 \le y \le a \\ B\frac{m\pi}{w} k_y^b \cos\left[\frac{m\pi}{w}\left(x+\frac{w}{2}\right)\right] \sin\left[k_y^b (b-y)\right], & a < y \le b \end{cases} \tag{2.64}$$

$$E_y = \begin{cases} A k_c^2 \sin\left[\frac{m\pi}{w}\left(x+\frac{w}{2}\right)\right] \sin\left[k_y^a y\right], & 0 \le y \le a \\ B k_c^2 \sin\left[\frac{m\pi}{w}\left(x+\frac{w}{2}\right)\right] \cos\left[k_y^b (b-y)\right], & a < y \le b \end{cases} \tag{2.65}$$

$$E_z = \begin{cases} A(-i\beta) k_y^a \sin\left[\frac{m\pi}{w}\left(x+\frac{w}{2}\right)\right] \cos\left[k_y^a y\right], & 0 \le y \le a \\ B(-i\beta) k_y^b \sin\left[\frac{m\pi}{w}\left(x+\frac{w}{2}\right)\right] \sin\left[k_y^b (b-y)\right], & a < y \le b \end{cases} \tag{2.66}$$

$$H_x = \begin{cases} -A\omega\epsilon_0\beta \sin\left[\frac{m\pi}{w}\left(x+\frac{w}{2}\right)\right] \sin\left[k_y^a y\right], & 0 \le y \le a \\ -B\omega\epsilon\beta \sin\left[\frac{m\pi}{w}\left(x+\frac{w}{2}\right)\right] \cos\left[k_y^b (b-y)\right], & a < y \le b \end{cases} \tag{2.67}$$

$$H_z = \begin{cases} Ai\omega\epsilon_0 \frac{m\pi}{w} \cos\left[\frac{m\pi}{w}\left(x+\frac{w}{2}\right)\right] \sin\left[k_y^a y\right], & 0 \le y \le a \\ -Bi\omega\epsilon \frac{m\pi}{w} \cos\left[\frac{m\pi}{w}\left(x+\frac{w}{2}\right)\right] \cos\left[k_y^b (b-y)\right], & a < y \le b \end{cases} \tag{2.68}$$

where $k_c^2 = (\frac{m\pi}{w})^2 + \beta^2$ and the subscript mn has been dropped for conciseness. The tangential electric and magnetic field components are continuous on the boundary, $y = a$, leading to

$$\begin{aligned} Ak_y^a \cos\left(k_y^a a\right) &= Bk_y^b \sin\left(k_y^b(b-a)\right) \\ A\sin\left(k_y^a\right) &= B\epsilon_r \cos\left(k_y^b(b-a)\right) \ . \end{aligned} \tag{2.69}$$

The two simultaneous equations in Equation (2.69) are solved to cancel the constants, giving the dispersion relation;

$$k_y^b \tan\left(k_y^b(b-a)\right) = \epsilon_r k_y^a \cot\left(k_y^a a\right) \ . \tag{2.70}$$

This is a function of ω and β, and must be solved numerically. Solutions to $\beta(\omega)$ were found using *Mathematica* for all dispersion relations, unless otherwise stated. A built-in root finding algorithm was used to find values of β for a given m and ω, which satisfy Equation (2.70). There an infinite number of values of β which satisfy the dispersion relation, each corresponding to a value of n. To obtain a full solution, $\beta(\omega)$, a frequency range was specified, the value of β for a given m and n found at each frequency, and the resulting list interpolated to give an interpolated function. The accuracy of this function depends on the step size and is only valid in the frequency range specified. Different values of m and n correspond to a different LSM_{mn} mode [97]. The solutions to Equation (2.70) are 'odd' because $m = 1, 3, 5, \ldots$, corresponding to modes with an on-axis E_z field.

Even modes

The field components of the 'even' solutions ($n = 0, 2, 4, \ldots$) are given by

$$E_x = \begin{cases} A\frac{m\pi}{w}k_y^a \cos\left[\frac{m\pi}{w}\left(x+\frac{w}{2}\right)\right]\sin\left[k_y^a y\right], & 0 \le y \le a \\ B\frac{m\pi}{w}k_y^b \cos\left[\frac{m\pi}{w}\left(x+\frac{w}{2}\right)\right]\sin\left[k_y^b(b-y)\right], & a < y \le b \end{cases} \tag{2.71}$$

$$E_y = \begin{cases} Ak_c^2 \sin\left[\frac{m\pi}{w}\left(x+\frac{w}{2}\right)\right]\cos\left[k_y^a y\right], & 0 \le y \le a \\ Bk_c^2 \sin\left[\frac{m\pi}{w}\left(x+\frac{w}{2}\right)\right]\cos\left[k_y^b(b-y)\right], & a < y \le b \end{cases} \tag{2.72}$$

$$E_z = \begin{cases} A(-i\beta)k_y^a \sin\left[\frac{m\pi}{w}\left(x+\frac{w}{2}\right)\right]\sin\left[k_y^a y\right], & 0 \le y < a \\ B(-i\beta)k_y^b \sin\left[\frac{m\pi}{w}\left(x+\frac{w}{2}\right)\right]\sin\left[k_y^b(b-y)\right], & a < y < b \end{cases} \tag{2.73}$$

$$H_x = \begin{cases} -A\omega\epsilon_0\beta \sin\left[\frac{m\pi}{w}\left(x+\frac{w}{2}\right)\right]\cos\left[k_y^a y\right], & 0 \le y \le a \\ -B\omega\epsilon\beta \sin\left[\frac{m\pi}{w}\left(x+\frac{w}{2}\right)\right]\cos\left[k_y^b(b-y)\right], & a < y \le b \end{cases} \tag{2.74}$$

$$H_z = \begin{cases} Ai\omega\epsilon_0\beta\frac{m\pi}{w} \cos\left[\frac{m\pi}{w}\left(x+\frac{w}{2}\right)\right]\cos\left[k_y^a y\right], & 0 \le y \le a \\ -Bi\omega\epsilon\beta\frac{m\pi}{w} \cos\left[\frac{m\pi}{w}\left(x+\frac{w}{2}\right)\right]\cos\left[k_y^b(b-y)\right], & a < y \le b \end{cases} \tag{2.75}$$

with the dispersion relation

$$k_y^b \tan\left(k_y^b(b-a)\right) = -\epsilon_r k_y^a \tan\left(k_y^a a\right) \ . \tag{2.76}$$

This is solved as with Equation (2.70), and corresponds to modes with $E_z = 0$ on-axis. The modes are 'even' because $m = 0, 2, 4, \ldots$.

Modes considered in this thesis

The modes considered in this work are the deflecting LSM_{01} mode, for which only the transverse fields are non-zero on-axis, and the accelerating LSM_{11} mode, for which the longitudinal electric field is non-zero on-axis.

2.3.2 Longitudinal Section Electric modes

The longitudinal section electric (LSE) modes are found by setting $\psi_e = 0$. As with the LSM modes, odd and even modes can be defined. The LSE modes are not explicitly studied in this thesis, but are included for completeness of the DLW mode solutions. In particular, the LSE_{11} mode has a non-zero E_z field component. Based purely on this observation, the mode has uses in acceleration.
For 'odd' modes,

$$\psi_{hmn} = \begin{cases} C_{mn}\frac{1}{i\omega\mu_0} \cos\left[\frac{m\pi}{w}\left(x+\frac{w}{2}\right)\right]\cos\left(k_y^a y\right) & \text{if } 0 \le y \le a \\ D_{mn}\frac{1}{i\omega\mu_0} \cos\left[\frac{m\pi}{w}\left(x+\frac{w}{2}\right)\right]\sin\left[k_y^b(b-y)\right] & \text{if } a < y \le b \end{cases} \tag{2.77}$$

where the exponential components has been dropped for conciseness. C_{mn} and D_{mn} are frequency-dependent coefficients. The field components are then given by

$$E_x = \begin{cases} C(-i\beta)\cos\left[\frac{m\pi}{w}\left(x+\frac{w}{2}\right)\right]\cos\left[k_y^a y\right], & 0 \le y \le a \\ D(-i\beta)\cos\left[\frac{m\pi}{w}\left(x+\frac{w}{2}\right)\right]\sin\left[k_y^b(b-y)\right], & a < y \le b \end{cases} \tag{2.78}$$

$$E_z = \begin{cases} C\frac{m\pi}{w}\sin\left[\frac{m\pi}{w}\left(x+\frac{w}{2}\right)\right]\cos\left[k_y^a y\right], & 0 \le y \le a \\ D\frac{m\pi}{w}\sin\left[\frac{m\pi}{w}\left(x+\frac{w}{2}\right)\right]\sin\left[k_y^b(b-y)\right], & a < y \le b \end{cases} \tag{2.79}$$

$$H_x = \begin{cases} C\frac{1}{i\omega\mu_0}k_y^a\frac{m\pi}{w}\sin\left[\frac{m\pi}{w}\left(x+\frac{w}{2}\right)\right]\sin\left[k_y^a y\right], & 0 \le y \le a \\ D\frac{1}{i\omega\mu_0}k_y^b\frac{m\pi}{w}\sin\left[\frac{m\pi}{w}\left(x+\frac{w}{2}\right)\right]\cos\left[k_y^b(b-y)\right], & a < y \le b \end{cases} \tag{2.80}$$

$$H_y = \begin{cases} C\frac{1}{i\omega\mu_0}k_c^2\cos\left[\frac{m\pi}{w}\left(x+\frac{w}{2}\right)\right]\cos\left[k_y^a y\right], & 0 \le y \le a \\ D\frac{1}{i\omega\mu_0}k_c^2\cos\left[\frac{m\pi}{w}\left(x+\frac{w}{2}\right)\right]\sin\left[k_y^a y\right], & a < y \le b \end{cases} \tag{2.81}$$

$$H_z = \begin{cases} C\frac{1}{\omega\mu_0}\beta k_y^a\cos\left[\frac{m\pi}{w}\left(x+\frac{w}{2}\right)\right]\sin\left[k_y^a y\right], & 0 \le y \le a \\ D\frac{1}{\omega\mu_0}\beta k_y^b\cos\left[\frac{m\pi}{w}\left(x+\frac{w}{2}\right)\right]\cos\left[k_y^b(b-y)\right], & a < y \le b \end{cases} \tag{2.82}$$

The dispersion relation is solved in the same way as the LSM_{mn} modes, giving

$$k_y^b \cot\left[k_y^b(b-a)\right] = k_y^a \tan\left[k_y^a a\right] \ , \tag{2.83}$$

which is similar to Equation 2.70. This corresponds to an accelerating mode with an on-axis E_z field.
For the 'even' modes,

$$\psi_{emn} = \begin{cases} C_{mn}\frac{1}{i\omega\mu_0}\cos\left[\frac{m\pi}{w}\left(x+\frac{w}{2}\right)\right]\sin\left(k_y^a y\right) & \text{if } 0 \le y \le a \\ D_{mn}\frac{1}{i\omega\mu_0}\cos\left[\frac{m\pi}{w}\left(x+\frac{w}{2}\right)\right]\sin\left[k_y^b(b-y)\right] & \text{if } a < y \le b \end{cases} \tag{2.84}$$

where the exponential components has been dropped for conciseness. C_{mn} and D_{mn} are frequency-dependent coefficients. The field components are then given by

$$E_x = \begin{cases} C(-i\beta)\cos\left[\frac{m\pi}{w}\left(x+\frac{w}{2}\right)\right]\sin\left[k_y^a y\right], & 0 \le y \le a \\ D(-i\beta)\cos\left[\frac{m\pi}{w}\left(x+\frac{w}{2}\right)\right]\sin\left[k_y^b(b-y)\right], & a < y \le b \end{cases} \tag{2.85}$$

$$E_z = \begin{cases} C\frac{m\pi}{w}\sin\left[\frac{m\pi}{w}\left(x+\frac{w}{2}\right)\right]\sin\left[k_y^a y\right], & 0 \le y \le a \\ D\frac{m\pi}{w}\sin\left[\frac{m\pi}{w}\left(x+\frac{w}{2}\right)\right]\sin\left[k_y^b(b-y)\right], & a < y \le b \end{cases} \tag{2.86}$$

$$H_x = \begin{cases} C\frac{1}{i\omega\mu_0}k_y^a\frac{m\pi}{w}\sin\left[\frac{m\pi}{w}\left(x+\frac{w}{2}\right)\right]\cos\left[k_y^a y\right], & 0 \le y \le a \\ D\frac{1}{i\omega\mu_0}k_y^b\frac{m\pi}{w}\sin\left[\frac{m\pi}{w}\left(x+\frac{w}{2}\right)\right]\cos\left[k_y^b(b-y)\right], & a < y \le b \end{cases} \tag{2.87}$$

$$H_y = \begin{cases} C\frac{1}{i\omega\mu_0}k_c^2\cos\left[\frac{m\pi}{w}\left(x+\frac{w}{2}\right)\right]\sin\left[k_y^a y\right], & 0 \le y \le a \\ D\frac{1}{i\omega\mu_0}k_c^2\cos\left[\frac{m\pi}{w}\left(x+\frac{w}{2}\right)\right]\sin\left[k_y^a y\right], & a < y \le b \end{cases} \tag{2.88}$$

$$H_z = \begin{cases} C\frac{1}{\omega\mu_0}\beta k_y^a\cos\left[\frac{m\pi}{w}\left(x+\frac{w}{2}\right)\right]\cos\left[k_y^a y\right], & 0 \le y \le a \\ D\frac{1}{\omega\mu_0}\beta k_y^b\cos\left[\frac{m\pi}{w}\left(x+\frac{w}{2}\right)\right]\cos\left[k_y^b(b-y)\right], & a < y \le b \end{cases} \tag{2.89}$$

The dispersion relation is solved in the same way as the LSM_{mn} modes, giving

$$k_y^b \cot\left[k_y^b(b-a)\right] = k_y^a \cot\left[k_y^a a\right] \ . \tag{2.90}$$

2.4 Properties of dielectric lined waveguides

In this section two different waveguides are considered. The first was designed for deflection of 100 keV electrons, and the second was designed for acceleration of 35 MeV electrons. The dimensions and other properties are detailed in Table 2.1. In both cases quartz is used as the dielectric. Electron velocity, v_e, is defined by the energy and is different for the two DLWs. The cut-off frequency, f_c, is the frequency below which the real component of $\beta(\omega)$ is zero. The operating frequency, f_{op}, is the frequency at which the phase velocity, $v_p(\omega) = \frac{\omega}{\beta(\omega)}$, is equal to v_e.

2.4.1 Dispersion relation

The solutions to the dispersion relations of the LSM_{01}, LSM_{11} and LSE_{11} modes for each design are discussed with regards to their functional forms, and frequencies of interest f_c and f_{op}. Both real and imaginary components of $\beta(\omega)$ are considered. The transverse wavenumbers, k_y^a and k_y^b, are also investigated with regards to how they influence the form of $\beta(\omega)$. In all cases, the dispersion relations are solved in *Mathematica*, using the method discussed in 2.3.1.

Table 2.1: Parameters of the two DLWs. One was designed for the deflection of 100 keV electrons, operating in the LSM_{01} mode. The other was designed for acceleration of 35 MeV electrons, operating in the LSM_{11} mode. The cut-off and operating frequencies are given for the operating mode.

	Waveguide design	
Parameter	100 keV deflection	35 MeV acceleration
a [μm]	100	250
w [μm]	1000	1200
δ [μm]	240	50
ϵ_r	3.75	3.75
Operating mode	LSM_{01}	LSM_{11}
v_e [c]	0.5482	0.9999
f_c [THz]	0.1014	0.2693
f_{op} [THz]	0.5036	0.4729

100 keV deflection design

The properties of the DLW designed for deflection of 100 keV electrons are detailed in Table 2.1. The dispersion relations of the LSM_{01}, LSM_{11} and LSE_{11} modes are shown in Figure 2.2. The values of f_c, f_{op}, and f_{light}, the frequency at which $v_p = c$, are given in Table 2.2. For each mode $v_p \to \frac{c}{\sqrt{\epsilon_r}}$, or the speed of light in the dielectric,

Table 2.2: Frequencies of interest for the LSM_{01}, LSM_{11}, and LSE_{11} modes of the DLW designed for deflection of 100 keV electrons, described in Table 2.1.

	Value [THz]		
Frequency	LSM_{01}	LSM_{11}	LSE_{11}
f_c	0.1014	0.1645	0.1739
f_{op}	0.5036	0.5075	0.8723
f_{light}	0.1330	0.1930	0.2234

as $\omega \to \infty$. LSM_{01} is the lowest order mode as it has the lowest cut-off frequency. The phase velocity is equal to c at the lowest frequency, and the mode has the smallest f_{op}. LSM_{11} is the next occurring mode, with f_{op} close to that of LSM_{01}. The cut-off frequency of LSE_{11} is slightly higher than that of LSM_{11}, with a higher f_{op}. Although $\beta(\omega)$ of each mode tends to the speed of light in the dielectric, LSE_{11} takes longer to approach this limit.

The real and imaginary components of $\beta(\omega)$ are plotted in Figure 2.3 for the LSM_{01}, LSM_{11} and LSE_{11} modes. In each case the imaginary component of $\beta(\omega)$ is zero after f_c, and the real component is zero before f_c.

The transverse wavenumbers, k_y^a and k_y^b, are shown in Figures 2.4, 2.5, and 2.6 for LSM_{01}, LSM_{11} and LSE_{11} respectively. $\beta(\omega)$ is also plotted. There is no real com-

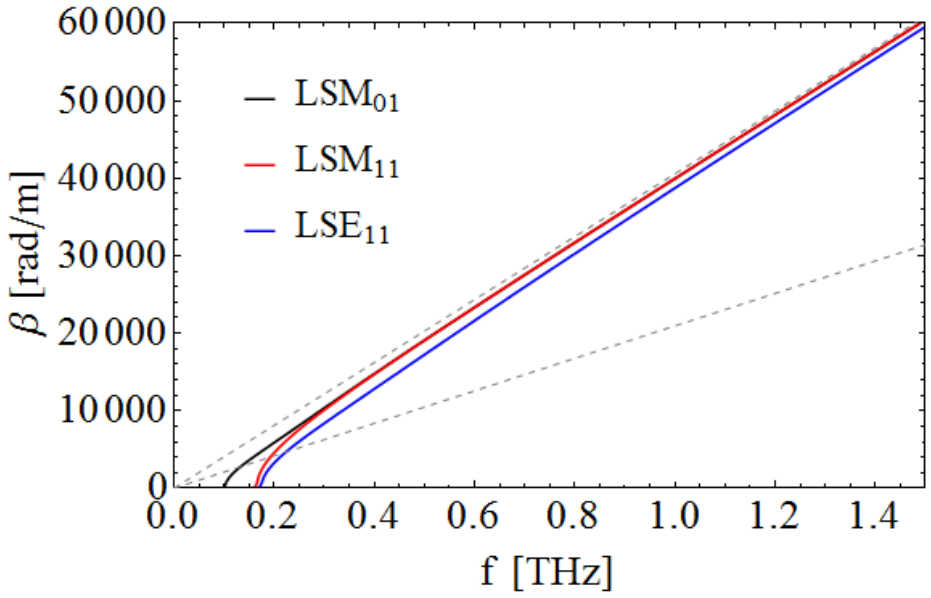

Figure 2.2: Dispersion relations of the LSM_{01}, LSM_{11}, LSE_{11} modes for a DLW designed for deflection of 100 keV electrons, with properties detailed in Table 2.1. The dashed lines represent the propagation of light in a vacuum and in a dielectric with $\epsilon_r = 3.75$.

ponent of k_y^a for the LSM_{01} mode, and the imaginary component is non-zero for all frequencies. The gradient is discontinuous at f_c and $\mathbb{I}(k_y^a)$ crosses $\beta(\omega)$ at 0.1574 THz, which does not correspond to any frequency of interest considered previously. The imaginary component of k_y^b is non-zero below 0.0774 THz. Above this, the real component is non-zero, crossing $\beta(\omega)$ at 0.1546 THz.

There is a real component of k_y^a for the LSM_{11} mode, which is non-zero only around f_c (between 0.1614 THz and 0.1697 THz), and maximum at f_c itself. The imaginary component is non-zero for all frequencies except those where $\mathbb{R}(k_y^a)$ is non-zero, and $\mathbb{R}(k_y^a)$ crosses the dispersion relation at approximately 0.1667 THz. The imaginary component of k_y^b is non-zero below 0.1285 THz. Above this, the real component is non-zero. At f_c, the gradient of $\mathbb{R}(k_y^b)$ becomes discontinuous, and it crosses $\beta(\omega)$ at 0.2209 THz.

There is a real component of k_y^a for the LSE_{11} mode, which is non-zero only around f_{op}, and maximum at f_c itself. The imaginary component is non-zero for all frequencies except those where $\mathbb{R}(k_y^a)$ is non-zero. The imaginary component of k_y^b is non-zero below 0.1245 THz. Above this, the real component is non-zero. The gradient of $\mathbb{R}(k_y^b)$ becomes discontinuous at f_c, and it crosses $\beta(\omega)$ at 0.2959 THz.

Except for the discontinuous gradients of k_y^a and k_y^b of the three modes considered, which occur at f_c, the cut-off frequencies of the transverse wavenumbers and the

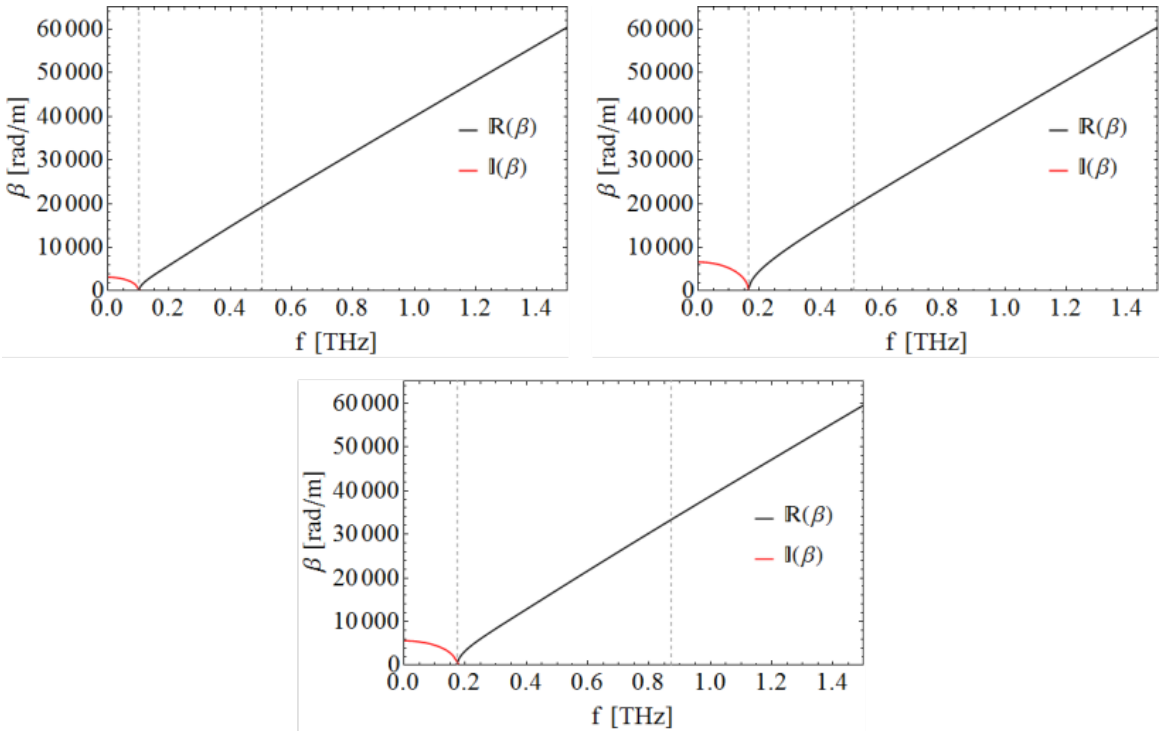

Figure 2.3: Real and imaginary components of the dispersion relation of the DLW designed for deflection of 100 keV electrons, described in Table 2.1. Clockwise from top left: DLW operating in the LSM_{01}, LSM_{11}, and LSE_{11} modes. Dashed lines represent f_c and f_{op}.

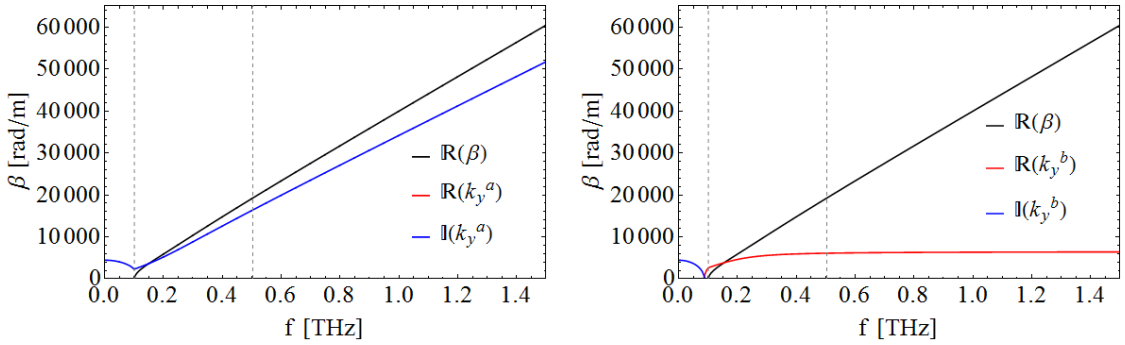

Figure 2.4: Transverse wavenumbers k_y^a and k_y^b for the LSM_{01} mode of the DLW designed for deflection of 100 keV electrons, with parameters detailed in Table 2.1. $\beta(\omega)$ is also plotted for comparison. Left: real and imaginary components of k_y^a. Right: real and imaginary components of k_y^b. Dashed lines represent f_c and f_{op}.

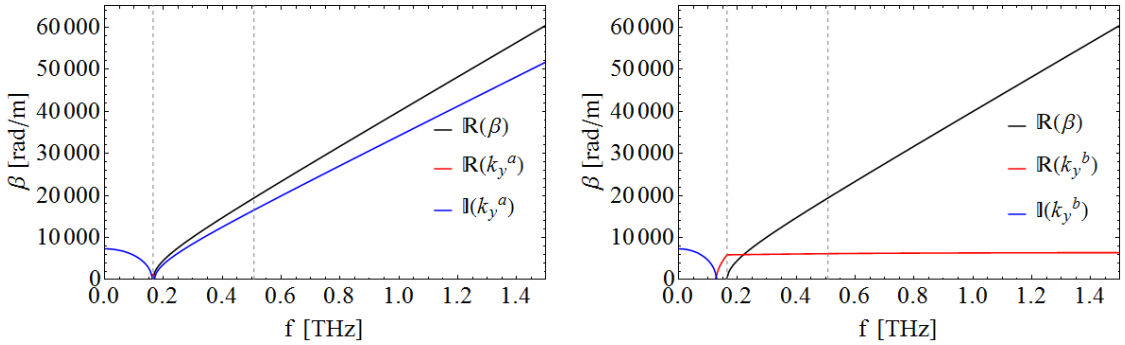

Figure 2.5: Transverse wavenumbers k_y^a and k_y^b for the LSM_{11} mode of the DLW designed for deflection of 100 keV electrons, with parameters detailed in Table 2.1. $\beta(\omega)$ is also plotted for comparison. Left: real and imaginary components of k_y^a. Right: real and imaginary components of k_y^b. Dashed lines represent f_c and f_{op}.

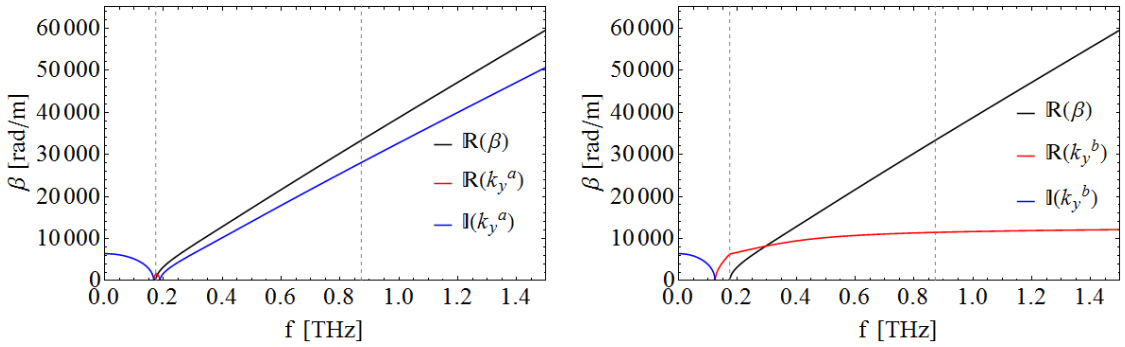

Figure 2.6: Transverse wavenumbers k_y^a and k_y^b for the LSE_{11} mode of the DLW designed for deflection of 100 keV electrons, with parameters detailed in Table 2.1. $\beta(\omega)$ is also plotted for comparison. Left: real and imaginary components of k_y^a. Right: real and imaginary components of k_y^b. Dashed lines represent f_c and f_{op}.

Table 2.3: Frequencies of interest for the LSM_{01}, LSM_{11}, and LSE_{11} modes of the DLW designed for acceleration of 35 MeV electrons, described in Table 2.1.

	Value [THz]		
Frequency	LSM_{01}	LSM_{11}	LSE_{11}
f_c	0.1014	0.2693	0.2763
f_{op}	0.3017	0.4729	0.9340
f_{light}	0.3015	0.4728	0.9337

crossing points with $\beta(\omega)$ do not correspond to any frequencies of interest. It is of note that in each case the value of k_y^a is imaginary at f_{op} and k_y^b is real.

35 MeV acceleration design

The properties of the DLW designed for acceleration of 35 MeV electrons are detailed in Table 2.1. The dispersion relations of the LSM_{01}, LSM_{11}, and LSE_{11} modes are shown in Figure 2.8. The values of f_c, f_{op}, and f_{light} are given in Table

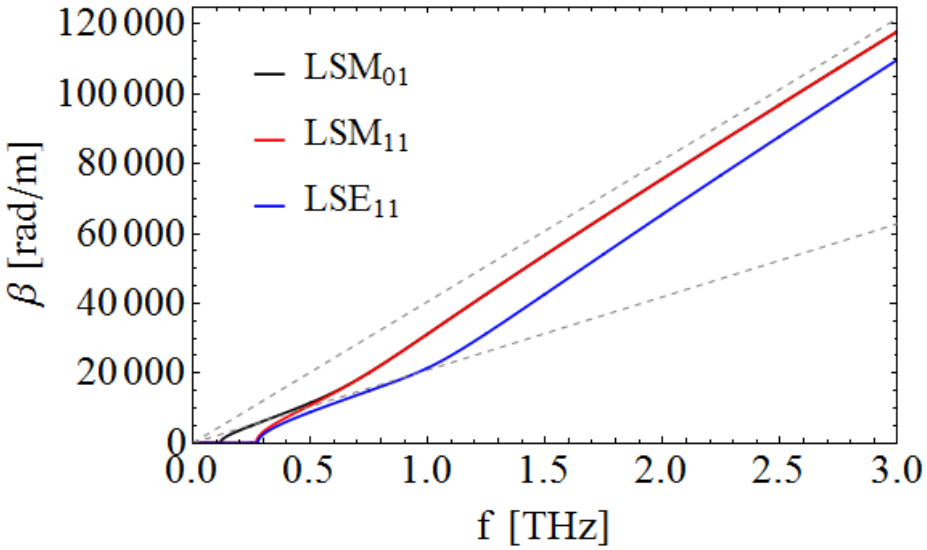

Figure 2.7: Dispersion relations of the LSM_{01}, LSM_{11}, LSE_{11} modes for a DLW designed for acceleration of 35 MeV electrons, with properties detailed in Table 2.1. The dashed lines represent the propagation of light in a vacuum and in a dielectric with $\epsilon_r = 3.75$.

2.3. As $v_e = 0.9999\ c$, f_{op} and f_{light} are close to each other. As with the 100 keV deflection DLW, $v_p \to \frac{c}{\sqrt{\epsilon_r}}$ as $\omega \to \infty$, although in this examples all modes take longer to approach this limit, compared to the 100 keV deflection design. The real and imaginary components of $\beta(\omega)$ are plotted in Figure 2.8 for LSM_{01}, LSM_{11} and LSE_{11}. In each case the imaginary component of $\beta(\omega)$ is zero after f_c, and the real component is zero before f_c.

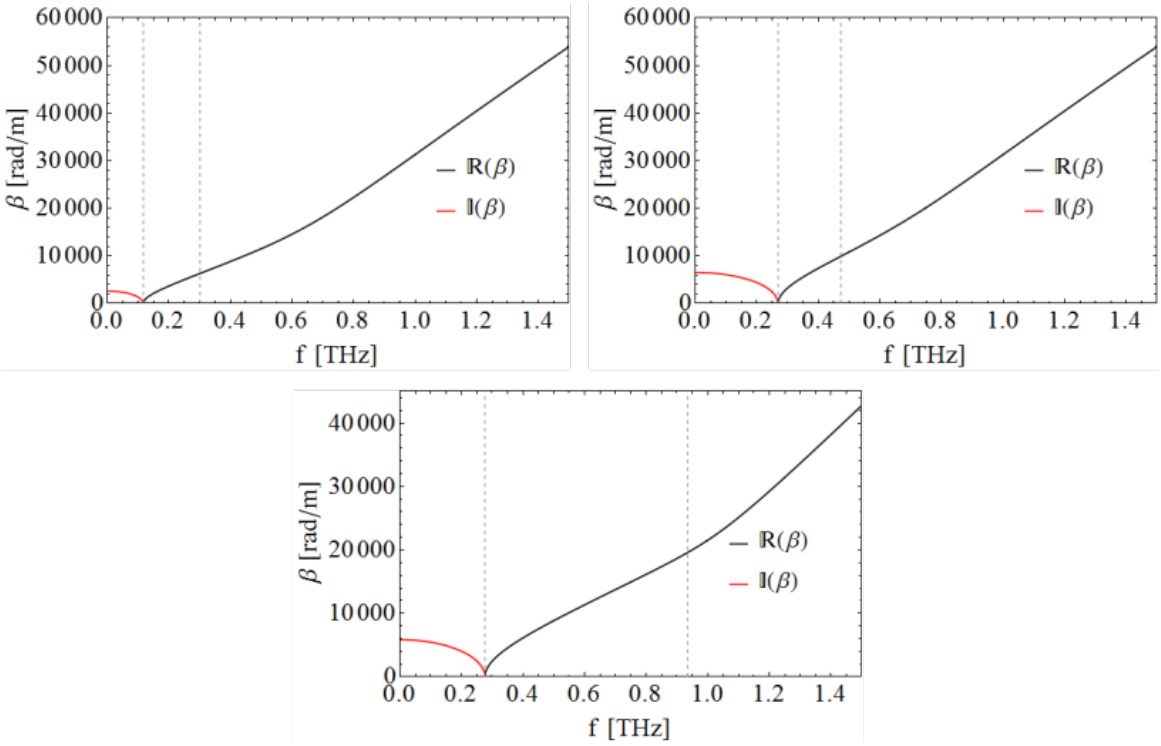

Figure 2.8: Real and imaginary components of the dispersion relation of the DLW design for acceleration of 35 MeV electrons, described in Table 2.1. Clockwise from top left: DLW operating in the LSM_{01}, LSM_{11}, and LSE_{11} modes. Dashed lines represent f_c and f_{op}.

The transverse wavenumbers, k_y^a, and k_y^b, are shown in Figures 2.9, 2.10, and 2.11 respectively, with $\beta(\omega)$ also plotted. $\mathbb{R}(k_y^a)$ of the LSM_{01} is zero for all frequencies, and $\mathbb{I}(k_y^a)$ is always real, with a gradient discontinuity at f_c. $\mathbb{I}(k_y^a)$ is equal to $\beta(\omega)$ at 0.1249 THz. Considering instead k_y^b, the imaginary part is non-zero below 0.0797 THz, and the real part is non-zero above this frequency, with a discontinuity in the gradient at f_c. $\mathbb{R}(k_y^b)$ crosses the dispersion relation at 0.8399 THz.

Moving to the LSM_{11} mode, the real part of k_y^a is non-zero between 0.2207 THz and 0.4438 THz, and the gradient is discontinuous at f_c. $\mathbb{R}(k_y^a)$ is equal to $\beta(\omega)$ at 0.3234 THz. The imaginary part of k_y^a is non-zero below 0.2207 THz and above 0.4438 THz, which is below f_{op}. The form of k_y^b is similar to that of the LSM_{01} mode, with the switch from the imaginary component to the real component at 0.1499 THz. $\mathbb{R}(k_y^b)$ crosses the dispersion relation at 0.8401 THz and its gradient is discontinuous at f_c.

Finally, the transverse wavenumbers of the LSE_{11} mode have a similar form to LSM_{11}. The real part of k_y^a is real between 0.2153 THz and 0.9039 THz, with the imaginary part real outside of this range. The gradient of $\mathbb{R}(k_y^a)$ is discontinuous at

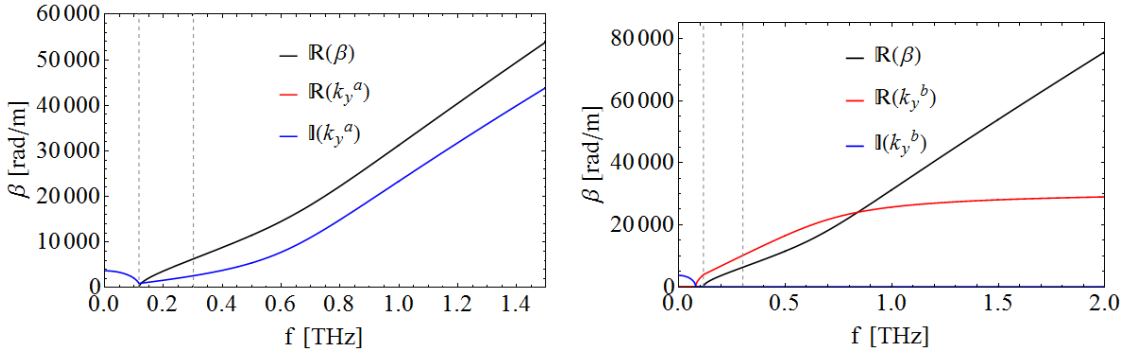

Figure 2.9: Transverse wavenumbers k_y^a and k_y^b for the LSM_{01} mode of the DLW designed for acceleration of 35 MeV electrons, with parameters detailed in Table 2.1. $\beta(\omega)$ is also plotted for comparison. Left: real and imaginary components of k_y^a. Right: real and imaginary components of k_y^b. Dashed lines represent f_c and f_{op}.

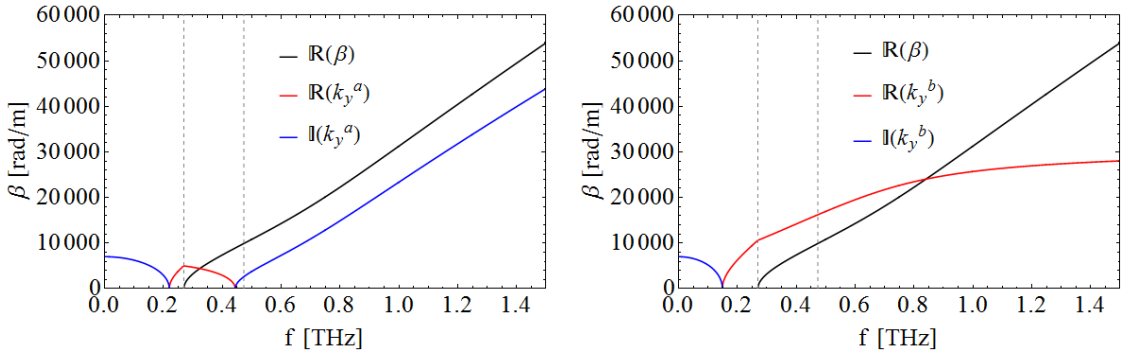

Figure 2.10: Transverse wavenumbers k_y^a and k_y^b for LSM_{11} mode of the DLW designed for acceleration of 35 MeV electrons, with parameters detailed in Table 2.1. $\beta(\omega)$ is also plotted for comparison. Left: real and imaginary components of k_y^a. Right: real and imaginary components of k_y^b. Dashed lines represent f_c and f_{op}.

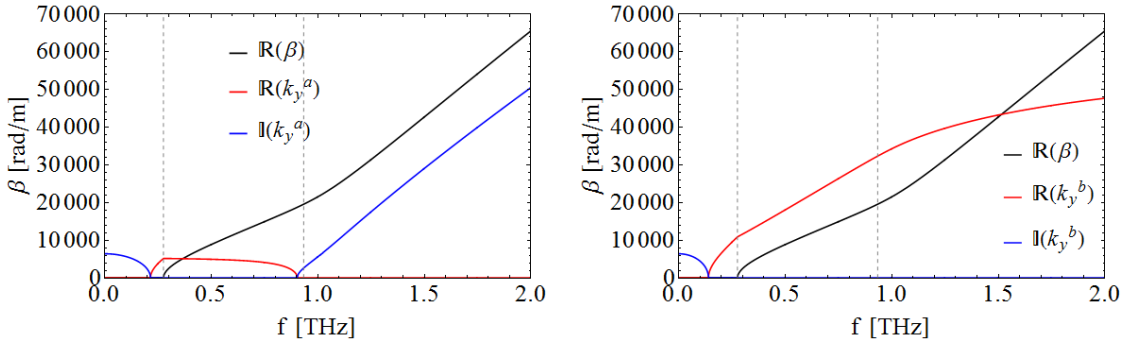

Figure 2.11: Transverse wavenumbers k_y^a and k_y^b for LSE_{11} mode of the DLW designed for acceleration of 35 MeV electrons, with parameters detailed in Table 2.1. $\beta(\omega)$ is also plotted for comparison. Left: real and imaginary components of k_y^a. Right: real and imaginary components of k_y^b. Dashed lines represent f_c and f_{op}.

f_c. k_y^b is imaginary below 0.1402 THz, and real above this frequency. The gradient of $\mathbb{R}(k_y^b)$ is discontinuous at f_c, and it crosses the dispersion relation at 1.5147 THz.

Except for the discontinuous gradients of k_y^a and k_y^b of the three modes considered, which occur at f_c, the cut-off frequencies of the transverse wavenumbers, and the crossing points with $\beta(\omega)$ do not correspond to any frequencies of interest. It is of note that, in each case, the value of k_y^a is imaginary at f_{op} and k_y^b is real, as with the 100 keV deflection DLW. One difference is that $\mathbb{R}(k_y^a)$ is non-zero for a greater range of frequencies in the LSM_{11} and LSE_{11} modes, and the range is largest for the LSE_{11} mode. Another difference is that $\mathbb{R}(k_y^a)$ crosses $\beta(\omega)$ above the operating frequency.

2.4.2 Phase and group velocity

As the study of the transverse wavenumbers of each mode showed that the gradients of k_y^a and k_y^b were discontinuous at f_c, it is useful to investigate the phase and group velocities. In free space $\omega = c\beta$; the medium is non dispersive and so all frequencies propagate with $v_p = c$. In a waveguide, the boundary conditions mean that $\omega = v_p\beta$, where v_p is the phase velocity, the velocity at which the phase of a sine wave with angular frequency ω propagates. A non-linear dispersion relation, $\beta = \beta(\omega)$, means that v_p is also a non-linear function of ω. In a hollow waveguide, $v_p > c$. However this is not the velocity at which the energy propagates. This is assumed to be equal to be the group velocity, v_g, the velocity of the envelope of a wave packet;

$$v_g(\omega) = \frac{\mathrm{d}\omega}{\mathrm{d}\beta(\omega)} \ . \tag{2.91}$$

v_g is a constant for a non-dispersive or weakly dispersive media, but in a waveguide v_g is a function of ω which implies that dispersion is nonlinear with frequency. This will be discussed in more detail in Chapter 3, but for now it is sufficient to state that for hollow rectangular waveguides $v_g < c$, such that $v_p v_g = c^2$ at all frequencies above the cut-off frequency [96]. v_p and v_g for the LSM_{01}, LSM_{11} and LSE_{11} modes of the DLWs designed for 100 keV deflection and 35 MeV acceleration are shown in Figures 2.12 and 2.13 respectively. As group velocity is the inverse of the gradient of $\beta(\omega)$, the large variation with frequency for both designs show they are strongly dispersive. In both cases, the velocites are related by $v_p v_g = \left(c/\sqrt{\epsilon_r}\right)^2$ as $f \to \infty$, although the LSE_{11} mode takes longer to reach the limit. With the 100 keV design the forms of v_p and v_g with frequency do not reveal any notable features. Moving to the 35 MeV design, there is a clear peak in v_g. In the case of the LSM_{01} and LSM_{11} modes, v_g is maximum just after f_{op}, whereas with the LSE_{11} mode the maximum point is before f_{op}. These do not correspond to any frequencies of interest.

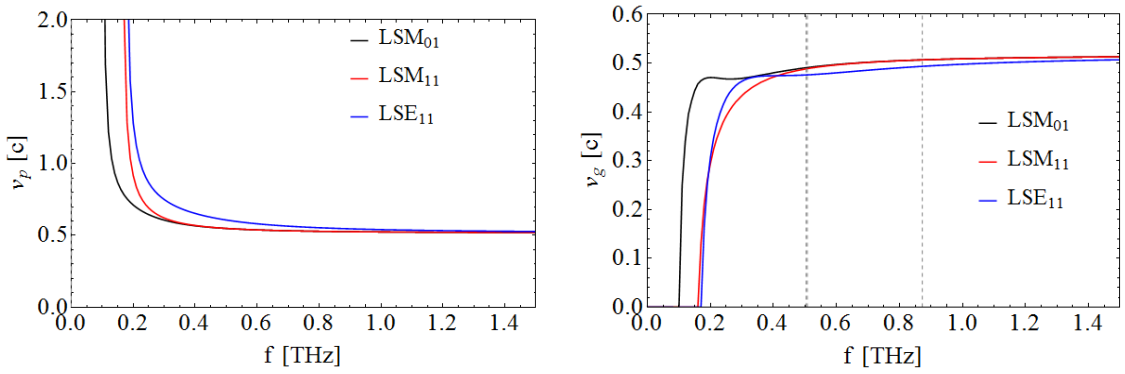

Figure 2.12: Phase and group velocity of the LSM_{01}, LSM_{11}, and LSE_{11} modes of the DLW designed for deflection fo 100 keV electrons, with parameters detailed in Table 2.1. Left: phase velocity, right: group velocity. Dashed lines represent the operating frequency of the modes.

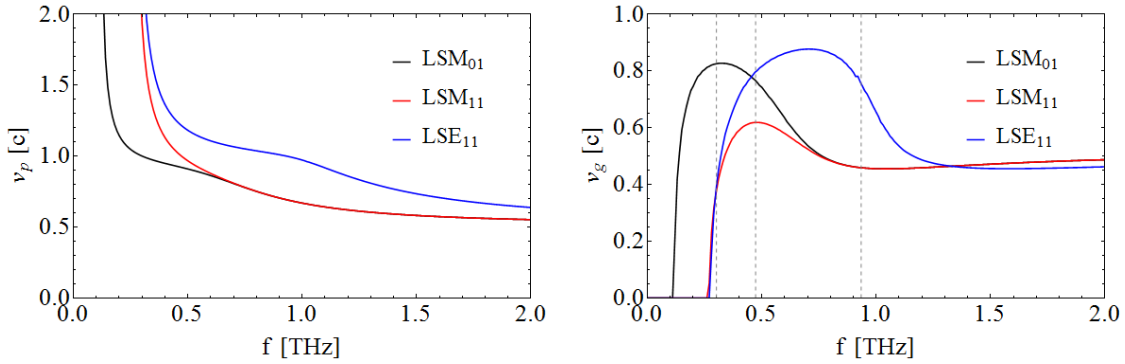

Figure 2.13: Phase and group velocity of the LSM_{01}, LSM_{11}, and LSE_{11} modes of the DLW design for acceleration of 35 MeV electrons, with parameters detailed in Table 2.1. Left: phase velocity, right: group velocity. Dashed lines represent the operating frequency of the modes.

Close to f_c, $v_p \to \infty$ and $v_g \to 0$, which implies that a monochromatic wave with frequency near f_c would be stationary and the energy does not propagate. Below f_c the wave is not supported by the waveguide and so decays evanescently at the entrance.

2.4.3 Fields in the vacuum and dielectric

β has been considered as a function of frequency, but as the field components are not linearly dependent it is useful to understand how the field varies both with frequency and position in the DLW. Only the accelerating modes LSM_{11} and LSE_{11} modes are considered in this section.

The fields are normalised such that the stored energy at each frequency is the same. The field components are multiplied by $1/\sqrt{U_{stored}(\omega)}$, where $U_{stored}(\omega)$ is the total energy per unit length in the DLW at each frequency. This is calculated by

$$U_{stored}(\omega) = \frac{\epsilon_0}{2L}\int_V |\mathbf{E}|^2 \,\mathrm{d}V = \frac{1}{2\mu_0 L}\int_V |\mathbf{E}|^2 \,\mathrm{d}V \ . \tag{2.92}$$

For the purposes of comparison, the fields are then also scaled such that the maximum magnitude of $E_z(x=0, y=0, \omega)$ of the LSM_{11} mode is equal to one. The magnitude and phase of the on-axis E_z field of the LSM_{11} mode is shown as a function of frequency in Figure 2.14 for the 100 keV deflection design (operating in the LSM_{11} accelerating mode), and Figure 2.15 for the 35 MeV acceleration design. In both cases the magnitude of axial E_z is not maximum at f_{op}, it is instead maximum at 0.195 THz for the 100 keV design and 0.31 THz for the 35 MeV design. These are close to the frequencies at which $\mathbb{R}(k_y^a)$ is equal to $\beta(\omega)$, but not equal. The magnitude of the E_z field decreases with frequency; at f_{op} it is 20% and 60% of the maximum for the 100 keV deflection and 35 MeV acceleration designs respectively. The phase of the axial E_z field is non-zero only between f_{op}, and the frequency at which k_y^a switches from real to imaginary.

An example vector plot of the LSM_{11} electric field components, as calculated at f_{op}, is shown in Figure 2.16. The transverse electrics field are shown in the xy-plane. As expected due to symmetry and from Equations (2.64) and (2.65), they are both zero on-axis. A feature of the LSM_{11} mode is a quadrupole-like field. However the E_x field is significantly weaker than the E_y field. The E_y and E_z fields are shown in the yz-plane; the maxima of the two fields are separated by a quarter of a wavelength. The effect of frequency on the y-dependent E_z field is shown in Figure 2.17 for the two DLW designs. The E_z field on the vacuum-dielectric boundary is not equal to the axial E_z field at any of the frequencies shown in the plots. This field on the boundary

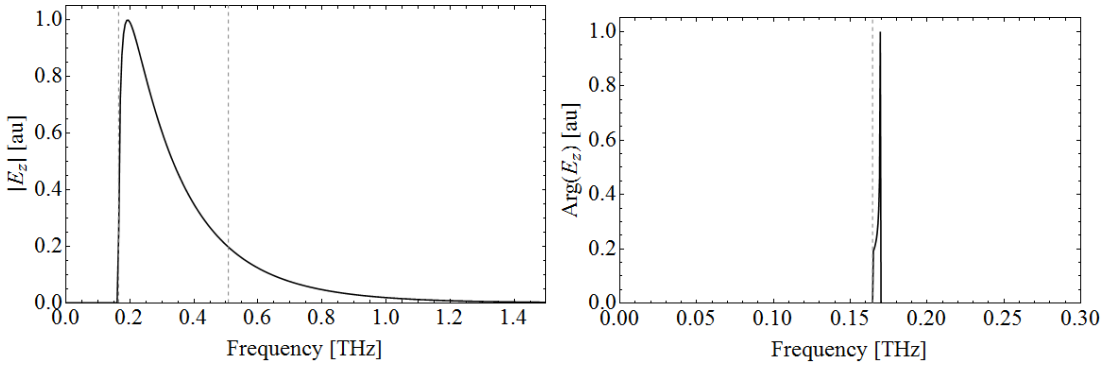

Figure 2.14: Axial E_z as a function of frequency for the LSM_{11} mode of the DLW designed for deflection of 100 keV electrons, with parameters detailed in Table 2.1. The magnitude of the field is normalised such that each frequency component of the total field has the same stored energy. The values have also been scaled such that maximum $|E_z|$ is equal to one. Left: magnitude of axial E_z, right: phase of axial E_z. Dashed lines represent f_c and f_{op}.

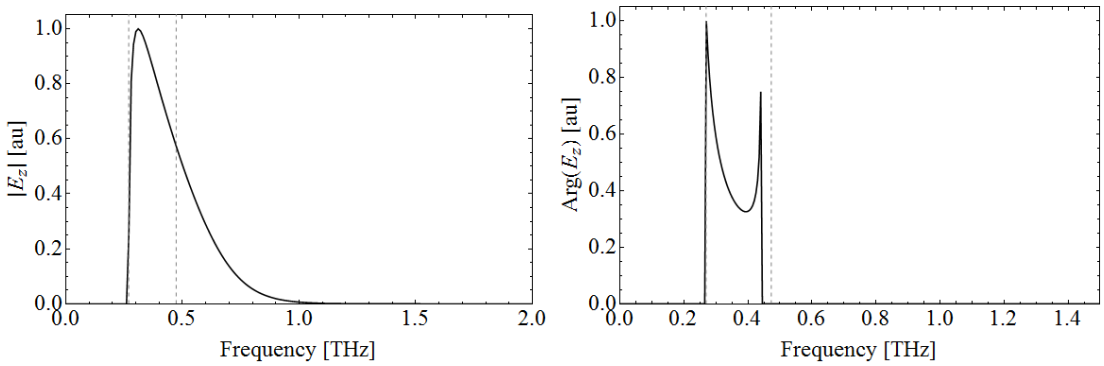

Figure 2.15: Axial E_z as a function of frequency for the LSM_{11} mode of the DLW designed for acceleration of 35 MeV electrons, with parameters detailed in Table 2.1. The magnitude of the field is normalised such that each frequency component of the total field has the same stored energy. The values have also been scaled such that maximum $|E_z|$ is equal to one. Left: magnitude of axial E_z, right: phase of axial E_z. Dashed lines represent f_c and f_{op}.

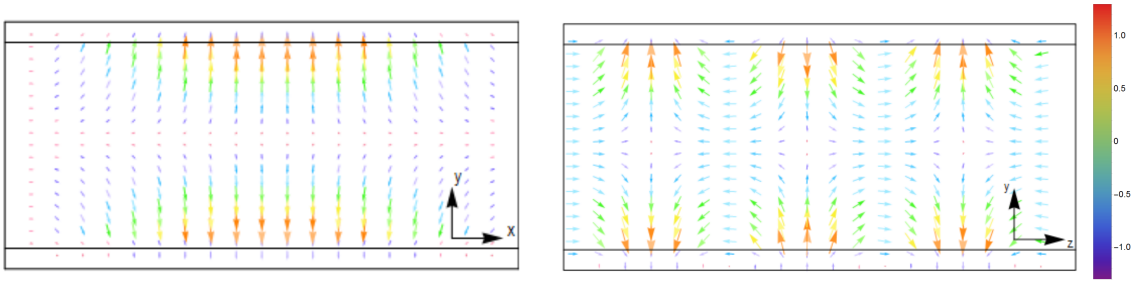

Figure 2.16: Example vector plots of the E-field of the LSM_{11} mode in the xy- and yz-plane. The dielectric components of the DLW are on the top and bottom of the cross-sections. Left: E_y and E_x profiles are shown in the xy-plane. Right: E_y and E_z are shown in the yz-plane, assuming the field is sinusoidal in z.

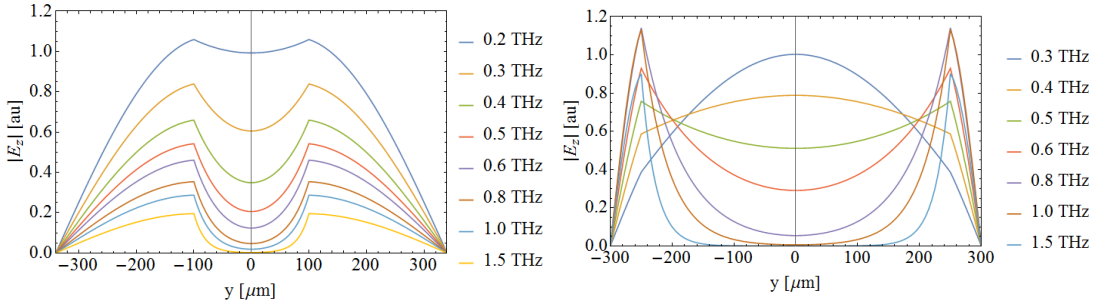

Figure 2.17: $E_z(x = 0, y)$ of the LSM_{11} mode for a range of frequencies. The fields are normalised such that the maximum axial E_z field is equal to one. Left: DLW designed for deflection of 100 keV electrons, right: DLW designed for acceleration of 35 MeV electrons. The parameters of the DLWs are described in Table 2.1.

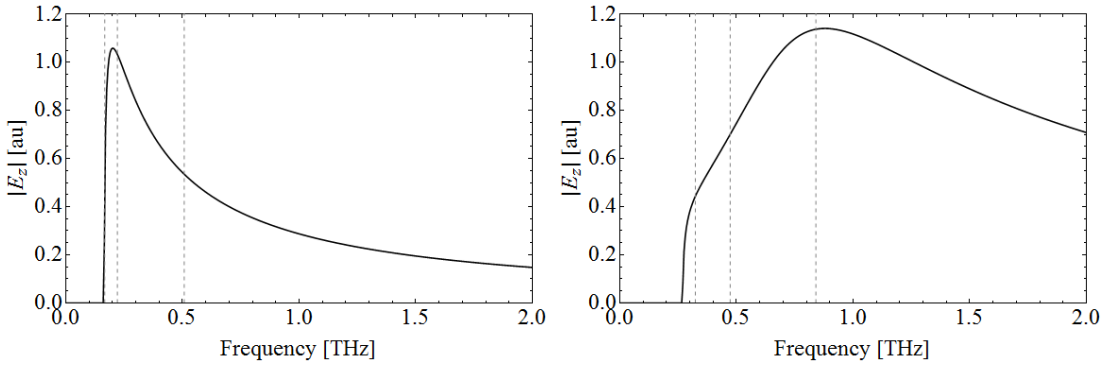

Figure 2.18: $E_z(f, x = 0, y = a)$ of the LSM_{11} mode as a function of frequency. Dashed lines represent the operating frequency and the frequencies at which $\mathbb{R}(k_y^a)$ and $\mathbb{R}(k_y^b)$ cross the dispersion relation. Left: DLW designed for deflection of 100 keV electrons, right: DLW designed for acceleration of 35 MeV electrons. The parameters of the DLWs are described in Table 2.1. Dashed lines represent the frequency at which $\mathbb{R}(k_y^a)$ is equal to $\beta(\omega)$, frequency at which $\mathbb{R}(k_y^b)$ is equal to $\beta(\omega)$), and f_{op}.

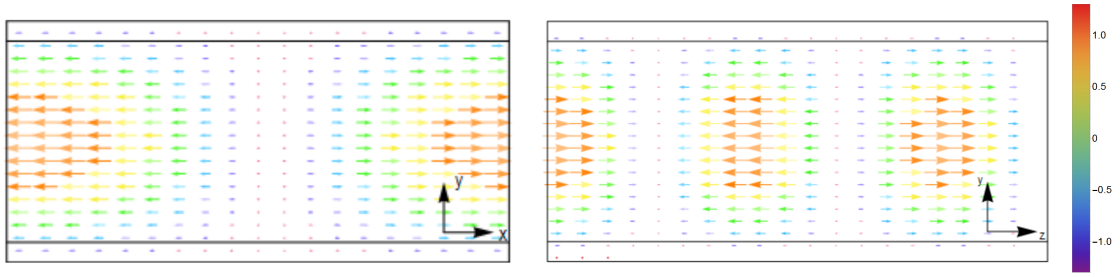

Figure 2.19: Example vector plots of the E-field of the LSE_{11} mode in the xy- and yz-plane. The dielectric components of the DLW are on the top and bottom of the cross-sections. Left: E_y and E_x profiles are shown in the xy-plane. Right: E_y and E_z are shown in the yz-plane, assuming the field is sinusoidal in z.

also peaks at a different frequency; this is shown in Figure 2.18 for the two DLW designs. The E_z field on the boundary is maximum at 0.21 THz and 0.88 THz for the 100 keV and 35 MeV designs respectively, close to the frequency at which $\mathbb{R}(k_y^b)$ crosses the dispersion relation. Additionally, E_z(f,x=0,y=0) is equal to E_z(f,x=0,y=a) at 0.1697 THz and 0.4438 THz, the frequencies at which k_y^a switches from real to imaginary for the 100 keV and 35 MeV designs respectively. As the maximum field on the boundary is also higher than that on-axis, the maximum accelerating gradient is limited by the breakdown field of the dielectric.

It is useful to compare the E_z field of the LSM_{11} mode to the E_z field of the LSE_{11} mode to discuss why the LSM_{11} mode is chosen for operation. Vector plots are shown in Figure 2.19 for fields at the operating frequency. There is no E_y field; the transverse component acts to focus and defocus only in the x-direction. The

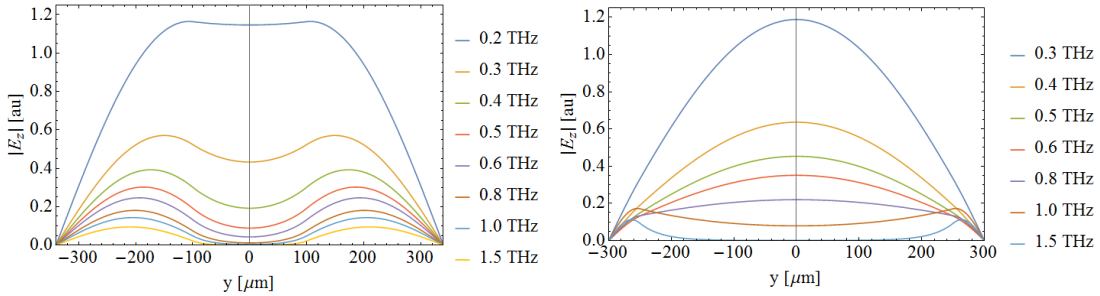

Figure 2.20: $E_z(x = 0, y)$ of the LSM_{11} mode for a range of frequencies. The fields are normalised such that the maximum axial E_z field of the LSM_{11} mode of the same DLW design is equal to one to compare the modes. Left: DLW designed for deflection of 100 keV electrons, right: DLW designed for acceleration of 35 MeV electrons. The parameters of the DLWs are described in Table 2.1.

longitudinal field peaks in the centre, and is lower closer to the dielectric, before decaying inside the dielectric itself. The y-dependent E_z field is shown in Figure 2.20 as a function of frequency. The E_z field is maximum at low frequency, and the amplitude is greater than that of the LSM_{11} mode. The operating frequency is at 0.8723 THz and 0.9340 THz for the 100 keV and 35 MeV designs respectively, at which the axial E_z field is about 30% of the axial E_z field of the LSM_{11} mode at f_{op}. This means that is preferable to use the LSM_{11} mode over the LSE_{11} mode for acceleration, especially for the 35 MeV design.

2.5 Summary

This chapter has provided a general overview of the theory behind waveguide modes, with a specific focus on dielectric-lined waveguides. Mode designations unique to DLWs have been introduced and discussed the two accelerating mode configurations; LSM_{11} and LSE_{11} for two different DLW designs. The transverse wavenumber as a function of frequency was investigated to see how it affected the dispersion relation and the E_z fields of the waveguide.

The dispersion relation and field components derived in this chapter will be used throughout the thesis during investigation of DLW design. This includes choice of structure dimensions, pulse propagation, and the effect on interaction between an electron bunch and THz pulse.

Chapter 3

Dispersion in dielectric-lined waveguides

The dispersion relation of a DLW is highly non-linear due to the hybrid nature of the propagating modes. Dispersion can be approximated by applying a Taylor expansion and thus develop an understanding of how each term affects the propagation of a pulse through the DLW. This is vital to understand how an electron will interact with the fields of the pulse over time. The effect of dispersion on two types of pulses is considered; a Gaussian and a 'modified Gaussian', which is typically described as an ultrashort pulse. The approximation is compared with the effect of the full dispersion relation. The two DLW designs which were investigated in Chapter 2 are again considered here; the parameters of these DLWs are given in Table 2.1.

3.1 Pulse propagation

The solutions to the wave equations without inclusion of the time dependency have been discussed in Chapter 2. It is therefore necessary to add the pulse propagation in terms of z and t back into the field equations. The wave equations are satisfied by travelling plane waves;

$$\mathbf{A}(x, y, z, \omega, t) = \mathbf{A_0}(x, y, z, \omega) \exp\left[i\left(\left(\beta(\omega) + i\alpha(\omega)\right) z - \omega t\right)\right] \ , \tag{3.1}$$

where α is the attenuation coefficient. $\mathbf{A}$ denotes either $\mathbf{E}$ or $\mathbf{H}$, and $\mathbf{A_0}$ is the magnitude of each wave. The complex wavenumber is given by $\beta(\omega)+i\alpha(\omega)$. Tracking a given phase $\phi = \left(\beta(\omega) + i\alpha(\omega)\right) z - \omega t$, the amplitude remains constant with time provided

$$v_p = \frac{z}{t} = \frac{\omega}{\mathrm{Re}\left[\beta(\omega) + i\alpha(\omega)\right]} \ , \tag{3.2}$$

where v_p is the phase velocity. α is neglected throughout this work, but at no point is it assumed that β is purely real-valued. A solution to the wave equation made up of a superposition of plane waves of different periodicity is also valid;

$$\mathbf{A}(x,y,z,t) = \int_{-\infty}^{+\infty} \mathbf{A_0}(x,y,z,\omega) \exp\left[i\left(\beta(\omega)z - \omega t\right)\right] \mathrm{d}\omega \ . \tag{3.3}$$

This is the basis of the Fourier transform, relating a function in time to its components in the frequency domain. Non-linear variation of $\beta(\omega)$ with ω means each individual wave propagates with a different v_p, leading to a change in the pulse shape with time. This dispersion is a characteristic of waveguides, as the propagation constant is a function of both waveguide dimensions and frequency. To investigate the effect on pulse propagation of each dispersive order in turn, the dispersion relation is decomposed into a Taylor series expansion. The discussion in this chapter is valid for all pulses propagating through a non-linear dispersive region. Specific examples of Gaussian and ultrashort pulses as they propagate through a DLW are used. The dispersion relations of the two DLWs discussed in Chapter 2 are considered, with the Taylor series expansion centred on the operating frequency in both cases. A different centre frequency is also considered for the DLW designed for acceleration of 35 MeV electrons in order to show the sensitivity of the Taylor approximation to choice of frequency.

3.2 Taylor approximation of the dispersion relation

A Taylor approximation about a given frequency breaks $\beta(\omega)$ down into a sum of terms;

$$\begin{aligned}\beta(\omega) =& \beta(\omega_0) + \left.\frac{\partial\beta(\omega)}{\partial\omega}\right|_{\omega_0}(\omega-\omega_0) + \frac{1}{2!}\left.\frac{\partial^2\beta(\omega)}{\partial\omega^2}\right|_{\omega_0}(\omega-\omega_0)^2 + \frac{1}{3!}\left.\frac{\partial^3\beta(\omega)}{\partial\omega^3}\right|_{\omega_0}(\omega-\omega_0)^3 \\ &+ \cdots + \frac{1}{N!}\frac{\partial^N\beta(\omega)}{\partial\omega^N}(\omega-\omega_0)^N \ , \\ =& \beta_0 + \beta_0'(\omega-\omega_0) + \frac{1}{2!}\beta_0''(\omega-\omega_0)^2 + \frac{1}{3!}\beta_0'''(\omega-\omega_0)^3 + \cdots + \frac{1}{N!}\beta_0^{(N)}(\omega-\omega_0)^N \ ,\end{aligned} \tag{3.4}$$

where ω_0 is an arbitrarily chosen frequency, and β_0 is the dispersion function at that frequency, and N is maximum order considered in the approximation. Throughout this chapter ω_0 is taken to be the operating frequency at which $v_p = v_e$, transformed to angular frequency, with the initial THz pulse having maximum amplitude at this

frequency. Defining an arbitrary pulse propagating in z:

$$\tilde{E}(\omega, \omega_0, z) = \tilde{A}(\omega, \omega_0) \exp[i\beta(\omega)z] \ , \tag{3.5}$$

where $\tilde{A}(\omega)$ is an initial pulse envelope. This is transformed into the time domain by the Fourier transform,

$$E(t, \omega_0, z) = \int_{-\infty}^{+\infty} \tilde{E}(\omega, \omega_0, z) \exp[-i\omega t] \mathrm{d}\omega \ . \tag{3.6}$$

100 keV deflection design

The values of β_0 and ω_0 for the LSM_{01} mode were calculated using Equation (2.76) for a DLW with parameters given in Table 2.1. Each term in Equation (3.4) was found by solving the dispersion relation, and then calculating the derivatives of $\beta(\omega)$ at $\omega_0 = 2\pi f_{op}$; these are found in Table 3.1.

Table 3.1: Values of ω_0 and β_0, including its derivatives, up to third order, for a DLW designed for deflection of 100 keV electrons, operating in the LSM_{01} mode. The DLW parameters are given in Table 2.1. The operating frequency is used as ω_0.

Variable	Value
ω_0	3.164×10^{12}
β_0	19253
β_0'	6.800×10^{-9}
β_0''	-1.831×10^{-22}
β_0'''	1.267×10^{-34}

35 MeV acceleration design

The values of β_0 and ω_0 for the LSM_{11} mode were calculated using Equation (2.70) for a with parameters given in Table 2.1. Each term in Equation (3.4) was found by solving the dispersion relation, and then calculating the derivatives of $\beta(\omega)$ at two different values of ω_0; these are found in Table 3.2. The first frequency chosen was $\omega_0 = 2\pi f_{op}$. The second frequency was chosen to be that at which $\beta_0''' = 0$, corresponding to no third order dispersion (TOD). This gives a different set of dispersion parameters, selected from the same dispersion function but at different frequencies, to show how the pulse propagation is affected. When $\beta_0''' = 0$ the second order dispersion is an order of magnitude larger.

Table 3.2: Values of ω_0 and β_0, including its derivatives, up to third order, for a DLW designed for acceleration of 35 MeV electrons, operating in the LSM_{11} mode. The DLW parameters are given in Table 2.1. Two values are considered for ω_0; the operating frequency, and the frequency at which third order dispersion is zero.

	Choice of ω_0	
Parameter	Operating frequency	No third order dispersion
ω_0	2.971×10^{12}	4.265×10^{12}
β_0	9913	17270
β_0'	5.387×10^{-9}	6.218×10^{-9}
β_0''	-5.548×10^{-23}	1.009×10^{-21}
β_0'''	1.669×10^{-33}	0

3.3 Gaussian pulses

In the Gaussian case,

$$\tilde{A}(\omega, \omega_0, \sigma_0) = C \exp\left[-\frac{(\omega - \omega_0)^2}{2\sigma_0^2}\right] , \tag{3.7}$$

where σ_0 is the root mean square (RMS) bandwidth of the pulse, related to the full width at half maximum ($FWHM$) by FWHM $= 2\sqrt{2\ln 2}\ \sigma_0$, and C is a constant, which is set to 1 throughout this chapter. The FWHM was set to be 0.33 THz, as can be seen in Figure 3.1. The choice of bandwidth was kept the same for each set of

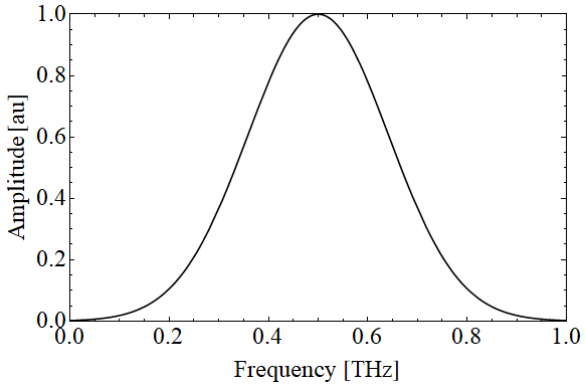

Figure 3.1: Gaussian pulse in the frequency domain with a FWHM of 330 GHz.

dispersion parameters and ω_0 equal to the centre frequency. In each case the frequency range encompassed frequencies below cut-off of the DLW, without the pulse extending into negative frequencies. In the time domain, the pulse is given as

$$E(t, \omega_0, \Gamma_0, z) = \frac{1}{\Gamma_0} \exp\left[-\frac{t^2}{2\Gamma_0^2}\right] \exp\left[i\omega_0 t\right] . \tag{3.8}$$

$\Gamma_0 = 1/\sigma_0$ is the pulse width in the time domain. The pulse is therefore described by a Gaussian envelope with an oscillatory term which oscillates with angular frequency ω_0. This oscillation describes the phase fronts of the pulse, whereas the envelope controls the amplitude. The form of the pulse is shown in Figure 3.2 at $z = 0$ mm.

3.3.1 Zero dispersion

Considering only the zeroth order term of the Taylor expansion, the dispersion has no frequency dependence and therefore acts only as a z-dependent amplitude term. In the frequency domain, the pulse is given as

$$E(\omega, \omega_0, \sigma_0, z) = \exp\left[-\frac{(\omega - \omega_0)^2}{2\sigma_0^2}\right] \exp\left[i\beta_0 z\right] \ , \tag{3.9}$$

Performing a Fourier transform gives the pulse in the time domain as

$$E(t, \omega_0, \Gamma_0, z) = \frac{1}{\Gamma_0} \exp\left[-\frac{t^2}{2\Gamma_0^2}\right] \exp\left[i\left(\omega_0 t - \beta_0 z\right)\right] \ , \tag{3.10}$$

which is also a Gaussian. The $(\omega_0 t - \beta_0 z)$ in the oscillatory term transfers the profile between real and imaginary components, but there is no pulse propagation in z as the envelope function is unchanged, which can be seen in Figure 3.2 for the 100 keV deflection design and Figure 3.3 for the 35 MeV acceleration design, using ω_0 equal to the operating frequency. The only difference between pulse propagation in the two DLWs is a change in the phase of the oscillations at each value of z due to the different values of $v_{p,0}$. Changing the choice of ω_0 for the 35 MeV design, the effect of zeroth order dispersion on the pulse is the same, shown in Figure 3.4. The periodicity of oscillations is different in Figures 3.3 and 3.4 because of the different values of ω_0, but the length of the pulse envelope in time is the same. Setting

$$\omega_0 t - \beta_0 z = 0 \tag{3.11}$$

allows for calculation of the velocity of the underlying phase fronts, which is termed the matched phase velocity, $v_{p,0}$;

$$v_{p,0} = \frac{\omega_0}{\beta_0} \ . \tag{3.12}$$

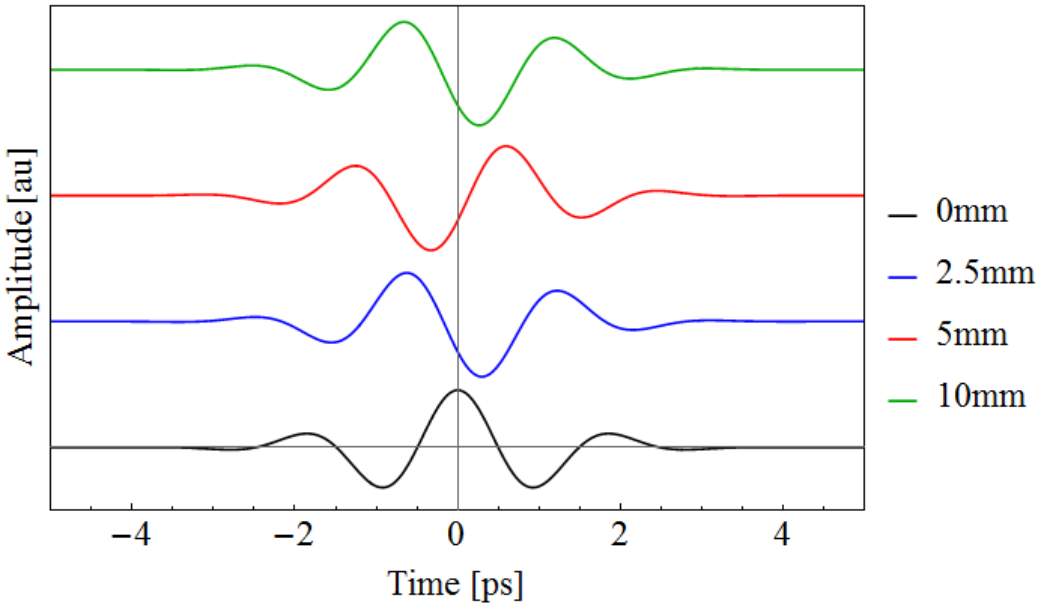

Figure 3.2: Gaussian pulse in the time domain at different values of z for dispersion of zeroth order, for a DLW designed for deflection of 100 keV electrons, described in Table 2.1, using ω_0 equal to the operating frequency. The pulse itself does not propagate, so the pulses are shown with an offset in amplitude. The underlying oscillatory component propagates with $v_{p,0}$.

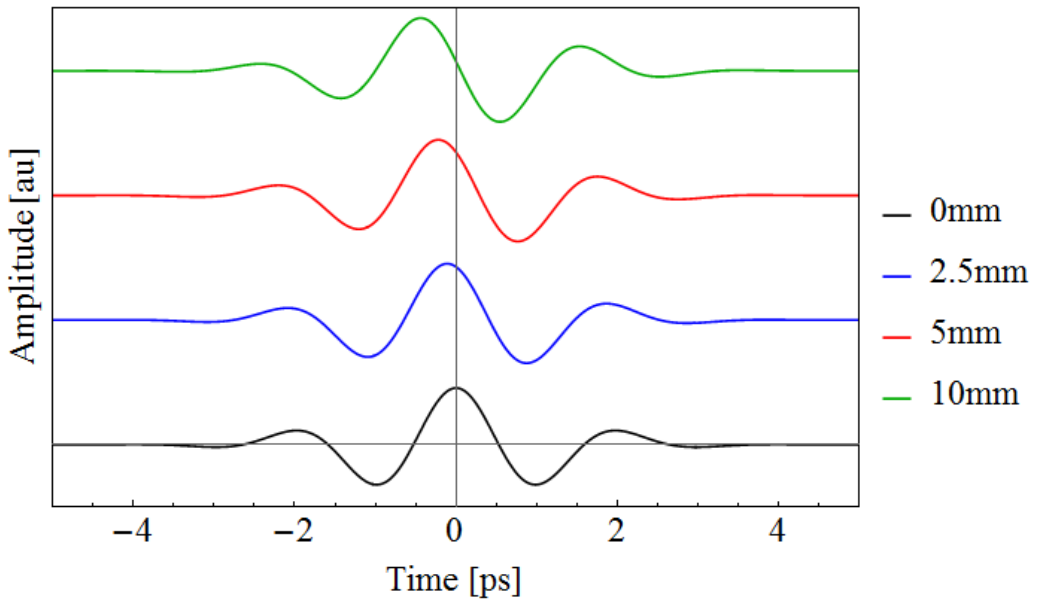

Figure 3.3: Gaussian pulse in the time domain at different values of z for dispersion of zeroth order, for a DLW designed for acceleration of 35 MeV electrons, described in Table 2.1, using ω_0 equal to the operating frequency. The pulse itself does not propagate, so the pulses are shown with an offset in amplitude. The underlying oscillatory component propagates with $v_{p,0}$.

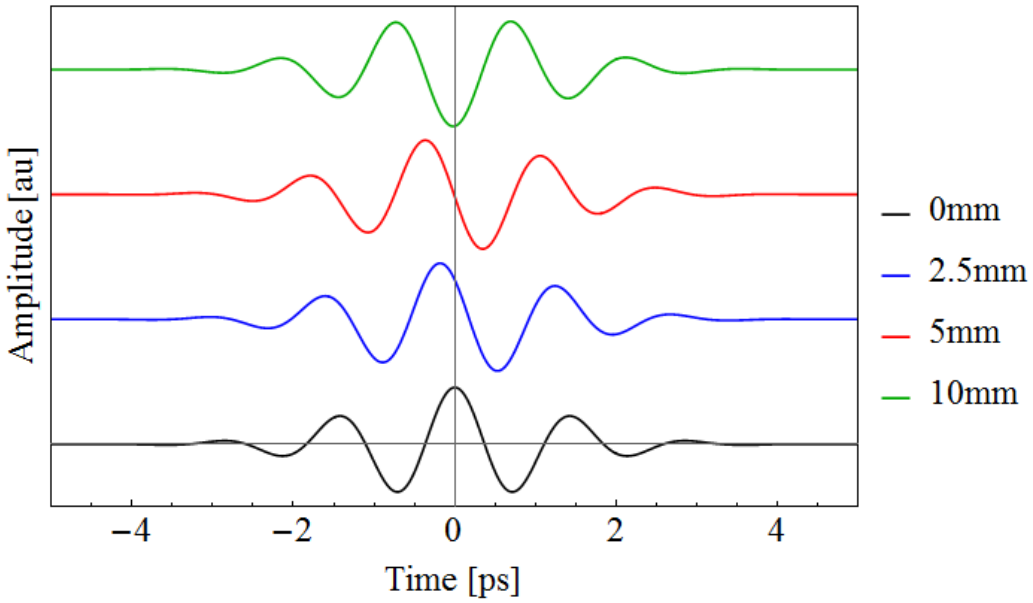

Figure 3.4: Gaussian pulse in the time domain at different values of z for dispersion of zeroth order, for a DLW designed for acceleration of 35 MeV electrons, described in Table 2.1, using ω_0 equal to the frequency at which TOD is zero. The pulse itself does not propagate, so the pulses are shown with an offset in amplitude. The underlying oscillatory component propagates with $v_{p,0}$.

3.3.2 First order dispersion

Taking the first approximation of the Taylor expansion,

$$\begin{aligned}\tilde{E}(\omega,\omega_0,z) &= \tilde{A}(\omega,\omega_0)\exp\left[i\left(\beta_0+\beta_0'\left(\omega-\omega_0\right)\right)z\right] \ , \\ &= \tilde{A}(\omega,z_0)\exp\left[i\left(\beta_0-\beta_0'\omega_0\right)z\right]\exp\left[-i\beta_0'\omega z\right] \ , \end{aligned} \tag{3.13}$$

where the terms with an ω dependence have been separated. By application of the Fourier transform, $\mathcal{F}[\ ]$, the identities

$$\begin{aligned}\mathcal{F}\left[g(t-a)\right] &= \exp\left[-i\omega a\right]G(\omega) \ , \\ \mathcal{F}\left[g(t)\exp\left[-ibt\right]\right] &= G(\omega-b) \ , \end{aligned} \tag{3.14}$$

where a is some time shift and b is a frequency shift, are used to give the field in the time-domain as

$$E(t,\omega_0,z) = A(t-\tau_0,z_0)\exp\left[i(\beta_0 z-\omega_0 t)\right] \ . \tag{3.15}$$

The time shift of the envelope function is defined as

$$\tau_0(z) = \beta_0' z \ , \tag{3.16}$$

and therefore the envelope, or group, velocity, v_g, is given as

$$v_g = \frac{z}{\tau_0} \ . \tag{3.17}$$

In the time domain, the pulse is described by

$$E(t, z, \omega_0, \Gamma_0) = \frac{1}{\Gamma_0} \exp\left[-\frac{1}{2}\frac{(t-\tau_0)^2}{\Gamma_0^2}\right] \exp\left[i(\beta_0 z - \omega_0 t)\right] \ . \tag{3.18}$$

It can be shown that all parts of the envelope propagate at v_g by setting the term in the first exponential to equal some constant x;

$$\frac{(t-\beta_0' z)^2}{2\Gamma_0^2} = x \ . \tag{3.19}$$

Rearranging for time, after propagating a distance z that same part of the pulse is now found at a time given by

$$t(z) = \begin{cases} \beta_0' z & \text{if } x = 0 \\ \beta_0' z \pm \Gamma_0\sqrt{2x} & \text{if } x \neq 0 \end{cases} \tag{3.20}$$

The $2\Gamma_0\sqrt{x}$ term is a constant, and so the time shift as a function of propagation is always $\tau_0(z) = \beta_0' z$. The pulse at a range of z values as a function of time is shown in Figure 3.5 for the 100 keV deflection design and Figure 3.6 for the 35 MeV acceleration design. All parts of the pulse propagate at $v_{g,0}$, and the form of the pulse envelope does not change. The underlying phase fronts propagate at $v_{p,0}$. The difference between the propagation in the two DLWs is that $v_{p,0}$ is larger in the 35 MeV acceleration design, and so the underlying oscillations propagate more quickly. $v_{g,0}$ is smaller in the 35 MeV acceleration design, and so the pulse envelope propagates more slowly. Changing ω_0 for the 35 MeV design to that at which third order dispersion is zero, shown in Figure 3.7, results in the same effects. The main difference between Figures 3.6 and 3.7 is the speed of propagation of the envelope and the underlying oscillations. As β_0' is smaller for $\omega_0 = 2\pi f_{op}$, v_g is larger and therefore the pulse propagates more quickly.

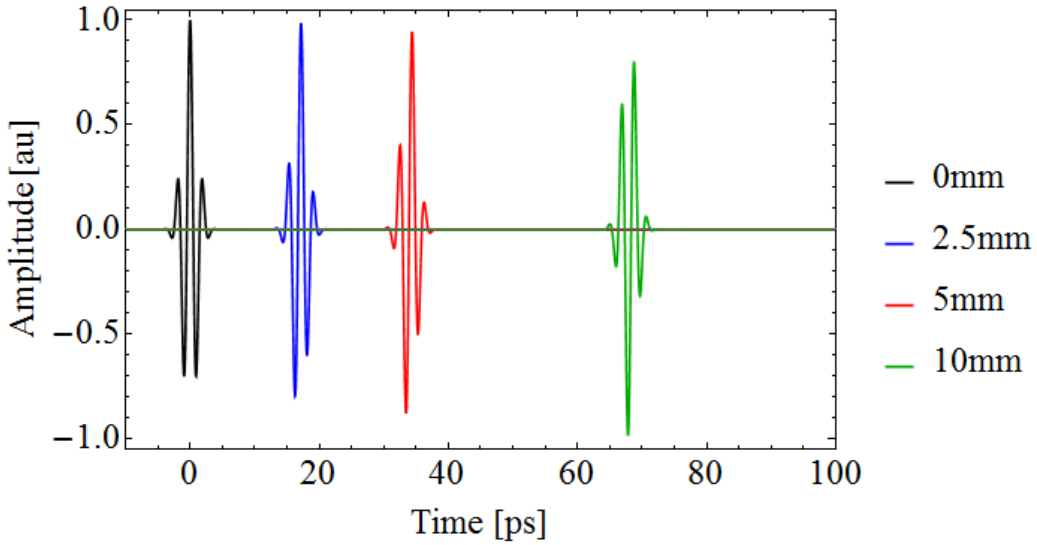

Figure 3.5: Gaussian pulse in the time domain with different values of z for dispersion of first order, for a DLW designed for deflection of 100 keV electrons, described in Table 2.1, using ω_0 equal to the operating frequency. The pulse itself does not propagate, so the pulses are shown with an offset in amplitude. The underlying oscillatory component propagates with $v_{p,0}$.

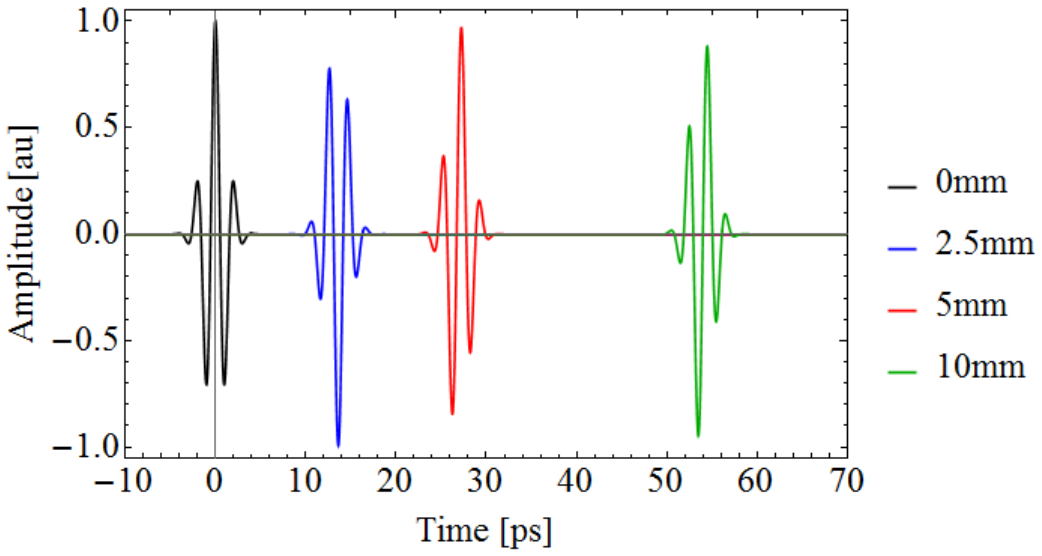

Figure 3.6: Gaussian pulse in the time domain with different values of z for dispersion of first order, for a DLW designed for acceleration of 35 MeV electrons, described in Table 2.1, using ω_0 equal to the operating frequency. The pulse itself does not propagate, so the pulses are shown with an offset in amplitude. The underlying oscillatory component propagates with $v_{p,0}$.

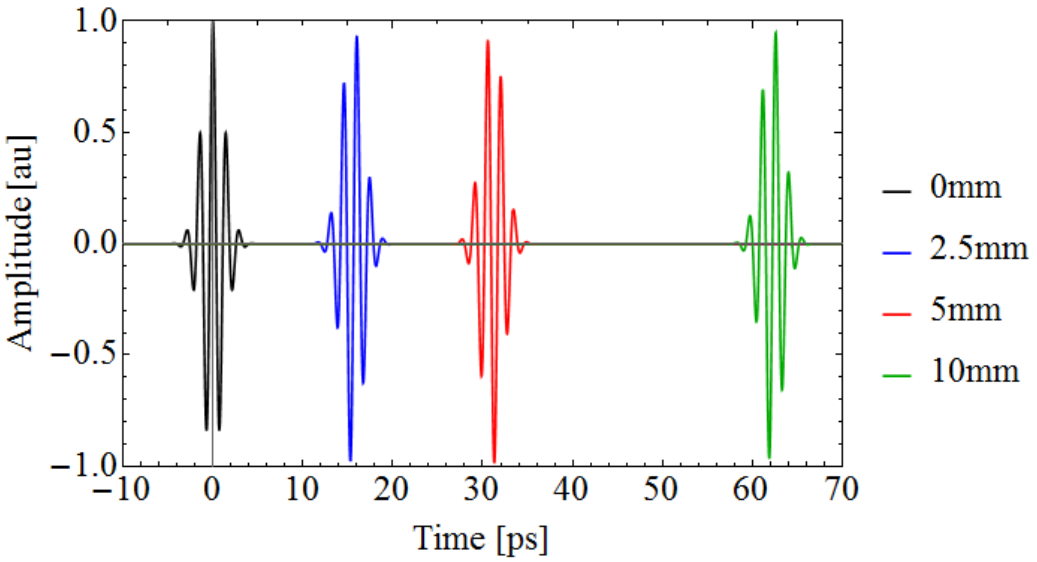

Figure 3.7: Gaussian pulse in the time domain with different values of z for dispersion of first order, for a DLW designed for acceleration of 35 MeV electrons, described in Table 2.1, using ω_0 equal to the frequency at which TOD is zero. The pulse itself does not propagate, so the pulses are shown with an offset in amplitude. The underlying oscillatory component propagates with $v_{p,0}$.

Group velocity in the frequency domain can be understood by considering the superposition of two waves, y_- and y_+, which have frequency $\omega_0 \pm \Delta\omega$ and wavenumber $\beta_0 \pm \Delta\beta$;

$$\begin{aligned} y_- &= \cos\left[(\beta_0 - \Delta\beta) - (\omega_0 - \Delta\omega)\, t\right] \ , \\ y_+ &= \cos\left[(\beta_0 + \Delta\beta) - (\omega_0 + \Delta\omega)\, t\right] \end{aligned} \tag{3.21}$$

Adding the two together gives the resulting motion;

$$y_- + y_+ = 2\cos\left[\omega_0 t - \beta_0 z\right]\cos\left[\Delta\omega t - \Delta\beta z\right] \ . \tag{3.22}$$

This describes two wave effects; a cosine wave propagating with frequency ω_0, whose phase velocity is $v_{p,0}$, and a slowly varying modulation, moving with a velocity $\frac{\Delta\omega}{\Delta\beta}$. In the limit that $\Delta\omega \to 0$, the group velocity can be defined,

$$v_g = \frac{\partial\omega}{\partial\beta} \ . \tag{3.23}$$

This is the inverse of the derivative in the first order expansion of β. v_g is therefore defined in both time and frequency domain.

As $v_g \neq v_p$, a given phase of the oscillation propagates through the pulse. Therefore this phase will only have a significant amplitude for a given propagation distance. The distance L, at which the amplitude of the peak becomes negligible, is calculated by finding the point on the pulse envelope itself at which the amplitude is negligible. The term in the oscillatory exponential is set to $2n\pi$, corresponding to peaks:

$$\beta_0 z - \omega_0 t = 2n\pi \ , \tag{3.24}$$

where n is an integer. The position of each peak in time is

$$t = \frac{\beta_0 z - 2n\pi}{\omega_0} \ . \tag{3.25}$$

At $z = 0$, the start of the structure, the peak n is found at time

$$t_p(z=0) = -\frac{2n\pi}{\omega_0} \tag{3.26}$$

This peak is at a point within the envelope given by

$$t_{g,x_1}(z=0) = -\Gamma_0\sqrt{2x_1} \ , \tag{3.27}$$

where x_1 is a constant defined in Equation 3.19. After a distance L the oscillatory peak is at time

$$t_p(z=L) = \frac{\beta_0 L - 2n\pi}{\omega_0} \ . \tag{3.28}$$

This is no longer at t_{g,x_1}; it is instead found at a point on the envelope

$$t_{g,x_2}(L) = \beta_0' L - \Gamma_0\sqrt{2x_2} \ , \tag{3.29}$$

where x_2 is the constant at which the envelope amplitude is negligible. The distance L is therefore given by equating $t_p(L)$ and $t_{g,x_2}(L)$;

$$L = \frac{2\pi n - \omega_0\Gamma_0\sqrt{2x_2}}{\beta_0 - \omega_0\beta_0'} \ . \tag{3.30}$$

In terms of $v_{p,0}$ and v_g:

$$L = \frac{2\pi n - \omega_0\Gamma_0\sqrt{2x_2}}{\omega_0\left(\frac{1}{v_{p,0}} - \frac{1}{v_g}\right)} \ . \tag{3.31}$$

3.3.3 Second order dispersion

Adding in second order dispersion to the Gaussian pulse;

$$E(\omega,\omega_0,\sigma_0,z)=\exp\left[-\frac{(\omega-\omega_0)^2}{2\sigma_0^2}\right]\exp\left[i\left(\beta_0+\beta_0'(\omega-\omega_0)+\frac{1}{2}\beta_0''(\omega-\omega_0)^2\right)z\right]\ . \tag{3.32}$$

In the time domain;

$$E(t,z,\omega_0,\Gamma_0)=\frac{1}{\sqrt{\Gamma_0^2-i\beta_0''z}}\exp\left[-\frac{1}{2}\frac{(t-\tau_0)^2}{\Gamma_0^2-i\beta_0''z}\right]\exp\left[i\left(\beta_0 z-\omega_0 t\right)\right]\ . \tag{3.33}$$

In order to find the envelope function the first exponential must be split into real and imaginary terms. The real component of the resulting exponential represents the propagation of the envelope,

$$E_{env}(t,z)=\exp\left[\frac{1}{2}\frac{\Gamma_0^2(t-\tau_0)^2}{\Gamma_0^4+(\beta_0''z)^2}\right]\ . \tag{3.34}$$

As with the first order dispersion, the term in the exponential is set equal some constant x_1, equivalent to fixing the amplitude of the envelope function;

$$\frac{1}{2}\frac{\Gamma_0^2(t-\tau_0)^2}{\Gamma_0^4+(\beta_0''z)^2}=-x\ , \tag{3.35}$$

where $\exp[x_1]=k$. k is a constant between 0 and 1. The selected point on the envelope function, after propagating a distance z, has shifted in time by an amount given by

$$t_g(z,x)=\begin{cases}\beta_0'z=\tau_0 & \text{if } x=0\\ \beta_0'z\pm\sqrt{2x\left(\Gamma_0^2+\left(\frac{\beta_0''z}{\Gamma_0}\right)^2\right)} & \text{if } x\neq 0\end{cases} \tag{3.36}$$

There is a non-linear time shift associated with z for any point other than $x=0$, the peak of the envelope, and so the pulse shape must also change. With increasing z the pulse broadens. This broadening is symmetric as x can correspond to a position on either side of the centre of the pulse. There is therefore a new group velocity which is now dependent on x and z,

$$v_g(z,x)=\frac{z}{\tau}=\frac{z}{\beta_0'z+\sqrt{2x\left(\Gamma_0^2+\left(\frac{\beta_0''z}{\Gamma_0}\right)^2\right)}}\ . \tag{3.37}$$

The addition of the second order term causes a change in v_g with position in the pulse. This is defined as group velocity dispersion (GVD). The pulse broadening means that there is a new pulse length,

$$\Gamma_0 \rightarrow \sqrt{\Gamma_0^2 + \left(\frac{\beta_0'' z}{\Gamma_0}\right)^2} \ . \tag{3.38}$$

As the pulse length has changed after propagating a distance z, the amplitude also changes. The amplitude of the envelope function, initially defined as x, is now defined as x_{new} after propagating a distance z:

$$\frac{1}{2}\frac{\Gamma_0^2 \left(t_g(z,x) - \tau_0\right)^2}{\Gamma_0^4 + \left(\beta_0'' z\right)^2} = -x_{new} \ . \tag{3.39}$$

This can be rearranged to give the distance, $L_x(x, x_{new})$, over which the pulse envelope broadening has caused the amplitude of a point on the envelope to change such that the envelope function has a new amplitude x_{new}.;

$$L_x(x, x_{new}) = \frac{\Gamma_0^2 \sqrt{x_{new} - x}}{x\beta_0'^2 - x_{new}\beta_0''^2} \ . \tag{3.40}$$

If $x = 0$, corresponding to the centre of the envelope, the amplitude does not change. Considering the imaginary terms in the exponential allows one to investigate the effect of GVD on the phase fronts of the pulse,

$$E_{osc} = \exp\left[-\frac{i}{2}\frac{\beta_0'' z(t - \beta_0' z)^2}{\Gamma_0^4 + \beta_0''^2 z^2}\right] \exp\left[i\left(\beta_0 z - \omega_0 t\right)\right] \ . \tag{3.41}$$

The term in the exponential is set to $2n\pi$, where n is some integer, to find the phase velocity of a peak 'n' at time t after propagating a distance z:

$$-\frac{1}{2}\frac{\beta_0'' z(t - \beta_0' z)^2}{\Gamma_0^4 + \beta_0''^2 z^2} + \left(\beta_0 z - \omega_0 t\right) = 2\pi n \ . \tag{3.42}$$

The choice of tracking a peak is arbitrary; any individual phase can be chosen. After propagating a distance z, a phase is now found at a time t_p:

$$t_p(z,n) = \beta_0' z + \omega_0 \left(\frac{\Gamma_0^4 + (\beta_0'' z)^2}{\beta_0'' z} \right) \pm \sqrt{\omega_0^2 \left(\frac{\Gamma_0^4 + (\beta_0'' z)^2}{\beta_0'' z} \right)^2 + 2\left(\beta_0 z - \omega_0 \beta_0' z - 2n\pi\right) \left(\frac{\Gamma_0^4 + (\beta_0'' z)^2}{\beta_0'' z} \right)} \tag{3.43}$$

The phase velocity is then written as

$$v_p(z,n) = \frac{z}{\beta_0' z + \omega_0 \left(\frac{\Gamma_0^4 + \left(\beta_0'' z\right)^2}{\beta_0'' z} \right) \pm \sqrt{\omega_0^2 \left(\frac{\Gamma_0^4 + \left(\beta_0'' z\right)^2}{\beta_0'' z} \right)^2 + 2\left(\beta_0 z - \omega_0 \beta_0' z - 2n\pi\right) \left(\frac{\Gamma_0^4 + \left(\beta_0'' z\right)^2}{\beta_0'' z} \right)}} . \tag{3.44}$$

Setting $n = 0$ does not yield any special case. For any n the phase velocity changes with z and so the frequency of the oscillations of the pulse must also change. This introduces the concept of instantaneous frequency, ω_{inst};

$$\omega_{inst}(z,t) = \frac{\partial}{\partial \mathrm{t}} \phi(z,t) \ , \tag{3.45}$$

where ϕ is the phase of oscillations,

$$\phi(z,t) = -\frac{1}{2} \frac{\beta_0'' z (t - \beta_0' z)^2}{\Gamma_0^4 + \beta_0''^2 z^2} + (\beta_0 z - \omega_0 t) \ . \tag{3.46}$$

Inserting this into Equation (3.45) gives

$$\omega_{inst}(z,t) = \omega_0 - \frac{\beta_0'' z (t - \beta_0' z)}{\Gamma_0^4 + \beta_0''^2 z^2} \ . \tag{3.47}$$

$\omega_{inst} \neq \omega_0$ unless $z = 0$ or the oscillations propagate at v_g, which is not the case in this example. The pulse is linearly chirped, meaning that the instantaneous frequency varies linearly through the pulse. A new distance L, which includes second order dispersion, can be defined. The same procedure as in Section 3.3.2 is followed. At $z = 0$, a peak n is found at time

$$t_p(z=0) = -\frac{2\pi n}{\omega_0} \ , \tag{3.48}$$

and this peak is found at a point within the envelope given by

$$t_g(z=0) = \pm\Gamma_0\sqrt{2x_1}\ . \tag{3.49}$$

These are the same as in Section 3.3.2. After a distance L, the peak is now at $t_p(z=L)$, as given by Equation (3.43), and now at a point on the envelope given by x_2. This is at a point on the envelope given by

$$t_{g,x_2}(z=L) = \beta_0' L - \sqrt{2x_2\left(\Gamma_0^2 + \left(\frac{\beta_0'' L}{\Gamma_0}\right)^2\right)}\ . \tag{3.50}$$

Equating $t_p(z=L)$ and $t_{g,x_2}(z=L)$ then rearranging for L gives

$$\begin{aligned} L =& \frac{1}{x_2^2\beta_0''^2 + \Gamma_0^4\left(\beta_0 - \beta_0'\omega_0\right)^2 - 2x_2\Gamma_0^2\beta_0''\left(\beta_0 - \omega_0\beta_0' + \omega_0^2\beta_0''\right)} \times \\ & \Bigg(2n\pi\Gamma_0^2\left(\Gamma_0^2\beta_0 - \Gamma_0^2\omega_0\beta_0' - x_2\beta_0''\right) \\ & + \sqrt{2x_2\Gamma_0^6\omega_0^2\left(\left(4n\pi^2 + x_2^2\right)\beta_0''^2 + \Gamma_0^4\left(\beta_0 - \omega_0\beta_0'\right)^2 - 2x_2\Gamma_0^2\beta_0''\left(\beta_0 - \omega_0\beta_0' + \omega_0^2\beta_0''\right)\right)}\Bigg)\ . \end{aligned} \tag{3.51}$$

A 'slippage length' can be defined as the distance over which an oscillatory peak n, propagates through the pulse to a point x_2 where amplitude is negligible. x_1 is defined by the choice of peak, n, by equating Equations (3.48) and (3.49):

$$x_1 = \frac{1}{2}\left(\frac{2\pi n}{\omega_0}\right)^2\ . \tag{3.52}$$

A further effect is the change of amplitude with z. The energy contained within the pulse must stay constant, assuming zero losses, and so a pulse which broadens must decrease in amplitude. In order to include the amplitude change, the magnitude of the amplitude term at $z = L$ must be included, which reduces the amplitude by a factor

$$\frac{1}{\left|\sqrt{\Gamma_0^2 - i\beta_0'' L}\right|}\ . \tag{3.53}$$

A corrective term is therefore added to the calculation of x_2. Instead of setting $\exp[x_2] = k$, where k is the amplitude at which the field is considered negligible

(normalised to one) and x_2 is a constant with L, the factor is also included:

$$k = \frac{1}{\Gamma_0^2 - i\beta_0'' L} \exp\left[x_2\right] \ . \tag{3.54}$$

Rearranging for x_2 gives:

$$x_2(L) = \log\left[k \left| \sqrt{\Gamma_0^2 - i\beta_0'' L} \right| \right] \ . \tag{3.55}$$

As this is a function of L it must be substituted into Equation (3.51). However this results in an equation which must be solved numerically.

Pulse propagation is shown in Figure 3.8 for the 100 keV deflection design and Figure 3.9 for the 35 MeV acceleration design. The appearance of extra peaks with increasing z is clear in Figure 3.8, but not Figure 3.9. This is explained by the values of β_0'', shown in Tables 3.1 and 3.2; it is approximately halved in the latter when $\omega_0 = 2\pi f_{op}$, and so has less of an effect. In addition, the value is negative; however as a given point on the envelope experiences a time shift which is dependent on the square of β_0'' this does not have an effect on the pulse broadening, as seen in Equation (3.36). Changing ω_0 for the 35 MeV design to that at which third order dispersion is zero, shown in Figure 3.10, exaggerates the effect of GVD. The value of β_0'' is both positive and an order of magnitude larger than in the other two examples; as a result, broadening of the envelope and the chirping effect are easily observed. In comparison to Figures 3.9 and 3.9, the chirp is flipped with respect to time.

3.3.4 Third order dispersion

Adding third order dispersion (TOD) is necessary to take into account asymmetric broadening of the pulse. The Fourier transform is applied via the use of the cubic formula, resulting in a time domain pulse described using an Airy function. The spectrum of the pulse is given as

$$\begin{aligned} E(\omega, \omega_0, \sigma_0, z) = &\exp\left[-\frac{(\omega-\omega_0)^2}{2\sigma_0^2}\right] \\ &\times \exp\left[i\left(\beta_0 + \beta_0'(\omega-\omega_0) + \frac{1}{2}\beta_0''(\omega-\omega_0)^2 + \frac{1}{6}\beta_0'''(\omega-\omega_0\right)^3 z\right] \ . \end{aligned} \tag{3.56}$$

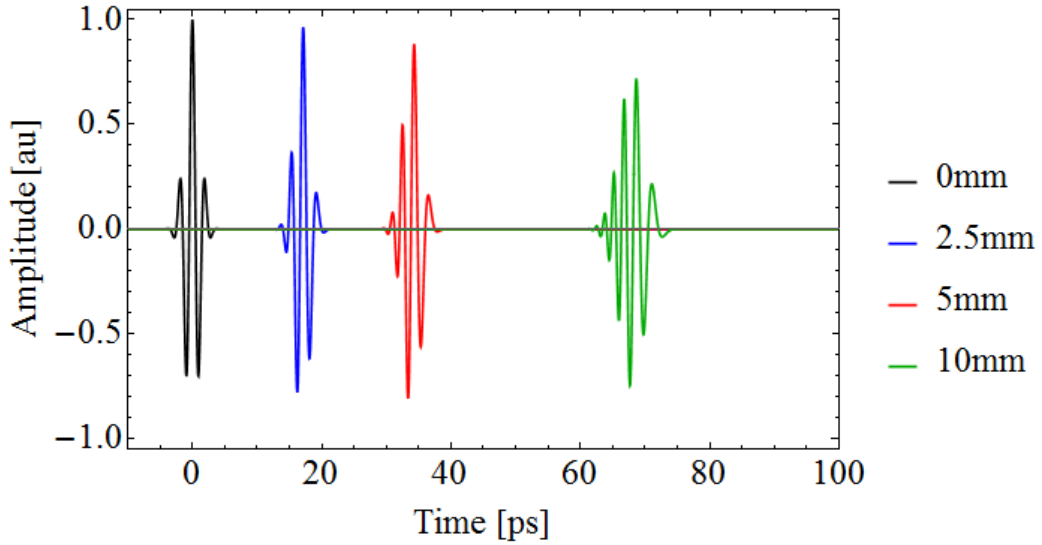

Figure 3.8: Gaussian pulse in the time domain with different values of z for dispersion up to second order, for a DLW designed for deflection of 100 keV electrons, described in Table 2.1, using ω_0 equal to the operating frequency. The pulse propagates with a v_g dependent on distance from the centre of the envelope, and the underlying oscillatory component propagates with v_p. The phase velocity depends on position within the bunch, leading to a chirping effect.

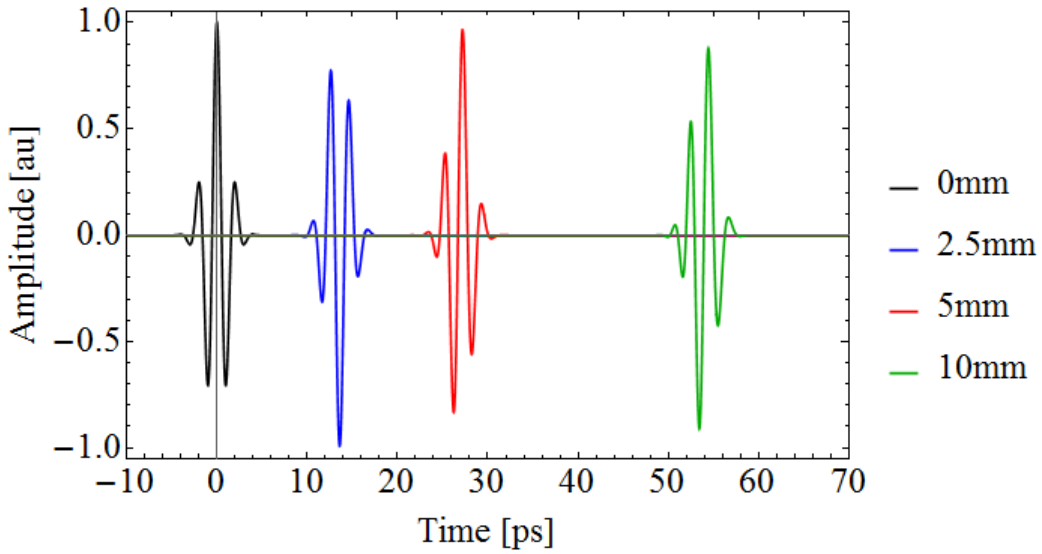

Figure 3.9: Gaussian pulse in the time domain with different values of z for dispersion up to second order, for a DLW designed for acceleration of 35 MeV electrons, described in Table 2.1, using ω_0 equal to the operating frequency. The pulse propagates with a v_g dependent on distance from the centre of the envelope, and the underlying oscillatory component propagates with v_p. There is no clear chirping effect.

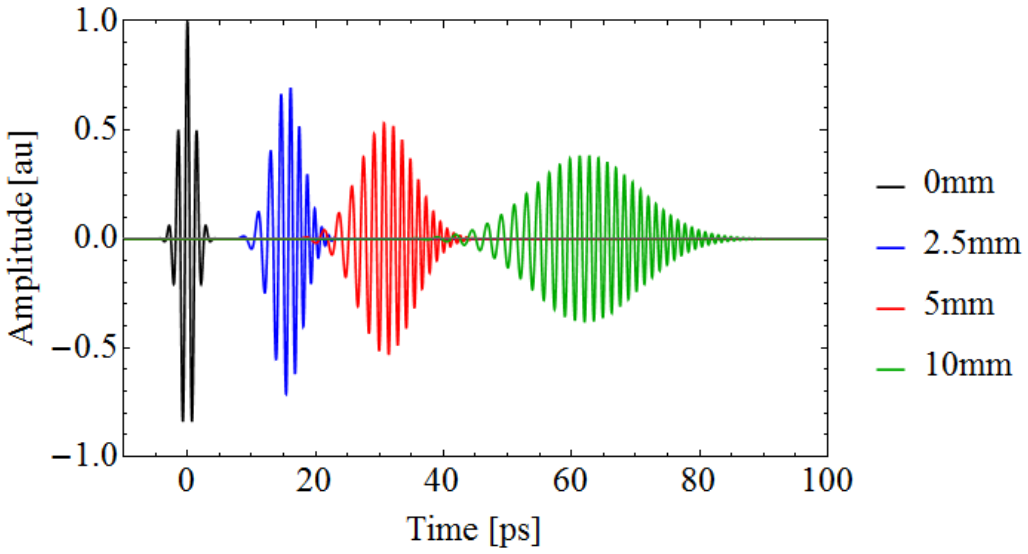

Figure 3.10: Gaussian pulse in the time domain with different values of z for dispersion up to second order, for a DLW designed for acceleration of 35 MeV electrons, described in Table 2.1, using ω_0 equal to the operating frequency. The pulse propagates with a v_g dependent on distance from the centre of the envelope, and the underlying oscillatory component propagates with v_p. The phase velocity depends on position within the bunch, leading to a chirping effect.

In the time domain the Gaussian pulse is written as

$$\begin{aligned}\tilde{E}(\omega, z) =& \frac{1}{\sqrt{2}} \int_{-\infty}^{+\infty} \exp\left[-\frac{1}{2}\Gamma_0^2 \omega'^2\right] \\ & \times \exp\left[i\left(\beta_0 + \beta_0'\omega' + \frac{1}{2}\beta_0''\omega'^2 + \frac{1}{6}\beta_0'''\omega'^3\right)\Delta z\right] \exp\left[i\omega t\right] \mathrm{d}\omega \ .\end{aligned} \tag{3.57}$$

This can only be solved with the use of the cubic formula [98]. Making the substitution $\omega_n = \omega'/(\sqrt{2}\ \sigma_0)$,

$$\begin{aligned}E(t, z) =& \frac{1}{\sqrt{2}\sigma_0} \int_{-\infty}^{\infty} \exp\left[i\frac{1}{3}\frac{\beta_0'''\Delta z}{12\sqrt{2}\sigma_0^3}\omega_n^3 + \left(-\frac{1}{4\sigma_0^4} + i\frac{\beta_0''' z}{4\sigma_0^2}\right)\omega_n^2\right. \\ & \left. + \left(-i\frac{t}{\sqrt{2}\sigma_0} + i\frac{\beta_0' z}{\sqrt{2}\sigma_0^2}\right)\omega_n + i\beta_0 z - i\omega_0 t\right] \mathrm{d}\omega_n \ .\end{aligned} \tag{3.58}$$

gives an expression of the form $i\frac{a}{3}\omega^3 + ib\omega^2 + ic\omega$. Defining $\xi = a^{1/3}\omega$, this becomes

$$i\frac{1}{3}\xi^3 + ia^{-2/3}b\xi^2 + ia^{-1/3}c\xi \ . \tag{3.59}$$

Letting $\xi = u - \lambda$, and setting $\lambda = -ia^{-2/3}b$ removes the ξ^2 term. Rewriting ω in terms of u gives

$$i\frac{1}{3}u^3 + i\left(-\frac{b^2}{a^{4/3}} + \frac{c}{a^{1/3}}\right)u + i\left(\frac{2b^3}{3a^2} - \frac{bc}{3a}\right) , \tag{3.60}$$

$$\mathrm{d}u = \mathrm{d}\xi = a^{1/3}\mathrm{d}\omega . \tag{3.61}$$

Equation (3.58) is rewritten as

$$\begin{aligned} E(t,z) =& \frac{1}{\sqrt{2}\sigma_0}\left(\frac{\beta_0'''z}{4\sqrt{2}\sigma_0^3}\right)^{-1/3}\exp\left[i\left(\beta_0 z - i\omega_0 t\right)\right] \\ &\times\exp\left[-\frac{64\sigma_0^6\left(-\frac{1}{4\sigma_0^4}+i\frac{\beta_0''}{4\sigma_0^4}\right)^3}{3\beta_0'''^2 z} + \frac{i4\sqrt{2}\left(-\frac{1}{4\sigma_0^4}+i\frac{\beta_0''z}{4\sigma_0^4}\right)\left(-i\frac{t}{\sqrt{2}\sigma_0}+i\frac{\beta_0' z}{\sqrt{2}\sigma_0}\right)}{\beta_0'''z}\right] \\ &\times\int_{-\infty}^{\infty}\exp\left[i\frac{1}{3}u^3 + \left(i\frac{2^{10/3}\left(-\frac{1}{4\sigma_0^4}+i\frac{\beta_0''z}{4\sigma_0^2}\right)^2}{\frac{\beta_0'''z}{\sigma_0^3}^{4/3}} + \frac{2^{5/6}\left(-i\frac{t}{\sqrt{2}\sigma_0}+i\frac{\beta_0' z}{\sqrt{2}\sigma_0}\right)}{\frac{\beta_0'''z}{\sigma_0^3}^{1/3}}\right)\right]\mathrm{d}u . \end{aligned} \tag{3.62}$$

The Airy function for an exponential function, $Ai(z) = \frac{1}{2\pi}\int_{-\infty}^{\infty}\exp\left[i\left(zt + \frac{t^3}{3}\right)\right]\mathrm{d}t$ is used to give the field as

$$\begin{aligned} E(t,z) =& \frac{1}{\sqrt{2}\sigma_0}\left(\frac{\beta_0'''z}{4\sqrt{2}\sigma_0^3}\right)^{-1/3}\exp\left[-i\left(\omega t - \beta_0 z\right)\right] \\ &\times\exp\left[-\frac{64\sigma_0^6\left(-\frac{1}{4\sigma_0^4}+i\frac{\beta_0''}{4\sigma_0^4}\right)^3}{3\beta_0'''^2 z} + \frac{i4\sqrt{2}\left(-\frac{1}{4\sigma_0^4}+i\frac{\beta_0''z}{4\sigma_0^4}\right)\left(-i\frac{t}{\sqrt{2}\sigma_0}+i\frac{\beta_0' z}{\sqrt{2}\sigma_0}\right)}{\beta_0'''z}\right] \\ &\times\mathrm{Ai}\left[i\frac{2^{10/3}\left(-\frac{1}{4\sigma_0^4}+i\frac{\beta_0''z}{4\sigma_0^2}\right)^2}{\frac{\beta_0'''z}{\sigma_0^3}^{4/3}} + \frac{2^{5/6}\left(-i\frac{t}{\sqrt{2}\sigma_0}+i\frac{\beta_0' z}{\sqrt{2}\sigma_0}\right)}{\frac{\beta_0'''z}{\sigma_0^3}^{1/3}}\right] . \end{aligned} \tag{3.63}$$

The Airy function, a Bessel-type function, is shown in Figure 3.11. It decays rapidly to zero at positive values of the argument. At negative values the frequency of oscillations increases with the magnitude of the argument with a mild damping effect. This directly corresponds to the chirping effect of TOD and the asymmetric pulse broadening, which can be seen in Figure 3.12 for the 100 keV deflection design and Figure 3.13 for the 35 MeV acceleration design, using the parameters given in Tables 3.1 and 3.2 respectively. In both Figures there is a clear non-linear chirping with

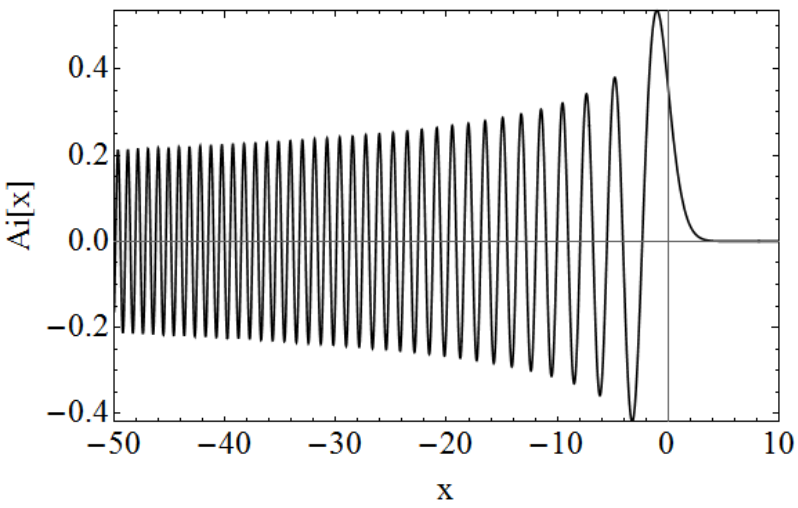

Figure 3.11: Form of the Airy function.

increasing z. The TOD is more significant in Figure 3.13, which is to be expected as, comparing Tables 3.1 and 3.2, β_0''' is approximately ten times larger.

3.3.5 Conclusions

The pulse propagation depends strongly on the dispersion of the waveguide. Adding higher orders of dispersion beyond the second order results in non-linear effect with both t and z. Changing the value of ω_0 for the 35 MeV design highlighted the limit of the Taylor approximation; as the dispersion function is highly non-linear it cannot be replicated fully. Inclusion of each dispersive effect is shown in Figure 3.14 for the 100 keV deflection design, and Figure 3.15 for the 35 MeV acceleration design, using $\omega_0 = 2\pi f_{op}$. In both cases the dispersion relation is well modelled over a small frequency range, and so is useful for a narrowband pulse. However the Taylor approximation is insufficient at frequencies close to cut-off as well as higher frequencies due to the non-linearity of the dispersion above ω_0. For broadband THz pulses the dispersion is likely to be underestimated. There is also a real (negative) β component which contributes to errors in the model.

It is of note that there is an asymmetry of the Taylor approximation about $\omega = 0$. This is addressed by modifying the limits of the Fourier transform to between zero and ∞. To account for the non-zero real component of the dispersion relation below the cut-off frequency, which is mostly clearly seen in Figure 3.15, which does not exist in the analytical solution to the dispersion relation, the integral is also integrated

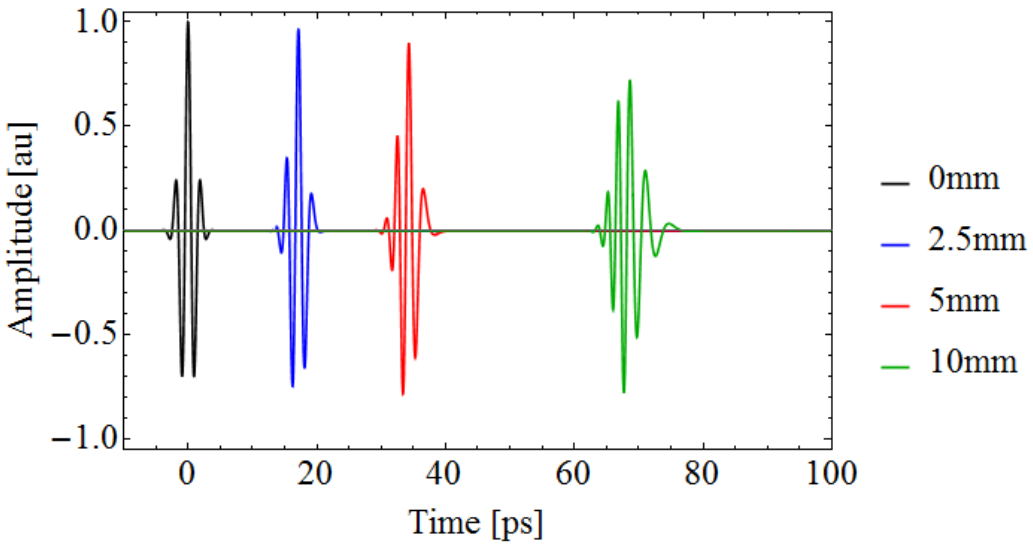

Figure 3.12: Gaussian pulse in the time domain with different values of z for dispersion of third order, for a DLW designed for deflection of 100 keV electrons, described in Table 2.1, using ω_0 equal to the operating frequency. The pulse propagates with v_g dependent asymmetrically on the distance from the centre of the pulse. The oscillatory component propagates with a velocity dependent on the position within the pulse, causing a non-linear chirping.

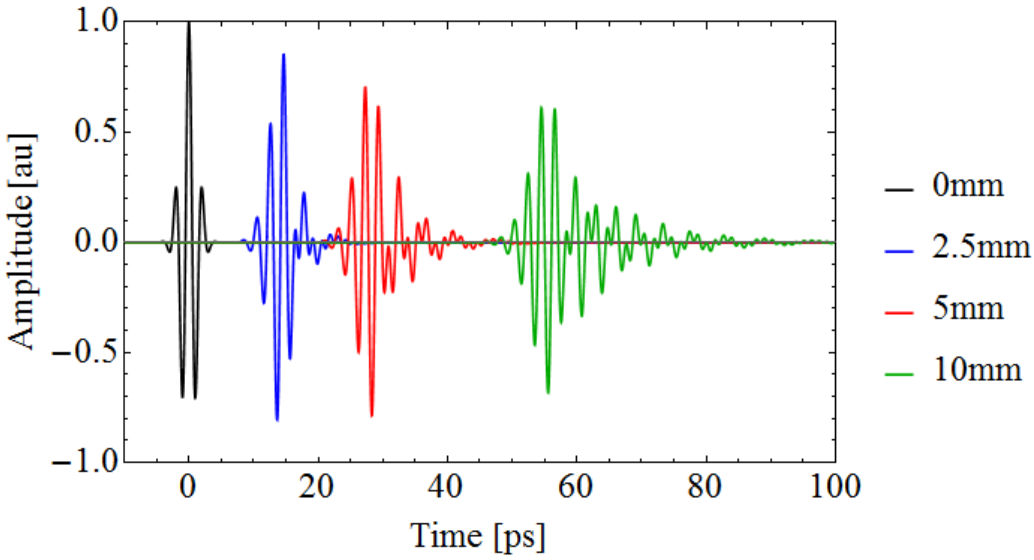

Figure 3.13: Gaussian pulse in the time domain with different values of z for dispersion of third order, for a DLW designed for acceleration of 35 MeV electrons, described in Table 2.1, using ω_0 equal to the operating frequency. The pulse propagates with v_g dependent asymmetrically on the distance from the centre of the pulse. The oscillatory component propagates with a velocity dependent on the position within the pulse, causing a non-linear chirping.

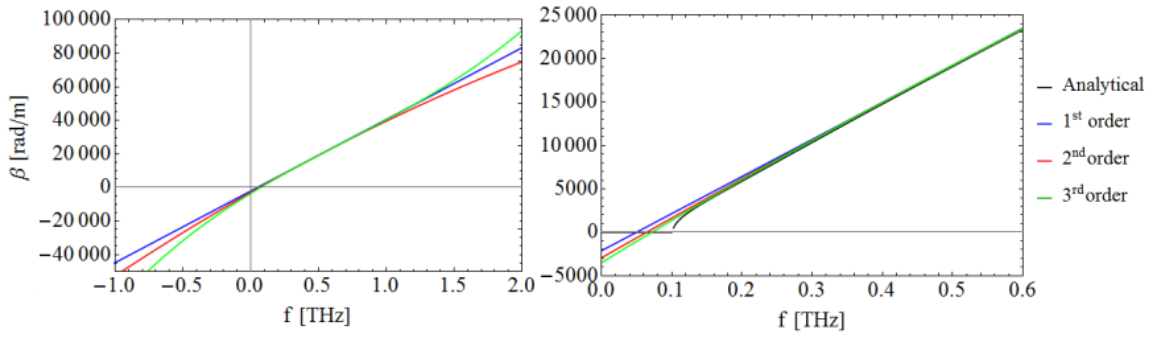

Figure 3.14: Solutions to the dispersion relation to different levels of approximation for a DLW designed for deflection of 100 keV electrons, described in Table 2.1, using ω_0 equal to the operating frequency. Black: dispersion relation as solved from the analytical expression. 1st order dispersion includes only v_g, 2nd order includes GVD, and 3rd order includes TOD.

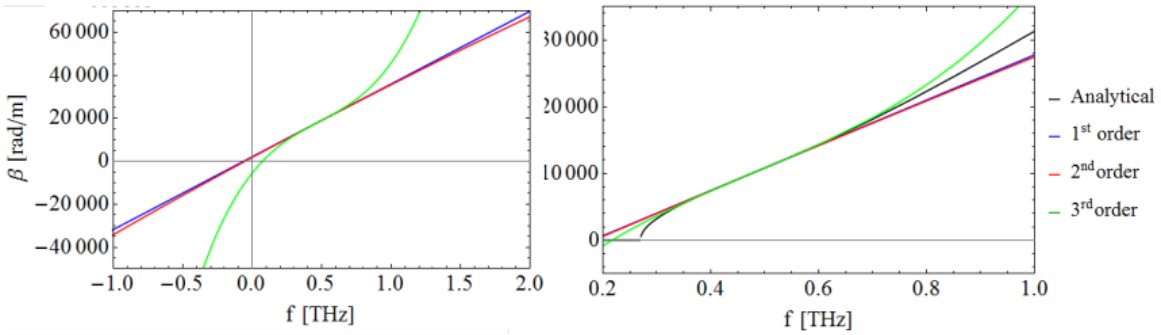

Figure 3.15: Solutions to the dispersion relation to different levels of approximation for a DLW designed for acceleration of 35 MeV electrons, described in Table 2.1, using ω_0 equal to the operating frequency. Black: Dispersion relation as solved from the analytical expression. 1st order dispersion includes only v_g, 2nd order includes GVD, and 3rd order includes TOD.

between ω_c and ∞,

$$\tilde{E}(t) = \frac{2}{2\pi} \int_{\omega_c}^{\infty} \tilde{A}(\omega) \exp\left[i\beta(\omega)z\right] \exp\left[-i\omega t\right] \mathrm{d}\omega \ . \tag{3.64}$$

There is no analytical solution to the Taylor approximation beyond the second order approximation. In the interests of conciseness the equation for each order of the Taylor approximation is not included here. In the Gaussian case the change in pulse propagation is negligible.

Two equations, defining the length over which a single oscillatory peak propagates inside the pulse, have been derived, first considering only the group velocity, and then the group velocity with GVD. Higher-order Taylor approximations do not produce

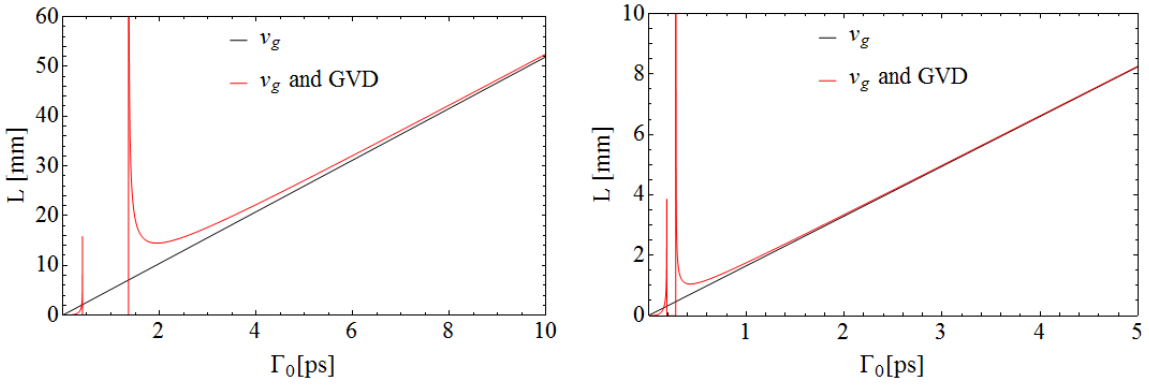

Figure 3.16: Slippage length, the distance over which oscillatory peak at centre of Gaussian pulse slips out of the pulse, as a function of initial pulse width. Left: DLW designed for deflection of 100 keV electrons, with parameters described in Table 2.1. Right: DLW designed for deflection of 100 keV electrons, with parameters described in Table 2.1. In both cases $\omega_0 = 2\pi f_{op}$.

an equation for L; it must be solved numerically. Setting $n = 0$ and $x_1 = 0$ and thus only considering the peak which initially starts at the centre of the envelope (at $t = 0$) gives the slippage length as a function of Γ_0. This is shown in Figure 3.16 for both the 100 keV deflection design and the 35 MeV acceleration design, using the parameters given in Tables 3.1 and 3.2 respectively, with $\omega_0 = 2\pi f_{op}$ in both cases. In both cases the slippage length using only v_g and the slippage length including both v_g and GVD are equal as $\Gamma_0 \to \infty$. This is because, as Γ_0 increases, GVD has less of an effect. This is to be expected; the interaction length in Equation (3.51) is non-linearly dependent on Γ_0. For large Γ_0 the β_0 and β_0' terms dominate. Therefore for narrowband pulses, Equation (3.31) can be used. At low values of Γ_0, there are other effects. The slippage length at $\Gamma_0 = 0$ is zero, as expected, and increases exponentially to infinity. There is then a region in which the slippage length is zero, bounded on both sides by points at which the slippage length is infinite. These points are found by setting the denominator in Equation 3.51 to zero. Beyond this, the interaction length decreases from infinity, reaches a local minima, and then tends towards the slippage length when only v_g is considered. Figure 3.17 shows the slippage length of the 35 MeV acceleration design, using the parameters given in Table 3.2, with ω_0 equal to that at which there is no third order dispersion. In this case, there is one point at which the slippage length is infinite. The difference is due to the sign of the β_0'' term. In both cases in Figure 3.16 it is negative, whereas it is positive in Figure 3.17. Equation (3.51) includes terms where β_0'' is raised to an odd power, so its sign has an effect.

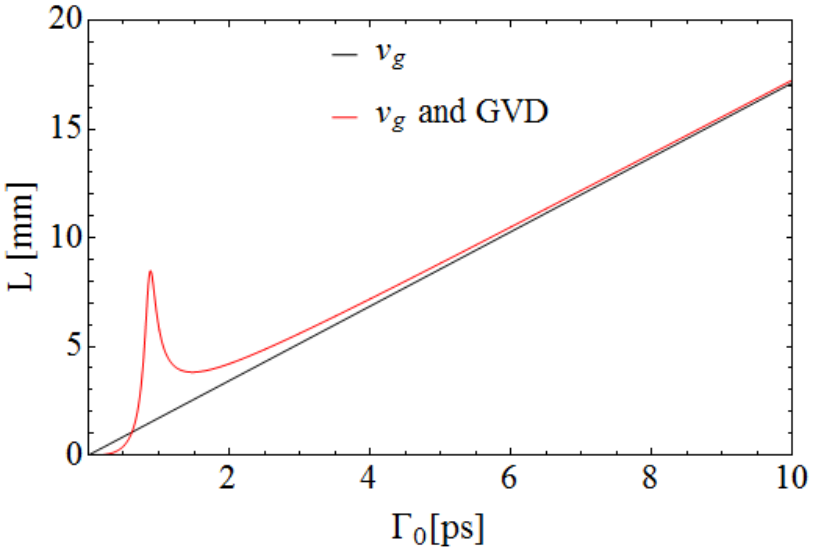

Figure 3.17: Slippage length, the distance over which oscillatory peak at centre of Gaussian pulse slips out of the pulse, as a function of initial pulse width. DLW designed for acceleration of 35 MeV electrons, with parameters described in Table 2.1. ω_0 is equal to the frequency at which there is no third order dispersion.

The value of L at these shorter pulse lengths is unphysical; as previously discussed the shortest physical length of a Gaussian pulse is fixed as greater bandwidths result in negative frequencies and so the slippage length as calculated from the Taylor approximation would not be used at the pulse lengths where it becomes infinite or zero. In each case, the inclusion of the amplitude correction term has negligible effect.

3.4 Ultrashort pulses

The ultrashort pulse is described in the frequency domain using a modified Gaussian function.

$$E(\omega) = \omega^2 \exp\left[\frac{\omega^2}{\sigma_0^2}\right] \quad . \tag{3.65}$$

This is shown in Figure 3.18 for $\sigma_0 = \omega_0$, corresponding to a maximum at ω_0. It is important to note that the modified Gaussian function is symmetrical about $\omega = 0$, and so the application of the Fourier transform using limits between $-\infty$ and ∞ does not produce the correct result as the dispersion function is not symmetric about ω_0. It is, however, of interest to see how this affects the pulse propagation and a correction is added in Section 3.4.5. In the time domain,

$$E(t,z) = \frac{1}{4\sqrt{2}}\sigma_0^3\left(\sigma_0^2 t^2 - 1\right)\exp\left[-\left(\frac{\sigma_0 t}{2}\right)^2\right] \quad . \tag{3.66}$$

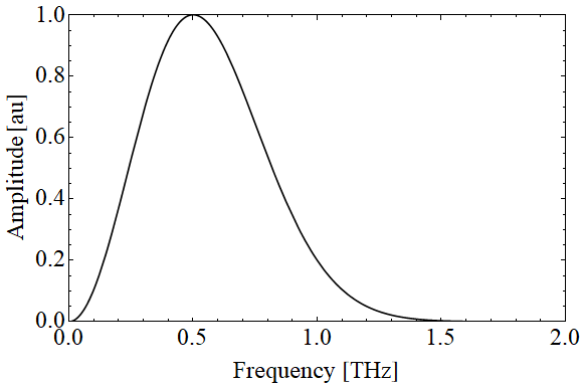

Figure 3.18: Frequency spectrum of an ultrashort pulse with maximum at $\omega_0 = (2\pi) \times 0.5$ THz. The pulse has a form similar to a Gaussian with a tail at higher frequencies.

The pulse in the time domain is shown in Figure 3.19 (at $z = 0$ mm) for the 100 keV deflection design and Figure 3.20 (at $z = 0$ mm) for the 35 MeV acceleration design, using ω_0 equal to the operating frequency only in both cases. Derivation of an analytical solution to the field in the time domain only possible up to and including second order dispersion; further terms require a numerical solution.

3.4.1 Zero dispersion

Approximating β using zeroth order dispersion leads to the definition of the electric field;

$$E(t,z) = \frac{1}{4\sqrt{2}}\sigma_0^3\left(\sigma_0^2 t^2 - 1\right)\exp\left[-\left(\frac{\sigma_0 t}{2}\right)^2\right]\exp\left[i\beta_0 z\right] \ . \tag{3.67}$$

The pulse at different values of z is shown Figure 3.19 for the 100 keV deflection design and Figure 3.20 for the 35 MeV acceleration design, using ω_0 equal to the operating frequency. An individual peak does not propagate, unlike the Gaussian pulse. Instead, the amplitude oscillates with frequency $\beta_0 z$.

3.4.2 First order dispersion

Adding first order dispersion, the electric field of the modified Gaussian pulse is described by:

$$E(t,z) = \frac{1}{4\sqrt{2}}\sigma_0^3\left(\sigma_0^2\left(t-\tau_0\right)^2 - 2\right)\exp\left[-\left(\frac{\sigma_0\left(t-\tau_0\right)}{2}\right)^2\right]\exp\left[i\left(\beta_0 z - \omega_0\tau_0\right)\right] \ . \tag{3.68}$$

The oscillatory component has no time dependency. As the pulse propagates, the amplitude of the envelope also oscillates. The oscillatory component propagates with the same velocity as the envelope. This is shown in Figure 3.21 for the 100 keV

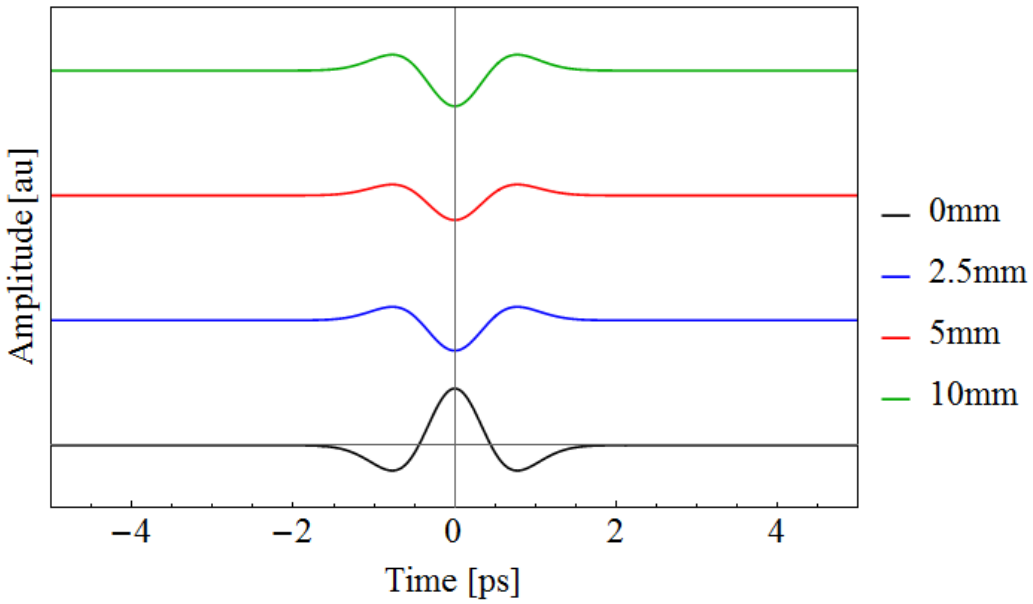

Figure 3.19: Modified Gaussian pulse in the time domain at different values of z for dispersion of zeroth order, for a DLW designed for deflection of 100 keV electrons, with parameters described in Table 2.1, using ω_0 equal to the operating frequency. The pulse itself does not propagate, so the pulses are shown with an offset in amplitude. The underlying oscillatory component propagates with $v_{p,0}$.

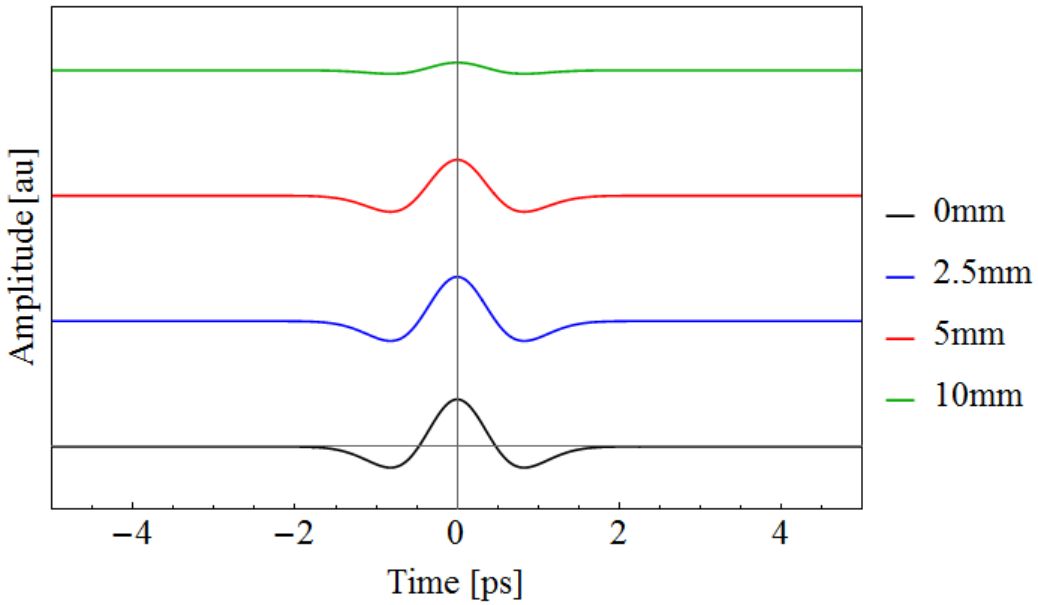

Figure 3.20: Modified Gaussian pulse in the time domain at different values of z for dispersion of zeroth order, for a DLW designed for acceleration of 35 MeV electrons, with parameters described in Table 2.1, using ω_0 equal to the operating frequency. The pulse itself does not propagate, so the pulses are shown with an offset in amplitude. The underlying oscillatory component propagates with $v_{p,0}$.

deflection design and Figure 3.22 for the 35 MeV acceleration design, using ω_0 equal to the operating frequency. These pulses are not realistic as the energy is not constant at each z.

3.4.3 Second order dispersion

The addition of second order dispersion produces

$$E(t,z) = \frac{\sigma_0^3\left(\sigma_0^2\left(t-\tau_0+\omega_0\beta_0''z\right)^2+i\sigma_0^2\beta_0''z-2\right)}{\left(2-i\sigma_0^2\beta_0''z\right)^2\sqrt{2-i\sigma_0^2\beta_0''z}} \times \exp\left[\frac{-\sigma_0^2\left(t-\tau_0+\omega_0\beta_0''z\right)^2}{2\left(2-i\sigma_0^2\beta_0''z\right)}\right]\exp\left[i\left(\beta_0 z-\omega_0\tau_0+\frac{1}{2}\omega_0^2\beta_0''z\right)\right] . \tag{3.69}$$

The inclusion of GVD adds an extra component to each term. As with the Gaussian pulse the modified Gaussian can also be split into the envelope and the oscillatory component. Taking the real part,

$$E_{env}(t,z) = \exp\left[-\frac{2\sigma_0^2\left(t-\tau_0+\omega_0\beta_0''z\right)^2}{4+\left(\sigma_0^2\beta_0''z\right)^2}\right] , \tag{3.70}$$

the pulse broadens as it propagates due to the z dependence. Taking the imaginary part;

$$E_{osc}(z,t) = \exp\left[i\left(\beta_0 z-\omega_0\tau_0+\left(\frac{1}{2}\omega_0^2\frac{\sigma_0^4}{4+\left(\sigma_0^2\beta_0''z\right)^2}\left(t-\tau_0+\omega_0\beta_0''z\right)^2\right)\beta_0''z\right)\right] , \tag{3.71}$$

the oscillations propagate with a different velocity to the envelope, which is now dependent on both t and z. Propagation of the pulse is shown in Figure 3.23 for the 100 keV deflection design and Figure 3.24 for the 35 MeV acceleration design, using ω_0 equal to the operating frequency. The pulse splits into two, each part propagating in different directions. This is again an effect of asymmetry of the Taylor approximation of the dispersion function about $\omega = 0$. However, the effect of GVD is observable as the instantaneous frequency of the oscillations varies in time in both examples.

3.4.4 Third order dispersion

TOD cannot be included in an analytical solution to the Taylor approximation as there are remaining terms of u in the integral, preventing the use of the Airy function. However, a numerical solution can be produced. This numerical solution was calculated using *Mathematica*; the Fourier transform was applied numerically and the field at each value of t calculated individually. Therefore the accuracy of the Fourier transform depended on the step size between each point in time, and the

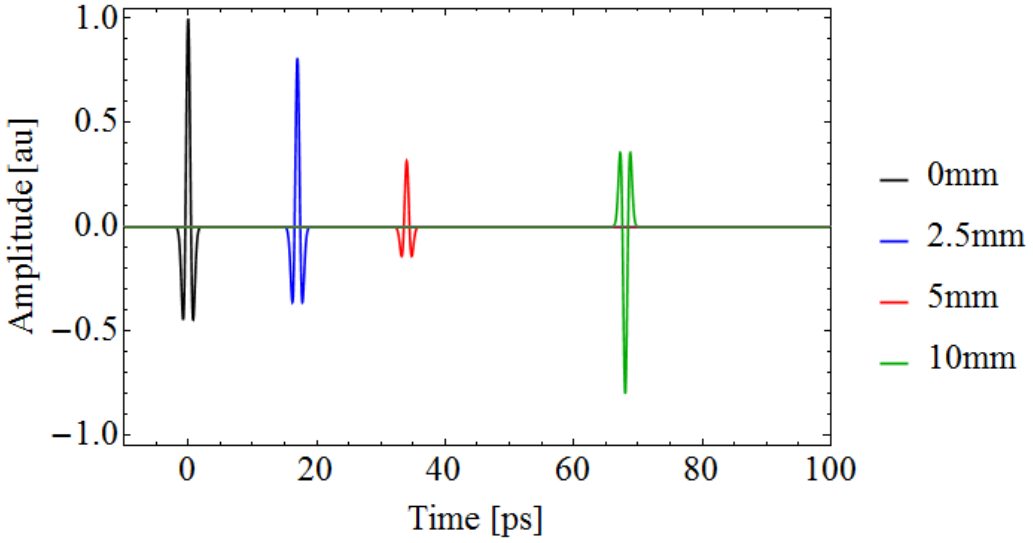

Figure 3.21: Modified Gaussian pulse in the time domain at different values of z for dispersion of first order, for a DLW designed for deflection of 100 keV electrons, with parameters described in Table 2.1, using ω_0 equal to the operating frequency. The pulse envelope and oscillations propagate with $v_{g,0}$.

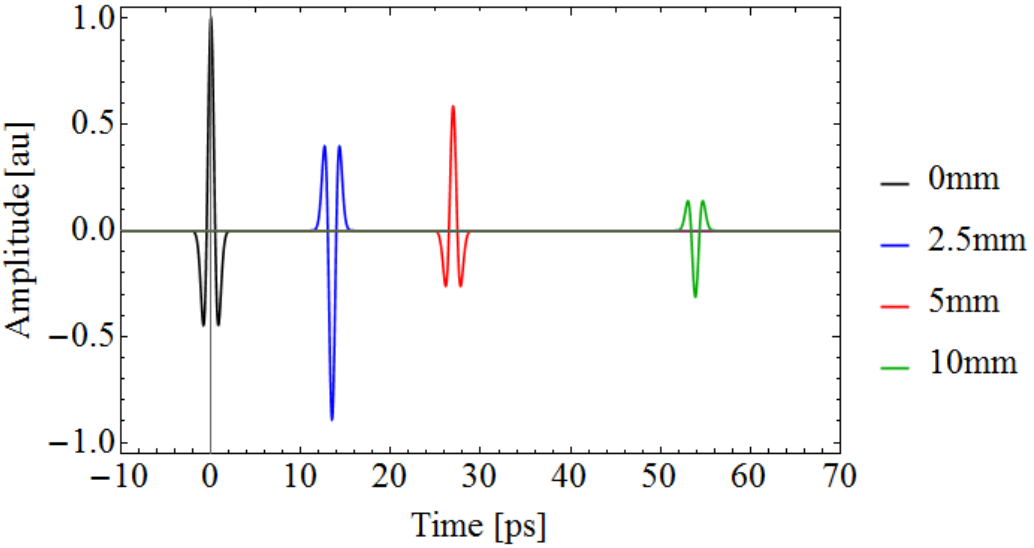

Figure 3.22: Modified Gaussian pulse in the time domain at different values of z for dispersion of first order, with parameters described in Table 2.1, for a DLW designed for acceleration of 35 MeV electrons, using ω_0 equal to the operating frequency. The pulse envelope and oscillations propagate with $v_{g,0}$.

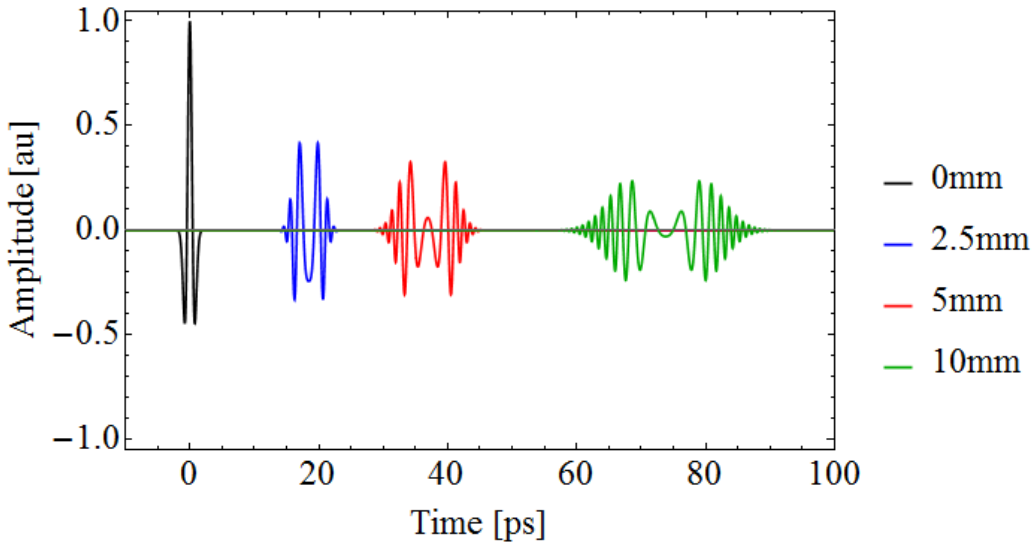

Figure 3.23: Modified Gaussian pulse in the time domain at different values of z for dispersion up to second order, for a DLW designed for deflection of 100 keV electrons, with parameters described in Table 2.1, using ω_0 equal to the operating frequency. The pulse envelope broadens as it propagates, and so the number of oscillations increases, with a chirping effect. The generation of two pulses is due to asymmetry in the frequency domain.

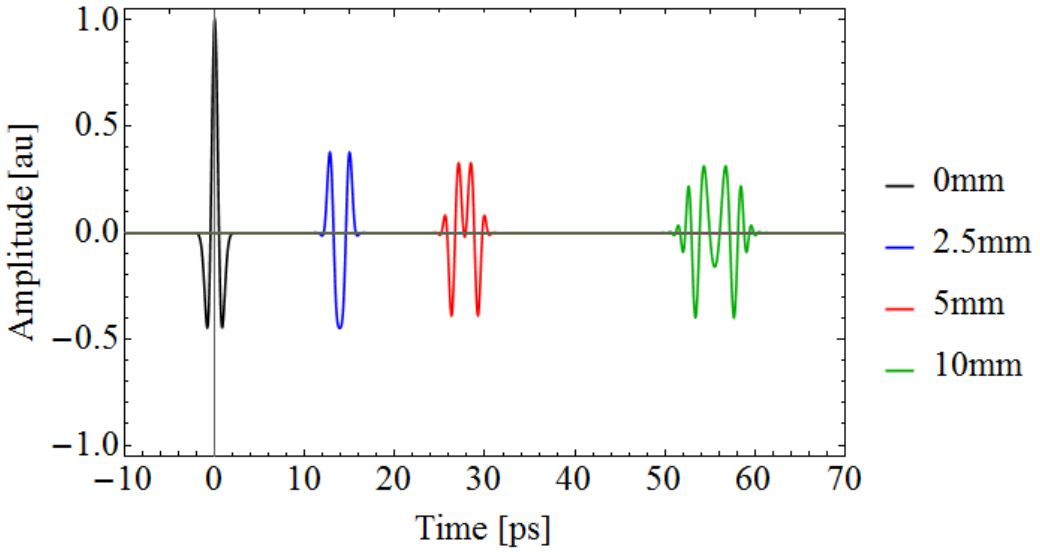

Figure 3.24: Modified Gaussian pulse in the time domain at different values of z for dispersion up to second order, for a DLW designed for acceleration of 35 MeV electrons, with parameters described in Table 2.1, using ω_0 equal to the operating frequency. The pulse envelope broadens as it propagates, and so the number of oscillations increases, with a chirping effect. The generation of two pulses is due to asymmetry in the frequency domain.

frequency range used in the integral. Pulse propagation is shown in Figure 3.25 for the 100 keV deflection design and Figure 3.26 for the 35 MeV acceleration design, using ω_0 equal to the operating frequency. The pulse splits into two, with two pulses propagating in different directions. These pulses are not symmetrical due to the asymmetric dispersion dispersion function about $\omega = 0$.

3.4.5 Correcting asymmetries in the frequency domain

As the modified Gaussian function is symmetric about $\omega = 0$, but the dispersion relation is asymmetric, the effect of adding a correction is expected to be large compared to the negligible effect on the Gaussian pulse. This asymmetry is corrected by performing the Fourier transform integral for positive frequencies. The effect of negative β below cut-off frequency is removed by only integrating above ω_c.

With inclusion of only zeroth order dispersion,

$$\begin{aligned} E(t,z) =& \frac{\sigma_0^3}{4\sqrt{2}} \exp\left[-\left(\frac{\sigma_0 t}{2}\right)^2\right] \exp\left[i\beta_0 z\right] \times \\ & \left(4\left(-\frac{\sigma_0 t}{t} + i\frac{\omega_c}{\sigma_0}\right) \exp\left[\left(-\frac{\sigma_0 t}{2} - i\frac{\omega_c}{\sigma_0}\right)^2\right]\right. \\ & \left. - \sqrt{\pi}\left(\sigma_0^2 t^2 - 2\right)\left(1 - \operatorname{erf}\left[\left(\frac{\sigma_0 t}{2} - i\frac{\omega_c}{\sigma_0}\right)\right]\right)\right). \end{aligned} \tag{3.72}$$

Given that β is a constant, the cut-off frequency ω_c can be removed as it has no meaning. The pulse in the time domain is shown in Figure 3.27 for the 100 keV deflection design and Figure 3.28 for the 35 MeV acceleration design, using ω_0 equal to the operating frequency. In comparison to Figure 3.19, the correction for the asymmetry about $\omega = 0$ has allowed for propagation of the underlying oscillations, comparable to the Gaussian pulse with zeroth order dispersion.

Adding higher orders of dispersion leads to equations in the time domain which are cumbersome to reproduce. Only the pulse propagation with addition of first order, second order, and third order dispersion are shown here, in Figures 3.29, 3.31, and 3.33 respectively for the 100 keV deflection design, and Figures 3.28, 3.30, and 3.32 for the 35 MeV acceleration design, using ω_0 equal to the operating frequency. The application of first order dispersion allows for propagation of both envelope and oscillations with velocities v_g and $v_{p,0}$ respectively. The removal of the asymmetry about $\omega = 0$ has corrected the missing propagation of the oscillations, which can be seen when compared with Figure 3.21. Second order dispersion no longer features two counter-propagating pulses at each position, as was the case in Figure 3.23. It

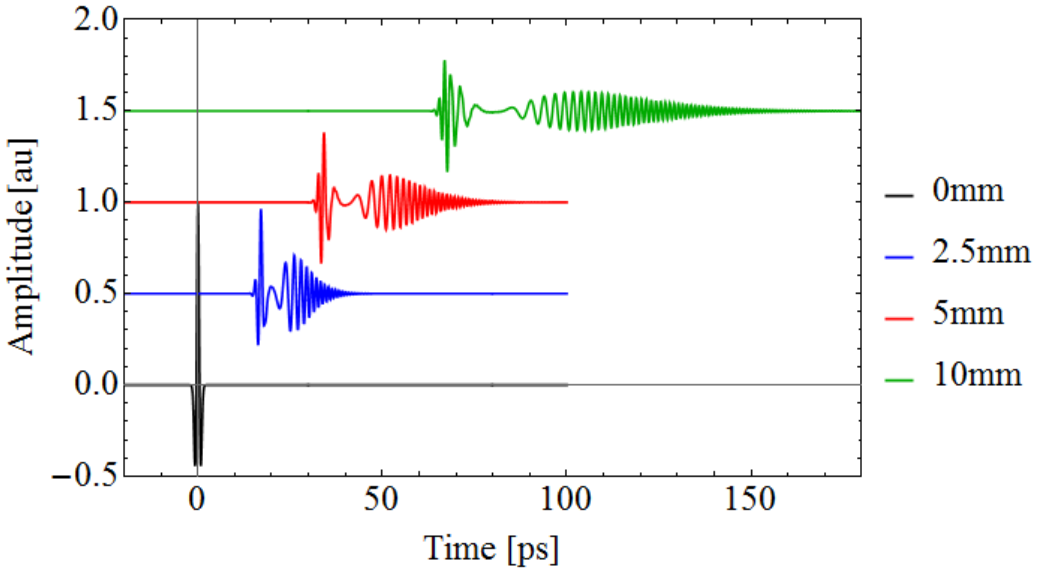

Figure 3.25: Modified Gaussian pulse in the time domain at different values of z for dispersion up to third order, for a DLW designed for deflection of 100 keV electrons, with parameters described in Table 2.1, using ω_0 equal to the operating frequency. The pulse envelope broadens asymmetrically as it propagates, and so the number of oscillations increases, with a chirping effect. The generation of two pulses, which are not the same, is due to asymmetry in the frequency domain. The pulses are offset in amplitude to avoid overlap.

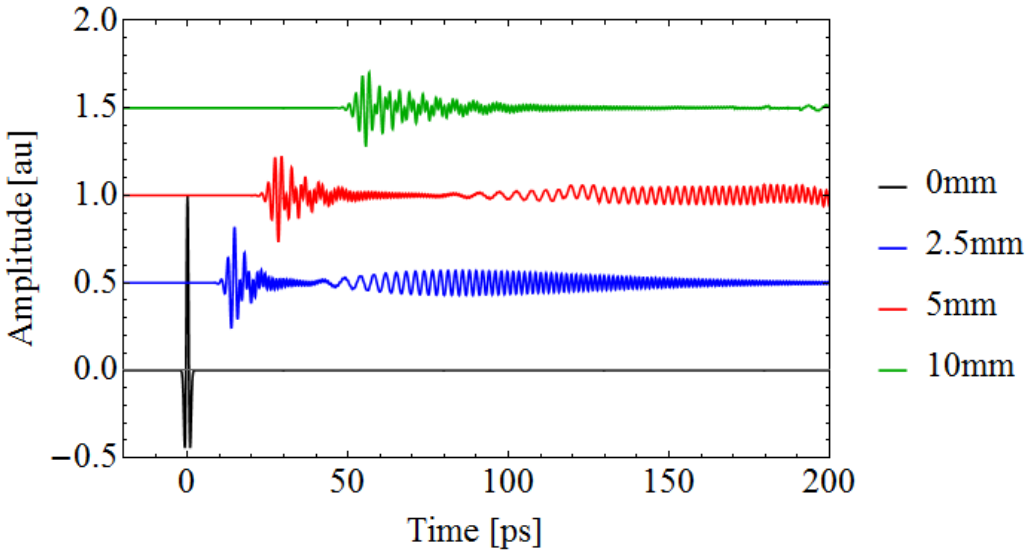

Figure 3.26: Modified Gaussian pulse in the time domain at different values of z for dispersion up to third order, for a DLW designed for acceleration of 35 MeV electrons, with parameters described in Table 2.1, using ω_0 equal to the operating frequency. The pulse envelope broadens asymmetrically as it propagates, and so the number of oscillations increases, with a chirping effect. The generation of two pulses, which are not the same, is due to asymmetry in the frequency domain. The pulses are offset in amplitude to avoid overlap.

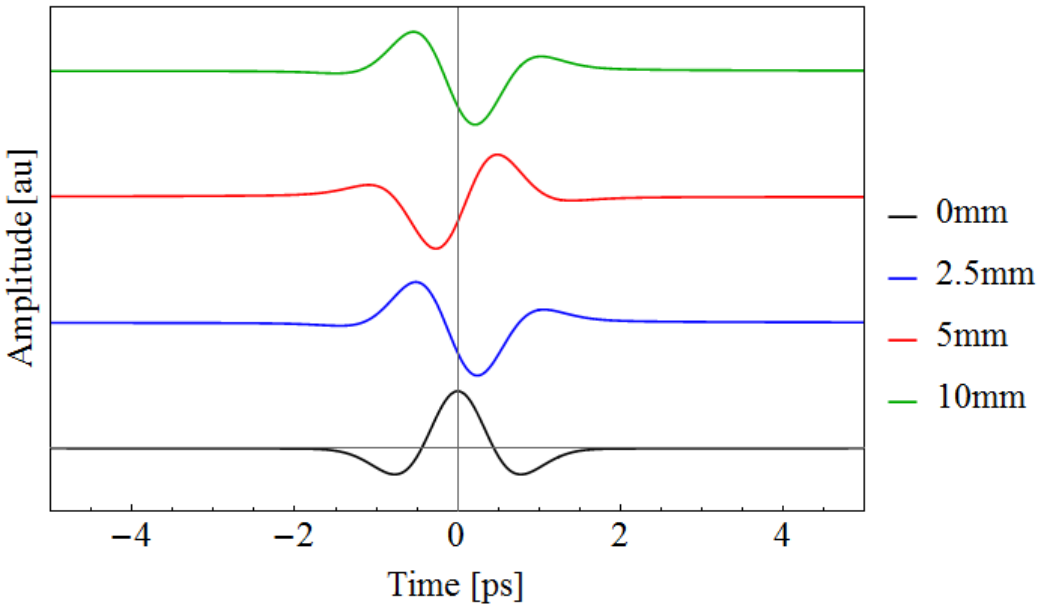

Figure 3.27: Modified Gaussian pulse in the time domain at different values of z for dispersion of zeroth order, corrected for asymmetries, for a DLW designed for deflection of 100 keV electrons, with parameters described in Table 2.1, using ω_0 equal to the operating frequency. There is no propagation of the envelope, but the underlying oscillations propagate with $v_{p,0}$.

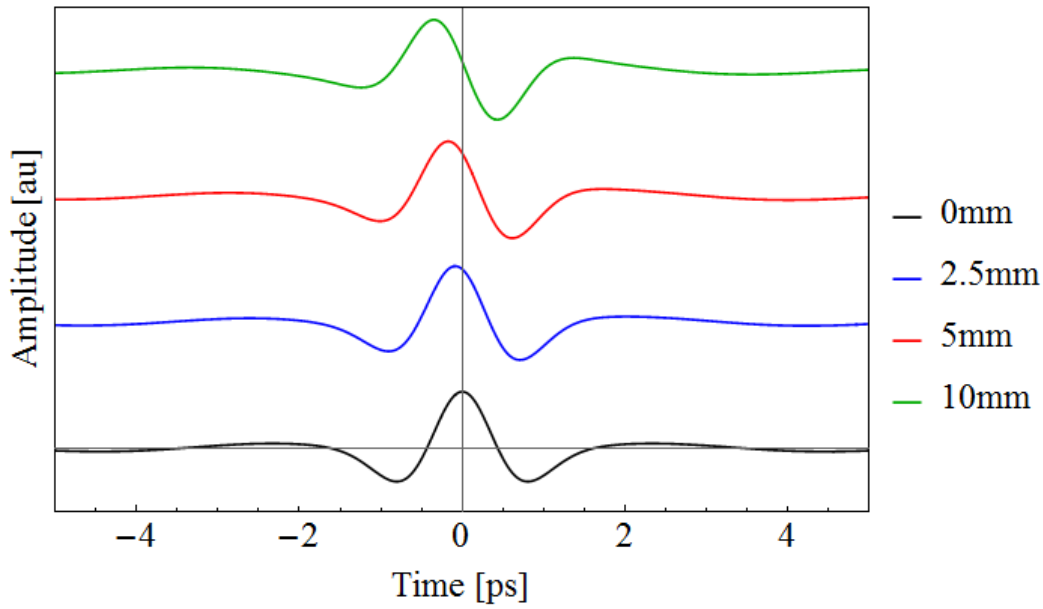

Figure 3.28: Modified Gaussian pulse in the time domain at different values of z for dispersion of zeroth order, corrected for asymmetries, for a DLW designed for acceleration of 35 MeV electrons, with parameters described in Table 2.1, using ω_0 equal to the operating frequency. There is no propagation of the envelope, but the underlying oscillations propagate with $v_{p,0}$.

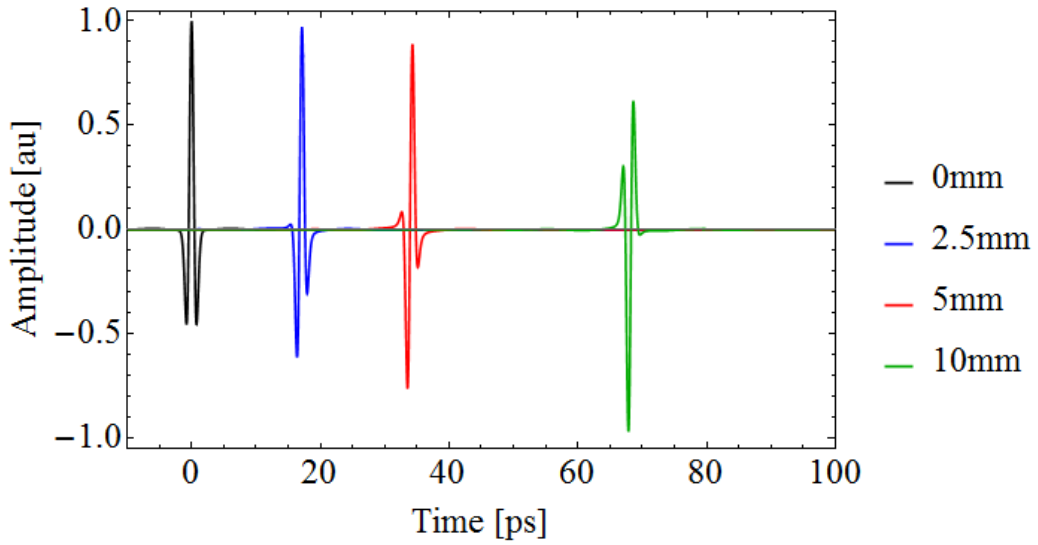

Figure 3.29: Modified Gaussian pulse in the time domain at different values of z for dispersion of first order, corrected for asymmetries,for a DLW designed for deflection of 100 keV electrons, using ω_0 equal to the operating frequency.

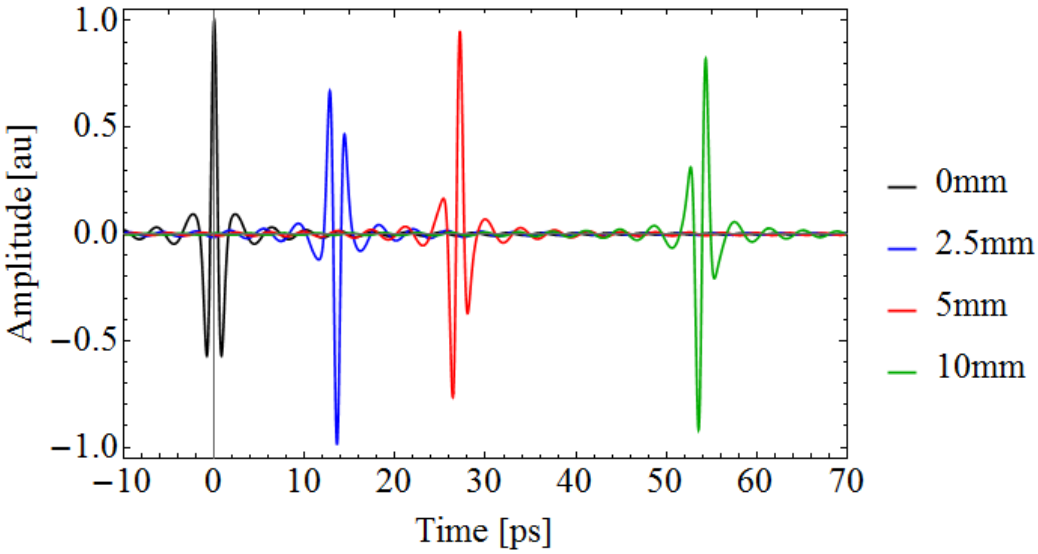

Figure 3.30: Modified Gaussian pulse in the time domain at different values of z for dispersion of first order and corrected for asymmetries, for a DLW designed for acceleration of 35 MeV electrons, using ω_0 equal to the operating frequency. The parameters are described in Table 2.1.

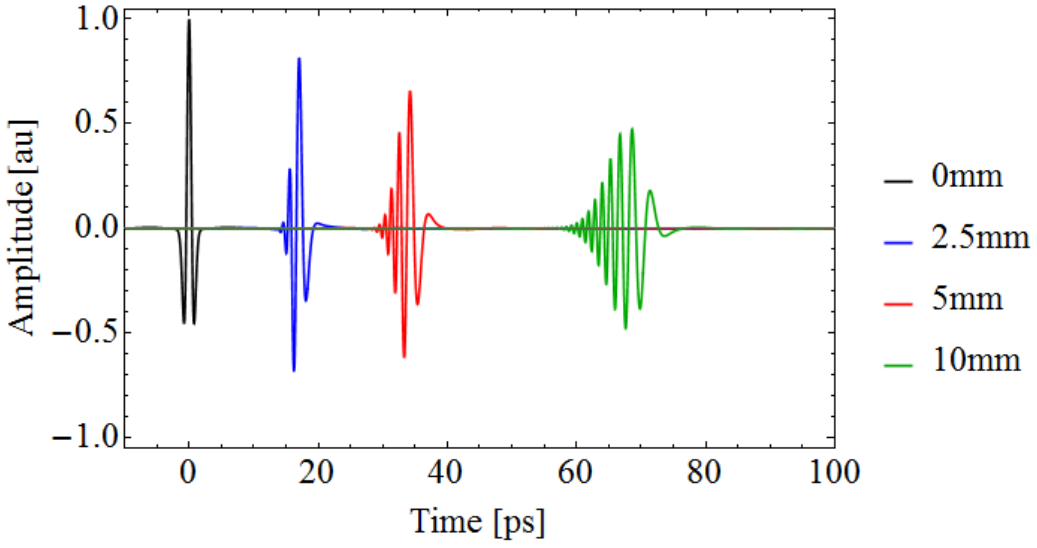

Figure 3.31: Modified Gaussian pulse in the time domain at different values of z for dispersion of second order, corrected for asymmetries, for a DLW designed for deflection of 100 keV electrons, using ω_0 equal to the operating frequency.

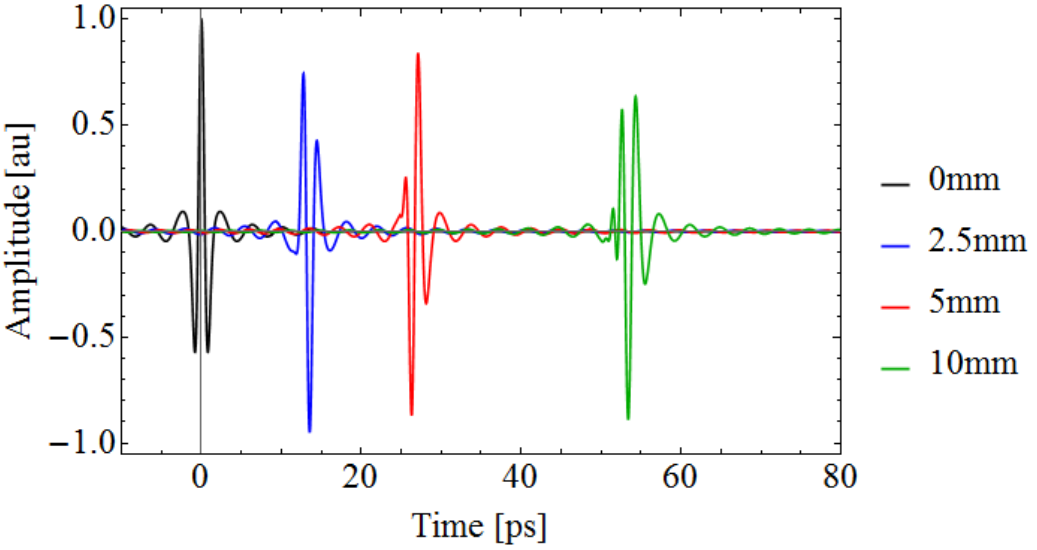

Figure 3.32: Modified Gaussian pulse in the time domain at different values of z for dispersion of second order, corrected for asymmetries, for a DLW designed for acceleration of 35 MeV electrons, using ω_0 equal to the operating frequency The parameters are described in Table 2.1.

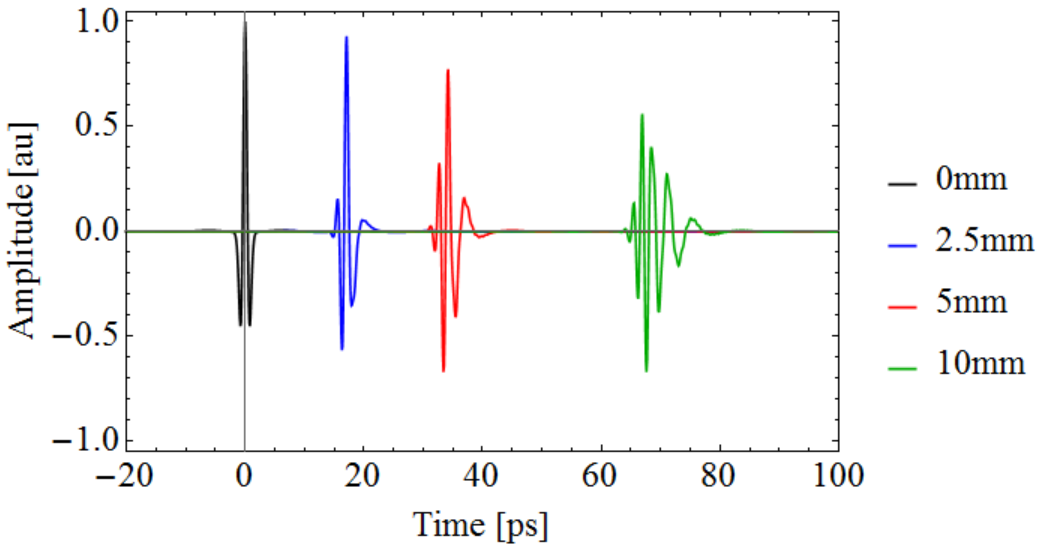

Figure 3.33: Modified Gaussian pulse in the time domain at different values of z for dispersion of third order, corrected for asymmetries,for a DLW designed for deflection of 100 keV electrons, using ω_0 equal to the operating frequency. The parameters are described in Table 2.1.

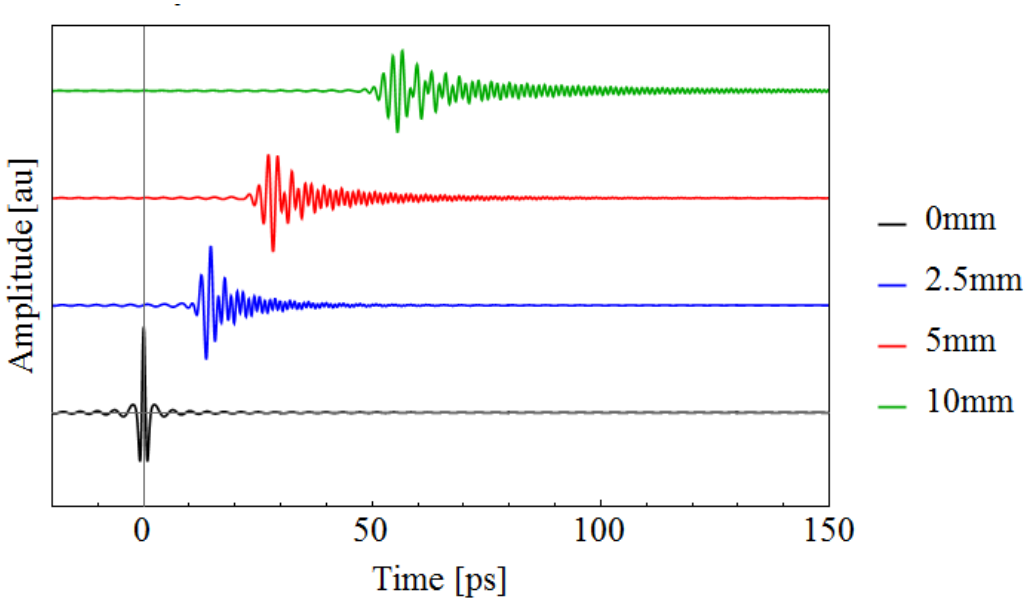

Figure 3.34: Modified Gaussian pulse in the time domain at different values of z for dispersion of third order, corrected for asymmetries, for a DLW designed for acceleration of 35 MeV electrons, using ω_0 equal to the operating frequency. The parameters are described in Table 2.1.

can now be verified that the correct pulse propagates such that higher frequencies have a larger group velocity, and thus the pulse spreads with increasing z. Addition of third order dispersion reduces the pulse spreading, resulting in asymmetric pulse length increase with z. The asymmetric spreading of the pulse, seen in Figures 3.25 and 3.26 has been removed.

There are oscillations outside the main pulse for each order of dispersion when considering the 35 MeV design. This also occurs for the 100 keV design, but is less pronounced. This is due to the integration range of the Fourier transform. The lower limit is the cut-off frequency of the DLW so as to remove the effect of negative β at low frequencies. However, this results in a sharp cut-off of the THz pulse in the frequency domain, which corresponds to a ringing effect in the time domain.

3.5 Comparison with dispersion relation

The dispersion relations of the DLW modes, Equations (2.70) and (2.76) for the examples considered here, must be solved numerically over a frequency range and then interpolated; there is no analytical solution for $\beta(\omega)$. The choice of frequency range and step size controls the accuracy of the interpolated function. This dispersion relation includes a cut-off frequency at which $v_p \to \infty$ and $v_g \to 0$. In the Taylor approximation the cut-off frequency decreases with the addition of each order of dispersion. Therefore compared to the exact solution it is expected that the resulting ringing of the pulse in the time domain will be less pronounced. Furthermore the form of the dispersion relation is less well modelled as f moves further from the operating frequency.

Figure 3.35 shows the form of a Gaussian pulse after propagating 10 mm for the 100 keV design, using both the interpolated dispersion relation and the third order Taylor approximation with ω_0 equal to the centre frequency. The same is shown in Figure 3.36 for the 35 MeV design. The Taylor approximation of the dispersion relation of the 100 keV is well matched to the interpolated function. However, considering the 35 MeV design, although the head and centre of the pulse are well matched in terms of periodicity of oscillations and amplitude, the tail of the pulse differs between the two.

The same comparison is shown in Figure 3.37 for the 100 keV design and in Figure 3.36 for the 35 MeV design, using a modified Gaussian pulse. The centre of the pulse is well matched in both cases, but the amplitude and periodicity of the head and tail of the pulses differ.

The propagation of a narrowband (0.1 THz FWHM) pulse is shown in Figure 3.39 for the 100 keV design and in Figure 3.40 for the 35 MeV design. The two

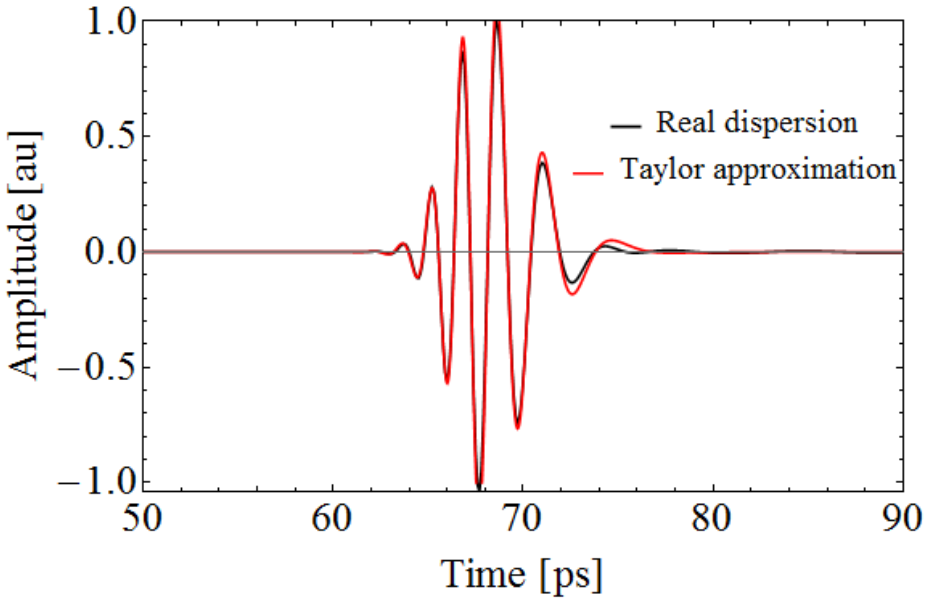

Figure 3.35: Comparison of a Gaussian pulse in the time domain after application of interpolated and Taylor approximated dispersion for a DLW designed for deflection of 100 keV electrons with parameters described in Table 2.1, using ω_0 equal to the operating frequency. The Taylor approximation includes TOD but no other higher order dispersion. The form of the Taylor-approximated pulse is well-matched, with the exception of the tail of the pulse.

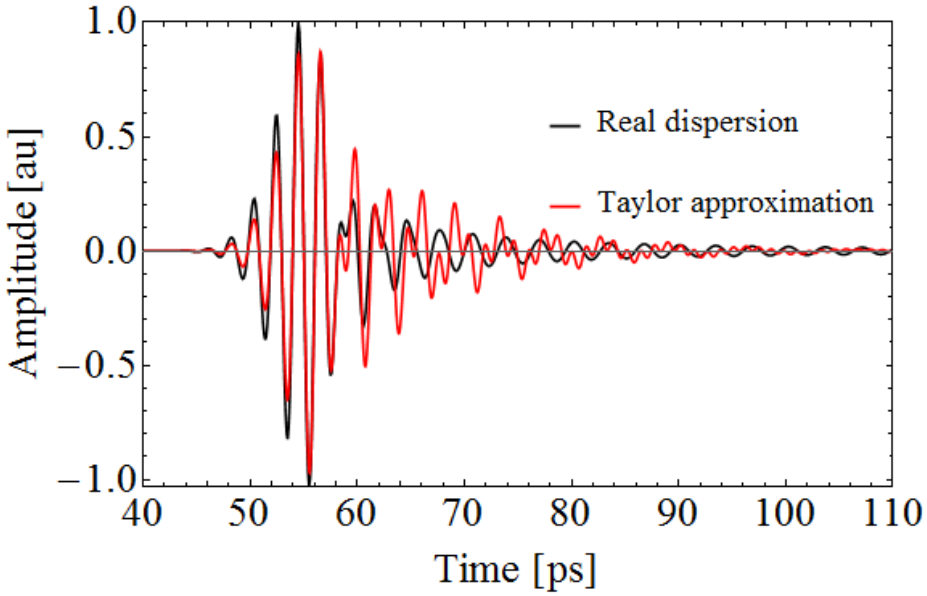

Figure 3.36: Comparison of a Gaussian pulse in the time domain after application of interpolated and Taylor approximated dispersion for a DLW designed for acceleration of 35 MeV electrons with parameters described in Table 2.1, using ω_0 equal to the operating frequency. The form of the Taylor-approximated pulse is well-matched, with the exception of the back of the pulse.

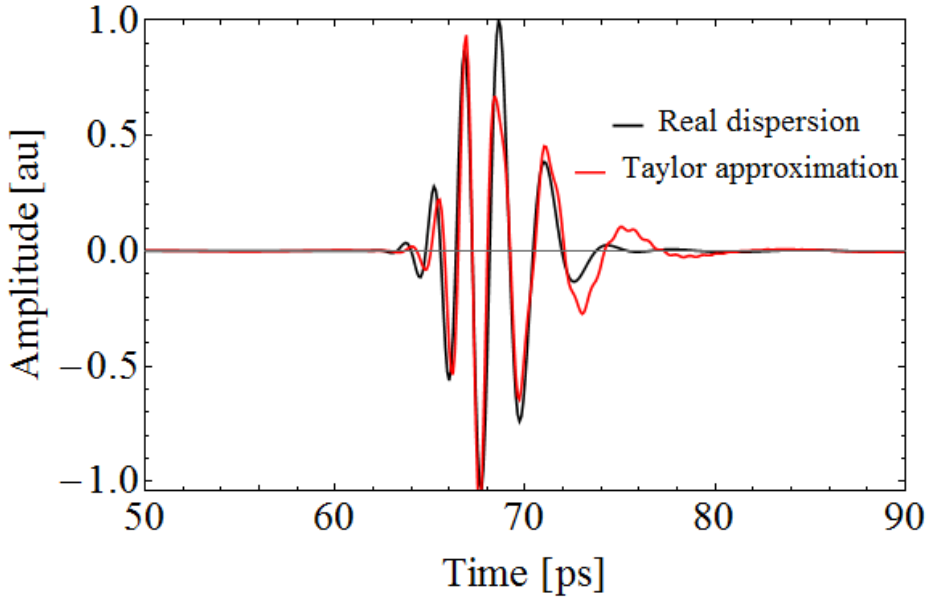

Figure 3.37: Comparison of an ultrashort pulse in the time domain after application of interpolated and Taylor approximated dispersion for a DLW designed for deflection of 100 keV electrons, with ω_0 equal to the operating frequency. The Taylor approximation includes TOD but no other higher order dispersion. The form of the Taylor-approximated pulse is well-matched, with the exception of the tail of the pulse.

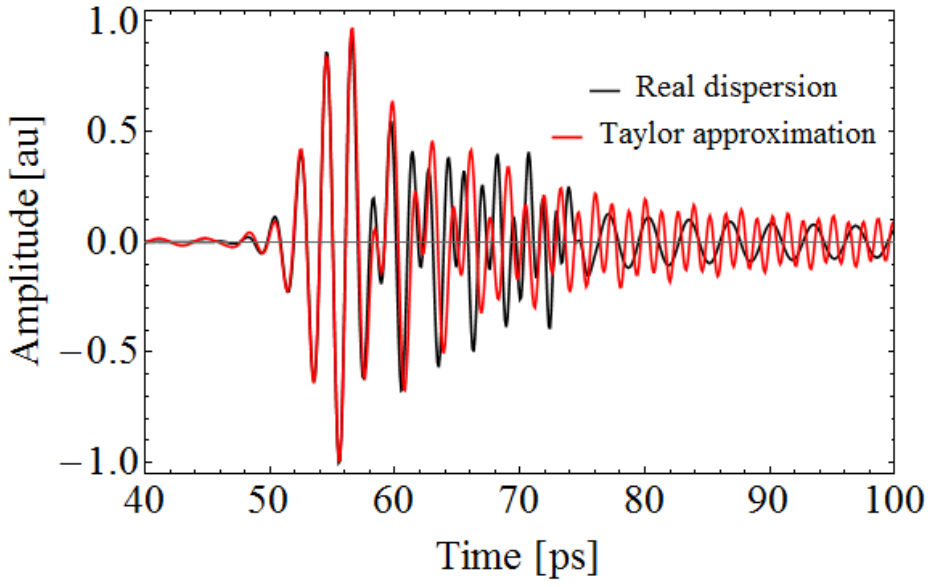

Figure 3.38: Comparison of an ultrashort pulse in the time domain after application of interpolated and Taylor approximated dispersion for a DLW designed for acceleration of 35 MeV electrons with parameters described in Table 2.1, using ω_0 equal to the operating frequency. The form of the Taylor-approximated pulse is well-matched, with the exception of the back of the pulse.

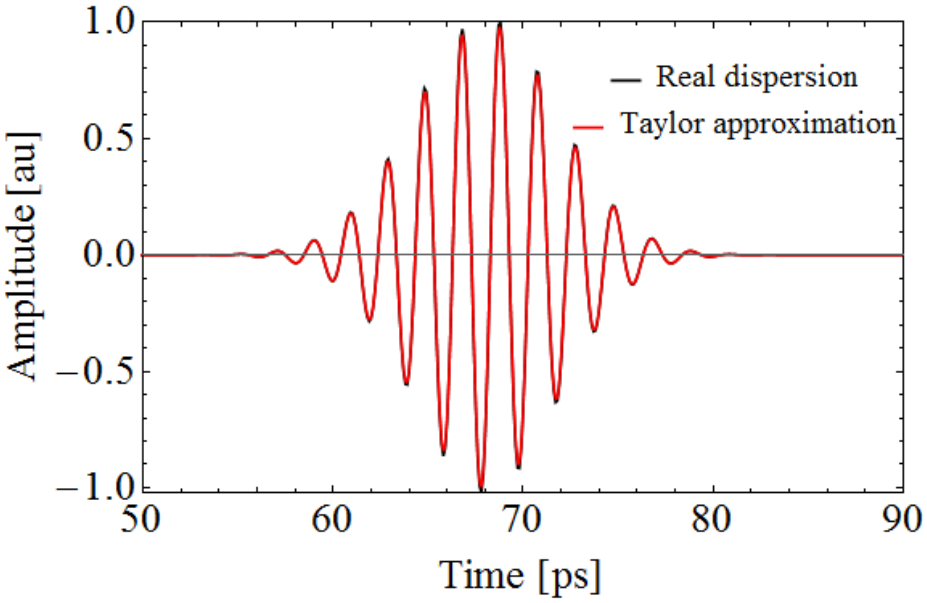

Figure 3.39: Comparison of a narrowband Gaussian pulse in the time domain after application of interpolated and Taylor approximated dispersion for a DLW designed for deflection of 100 keV electrons with parameters described in Table 2.1, using ω_0 equal to the operating frequency. The Taylor approximation includes TOD but no other higher order dispersion. The two pulses overlap with no visible differences.

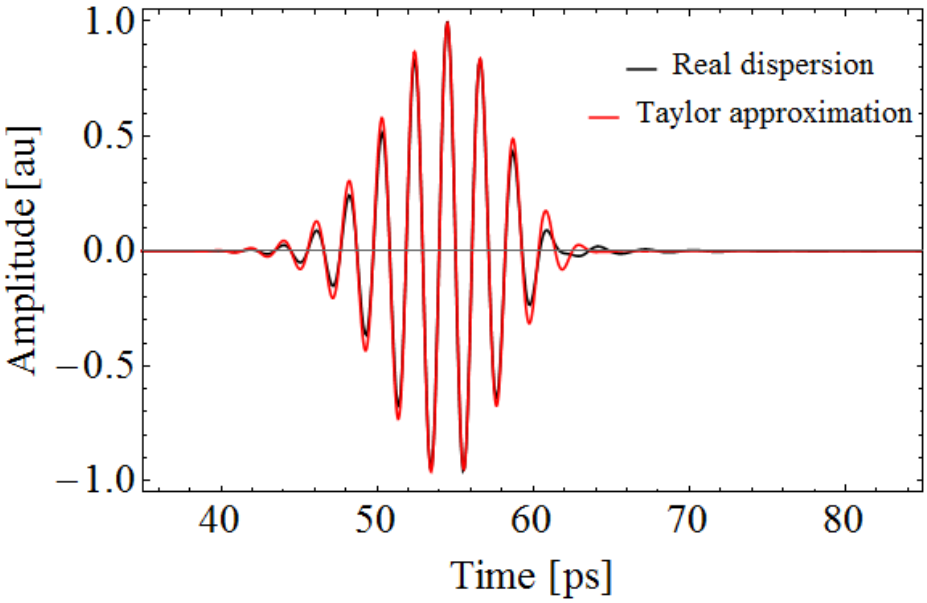

Figure 3.40: Comparison of Gaussian pulse in the time domain after application of interpolated and Taylor approximated dispersion for a DLW designed for acceleration of 35 MeV electrons with parameters described in Table 2.1, using ω_0 equal to the operating frequency. The form of the Taylor-approximated pulse is well-matched, with the exception of the back of the pulse.

pulses overlap almost exactly, showing that the approximation is a sufficient model for narrowband pulses for the 100 keV design. Considering the 35 MeV design, the centre of the pulse overlaps for both the interpolated and Taylor approximated dispersion relations, and only the tail of the pulse demonstrates any difference in periodicity of oscillations.

3.6 Summary

The Taylor expansion is a useful tool for understanding the effects of each order of dispersion. As pulses become narrower, it is expected that the approximation matches the interpolated solution to the dispersion relation. For broadband pulses which include frequencies far from ω_0, for example those close to cut-off where there is a rapid change in dispersion, the approximation is less accurate. As the Taylor approximation requires solving the dispersion relation it is no more efficient than using the full solution. The interaction between the THz pulse and electrons has not been considered in this chapter. However equations for pulse envelope and oscillating peak velocity can be adapted, as will be discussed in Chapter 4. An important point is that the peaks do not travel with constant velocity due to group velocity dispersion. As Γ_0 increases, this component has less of an effect, so for a monochromatic pulse this time and position dependence becomes negligible.

Chapter 4

Considerations for design of structures used for electron manipulation

In this chapter the pulse propagation discussed in Chapter 3 is applied to the use of waveguides for electron interaction. An overview of the figures of merit typically used in accelerator physics for optimising conventional accelerator cavities is provided. Co-propagation of electrons with THz pulses is then discussed, applying the concepts of slippage and interaction length to the figures of merit. A summary of the methods of coupling free space THz pulses into the DLW is given, taking into account the need to keep the electron beam path free of any obstructions. A discussion of the practical aspects of simulation of waveguide and coupler is presented.

4.1 Figures of merit

In conventional accelerating cavity design optimisation is performed with certain figures of merit in mind. Here these are discussed in the context of typical RF structures and their applicability to our structure. In each case the field is normalised to 1 J Hz^{-1} of total stored energy, as in Chapter 2.

4.1.1 Accelerating voltage

In a cavity the longitudinal field is given as $E_z(z,t)$. The accelerating voltage is that given by integration of this field over the length of the cavity.

$$V_z(t) = \int_0^L E_z(x=0, y=0, z, t)\mathrm{d}z \ , \tag{4.1}$$

where the maximum longitudinal field is assumed to be on axis. The maximum energy gained by an electron in the cavity is given by

$$\Delta E = eV_z \ , \tag{4.2}$$

which assumes that the electron experiences a constant peak field (no time dependence), achieved either by co-propagation with the peak of a sinusoidal field, or the use of a DC voltage. In reality there is slippage between a sinusoidal field and a propagating electron due to velocity mismatch. This mismatch arises either from acceleration of the electron causing a change in velocity, or the use of a non-monochromatic wave as discussed in Chapter 3.

4.1.2 Transit time factor

Considering an electric field on-axis,

$$E_z(x=0, y=0, z, t, \omega) = E_0 \exp\left[i\left(\omega t - \beta(\omega) z\right)\right] \ , \tag{4.3}$$

the energy gained by an electron beam over a distance L through interaction with this electric field is,

$$\Delta E = e \int_0^L E_z(x=0, y=0, z, t, \omega) \mathrm{d}z \ . \tag{4.4}$$

For a beam moving at $v_e \approx c$, meaning that an energy change does not result in a significant velocity change, t can be defined as $t = t_0 + z/v_e$, where t_0 defines the initial starting point. E_0 is defined by the parameters of the cavity. In the DLW case the cavity is longitudinally homogenous and so E_0 remains constant, assuming there are no losses. Redefining t in Equation 4.3 and inserting into Equation 4.4 gives

$$\begin{aligned} \Delta E &= e \int_0^L E_0 \exp\left[i\left(\omega\left(t_0 + \frac{z}{v_e}\right) - \beta(\omega) z\right)\right] \mathrm{d}z \ , \\ &= e \exp\left[i\omega t_0\right] \int_0^L E_0 \exp\left[iz\left(\frac{\omega}{v_e} - \beta(\omega)\right)\right] \mathrm{d}z \ , \\ &= e \exp\left[i\omega t_0\right] \int_0^L E_0 \exp\left[i\omega z\left(\frac{1}{v_e} - \frac{1}{v_p(\omega)}\right)\right] \mathrm{d}z \ . \end{aligned} \tag{4.5}$$

The maximum energy change is given when $v_e = v_p(\omega)$. The $\exp\left[i\omega t_0\right]$ term is a constant for monochromatic fields. The transit time factor, TT, is defined as the

ratio between the maximum and actual energy gain;

$$TT = \frac{1}{L}\int_0^L \exp\left[i\omega z\left(\frac{1}{v_e} - \frac{1}{v_p(\omega)}\right)\right]\mathrm{d}z \ . \tag{4.6}$$

This shows that for an oscillating field TT=1 if $v_e = v_p$. TT varies between -1 and 1, dependent on the mismatch between v_e and v_p. Final energy gain varies with t_0; in the $v_e = v_p$ case it means that the electron will experience a constant field with amplitude E_0. This is only true for a travelling wave. In a cavity, longitudinal changes in the walls result in variation in the longitudinal field along the length of the cavity. This means that the fields are not true travelling waves. In the case of a single pillbox cavity of length d, the energy change is given as

$$\Delta E = e\int_{-\frac{d}{2}}^{+\frac{d}{2}} E_{z,0}\cos\left[\omega\frac{v_e}{z} + \phi\right]\mathrm{d}z \ , \tag{4.7}$$

where the cavity is centred at $z = 0$, v_e is the electron velocity, and ϕ is the phase of the rf field when the particle enters the cavity. The transit time factor in this case is given as

$$TT = \frac{\sin\left[\frac{\omega d}{2v_e}\right]}{\frac{\omega d}{2v_e}} \ , \tag{4.8}$$

where $\phi = \frac{\pi}{2}$, which gives the maximum integral [99].

4.1.3 Quality factor

The quality factor, or Q_0, is often used to assess cavity performance;

$$Q_0 = \frac{\omega_0 U_{stored}}{P_{diss}} \ , \tag{4.9}$$

where U_{stored} is the stored energy per unit length, and P_{diss} is the dissipated power;

$$U_{stored} = \frac{\epsilon_0}{2L}\int_V |\mathbf{E}|^2\mathrm{d}V = \frac{\mu_0}{2}\int_V |\mathbf{H}|^2\mathrm{d}V \ , \tag{4.10}$$

$$P_{diss} = \frac{R_s}{2}\int_A |\mathbf{H}_\parallel|^2\mathrm{d}A \ . \tag{4.11}$$

R_s is the surface resistance of the wall material,

$$R_s = \sqrt{\frac{\mu\omega}{2\sigma}} \ . \tag{4.12}$$

where σ is the electrical conductivity. Q_0 is proportional to the ratio of energy stored in the cavity to the power lost per cycle through the walls, and it defines how quickly a resonator loses energy. For a given input power, a higher Q_0 means higher energy that can be stored, which means improved acceleration. Power is dissipated due to the finite conductivity of the metal walls and so the electric and magnetic fields are non-zero in the walls, decaying exponentially as determined by the skin depth,

$$\delta = \sqrt{\frac{2}{\mu\sigma\omega}} \ . \tag{4.13}$$

It is assumed that the wall material is copper, $\sigma = 5.96 \times 10^7$ S m^{-}1 [96], throughout this work. The manufactured structures considered in this work were fabricated from copper. The quality factor is not used in this thesis; as the acceleration due to an entire broadband pulse and not a single resonant frequency is of interest.

4.1.4 Shunt impedance

Shunt impedance is used as a figure of acceleration efficiency, describing the power to generate a given accelerating voltage V_z,

$$R_{shunt} = \frac{|V_z|^2}{P_{diss}} \ . \tag{4.14}$$

Therefore maximising R_{shunt} maximises efficiency of the cavity, and depends on both frequency and cavity parameters. In the case of a transverse deflecting cavity, examples of which are used in accelerators for applications requiring time-varying deflection of particles [100, 101], the Lorentz force equation is used to find the transverse momentum gain,

$$\mathbf{F}(x,y,z) = q\left(\mathbf{E}(x,y,z) + \mathbf{v}(x,y,z) \times \mathbf{B}(x,y,z)\right) \ . \tag{4.15}$$

For a deflecting cavity the transverse voltage, $V_\perp$, is required. In the case that $v_e = c$, the Panofsky-Wenzel theorem [102] can be used to define the transverse deflection in terms of the transverse variation of the longitudinal field,

$$V_\perp = -\frac{ic}{\omega_0}\int_0^L \nabla_\perp E_z(x,y)\mathrm{d}z \ , \tag{4.16}$$

which is valid for TM modes of hollow conducting waveguides. This replaces V_z in Equation (4.14) to give the transverse shunt impedance, which describes the efficiency of deflection. The transverse voltage is otherwise calculated using the transverse

component of the Lorentz force equation;

$$V_\perp = \int_0^L \frac{\mathbf{F}_\perp}{q} \mathrm{d}z. \tag{4.17}$$

4.1.5 Group velocity

The group velocity is the velocity at which the energy of an EM pulse propagates. It is also equivalent to the ratio of power flow to stored energy per unit length [103]:

$$v_g = \frac{P}{U_{stored}} \ , \tag{4.18}$$

where P is power flow through the structure,

$$P = \frac{1}{2} \int_A (\mathbf{E} \times \mathbf{H}^*) \cdot \hat{\mathbf{z}} \mathrm{d}A \ . \tag{4.19}$$

The group velocity determines the filling time of a cavity excited by a travelling wave.

4.1.6 R/Q

An alternative figure of merit to the use of shunt impedance is $^R/_Q$, which is a measure of accelerating field for a given stored energy:

$$\frac{E_z^2 v_g}{\omega_0 P} \ , \tag{4.20}$$

where E_z is chosen to be the maximum axial field. It is a figure which depends only on the geometry of the cavity and not the losses.

4.2 Electron-THz synchronisation

In conventional cavity design, the transit time factor describes the effects of longitudinal propagation on the interaction between the RF field and an electron. This approach is typically used for cavities excited by single frequency RF fields, which is not valid with the THz-driven structures considered in this thesis. The bandwidth of the input pulse depends on the method of THz generation, but it can be assumed that it is large enough for dispersion to have an effect. It is also assumed that $\Gamma_0 = 1/\sigma_0$.

It is useful to define an interaction length, which can be approximated in different ways. Considering purely monochromatic THz fields, $v_p(\omega)$ controls the interaction length. If $v_p = v_e$ the field will interact for infinite length. If $v_p \neq v_e$ the electron will experience an oscillating field amplitude. If the electron starts on the peak of the field, once it has slipped by a phase $\pm\pi/2$ the interaction switches from positive to

negative. The interaction length for a given frequency is

$$L_{phase}(\omega) = \frac{\pi}{2\omega\left(\frac{1}{v_p(\omega)} - \frac{1}{v_e}\right)} \ . \tag{4.21}$$

Extending to a THz pulse with non-zero bandwidth, the effect of pulse slippage must now be considered, i.e., $v_g \neq v_e$. The interaction length is instead determined by the distance over which an electron slips through the entire pulse;

$$L_{group} = \frac{t_0 + \Gamma_0\sqrt{2x_2}}{\frac{1}{v_g} - \frac{1}{v_e}} \ . \tag{4.22}$$

This is similar to Equation (3.31), but with $v_{p,0}$ replaced by v_e. t_0 is the initial starting point of the electron, and lies on the envelope at a point $t_0 = -\Gamma_0\sqrt{2x_1}$. The addition of GVD is more complex. v_p cannot simply be replaced with v_e as the phase velocity is dependent on starting position and distance propagated, whereas v_e is assumed to be a constant. Two interaction lengths including GVD are defined. The first is between electron and envelope;

$$L_{v_g,e} = \frac{v_e t_0 \Gamma_0^2 \left(-1 + v_e\beta_0'\right) + \sqrt{2}\sqrt{v_e^2 x_2 \Gamma_0^2 \left(\Gamma_0^4 \left(-1 + v_e\beta_0'\right)^2 - 2v_e^2 x_2 \Gamma_0^2 \beta_0''^2 + v_e^2 t_0^2 \beta_0''^2\right)}}{\left(-1 + v_e\beta_0'\right)^2 \Gamma_0^2 - 2v_e^2 x_2 \beta_0''^2}. \tag{4.23}$$

This was derived by equating t_g (Equation 3.36) with $t_0 + (\frac{z}{v_e})$, the time taken for an electron starting at time t_0 to propagate a distance z. The second approximation including the effect of GVD is between an electron and a specific peak. The electron starts at initial point $t_0 = \frac{\phi_0 - 2\pi n}{\omega_0}$, where phase $\phi_0 = 0$ means that the electron starts on a peak. After a distance $L_{v_p,e}$, the electron is found at a new phase ϕ_1. Setting $\phi_1 = \frac{\pi}{2}$ corresponds to a point on the oscillation with zero amplitude. The interaction length is found by solving

$$\begin{aligned}\frac{L_{v_p,e}}{v_e} =& \beta_0' L_{v_p,e} + \omega_0 \left(\frac{\Gamma_0^4 + \left(\beta_0'' L_{v_p,e}\right)^2}{\beta_0'' L_{v_p,e}}\right) - t_0 \pm \sqrt{\frac{\Gamma_0^4 + \left(\beta_0'' L_{v_p,e}\right)^2}{\beta_0'' L_{v_p,e}}} \times \\ & \sqrt{\omega_0^2 \left(\frac{\Gamma_0^4 + \left(\beta_0'' L_{v_p,e}\right)^2}{\beta_0'' L_{v_p,e}}\right) + 2\left(\beta_0 L_{v_p,e} - \omega_0 \beta_0' L_{v_p,e} - (2n\pi - \phi_1)\right)} \ .\end{aligned} \tag{4.24}$$

It has not been possible to find an analytical solution to this equation and so the interaction length is calculated numerically. The equations for interaction with a THz pulse as a function of Γ_0 are compared the plots in Figure 4.1. The interaction

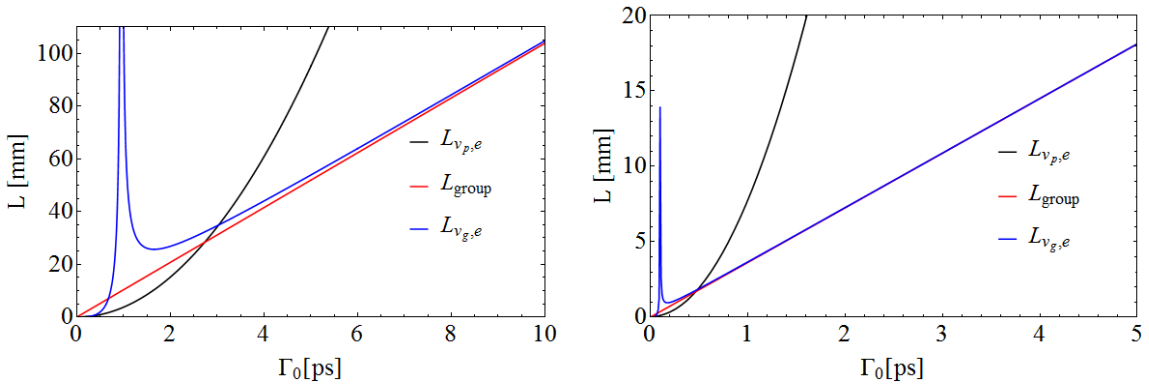

Figure 4.1: Interaction length between an electron and THz pulse as a function of initial THz pulse width, assuming the THz pulse is Gaussian. the electron starts behind the pulse where amplitdue is negligible. Left: DLW designed for deflection of 100 keV electrons, with parameters described in Table 2.1. Right: DLW designed for deflection of 100 keV electrons, with parameters described in Table 2.1. In both cases $\omega_0 = 2\pi f_{op}$. There are three interaction length calculations from Equations (4.24), (4.22), and (4.23).

lengths of the two structures considered in Chapter 3 are shown, with parameters given in Table 2.1, and with $\omega_0 = 2\pi f_{op}$. The largest estimate of interaction length is $L_{v_p,e}$ in both examples. As Γ_0 increases, the interaction increases exponentially. In the limit of an infinitely long pulse, an electron never leaves the pulse. At small values of Γ_0, the effect of GVD is more pronounced, and so the chirping of the pulse, which causes the periodicity of oscillations to change with t and z, become significant and so v_e is no longer equal to the velocity of the oscillations.

Considering L_{group} and $L_{v_g,e}$, they both tend to the same interaction length with increasing Γ_0 for both examples. Shorter THz pulses experience more pulse broadening than longer ones and so $L_{v_g,e}$ deviates from L_{group} at small Γ_0. Comparing Figure 4.1 to Figure 3.16, the form of the interaction length and slippage length are similar. The interaction length is larger as the electrons starts behind the pulse rather than at the peak of the envelope. The interaction length, $L_{v_g,e}$ tends to infinity at a different point compared to the slippage length discussed in Section 3.3. This point is found by setting the denominator in Equation (4.23) to zero;

$$\Gamma_0 = \frac{\sqrt{2v_e^2 x_2 \beta_0'' 2}}{v_e \beta_0' - 1} \ . \tag{4.25}$$

The denominator in Equation (4.23) is different to that in Equation (3.51), so this difference is expected. It was previously discussed in Section 3.3.5 that this is in

the region where the use of a Gaussian function to describe the pulse length is not physical as the frequency spectrum extends into negative frequencies. The simplest method to approximate interaction length is to use L_{group}, which is valid provided Γ_0 is sufficiently large. For small pulse lengths, it is sensible to take the smallest interaction length, which is $L_{v_p,e}$.

4.3 Coupling radiation into the waveguide

With any situation where the field source is launched outside of the waveguide, there is a difference between the field source profile and the propagating waveguide modes. Therefore not all of the field will transmit into the waveguide due to this mismatch. Transmission can be maximised by using a coupling system. In this section the different methods of coupling and their validity when using a broadband THz source are discussed. The theory behind coupler operation is presented, with particular emphasis on the scattering matrix and mode matching.

4.3.1 Methods of coupling

Coupling into waveguides in the THz regime can be accomplished by several methods, each of which is suitable for different regimes. Most studies into THz waveguide coupling have been performed with an emphasis on spectroscopy. The use of a waveguide in terahertz time-domain spectroscopy allows for low-loss THz propagation, and the resolution was found to be higher than another method which uses pellet samples [104] whilst also requiring less material, as only a small sample is placed inside the waveguide. Parallel-plate waveguides (PPWGs) in particular are used due to undistorted propagation of the TE_{01} mode [105, 106, 107]. Coupling the THz into a PPWG maximises pulse propagation, thus further improving the resolution of sample analysis. Three example methods are shown in Figure 4.2. Lenses such as plano-cylindrical silicon lenses [109, 105] have been used for focussing of an input pulse into a parallel-plate waveguide. However the refractive index of silicon (n=3.412) results in about 30% reflection [110]. The alternative use of a taper to focus a free space THz pulse into the waveguide improved coupling to 56% [110, 111]. Combining a focussed THz pulse with a tapered PPWG has been shown to improve coupling, achieving 80% transmission [112, 113]. Although the system is different, the concept of a taper confining to two dimensions instead of one is of interest.

Horn couplers, or two-dimensional tapers, have been used with THz-driven DLWs [114, 12], achieving 54% power coupling. This particular research focussed on the use of a cylindrical DLW and coupled a radial free space mode into the TM_{11} cylindrical mode. The need to co-propagate electrons and THz was considered during design

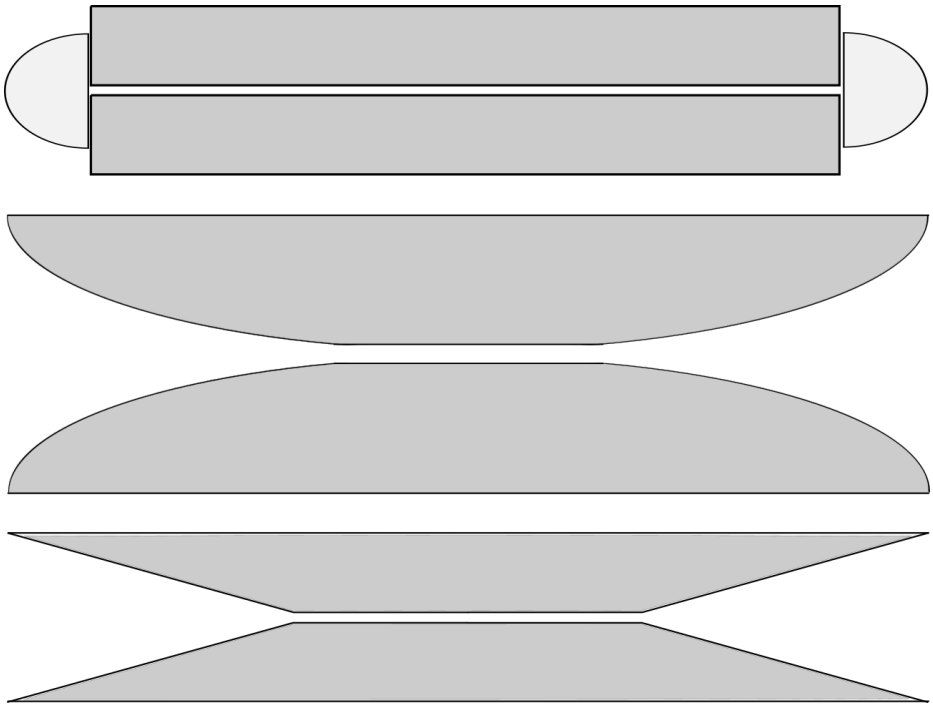

Figure 4.2: Examples of PPWGs with different coupling methods. Top: plano-cylindrical lens, middle: curved input [108], bottom: tapered input.

of this structure. THz pulses were generated transverse to the DLW, then reflected in using an off-axis parabolic mirror (OAP) through which a small central hole was drilled to allow electron propagation, as shown in Figure 4.3. Horns have also been used in dielectric wakefield accelerators for output of the generated THz wakefields [78, 115]. A detailed study of the emitted Cherenkov radiation was performed by Smirnov [116]. Alternatively, an angled exit of the DLW allows for output at an angle to electron propagation [117], valid for extraction of narrowband Cherenkov radiation. Another option is to use a pinhole [118], but this does not maximise power coupling. Focussing the THz at the entrance of the DLW to a spot size smaller than the entrance aperture has achieved up to 80% coupling into the HE_{11} mode [119]. Again this is not the same design as pursued in this thesis; to the author's knowledge there has been no published research into the coupling of a free space beam into the LSM_{11} mode of a rectangular DLW. Based on the work detailed here, the suggestion is that coupling will likely require a horn and focussing of the THz beam.

An alternative used for laser-driven structures is the grating coupler [36, 38, 39, 120] as they are ideal for transmission of monochromatic fields, with up to 100% transmission for individual frequencies [121]. These gratings are not used for coupling a longitudinally propagating THz pulse; instead this is for the generation of a standing

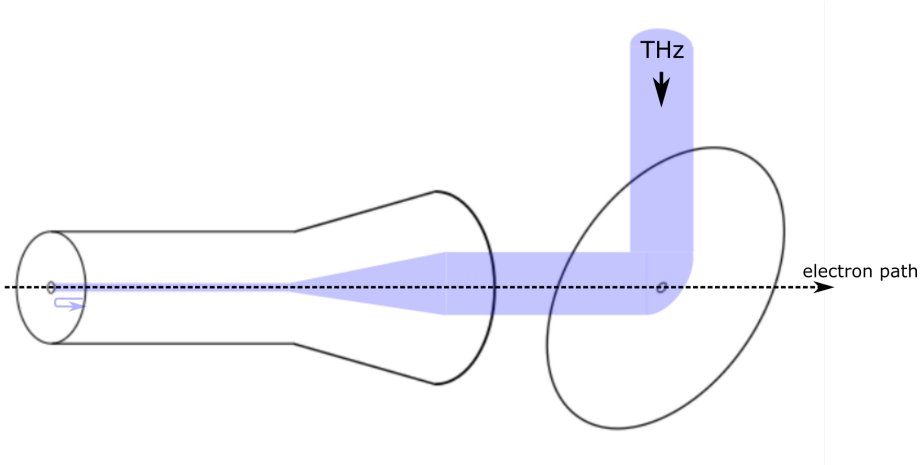

Figure 4.3: Cartoon of the waveguide structure used to accelerate 60 keV electrons [12]. THz is generated perpendicular to the longitudinal beam path and reflected into the waveguide using an off-axis parabolic mirror and coupled with a horn. This propagates in the opposite direction to the beam, as it is reflected by a pinhole at the start of the waveguide to co-propagate with an electron bunch. A hole in the centre of the mirror allows for electron propagation.

wave in the structure. Studies in the THz regime have been performed [122], although this was for quasi-monochromatic THz pulses. This limitation means that gratings are not considered for coupling in this thesis.

Due to the large number of coupling options for the wide range of RF accelerating cavities only an overview is provided here. A summary of the range of coupling techniques for RF linacs is detailed eleswhere [123]. Typically power is coupled in via the use of slots in the cavities. For travelling wave linacs, an input RF coupler is used to launch the wave at the start of the linac [124]. This is for a well-defined operating frequency, again not useful for THz sources considered in this work. For the rest of this thesis only the use of horn structures is considered in order to maximise broadband coupling into the DLW.

4.3.2 Optimisation of the coupler

In conventional cavity design, the coupler is used to propagate the RF power from source to cavity. It is designed so as to maximise power transmission and minimise reflections, whilst also propagating the power at the correct frequency so as to be matched to the cavity. As the use of any additional structure perturbs the cavity and therefore the fields, the effect on the beam must also be considered. The analysis used for travelling wave structures is considered here, as this is the closest analogy to the DLW considered in this work. The focus is on the use of a horn coupler which is best suited to broadband pulse transmission. Optimisation of the horn requires

maximising transmission of the full THz pulse into the correct mode of the DLW.

Scattering matrix

The scattering matrix is used in accelerating cavity design to describe the coupling of an input RF wave into the cavity. The system is described as a network made up of N ports, where a port is a connection to an external system. It is most common for a cavity to be modelled as a two-port network, with an input port and output port. Each port has an incident voltage wave, which is both transmitted and reflected. The scattering matrix describes the coefficients of transmission and reflection.

At each port n, the voltage is given by

$$V_n = V_n^- + V_n^+ \ , \tag{4.26}$$

where V_n^+ is the incident voltage wave and V_n^- the reflected voltage of a wave of angular frequency ω;

$$\begin{aligned} V^+ &= V_0 \exp\left[-i\beta(\omega)z\right] \ , \\ V^- &= V_0 \exp\left[i\beta(\omega)z\right] \ . \end{aligned} \tag{4.27}$$

The scattering matrix is defined in terms of these voltages at each port. For an N-port network, the matrix is given as

$$\begin{bmatrix} V_1^- \\ V_2^- \\ \vdots \\ V_N^- \end{bmatrix} = \begin{bmatrix} S_{11} & S_{12} & \cdots & S_{1N} \\ S_{21} & \ddots & & \vdots \\ \vdots & & \ddots & \\ S_{N1} & \cdots & & S_{NN} \end{bmatrix} \begin{bmatrix} V_1^+ \\ V_2^+ \\ \vdots \\ V_N^+ \end{bmatrix} \tag{4.28}$$

Each element of the S-matrix is found by

$$S_{ij} = \left.\frac{V_i^-}{V_j^+}\right|_{V_k^+=0 \text{ for } k\neq j} \ . \tag{4.29}$$

Experimentally the elements are measured using a network analyser. The reflection coefficient, S_{11}, is calculated by applying a voltage V^+ to the input port and then measuring the reflecting wave V^- from the same port:

$$S_{11} = \frac{V_1^+}{V_1^-} \ . \tag{4.30}$$

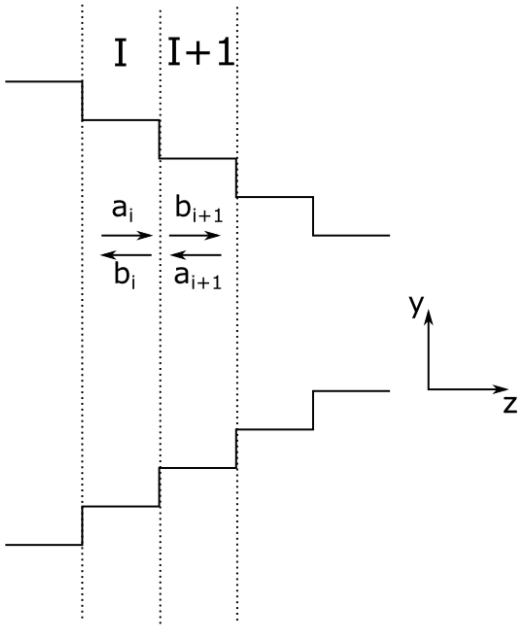

Figure 4.4: A waveguide horn approximated by a series of step discontinuities. Field propagation is modelled across each discontinuity to calculate the transmission through the horn.

To ensure that only S_{11} is measured the output port is terminated with a matched load, such that all of the energy is absorbed at the output port [125].

Analysis of transmission of an input signal through a horn coupler is performed by modelling the horn as a series of step discontinuities, as shown in Figure 4.4 [126]. This is equivalent to a series of two-port networks, each of which has its own scattering matrix. As there is mode conversion in each section, there are multiple modes in the structure. This is represented by a modal expansion, where the amplitude of each component controls the final field configuration. A method to calculate the transmission has been described in [126], and is summarised below.

The transverse field on the left (input side) of a step i is described by the expansion

$$\mathbf{E}_t^i = \sum_{m,n}^{\infty} \left(\frac{\mathbf{e}_{m,n}^{i,TE}(x,y)}{\sqrt{Y_{m,n}^{i,TE}}} \left(a_{m,n}^{i,TE} \exp\left[-\gamma_{m,n}^i z\right] + b_{m,n}^{i,TE} \exp\left[-\gamma_{m,n}^i z\right] \right) \right. \tag{4.31}$$
$$\left. + \frac{\mathbf{e}_{m,n}^{i,TM}(x,y)}{\sqrt{Y_{m,n}^{i,TM}}} \left(a_{m,n}^{i,TM} \exp\left[-\gamma_{m,n}^i z\right] + b_{m,n}^{i,TM} \exp\left[-\gamma_{m,n}^i z\right] \right) \right),$$

where $\mathbf{e}$ is the orthonormalised eigenfunction for a given mode, TE_{mn} or TM_{mn},

$$\mathbf{e}_{mn}^{i,TE} = A_{mn}^{i}\left(k_{y,n}^{i}\cos\left[k_{x,m}^{i}x\right]\sin\left[k_{y,n}^{i}y\right] - k_{x,m}^{i}\cos\left[k_{y,n}^{i}y\right]\sin\left[k_{x,m}^{i}x\right]\right) \ , \tag{4.32}$$

$$\mathbf{e}_{mn}^{i,TM} = A_{mn}^{i}\left(k_{y,n}^{i}\cos\left[k_{x,m}^{i}x\right]\sin\left[k_{y,n}^{i}y\right] + k_{x,m}^{i}\cos\left[k_{y,n}^{i}y\right]\sin\left[k_{x,m}^{i}x\right]\right) \ , \tag{4.33}$$

and Y is the corresponding wave admittance:

$$Y^{i} = \frac{I^{i}}{V^{i}} \ . \tag{4.34}$$

a and b are the transmitted and reflected waves respectively at the discontinuity, γ is the complex dispersion relation, and A is a normalisation constant. I^{i} is the current through the i^{th} step of the model. The voltage on either side of the discontinuity is described by the matrix

$$V = \begin{bmatrix} V^{EE} & V^{EM} \\ V^{ME} & V^{MM} \end{bmatrix} \ , \tag{4.35}$$

where superscript E represents the TE mode, and M represents the TM mode. Each component is solved using

$$V_{mn,kl}^{EE} = \sqrt{\frac{Y_{mn}^{i+1,TE}}{Y_{kl}^{i,TE}}}\int_{A^{i}} \mathbf{e}_{kl}^{i,TE}\cdot\mathbf{e}_{mn}^{i+1,TE}\mathrm{d}A^{i} \ , \tag{4.36}$$

$$V_{mn,kl}^{ME} = \sqrt{\frac{Y_{mn}^{i+1,TE}}{Y_{kl}^{i,TM}}}\int_{A^{i}} \mathbf{e}_{kl}^{i,TM}\cdot\mathbf{e}_{mn}^{i+1,TE}\mathrm{d}A^{i} \ , \tag{4.37}$$

$$V_{mn,kl}^{EM} = \sqrt{\frac{Y_{mn}^{i+1,TM}}{Y_{kl}^{i,TE}}}\int_{A^{i}} \mathbf{e}_{kl}^{i,TE}\cdot\mathbf{e}_{mn}^{i+1,TM}\mathrm{d}A^{i} \ , \tag{4.38}$$

$$V_{mn,kl}^{MM} = \sqrt{\frac{Y_{mn}^{i+1,TM}}{Y_{kl}^{i,TM}}}\int_{A^{i}} \mathbf{e}_{kl}^{i,TM}\cdot\mathbf{e}_{mn}^{i+1,TM}\mathrm{d}A^{i} \ . \tag{4.39}$$

A^{i} is the area of the i^{th} step, subscript kl represents the mode number in step i and subscript mn represents the mode number in step $i+1$. Using these equations the scattering matrix is populated for a discontinuity between steps i and $i+1$. The matrices for each step are then combined together in a cascaded network [127]. In the case of a DLW structure, the final step discontinuity is between the horn and the DLW, and so the LSM and LSE modes must be considered. This is accomplished by modifying Equations (4.36, 4.38, 4.37, 4.39) such that TE and TM are replaced by LSM and LSE for the last step $i+1$. The eigenmodes are also modified such that

they have the forms of the LSM and LSE modes, as described in Equations (2.64, 2.71, 2.78, 2.85).

Although this method gives the final S-matrix for an input wave of a given frequency, it is inefficient to calculate this numerically. Therefore the scattering parameters are solved in the time domain; specifically using discretised methods of tracking EM fields. Operating in the time domain also means that a window function can be applied to the fields, acting as a time-dependent filter. This is useful in the case that the steady state solution is not valid, such as with the pulses considered in this thesis.

4.4 Finite difference time domain simulations

Although the scattering matrix provides a full solution for the transmission of a wave through a discontinuity, they are typically used for steady state solutions. Instead it is desirable to analyse how an input travelling THz pulse propagates through the horn and DLW. The scattering matrix can still be used but the process is more intensive. Simulating the pulse propagation is performed via a range of techniques; one of the simplest methods is the finite difference time domain (FDTD). The FDTD and the discrete forms of electromagnetic fields required for the method are introduced.

The derivative forms of Ampere's and Faraday's laws are replaced with finite differences on a Cartesian grid. They are also discretised in a leap-frog format; the electric and magnetic fields are staggered in space and time. The magnetic fields are described as

$$H^{n+\frac{1}{2}}_{x,i,j-\frac{1}{2},k-\frac{1}{2}} = H^{n-\frac{1}{2}}_{x,i,j-\frac{1}{2},k-\frac{1}{2}} + \frac{\Delta t}{\mu_0}\left[\frac{E^n_{y,i,j-\frac{1}{2},k} - E^n_{y,i,j-\frac{1}{2},k-1}}{\Delta z} - \frac{E^n_{z,i,j,k-\frac{1}{2}} - E^n_{z,i,j-1,k-\frac{1}{2}}}{\Delta y}\right], \tag{4.40}$$

$$H^{n+\frac{1}{2}}_{y,i-\frac{1}{2},j,k-\frac{1}{2}} = H^{n-\frac{1}{2}}_{y,i-\frac{1}{2},j,k-\frac{1}{2}} + \frac{\Delta t}{\mu_0}\left[\frac{E^n_{z,i,j,k-\frac{1}{2}} - E^n_{z,i-1,j,k-\frac{1}{2}}}{\Delta x} - \frac{E^n_{x,i-\frac{1}{2},j,k} - E^n_{x,i-\frac{1}{2},j,k-1}}{\Delta z}\right], \tag{4.41}$$

$$H^{n+\frac{1}{2}}_{z,i-\frac{1}{2},j-\frac{1}{2},k} = H^{n-\frac{1}{2}}_{z,i-\frac{1}{2},j-\frac{1}{2},k} + \frac{\Delta t}{\mu_0}\left[\frac{E^n_{x,i-\frac{1}{2},j,k} - E^n_{x,i-\frac{1}{2},j-1,k}}{\Delta y} - \frac{E^n_{y,i,j-\frac{1}{2},k} - E^n_{y,i-1,j-\frac{1}{2},k}}{\Delta x}\right], \tag{4.42}$$

n is the current time step and Δx, Δy, and Δz are the dimensions of grid cells. (i, j, k) denotes the discrete grid:

$$(i, j, k) = (i\Delta x, j\Delta y, k\Delta z) \ . \tag{4.43}$$

The electric fields are given as

$$E^{n+1}_{x,i-\frac{1}{2},j,k} = \frac{2\epsilon - \sigma\Delta t}{2\epsilon + \sigma\Delta t} E^{n}_{x,i-\frac{1}{2},j,k} + \frac{2\Delta t}{2\epsilon + \sigma\Delta t}\left[\frac{H^{n+\frac{1}{2}}_{z,i-\frac{1}{2},j+\frac{1}{2},k} - H^{n+\frac{1}{2}}_{z,i-\frac{1}{2},j-\frac{1}{2},k}}{\Delta y} - \frac{H^{n+\frac{1}{2}}_{y,i-\frac{1}{2},j,k+\frac{1}{2}} - H^{n+\frac{1}{2}}_{y,i-\frac{1}{2},j,k-\frac{1}{2}}}{\Delta z}\right] , \tag{4.44}$$

$$E^{n+1}_{y,i,j-\frac{1}{2},k} = \frac{2\epsilon - \sigma\Delta t}{2\epsilon + \sigma\Delta t} E^{n}_{x,i,j-\frac{1}{2},k} + \frac{2\Delta t}{2\epsilon + \sigma\Delta t}\left[\frac{H^{n+\frac{1}{2}}_{x,i,j-\frac{1}{2},k+\frac{1}{2}} - H^{n+\frac{1}{2}}_{z,i,j-\frac{1}{2},k-\frac{1}{2}}}{\Delta z} - \frac{H^{n+\frac{1}{2}}_{z,i+\frac{1}{2},j-\frac{1}{2},k} - H^{n+\frac{1}{2}}_{z,i-\frac{1}{2},j-\frac{1}{2}},k}{\Delta x}\right] , \tag{4.45}$$

$$E^{n+1}_{z,i,j,k-\frac{1}{2}} = \frac{2\epsilon - \sigma\Delta t}{2\epsilon + \sigma\Delta t} E^{n}_{z,i,j,k-\frac{1}{2}} + \frac{2\Delta t}{2\epsilon + \sigma\Delta t}\left[\frac{H^{n+\frac{1}{2}}_{y,i+\frac{1}{2},j,k-\frac{1}{2}} - H^{n+\frac{1}{2}}_{y,i-\frac{1}{2},j,k-\frac{1}{2}}}{\Delta x} - \frac{H^{n+\frac{1}{2}}_{x,i,j+\frac{1}{2},k-\frac{1}{2}} - H^{n+\frac{1}{2}}_{x,i,j-\frac{1}{2},k-\frac{1}{2}}}{\Delta y}\right] , \tag{4.46}$$

For a one-dimensional scheme the fields are updated as shown in Figure 4.5. The electric field components are first defined at $t = 0$, and these are used to update the magnetic fields at a half time step ($^1/_2\Delta t$). The electric fields are then updated at time Δt, and the process is repeated until a final time T. This leap-frog scheme is also applied to the calculation of the fields in position. The electric field is calculated at $n\Delta z$ and magnetic field at $^1/_2 n\Delta z$.

In a three-dimensional scheme, the fields are staggered on a grid, as shown in Figure 4.6. This grid must be carefully defined such that the size of each cell, or mesh, is at least

$$(\Delta x, \Delta y, \Delta z) \leq \frac{\lambda_{min}}{10 n_{max}} \ , \tag{4.47}$$

where λ_{min} is the minimum wavelength in the simulation, and n_{max} is the maximum refractive index in the calculation domain. If mesh is too coarse, there is numerical

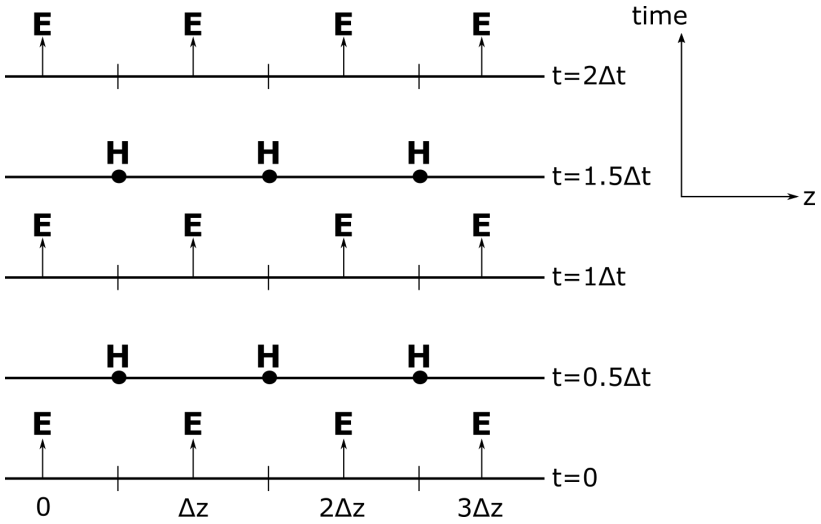

Figure 4.5: One-dimensional scheme for updating EM fields in space and time. The electric field is positioned spatially on the discrete grid k, and the H fields positioned with an offset on the grid $k + \frac{1}{2}$.

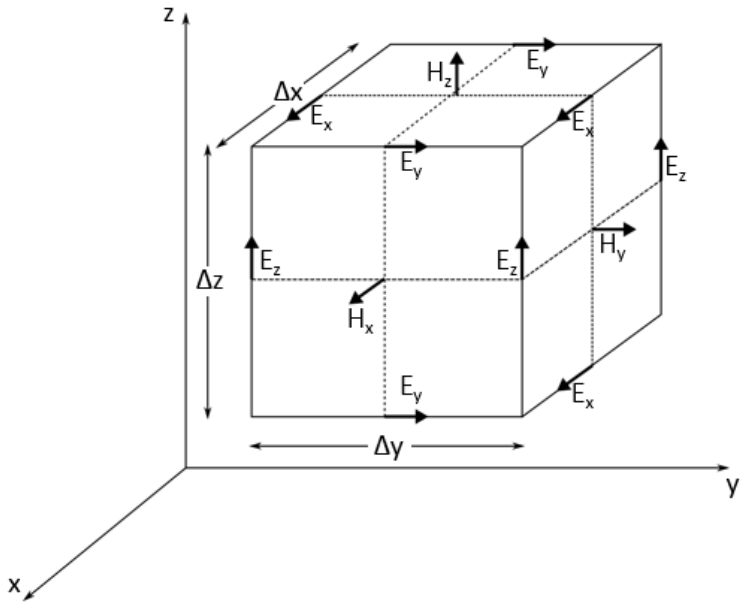

Figure 4.6: Three dimensional Yee cell and positioning of the field components. The field components are positioned on the cell, with E and H fields offset by half of the length of each side of the cell.

dispersion as the wavelength is not sampled correctly, and so the wave propagates at the wrong velocity. The time step must satisfy the Courant-Friedrichs-Levy (CFL) condition:

$$\Delta t \leq \frac{1}{v\sqrt{\frac{1}{\Delta x^2}+\frac{1}{\Delta y^2}+\frac{1}{\Delta z^2}}}\ , \tag{4.48}$$

where v is the speed of light in the medium. This means that the group velocity must be less than v in the medium to be stable [128]. This is minimised provided Equation (4.47) is obeyed.

A generalised method for modelling of the scattering matrix using FDTD has been presented elsewhere [129, 130]. The benefit of this is that hybrid mode problems can be solved without needing complex matrices to update the fields. Additionally it is more efficient to use the time domain to solve the scattering parameters over a broad bandwidth.

As the fields are calculated at discrete steps, errors due to this discretization are cumulative. This is reduced by satisfying Equations (4.47) and (4.48). However this means that, for finer meshes, the simulation time and computational requirements increase.

4.4.1 Finite Integration Technique

An alternative to FDTD is the Finite Integration Technique (FIT), which discretises the integral forms of Maxwell's equations. It is similar to FDTD but has the advantage that the structure of the grid used for discretization can be more general than the Yee cell. There are two meshes generated; the primary grid G and the dual grid $\tilde{G}$. The electric voltage and magnetic facet fluxes are held on G with electric flux and magnetic voltage held on $\tilde{G}$. FIT allows for non-Cartesian grids, thus reducing errors due to discretization of complex structures. However the two methods are equivalent for Cartesian grids when using the leap-frog scheme for updating in time [131]. In this thesis the FIT method is used when simulations are performed in the CST Time Domain solver. CST only supports particle-in-cell simulations with Cartesian grids, and so a Cartesian grid is also used for time domain simulations without particles to keep results consistent.

4.4.2 Scattering parameters for a finite pulse

The scattering matrix is defined for the steady state; this is not valid for this thesis as only interaction between an electron bunch and main THz pulse is considered. It is desirable to maximise the transmission of all frequencies of the pulse into the correct mode whilst neglecting reflections which will not have an effect on the electron bunch. The time window for calculation of the scattering parameters is therefore cut after the

main pulse has crossed the port boundary. The choice of window depends on the effect of reflections. A rectangular window causes a ringing effect in the frequency domain due to the sharp cut off, which is acceptable provided any reflections are separated from the main pulse. Other windows, which taper to zero outside the bounds, are affected by losses.

4.5 Summary

A summary of the figures of merit used in optimisation of accelerating cavities has been presented; these are general parameters which are not all suitable for the travelling wave, finite pulse structure discussed in this thesis. For example the Q-factor is not valid as it is used for resonant structures. The transit time factor itself is not used; instead the interaction length between THz pulse and an electron is used as the figure of merit.

Four versions of the interaction length were considered. The first, L_{phase}, is only valid for single frequencies. An analysis similar to that in Chapter 3 was performed, using first order dispersion (group velocity) to define L_{group}. This gives the length over which an electron stays inside a THz pulse. Third order dispersion was added to calculate $L_{v_g,e}$; this takes into account that the pulse spreads as it propagated. The final version is $L_{v_p,e}$ which gives the interaction length between an underlying oscillation of the THz pulse and an electron, taking into account the change in instantaneous frequency as the pulse propagates. By comparing the last three versions for three different DLWs , $L_{v_p,e}$ was found to be inaccurate as the pulse envelope was not included. As v_g is less than v_e in each case, the electron propagates faster than the THz pulse and therefore leaves the envelope. As a result it is more accurate to use L_{group} or $L_{v_g,e}$. They produce similar results for longer pulses as GVD has less of an effect. However for short pulses, $L_{v_g,e}$ is longer as pulse broadening is more significant. This does not take into account that as the pulse broadens, the amplitude decreases, and so the rate of energy change of an electron decreases.

The most common methods of coupling radiation into waveguide structures and their suitability for THz-driven DLWs has been discussed. It has been concluded that, to maximise transmission of a broadband pulse, a horn coupler is preferable. The methods of modelling such a coupler, with a focus on maximising the transmission, have been introduced. The scattering matrix and how it is calculated when considering propagation of a short pulse was also summarised.

Chapter 5

Methods of simulating dielectric-lined waveguide structures

Simulations of the DLW structures were performed using several methods. Solving the dispersion relation and calculating the figures of merit independent of the input THz source was performed using *Mathematica*. Modelling pulse propagation through only the DLW was also performed in both *Mathematica* and the time domain solver in CST (CST-TDS). Simple electron-THz interaction was modelled in *Mathematica*. Full simulation used CST Particle-in-Cell (PIC), and included coupling from free space and realistic electron bunches. It was also desirable, due to the long simulation times required by CST, to find ways to reduce computational effort. Although at least one full simulation of the structure had to be performed, it was also of interest to study if the coupler could be neglected. This was done by comparing both THz pulse propagation and THz-electron interaction with and without the coupler.

5.1 Dispersion relation

Calculation of the dispersion relation depended on the choice of simulation method. However all methods have some common features. β was calculated at single frequencies and the full solution to the dispersion relation was then found by interpolation of these points. As the calculation was numerical, the number of samples determined the accuracy of $\beta(\omega)$.

5.1.1 Mathematica

The dispersion relation was solved numerically using Equations (2.70) and (2.76), corresponding to accelerating and deflecting LSM modes respectively, by defining a

range of β and solving for f. Setting β to zero corresponds to the cut-off frequency and below this the propagation constant is purely imaginary. The root finding method was more stable when solving for a given β and so only gave the real part of the dispersion relation ($|f| > f_c$). By solving again for imaginary β the full solution was produced by interpolation over the given range. Therefore the equation was solved twice; once for real roots and again for imaginary roots. The figures of merit were calculated using the resulting interpolated dispersion relation. Operating frequency was found by replacing β with k_0/v_e before solving the dispersion relation for f. The operating frequency was calculated as 0.4729 THz for the LSM_{11} mode of a DLW with $w = 1200$ μm, $a = 250$ μm, $\delta = 50$ μm and $\epsilon_r = 3.75$, for an electron energy 35 MeV.

After defining a value for m there was still an infinite number of solutions for each β corresponding to different n, and so the limits of the numerical solver were carefully chosen to ensure the correct mode was selected. Field components were calculated for the chosen mode by the first obtaining the interpolated dispersion function, then using the relevant equations from 2.3.1 and 2.3.2. This method means that, for a given frequency, the fields are analytical functions which depend on transverse position. A spatial mesh is therefore not required.

5.1.2 CST

In CST the Eigenmode solver is used to analyse the field configuration of the N lowest modes at a given frequency, where N is defined by the user. Calculating the dispersion relation requires both consideration of the number of points in frequency and also the mesh of the structure. The frequency is calculated by

$$2\pi f = v_e \beta \ , \tag{5.1}$$

where β is defined in the Eigenmode solver by varying the phase shift of an input field, provided that the simulation domain has longitudinally periodic boundaries. Phase shift is given as

$$\theta = \beta L \ , \tag{5.2}$$

where L is the length of the periodic cell. The maximum frequency was expected to be approximately 1 THz, and thus the cell length was defined such that it was only a small part of a single 1 THz wavelength. A typical length is 20° of the wavelength, which corresponded in this case to $L = 16.655$ μm. The frequency is therefore given by defining a phase,

$$f = \frac{v_p \phi}{2\pi L} \ . \tag{5.3}$$

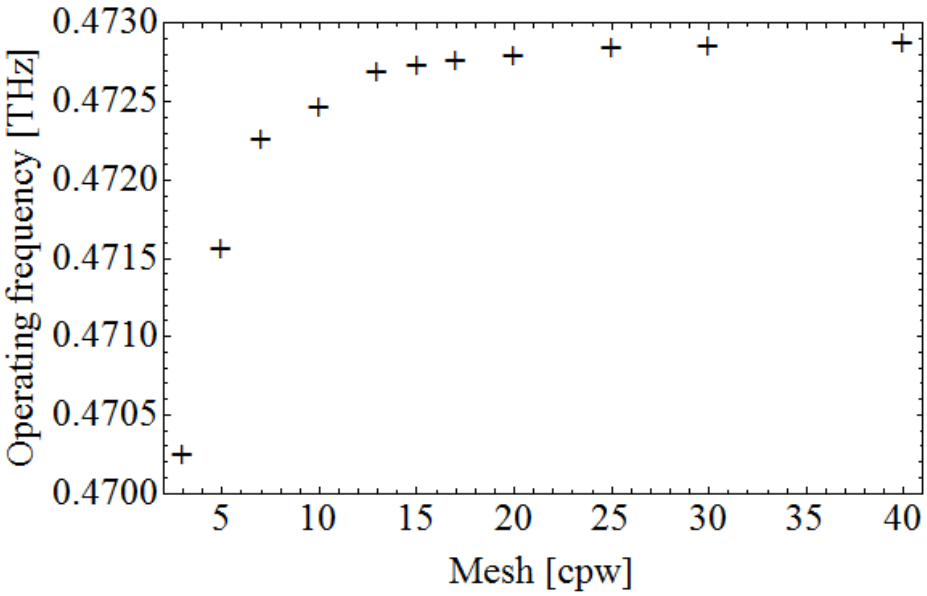

Figure 5.1: Effect of mesh, defined as the number of cells per wavelength *cpw*, on calculated operating frequency. The wavelength was taken to correspond to a frequency of 1THz.

The simulations were set such that frequency and figures of merit were displayed for each value of ϕ in a parameter sweep. f_{op} was found by calculating v_p at each value of ϕ and interpolating the resulting list. The calculation of the fields in the simulation domain require definition of a mesh. As other solvers use the hexahedral mesh, which is made up of cubic cells, this was also used here. However, Eigenmode also supports a tetrahedral mesh, which is more accurate. The fields profiles are solved by discretising Maxwell's equations. The effect of increasing the number of mesh cells per wavelength, *cpw*, is shown in Figure 5.1 for f_{op}. The value of f_{op} converges with increasing mesh, tending to 0.4729 THz, corresponding to the value found from solving the dispersion relation. As the wavelength for the mesh definition is determined from the upper limit of the frequency range of the simulation, it was expected that the accuracy of simulation would decrease with increasing frequency as the number of cells per wavelength decreases. This is shown by calculating the dispersion relation for different mesh values, such as in Figure 5.2. Two meshes were compared, 5 *cpw* and 20 *cpw* and it was concluded that, as expected, accuracy decreased with frequency. Clearly there was a compromise between accuracy and simulation time. It is also of note that, due to mode switching, tracking a single mode with change in propagation constant required post processing at each value of θ to check the field. This is because the Eigenmode solver does not define modes by their profiles, but by their frequency at a given β. The advantage of using CST is that the field is calculated for each

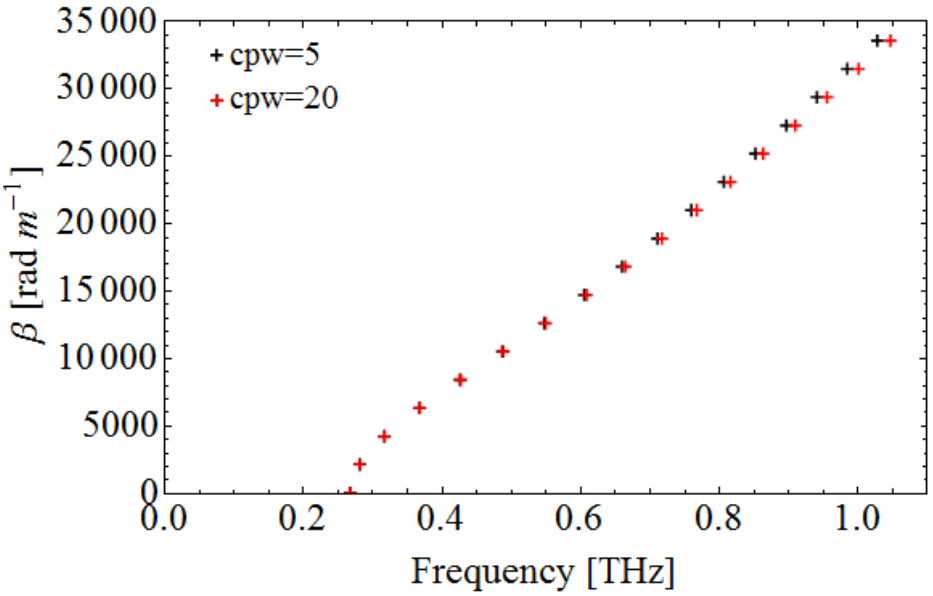

Figure 5.2: Effect of mesh on the dispersion relation as calculated by the CST Eigenmode solver. Black: $cpw = 5$, red: $cpw = 20$. Differences between the two increase with frequency.

mode at each value of ϕ and so figures of merit such as V_z, r_s, P_{flow} and P_{loss} are obtained with little further effort. Furthermore it can be used for any structure, including those with no analytical solution. Therefore it is well suited to analysis of complicated structures.

5.2 Pulse propagation

5.2.1 Mathematica

A *Mathematica* model was written to simulate propagation of a THz pulse through a DLW, using a given set of waveguide parameters and a choice of mode. The dispersion relation was first solved numerically, as discussed in Section 5.1, to give $\beta(\omega)$, an interpolated function. The field components were calculated as a function of frequency using this interpolated function. In this section, only propagation of the axial E_z field component is considered. The pulse shape in the frequency domain was chosen and a discrete Fourier transform (DFT) applied to propagate the pulse in the time domain. This required the pulse in the frequency domain to be symmetric about $\omega = 0$, which required an analytic signal:

$$S(t) = s(t) + i\ \tilde{s}(t)\ , \tag{5.4}$$

where $s(t)$ is a real valued pulse in the time domain, and $\tilde{s}(t)$ is the Hilbert transform of $s(t)$;

$$\tilde{s}(t) = -i \ \mathrm{sgn}(\omega)\mathcal{F}\left[s(t)\right](\omega) \ . \tag{5.5}$$

The use of an analytic signal was necessary to suppress the generation of a second pulse which propagates in the opposite direction. This is result of superfluous negative components in the frequency spectrum, which was seen in Chapter 3.

This *Mathematica* model was limited as only the DLW was considered in the simulation; the horn was not included as simulation of the pulse propagation was prohibitively time consuming. It was also assumed that there was no mode conversion inside the DLW; the pulse entered and exited the DLW in the mode of interest. The model was numerical and so accuracy depended on the frequency range and sample size used for interpolation of the dispersion relation, and the integration range and sample size of the DFT. However as the simulation was performed primarily in the frequency domain, the position, z, was defined before performing the DFT; there was no need to track the pulse to the position of interest. Although the *Mathematica* model was limited to pulse propagation in the DLW only, it was a useful comparison to CST, the results from which are strongly dependent on the solver and the setup of the calculation domain.

The effect of pulse bandwidth on propagation was investigated for four different pulse widths; $\sigma_f = 0.023$ THz, 0.046 THz, 0.069 THz, and an ultrashort pulse described by the modified Gaussian function. σ_f is the RMS bandwidth of the pulse; the subscript f denotes that it is defined explicitly in terms of frequency, rather than ω (as was the case in Chapter 3). Shown in Figure 5.3 is a THz pulse with $\sigma_f = 0.023$ THz. There is minimal dispersion over 10 mm. As there is little increase in calculation time to increase the length of the DLW the pulse shape was also calculated at 30 mm. There is no clear dispersion of the pulse envelope which is to be expected as the dispersion is relatively linear over the bandwidth.

The propagation of a THz pulse with $\sigma_f = 0.046$ THz is shown in Figure 5.4. Higher order dispersive effects are now visible with both pulse broadening and time-dependent frequency of oscillation. There is a small change in the pulse over 10 mm, but pulse broadening is not observed until greater distances. The decrease in amplitude is also observable.

The propagation of a pulse with $\sigma_f = 0.069$ THz is shown in Figure 5.5. There is a long dispersive tail and the pulse amplitude decreases significantly as it propagates. The choice of bandwidth here was such that frequencies below the cut-off of the LSM_{11} mode of the waveguide are minimal in order to reduce the ringing effect.

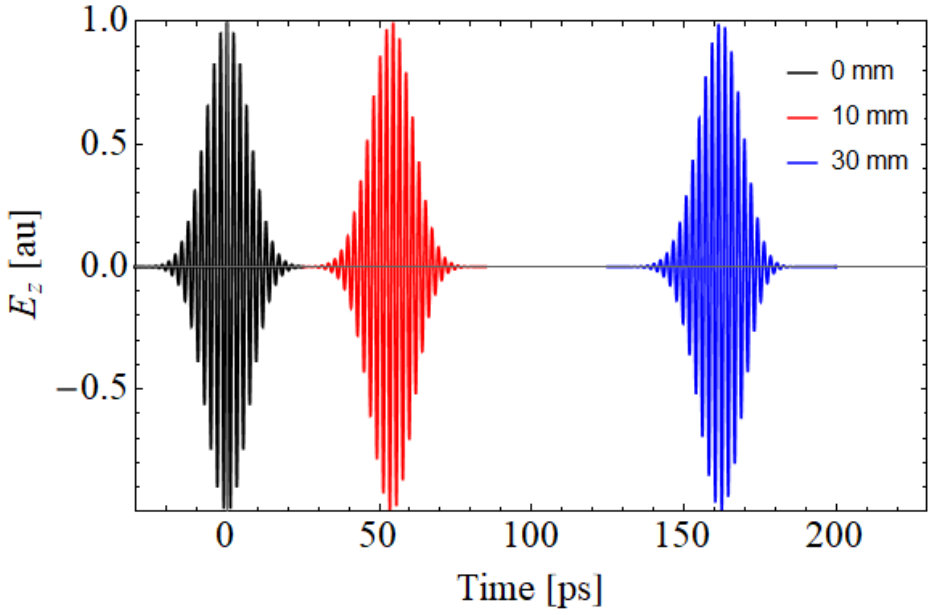

Figure 5.3: Propagation of a THz pulse with $\sigma_f = 0.023$ THz in the f domain, simulated using a *Mathematica* model. Pulse is shown at snapshots in z; 0 mm, 10 mm, and 30 mm.

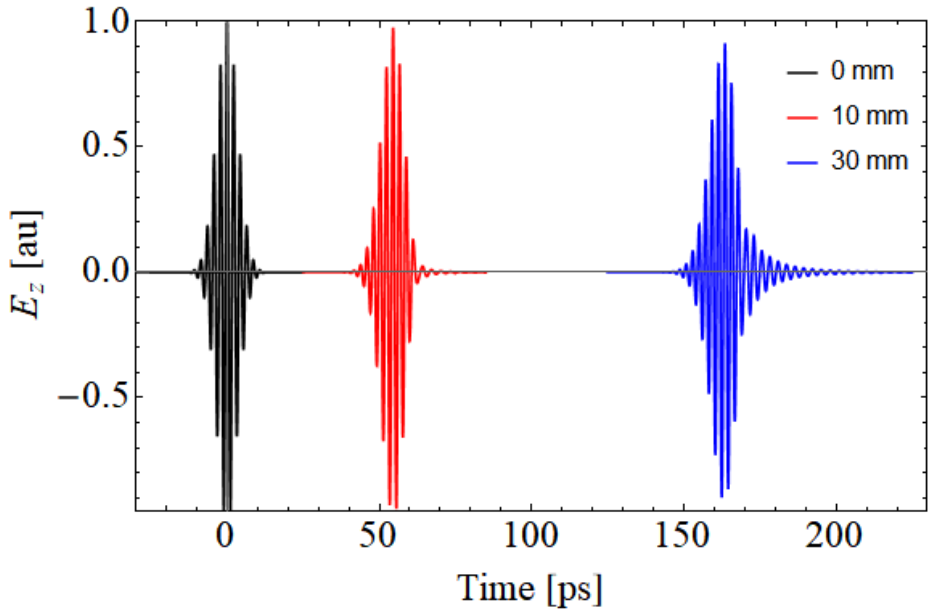

Figure 5.4: Propagation of a THz pulse with $\sigma_f = 0.046$ THz, simulated using a *Mathematica* model. Pulse is shown at snapshots in z; 0 mm, 10 mm, and 30 mm.

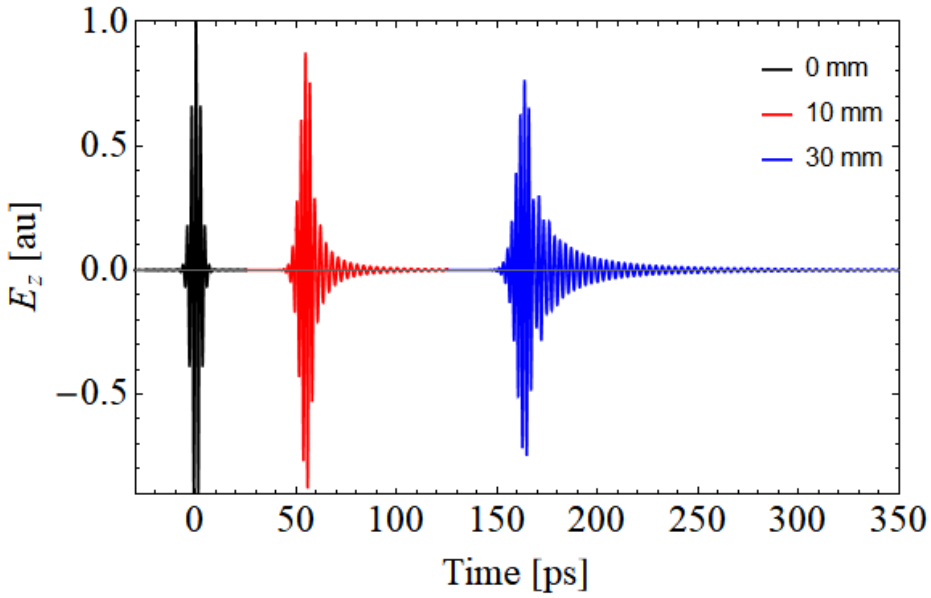

Figure 5.5: Propagation of a THz pulse with $\sigma_f = 0.069$ THz, simulated using a *Mathematica* model. Pulse is shown at snapshots in z; 0 mm, 10 mm, and 30 mm.

The final comparison is with a modified Gaussian pulse, which includes frequencies below cut-off. The pulse as propagated in Mathematica is shown in Figure 5.6. The initial pulse at $z = 0$ suffers from ringing as application of the frequency dependent terms in the amplitude of the field is independent of distance. Pulse ringing is more pronounced with increasing distance and the pulse amplitude decays significantly.

The advantage of the use of *Mathematica* is that the calculation of pulse propagation does not require modelling of the entire length of the structure; as the solution is semi-analytical (only the dispersion relation requires a numerical solution) finding the field at a specific position and time simply requires these values to be inserted into the field equation. However the full structure is not modelled; the coupler is neglected to simplify the analysis.

5.2.2 CST

The CST time-domain solver uses the finite integration technique, described in Section 4.4.1. This method requires the definition of a spatial mesh, the density of which is important for controlling the accuracy of the results. The CFL condition (Equation (4.48)) for the largest mesh cell size must be satisfied to prevent numerical dispersion, and the smallest mesh cell is constrained by the smallest feature of the simulation. The mesh size is therefore a trade off between accuracy and speed. Using more broadband pulses also means that the density of the mesh increases as the highest frequency increases.

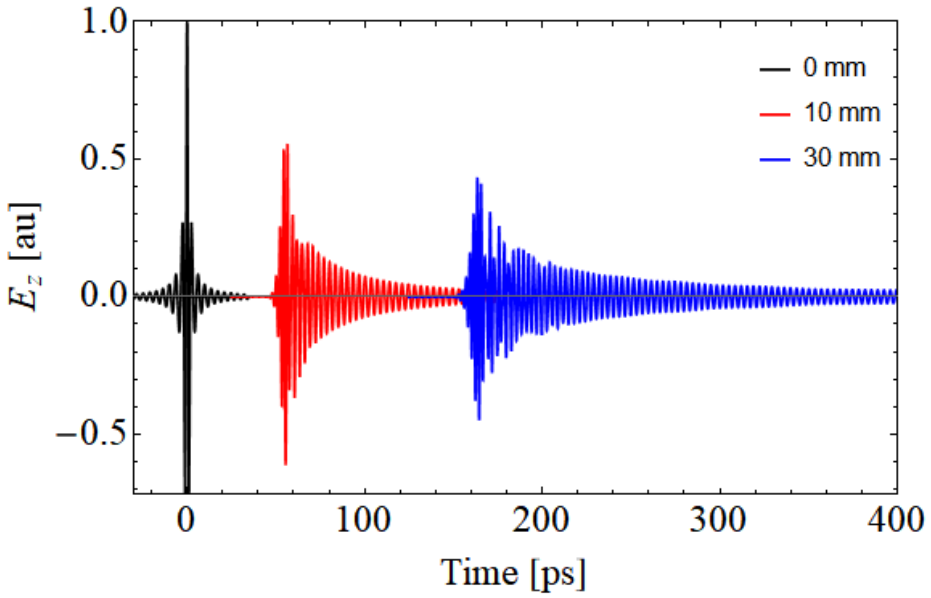

Figure 5.6: Propagation of a THz pulse described by a modified Gaussian pulse with maximum at f_{op}, simulated using a *Mathematica* model. Pulse is shown at snapshots in z; 0 mm, 10 mm, and 30 mm.

CST uses a range of techniques to improve accuracy without decreasing the size of each mesh cell. The mesh can be defined locally, for example increasing the mesh in the dielectric where the field varies more rapidly [132]. These features are available as CST uses FIT, which allows for a non-uniform mesh.

Using the rule of thumb of 10 cells per smallest wavelength, an estimate of the number of cells required in the 10 mm long DLW is 10^7. The addition of a horn drastically increases this. CST defines a rectangular simulation domain, so the transverse dimensions depend on the transverse coupler size. An example free space THz pulse with a 5 mm^2 spot size requires in the transverse plane at least $250,000$ cells per discrete longitudinal position. It is clear that the number of cells is large, which impacts upon the simulation time.

It was necessary to perform an initial study, without the coupler, on the effect of different solver settings. By default CST performs time domain simulations with the mode pattern calculated for a defined frequency. A number of other frequency samples can also be defined at which the mode pattern is also calculated; the maximum is 500 samples, equally spaced over the frequency range of the simulation. This is in comparison to a broadband analysis, which tracks individual modes over frequency to identify crossing points with other modes and field variation with frequency. The broadband analysis allows for single port mode excitation, useful for calculation of a propagating THz pulse in a single mode, while still considering the effects of higher

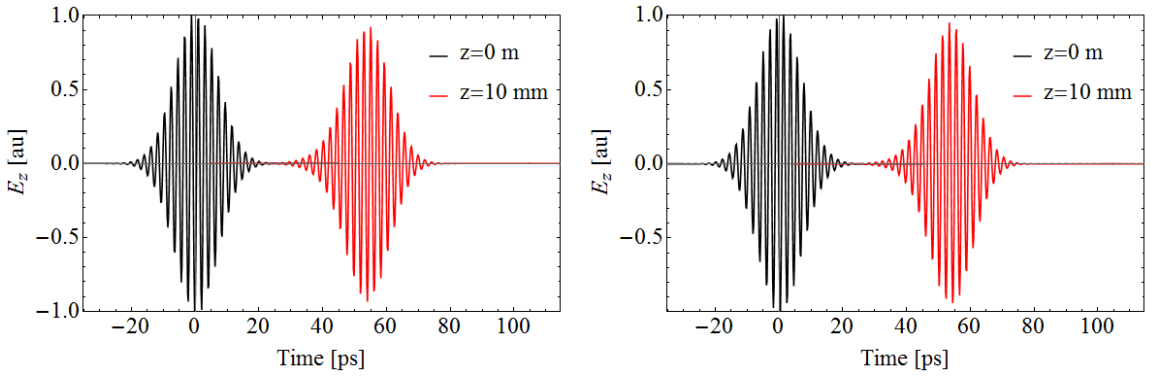

Figure 5.7: E_z field of a THz pulse with $\sigma_f = 0.023$ THz, at $z = 0$ mm and $z = 10$ mm, simulated using the time domain solver in CST. Left: using mode pattern calculated at 0.5 THz. Right: broadband mode calculation.

order modes in the simulation. This analysis is costly in terms of computational effort, and is not recommended for long structures of order multiple wavelengths which are considered here. Therefore this was only performed to confirm that the results were consistent between solver settings. An additional option was to absorb unconsidered modes. When activated, any fields occurring at the waveguide ports are removed from the simulation. These can arise due to numerical errors from calculation of the fields in a inhomogeneous waveguide when the broadband solver is not used. They can also result from mode excitations which are not considered in the simulation.

Starting with the standard waveguide solver, the mode pattern at 0.5 THz was calculated and this was used for all frequencies in the simulation. The definition of the mode calculation frequency is controlled by CST; it was not possible to set at the operating frequency. The mesh was initially set to 30 *cpw*.

With an initial pulse bandwidth $\sigma_f = 0.023$ THz the result from the standard solver was expected to be a close match with the pulse propagation as calculated in *Mathematica*. This is because a narrow bandwidth means that the mode pattern does not change significantly over the frequency range. Figure 5.7 shows the pulse at 0 mm and 10 mm for the generalised (mode tracking) solver, with the mode pattern calculated at 0.5 THz and the broadband analysis respectively. Others options are neglected as they either produced the same or unphysical results. Comparing to the same pulse as calculated using *Mathematica* in Figure 5.3, it cannot be concluded which solver is optimal as they have produced almost identical results.

Changing to $\sigma_f = 0.046$ THz, shown in Figure 5.8, there is now a small difference between the two solver settings. Neither replicate the pulse in Figure 5.4 exactly; however it appears that the broadband solver is more accurate. The front of the

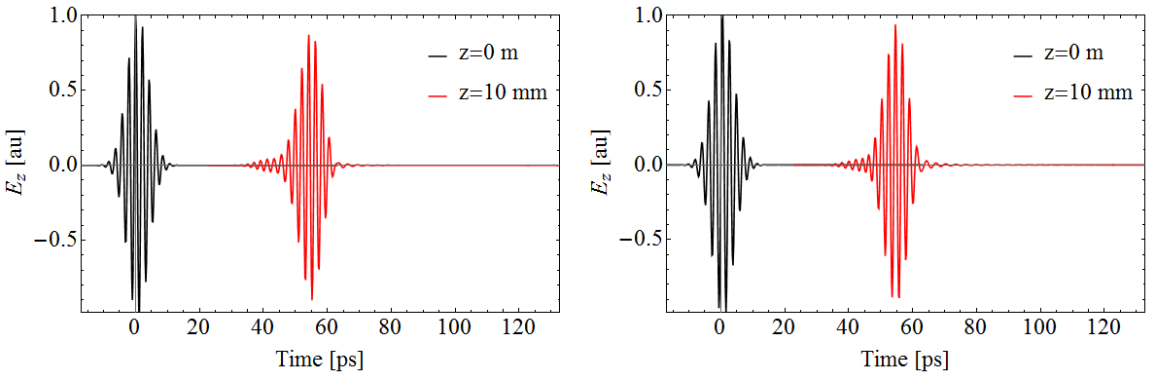

Figure 5.8: E_z field of a THz pulse with $\sigma_f = 0.046$ THz, at $z = 0$ mm and $z = 10$ mm, simulated using the time domain solver in CST. Left: using mode pattern calculated at 0.5 THz. Right: broadband mode calculation.

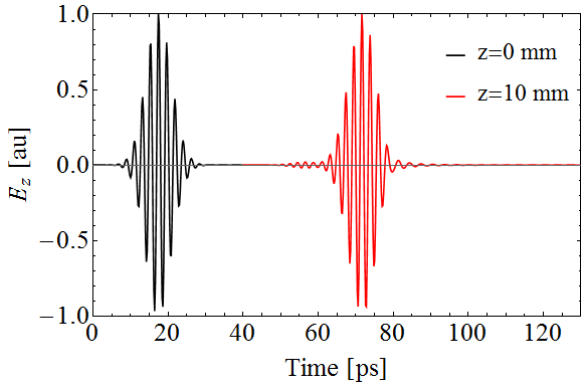

Figure 5.9: E_z field of a THz pulse with $\sigma_f = 0.046$ THz, at $z = 0$ mm and $z = 10$ mm, simulated using the time domain solver in CST. The mesh has been increased to 50 *cpw*.

pulse is less well modelled in both cases; by increasing the mesh to $cpw = 50$ for the broadband solver the pulse shape is much closer to that given by *Mathematica*, as shown in Figure 5.9. This is to be expected; the number of cells per wavelength has increased, and so the mesh is more dense at higher frequencies and so this part of the spectrum is better modelled.

Repeating the same analysis for the THz pulse with $\sigma_f = 0.069$ THz using a mesh of $cpw = 30$ for the standard and broadband solvers, as shown in Figure 5.10. Again the broadband solver better replicates the pulse in Figure 5.5. However in both cases the head of pulse is not as well modelled as there is an extra component in front. The use of the broadband solver results in a much longer tail, which is closer to the result in *Mathematica*. Increasing mesh to 50 *cpw* and using the broadband solver, the tail is unchanged but the small pulse in front of the head is suppressed. This is shown in

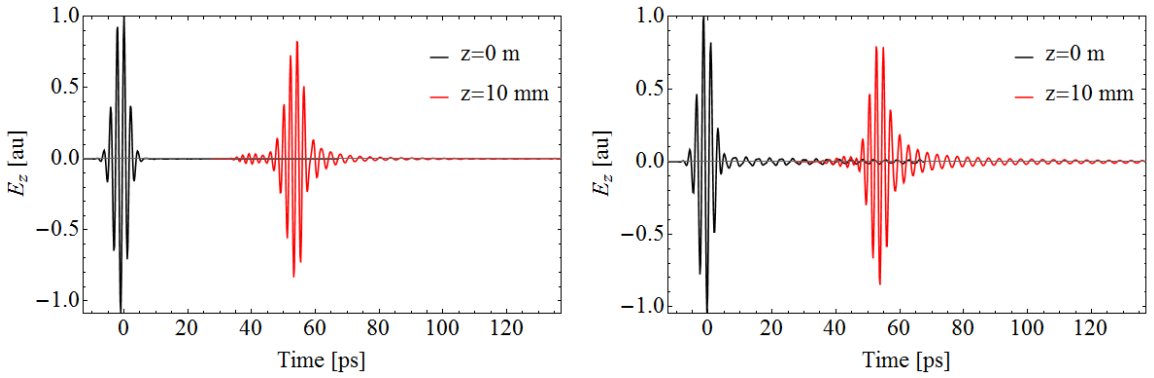

Figure 5.10: E_z field of a THz pulse with $\sigma_f = 0.069$ THz, at $z = 0$ mm and $z = 10$ mm, simulated using the time domain solver in CST. Left: using mode pattern calculated at 0.5 THz. Right: broadband mode calculation.

Figure 5.11. The pulse is still not exactly identical to that in Figure 5.5, as the small pulse in font of the head is still present. This suggests that this feature contains high frequencies, which are only present for more broadband pulses.

Effect of coupler

The previous simulations assumed that the pulse was launched directly at the entrance to the DLW. It was expected that, with the addition of a coupler, there would be other modes present and added dispersion due to the extra length. This has an effect on both the THz pulse propagation and the energy change of the electron bunch.

Again the pulse bandwidth was changed to see the effect on the final energy change. In each case, the initial pulse energy was the same, and the THz pulse was normalised such that the maximum field amplitude was 1.

First considered is a THz pulse with $\sigma_f = 0.023$ THz. Including the coupler, the pulse after propagating through a 10 mm DLW is shown in Figure 5.12. Also in the figure is the pulse after propagating through 10 mm of DLW without the coupler. The pulse energy at the start of the simulation is the same; as such the field amplitude is normalised to the maximum of the DLW only at 10 mm. There are three main differences due to the coupler; the maximum field amplitude is lower, the pulse is broadened, and there is a secondary part to the pulse with a different group velocity. The amplitude decrease is a direct effect of the pulse spreading.

Looking at the field profile in more detail, the second part of the pulse is due to the LSM_{31} mode; the transverse profile is shown in Figure 5.13. The transverse field is $\frac{\pi}{2}$ out of phase with the longitudinal field, and so the E_z field has a small amplitude in this figure. The appeareance of this mode shows that there is mode conversion due

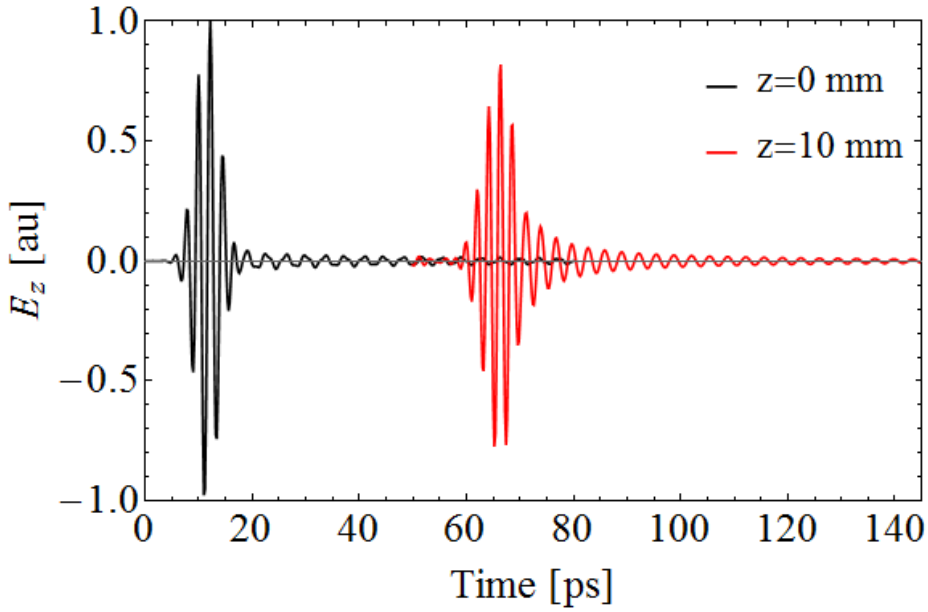

Figure 5.11: E_z field of a THz pulse with $\sigma_f = 0.046$ THz, at $z = 0$ mm and $z = 10$ mm, with mesh increased to 50 *cpw*, simulated using the time domain solver in CST. Left: using mode pattern calculated at 0.5 THz. Right: broadband mode calculation.

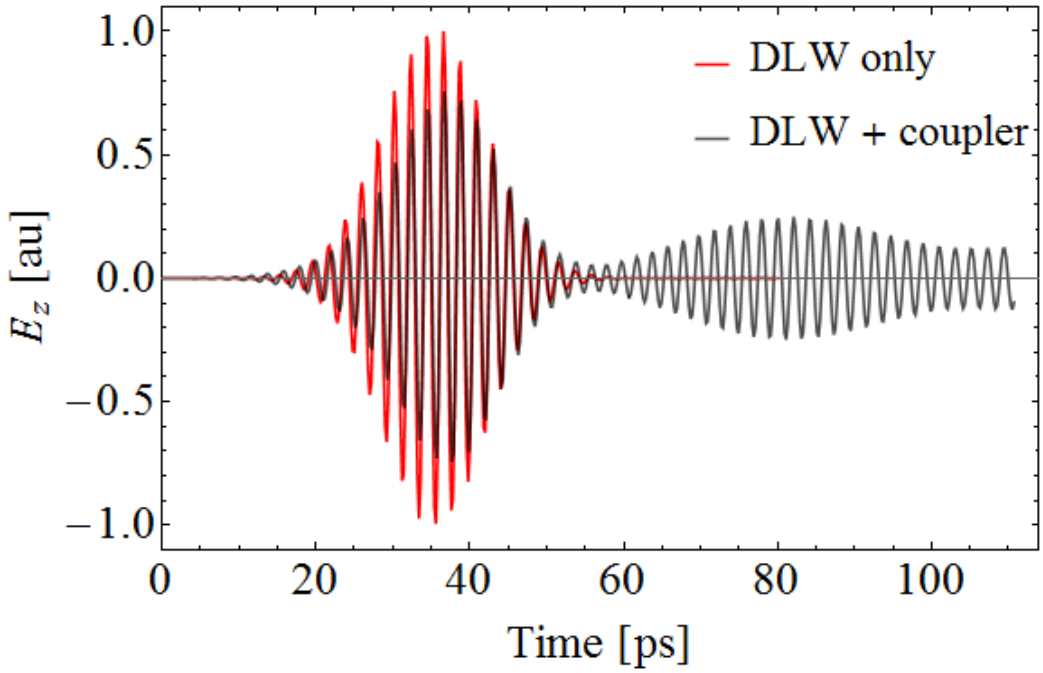

Figure 5.12: Normalised E_z field of a THz pulse with $\sigma_f = 0.023$ THz after propagating through 10 mm of a DLW, simulated using the time domain solver in CST. Red: DLW only. Black: THz pulse has propagated through the full DLW structure, including a 23 mm coupler and 10 mm DLW. The pulses have been shifted for comparison.

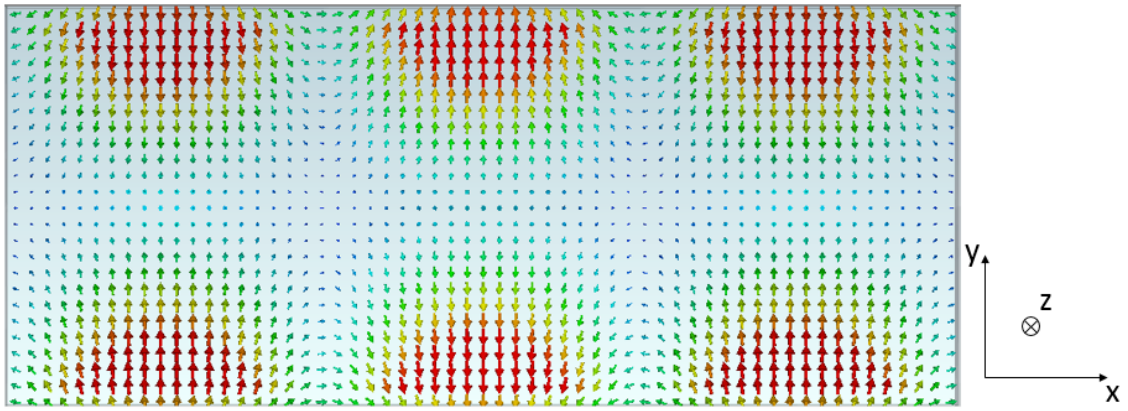

Figure 5.13: Transverse profile of the LSM_{31} mode generated in the structure as a result of the addition of the coupler, calculated at the operating frequency of the mode. Not shown is the field in the dielectric. There is a longitudinal E_z field on-axis, and on either side the longitudinal field faces the opposite direction. The E_y field amplitude is largest, and there is a smaller E_x component.

to the coupler, which reduces the energy in the main pulse. LSM_{31} has a lower group velocity and so the envelope propagates more slowly than the main pulse. This means that the coupler must be included for the full solution otherwise the amplitude of the THz field is overestimated.

Considering the THz pulse with $\sigma_f = 0.069$ THz, the coupler again has a similar effect on the THz pulse, as seen in Figure 5.14. The same normalisation as in Figure 5.12 has been applied. There is a decrease in amplitude and significant pulse spreading, along with generation of other modes. The main pulse is well replicated but the pulse is again split. However this is not as well defined as with $\sigma_f = 0.023$ THz.

5.2.3 Conclusion

Based on the comparison of pulse propagation through the DLW only, the use of *Mathematica* is preferable due to speed and simple set up, especially when considering a single field at one transverse point, as the full structure does not need to be simulated. A further benefit is that there is no need to consider the solver settings, which have an effect on the propagation of the pulse, especially with increasing bandwidth.

The inclusion of a coupler causes a significant effect on the propagation of the pulse even for narrow bandwidths. This is a result of mode conversion and pulse broadening due to the longer confinement. Therefore for the full pulse propagation it is necessary to simulate the full structure. Mode conversion does not necessarily have an effect on the final energy gain of an electron interacting with the THz pulse. The higher order modes have higher operating frequencies, and as a result the phase

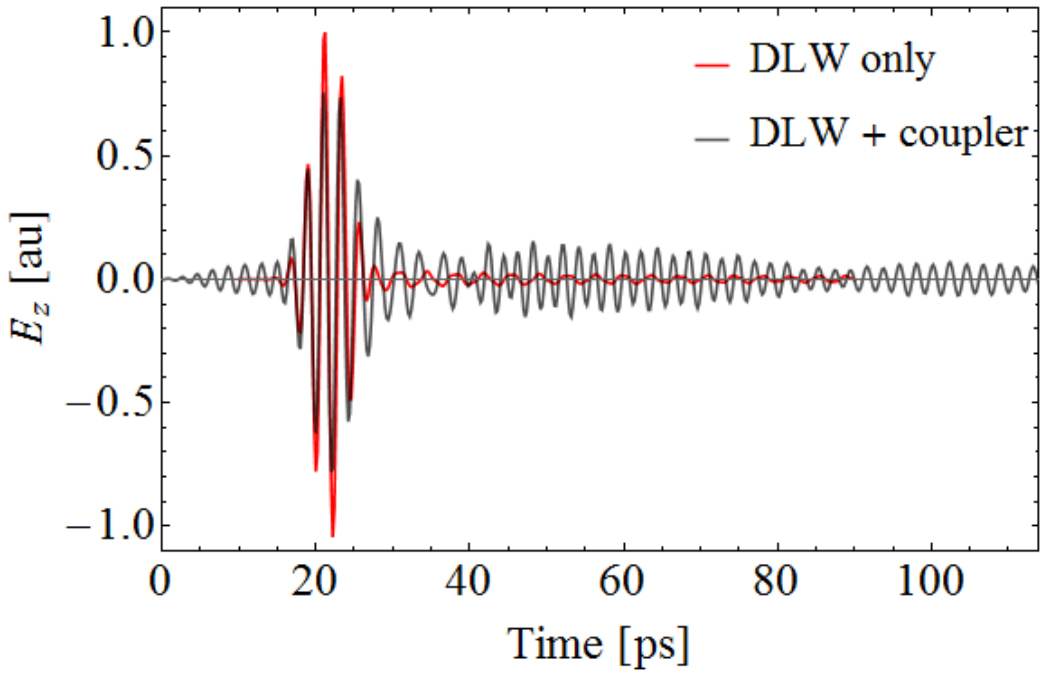

Figure 5.14: Normalised E_z field of a THz pulse with $\sigma_f = 0.069$ THz after propagating through 10 mm of a DLW, simulated using the time domain solver in CST. Red: DLW only. Black: THz pulse has propagated through the full DLW structure, including a 23 mm coupler and 10 mm DLW. The pulses have been shifted for comparison.

velocity of the mode is not equal to the electron velocity. As such, the electron only interacts with the mode over a short distance. It can be expected that, by neglecting the coupler, the amplitude of the main pulse is overestimated and so the final energy gain of an electorn is also overestimated.

5.3 THz-electron interaction

5.3.1 Mathematica

An extension of the pulse propagation in *Mathematica* is to monitor the field experienced by a co-propagating electron. In the case of THz-electron interaction where the change in momentum is sufficiently small, the velocity of the electron can be considered constant and therefore the change in momentum is calculated by

$$\dot{\mathbf{p}} = c\left(-\mathbf{E}\left(x, y, z, t = \frac{z}{v_e} + t_0\right) + \mu_0 \frac{\mathbf{p}}{\sqrt{|\mathbf{p}|^2 + m_e^2 c^4}} \times \mathbf{H}\left(x, y, z, t = \frac{z}{v_e} + t_0\right)\right) , \tag{5.6}$$

where m_e is the electron mass, v_e is the longitudinal electron velocity, and momentum $\mathbf{p}$ is given in electron volts (eV). For the full solution where v_e varies with z due to the interaction with the field, an additional differential equation must be solved simultaneously;

$$\dot{\mathbf{r}} = \frac{\mathbf{p}}{\sqrt{|\mathbf{p}|^2 + m_e^2 c^4}} , \tag{5.7}$$

where $\mathbf{r} = \{x, y, z\}$. Throughout this thesis, all calculations of momentum change using *Mathematica* assume that v_e is constant with z, and so only Equation (5.6) is used. This is valid as the calculation is only performed using 35 MeV electrons with $v_e = 0.999\ c$ and momentum change has negligible effect on this velocity. The momentum change is calculated numerically at each time step over a time period. The effect of t_0, the injection time of the electron, on $\mathbf{p}$ and $\mathbf{r}$ can be investigated. The fields in this case are solved beforehand for a predefined mesh, and the resulting matrix interpolated over the region of interest. This is especially useful for small simulations such as THz-electron interaction on axis, as the model can be made one- or two-dimensional with no loss of information about the fields. Energy gain as a function of time delay for a THz pulse with $\sigma_f = 0.023$ THz and $\sigma_f = 0.069$ THz, is shown in Figures 5.15 and 5.16 respectively. A field normalisation was applied to keep the energy of the pulse constant.

The energy change saturates after a certain distance in both cases. However later electrons continue to interact, gaining the same energy. For $\sigma_f = 0.069$ THz there is

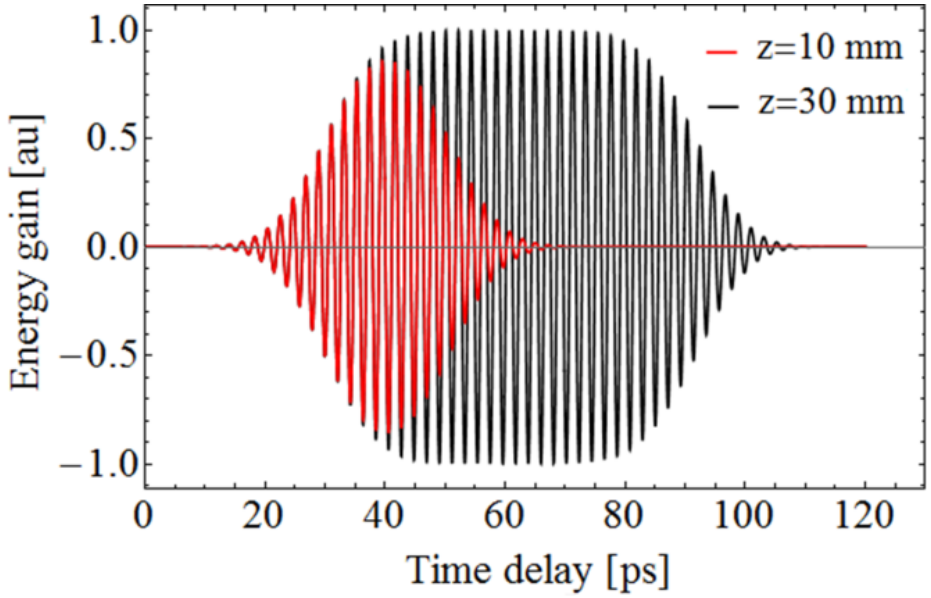

Figure 5.15: Energy gain of an electron propagating on-axis as a function of time delay between THz pulse and electron as calculated using *Mathematica*. The THz pulse has bandwidth $\sigma_f = 0.023$ THz. The energy gain after propagating through a DLW of length 10 mm and 30 mm is shown.

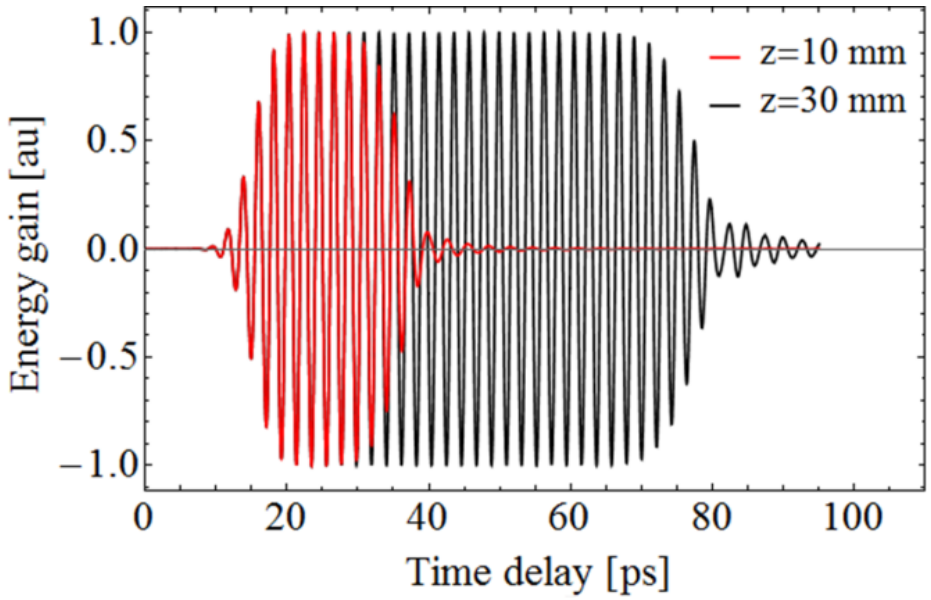

Figure 5.16: Energy gain of an electron propagating on-axis as a function of time delay between THz pulse and electron as calculated using *Mathematica*. The THz pulse has bandwidth $\sigma_f = 0.069$ THz. The energy gain after propagating through a DLW of length 10 mm and 30 mm is shown.

saturation after propagating 10 mm whereas maximum energy change has not been reached for $\sigma_f = 0.023$ THz. For both pulses, after propagating 30 mm, the interaction is sinusoidal with time delay. The choice of injection time is relaxed as synchronisation of order 10 ps is required. The energy gain is approximately the same in both cases.

5.3.2 CST

The use of the PIC solver in CST was appropriate for comparison with *Mathematica* and the use of realistic electron bunches. The fields are updated for each time step as described in Section 4.4, but the phase space of the electrons is continuous. Unlike in *Mathematica*, the full structure can be modelled, which is useful for investigating THz-electron interaction in the horn coupler. CST has multiple options for the particle bunches used in PIC. The simplest is to define a radially symmetric bunch with zero emittance, which is used here. Using the same settings as for the time domain solver improved the accuracy of the fields and thus the electron-THz interaction. However this was at the expense of long simulation time. Care also had to be taken when defining the field and particle monitors. As both field amplitude and the final energy gain of electrons are oscillatory with time, it was necessary to define the step size of these monitors to sufficiently sample the signals. The Nyquist criterion defines the required step size; the sampling frequency must be twice the signal frequency. Assuming that the frequency is f_{op}, a time step greater than $^2/_{f_{op}}$ is required.

Simulations were performed for THz pulses with $\sigma_f = 0.023$ THz and $\sigma_f = 0.069$ THz both with and without the coupler. In both cases the energy gain was normalised to the maximum energy gain using the DLW only. The electron bunch was modelled as a long line of electrons with zero emittance so that only the longitudinal interaction was studied.

The energy gain as a function of time delay using a THz pulse with $\sigma_f = 0.023$ THz is shown in Figure 5.17 for a DLW of length 10 mm. Compared to the use of a DLW only, the maximum energy gain was reduced. There was no saturation of the interaction as energy gain was not maximised. This saturation was achieved by increasing the length of the structure. Figure 5.18 shows the energy gain as a function of time for the full structure with the DLW length increased to 30 mm. As with Figure 5.15 there is now saturation of the energy gain. However the dispersion of the THz pulse has been imparted onto the interaction although this only has an effect on electrons which interact with the THz pulse towards the end of the structure.

The energy gain as a function of time delay using a THz pulse with $\sigma_f = 0.069$ THz is shown in Figure 5.19. In both cases, the DLW length was 10 mm. Although energy gain saturation occurred in the DLW, this was not the case in the full structure. This

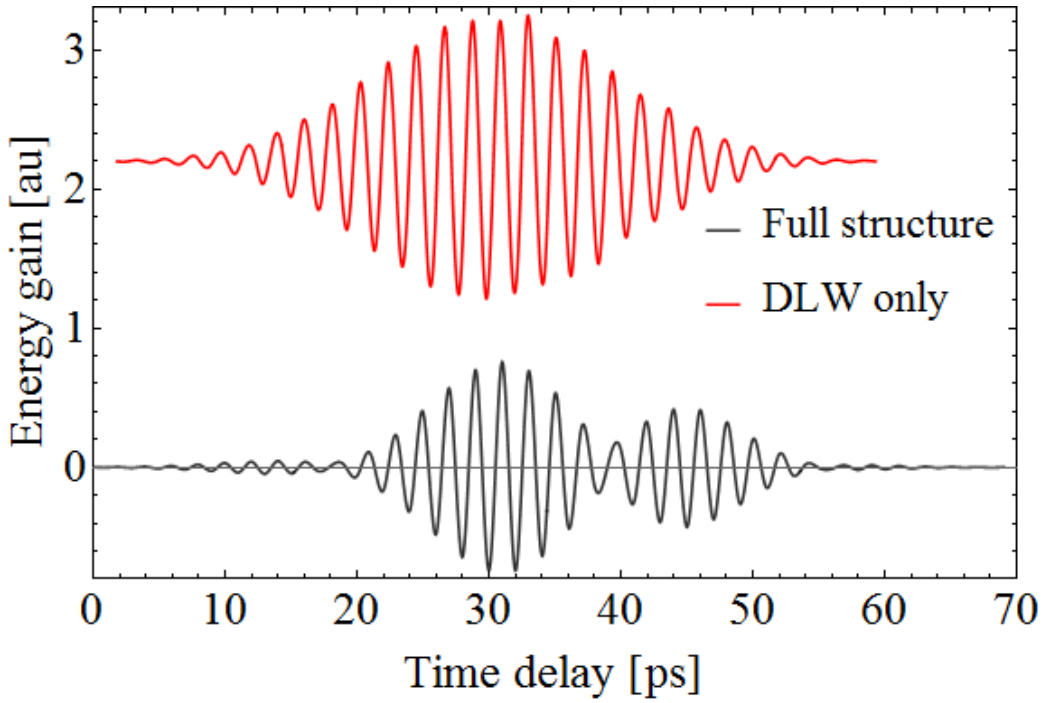

Figure 5.17: Energy gain of an electron propagating on-axis as a function of delay between THz pulse and electron for $\sigma = 0.023$ THz and DLW length 10 mm. The energy gain is normalised to the maximum axial E_z field at the start of the DLW section. The energy gain only through the DLW is also shown for comparison.

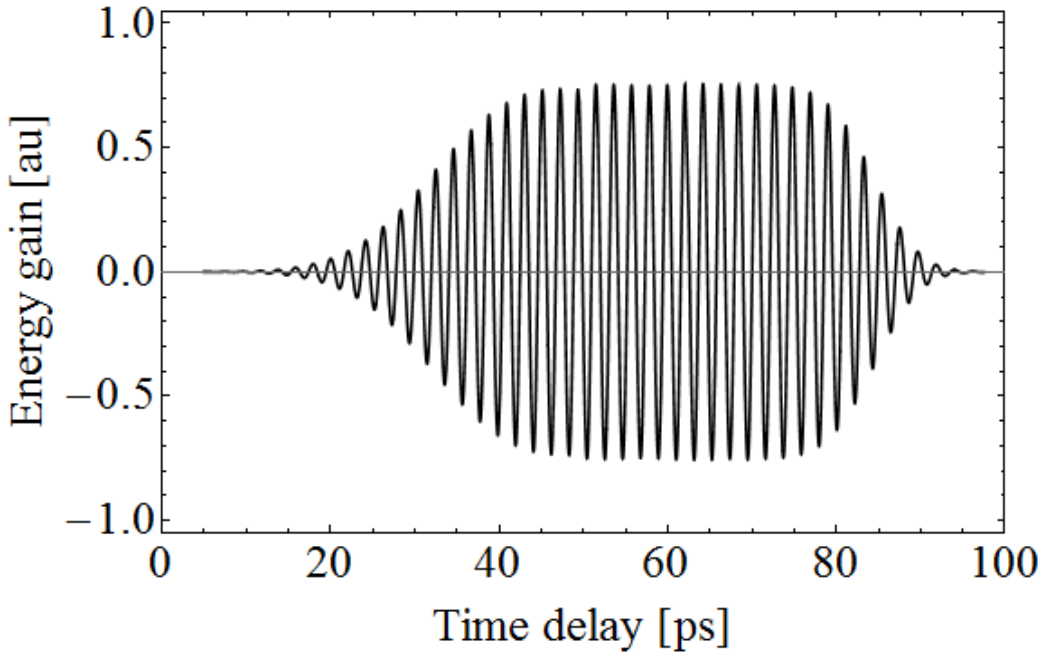

Figure 5.18: Energy gain of an electron propagating through a full structure on-axis as a function of delay between THz pulse and electron, as simulated using CST. The DLW length is 30 mm and $\sigma = 0.023$ THz.

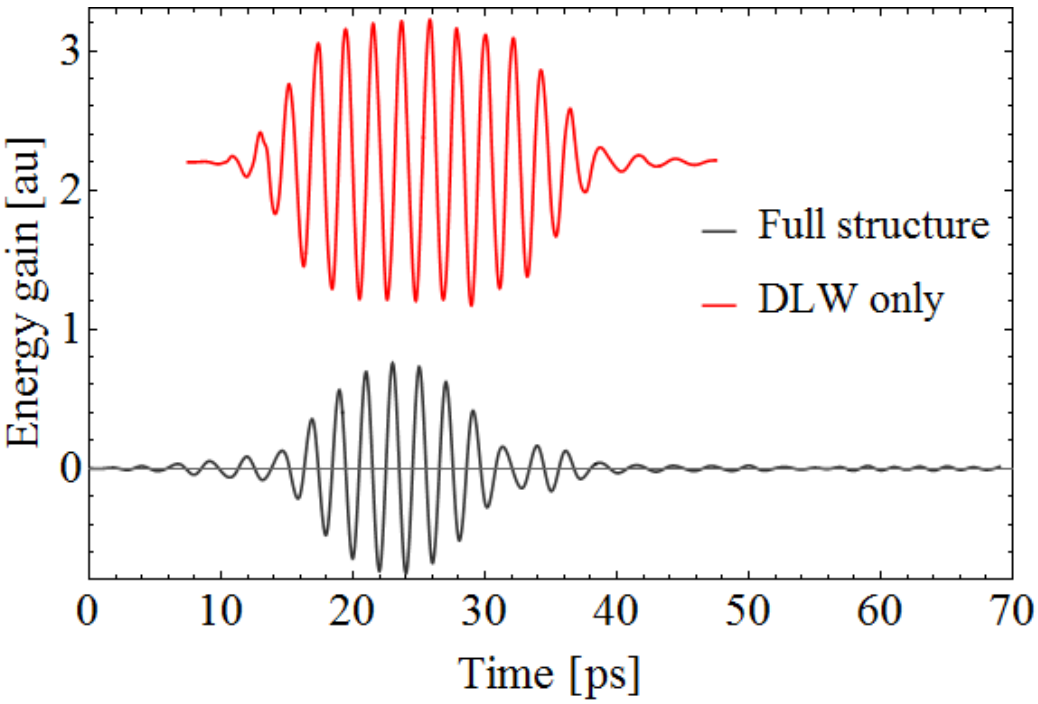

Figure 5.19: Energy gain of an electron propagating on-axis as a function of delay between THz pulse and electron for $\sigma = 0.069$ THz and DLW length 10 mm, as simulated using CST. The energy gain is normalised to the maximum axial E_z field at the start of the DLW section. The energy gain only through the DLW is also shown for comparison.

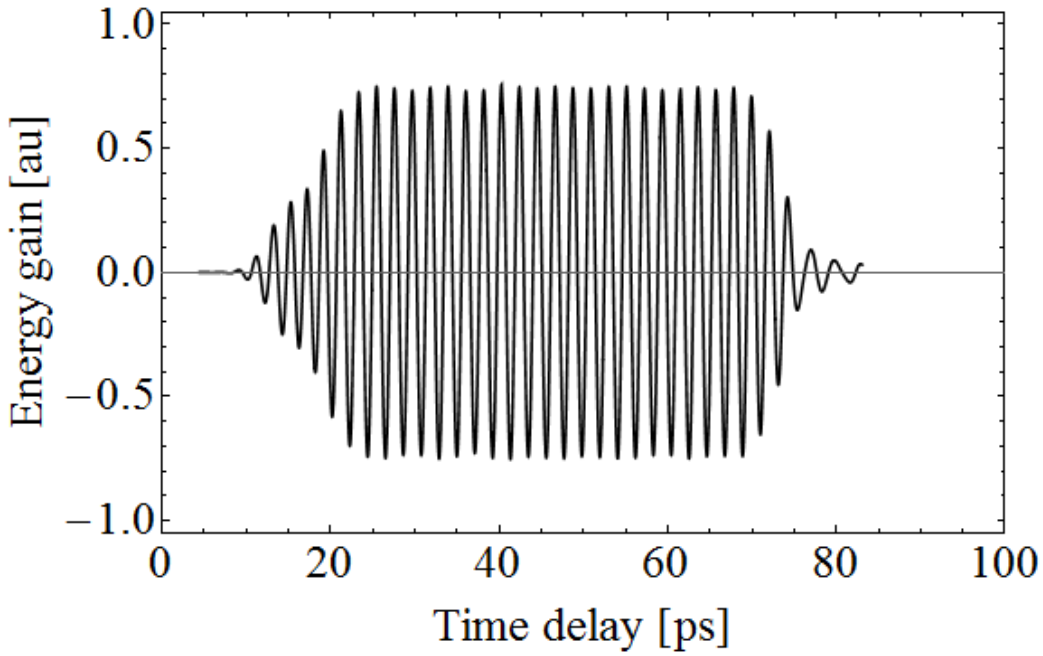

Figure 5.20: Energy gain of an electron propagating through a full structure on-axis as a function of delay between THz pulse and electron. The DLW length is 30 mm and $\sigma = 0.069$ THz.

is likely a result of the pulse broadening due to the coupler. Figure 5.20 shows that energy gain saturates when the length of the DLW was increased to 30 mm.

5.3.3 Conclusion

Measuring the relative energy gain as a function of time delay between and electron and a THz pulse is a useful way of comparing the effect of changes to the THz source and the DLW structure. The form of the energy gain as a function of time is the same when using *Mathematica* and CST, when considering only the DLW. This shows that using the faster, simpler simulation tool is favourable for the longitudinally homogenous DLW structure. The effect of addition of the coupler is clear when considering THz pulse propagation; there is a reduction in the relative maximum energy gain and a 'splitting' of the interaction is observed. However for full structures with a long DLW the final interaction is approximately sinusoidal with a smaller maximum energy gain than for the DLW only. As a result simulations of the DLW are appropriate for use in approximating the final interaction.

Chapter 6

Studies towards a THz-driven experiment

In this chapter parameter optimisation is presented as a means to maximise the figures of merit for the DLW design. The limitations of the figures of merit are discussed with respect to the lack of broadband analysis. This is included to define an overall figure of merit, the integrated voltage, which incorporates the dispersion relation and the choice of pulse shape.

The structure design is defined by the electron energy and the form of interaction required. The accelerating LSM_{11} mode is considered. Optimisation of the structure parameters is performed to maximise the energy gain of such an electron.

A DLW of full length is then simulated. The addition of a coupler to improve transmission from free space into the waveguide is investigated. By simulation of the THz pulse in the time domain (TD) through the entire structure the effect of THz pulse properties on energy modulation is studied both with and without the coupler. This uses particle-in-cell (PIC) simulation in CST. The effect of electron bunch properties on the observable interaction is also investigated.

6.1 Structure parameter optimisation

The effects of the structure parameters, a, w, δ, and ϵ_r, were analysed in turn with respect to the figures of merit discussed in Chapter 4. a is the half distance between the dielectric slabs in the DLW, w is the waveguide width, δ is the dielectric thickness, and ϵ_r is the relative permittivity of the dielectric. Only two parameters were changed at any one time to simplify analysis. The 'base' parameters, used as the fixed values, are shown in Table 6.1. These parameters were chosen for two reasons; 50 μm thick quartz ($\epsilon_r = 3.75$) was readily available and a, w were arbitrary

Table 6.1: Base parameters for the 35 MeV accelerating mode.

Parameters	Value
E [MeV]	35
a [μm]	250
w [μm]	1000
δ [μm]	50
ϵ_r	3.75

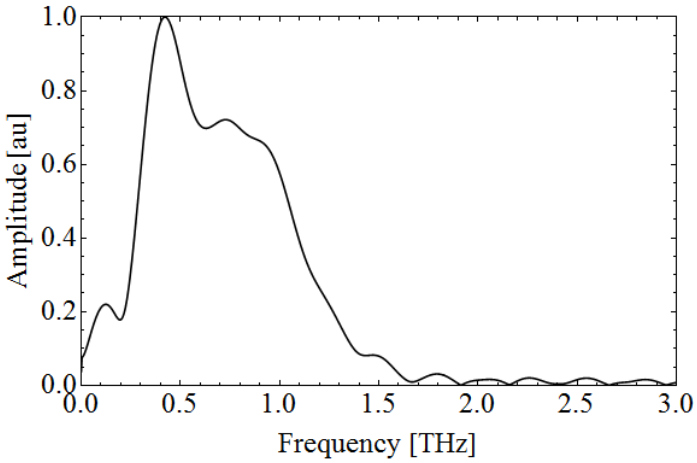

Figure 6.1: Measured data of the spectrum of the single-cycle THz source, originally proposed to be used in experiments.

values which produced an operating frequency close to 0.5 THz, as the peak spectral amplitude is approximately 0.5 THz when using lithium niobate as the non-linear crystal for THz generation [133]. The frequency spectrum of a source already in use for other THz-electron interaction experiments is shown in Figure 6.1. Multiple figures of merit were measured for each setting; the operating frequency, f_{op}, group velocity, v_g, accelerating voltage, V_z, and shunt impedance, r_s. The calculations for V_z and r_s include normalisation of the fields such that each frequency has a stored energy of 1 J Hz^{-1}. Table 6.2 details the figures and their variables. In each case the figure of merit is calculated only at f_{op}. Group velocity is used as a figure of merit, as the aim is to achieve $v_g = v_e$ to maximise interaction length for a given THz pulse. This does not include the effect of GVD, but matching group velocity to reduce slippage is of primary concern. The figures of merit for each set of variables are considered together in order to obtain an estimate of the 'best' parameters to maximise interaction.

Considering each figure in turn, Figure 6.2 shows the effect of a and w. Increasing both variables decreases f_{op}, and increases v_g. However, both V_z and r_s decrease. These figures of merit peak at around $a = 100$ μm, $w = 500$ μm in the plots.

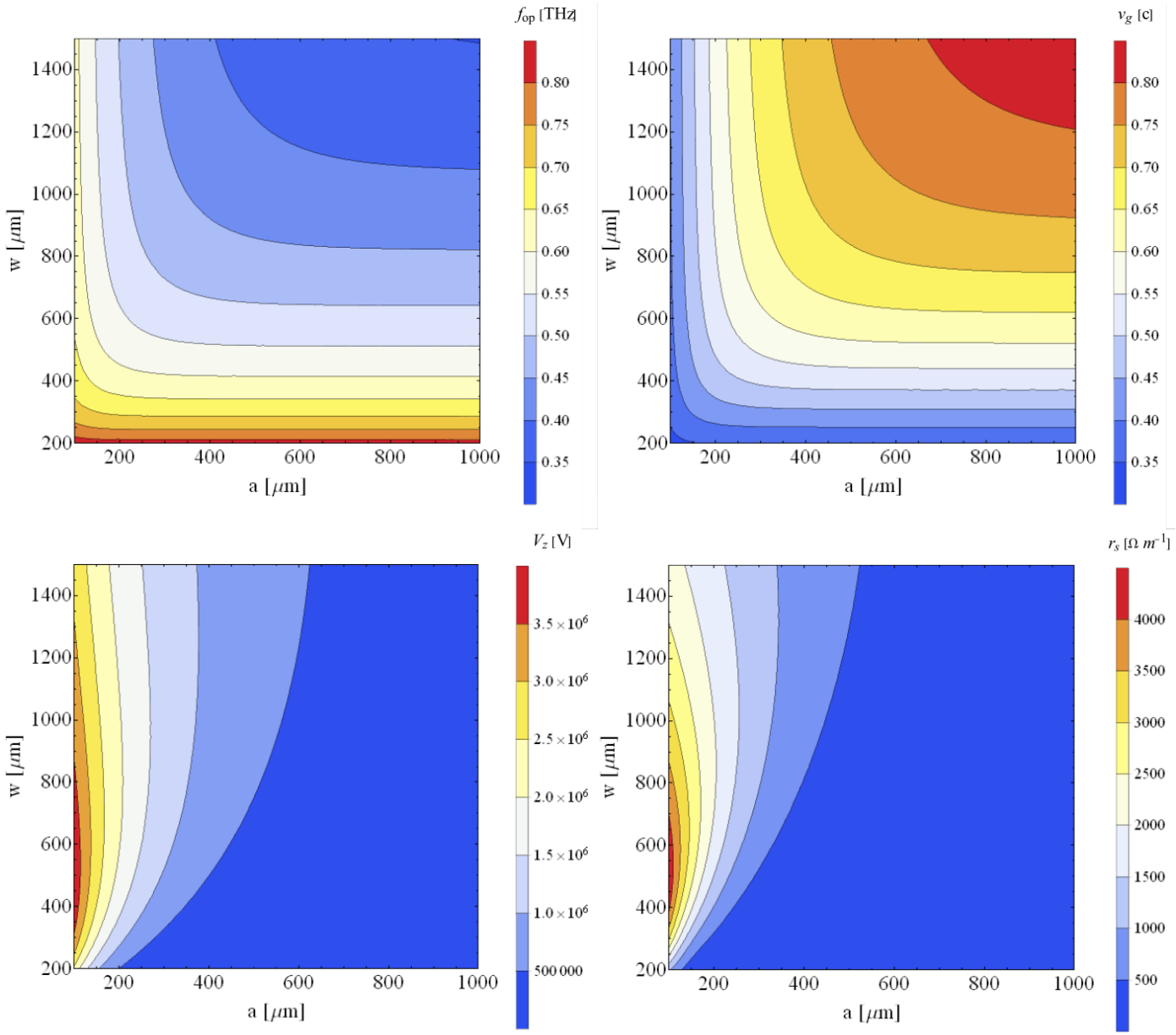

Figure 6.2: Effect of a and w on the figures of merit, for left to right: f_{op}, v_g, V_z, and r_s. Other variables are fixed as in Table 6.1.

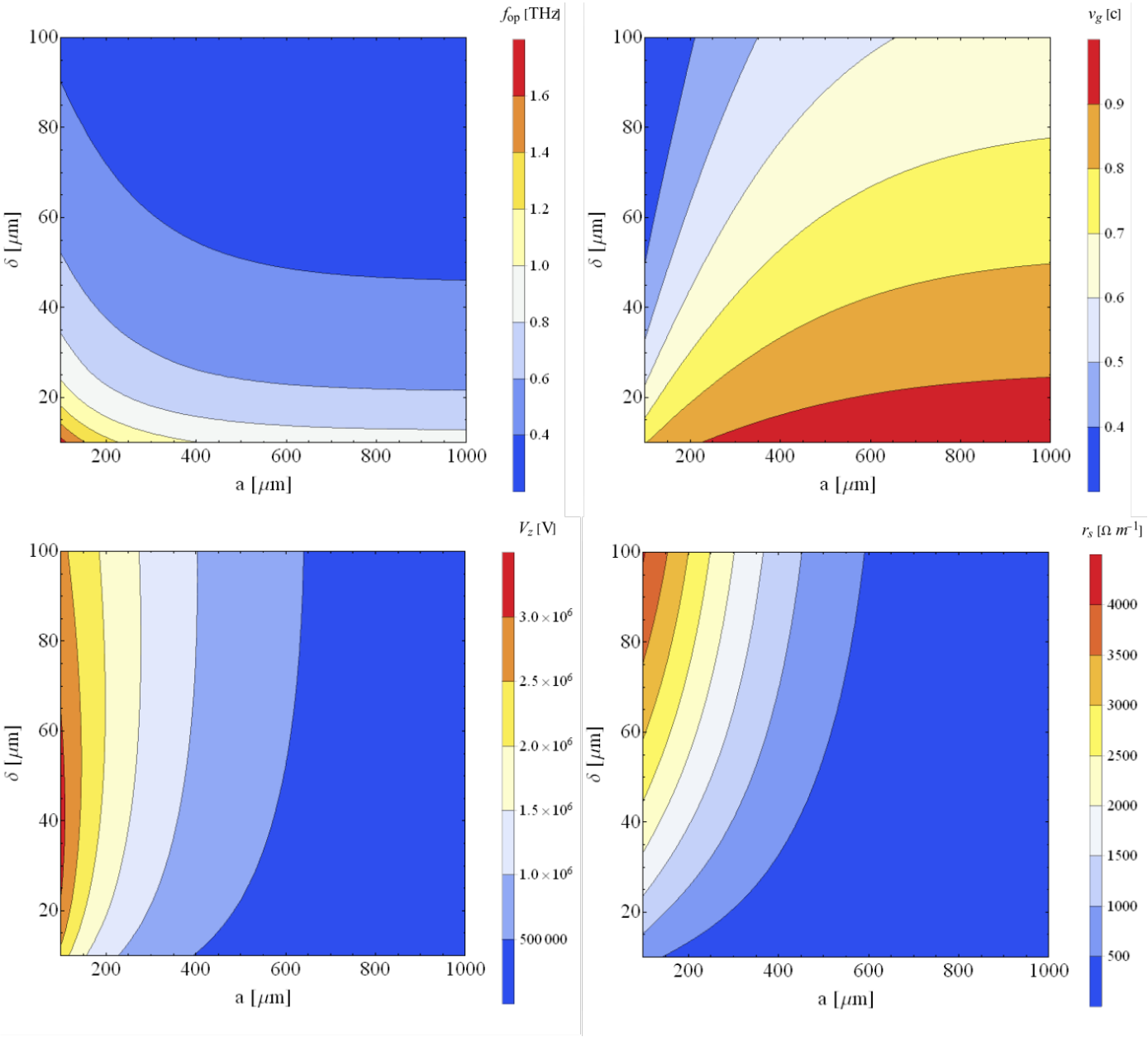

Figure 6.3: Effect of a and δ on the figures of merit, for left to right: f_{op}, v_g, V_z, and r_s. Other variables are fixed as in Table 6.1.

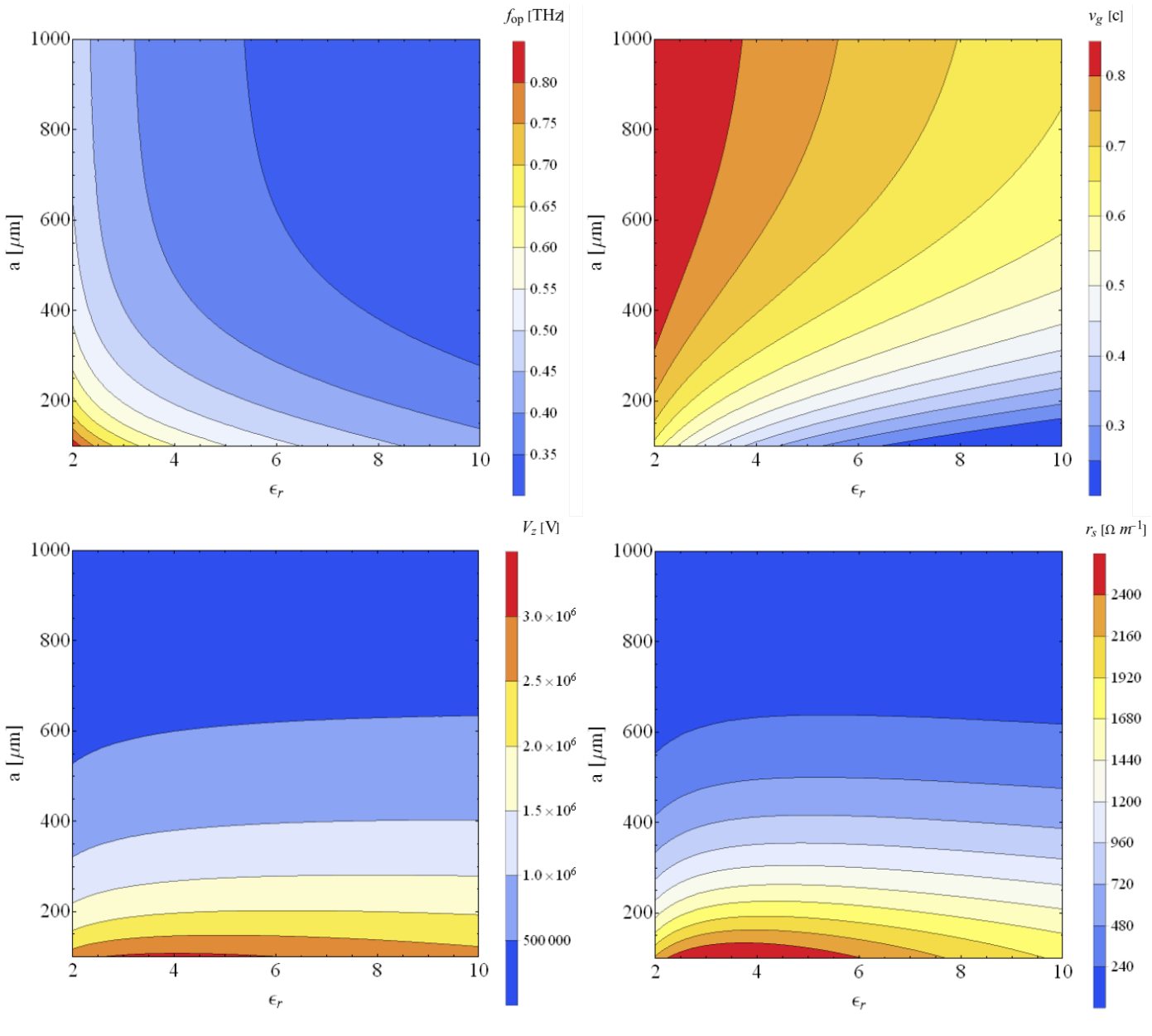

Figure 6.4: Effect of ϵ_r and a on the figures of merit, for left to right: f_{op}, v_g, V, and r_s. Other variables are fixed as in Table 6.1.

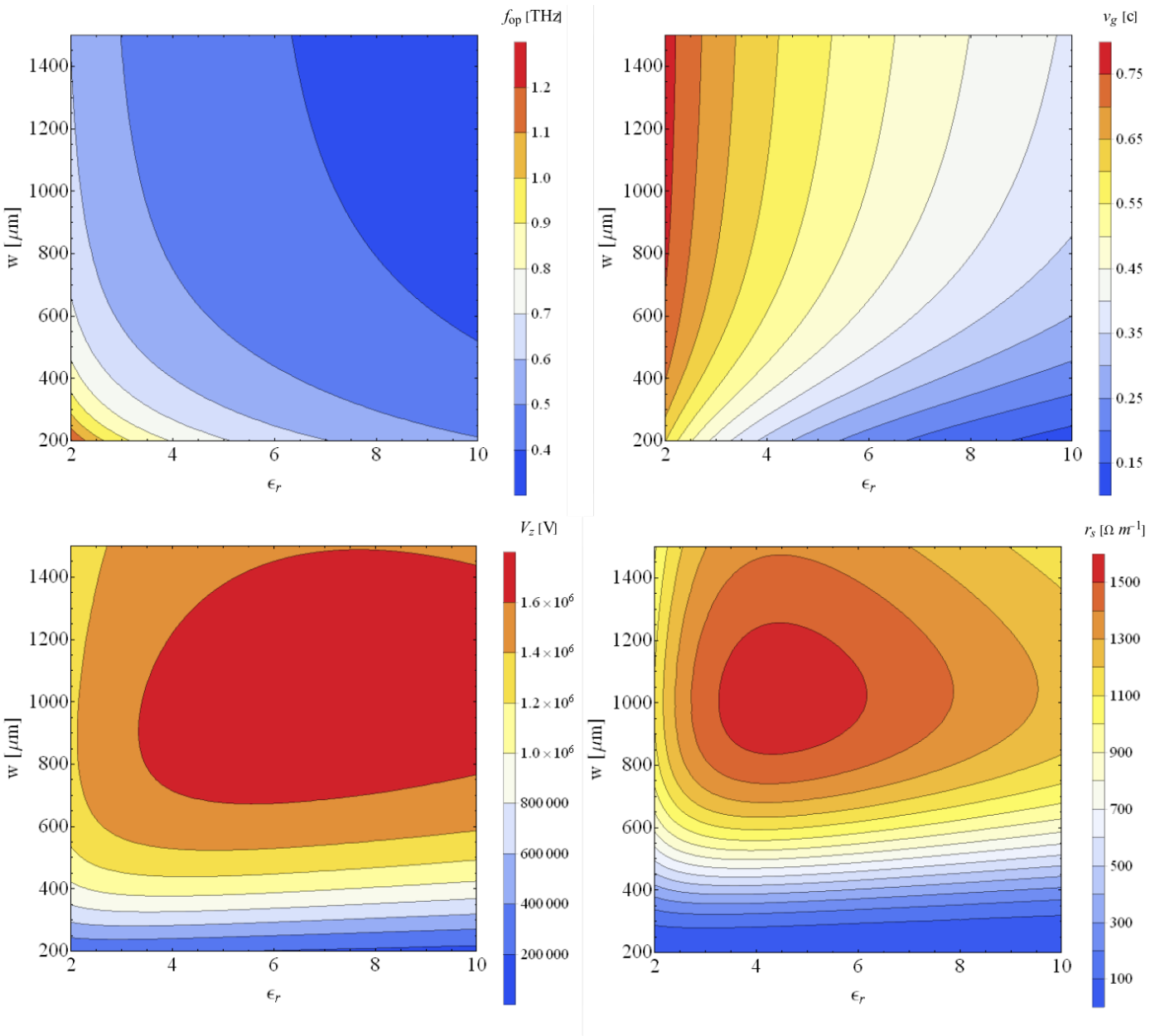

Figure 6.5: Effect of ϵ_r and w on the figures of merit, for left to right: f_{op}, v_g, V, and r_s. Other variables are fixed as in Table 6.1.

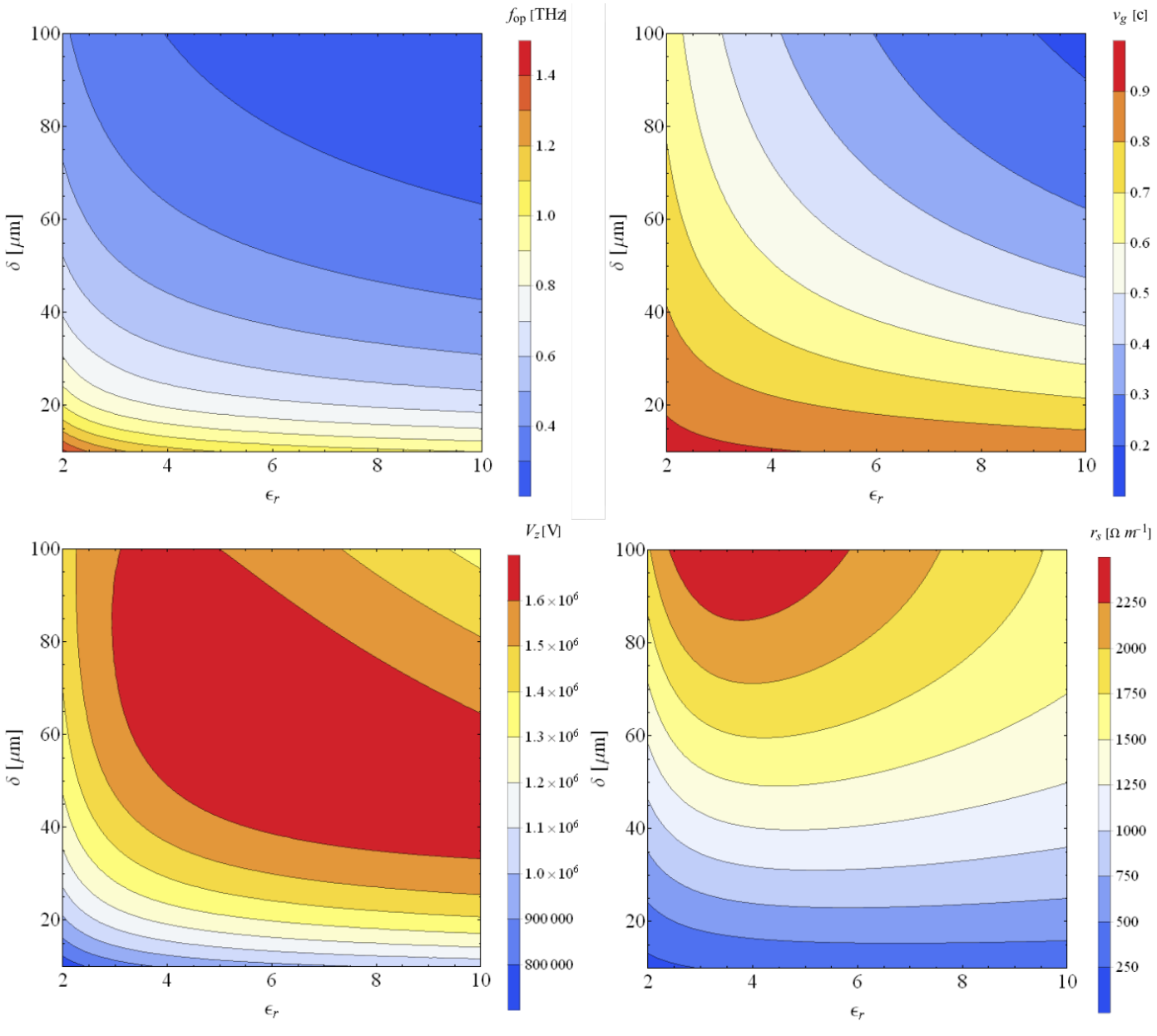

Figure 6.6: Effect of ϵ_r and δ on the figures of merit, for left to right: f_{op}, v_g, V, and r_s. Other variables are fixed as in Table 6.1.

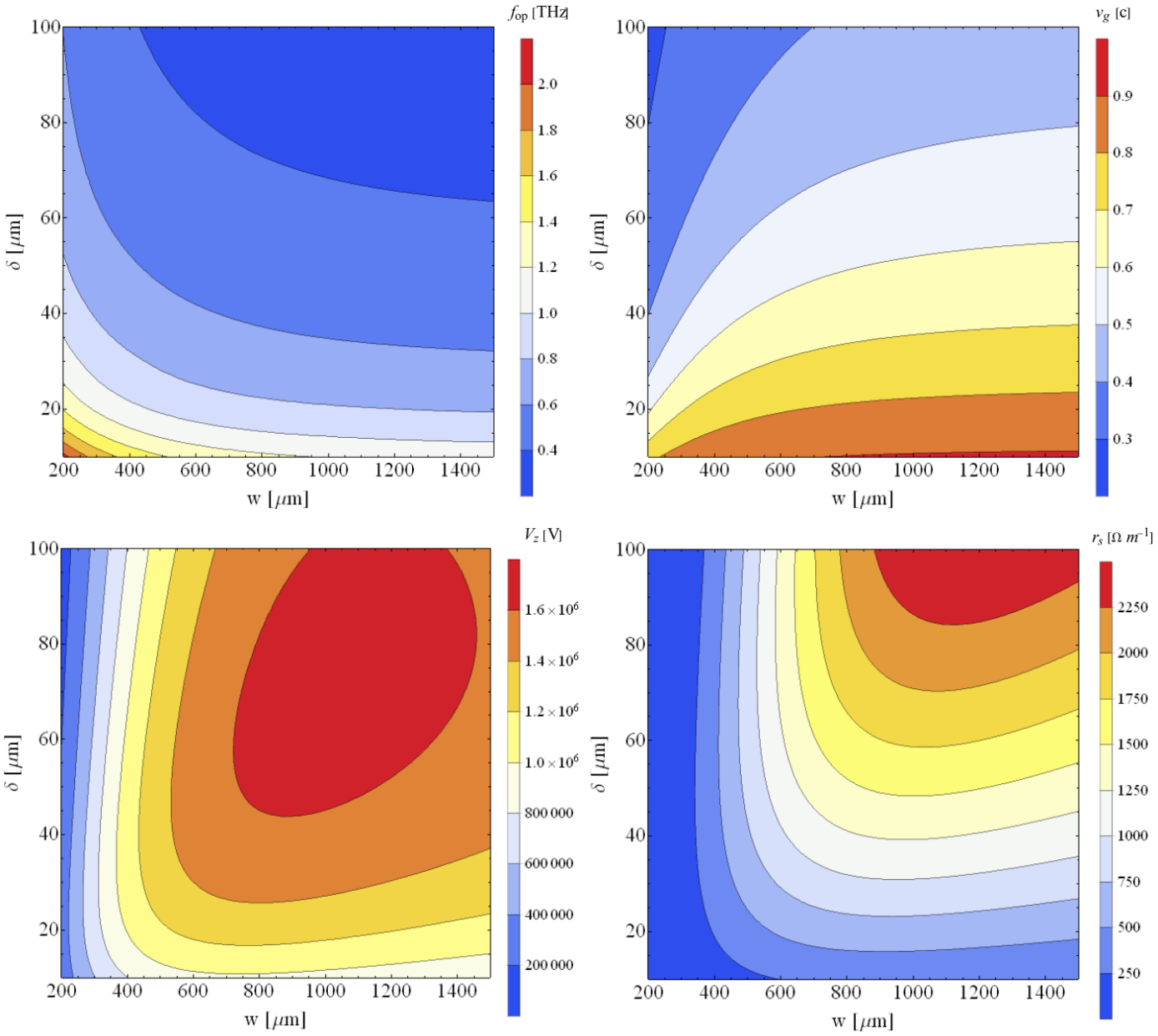

Figure 6.7: Effect of w and δ on the figures of merit, for left to right: f_{op}, v_g, V, and r_s. Other variables are fixed as in Table 6.1.

Table 6.2: Variables corresponding to each figure.

Figure number	x	y
6.2	a	w
6.3	a	δ
6.4	ϵ_r	a
6.5	ϵ_r	w
6.6	ϵ_r	δ
6.7	w	δ

Figure 6.3 shows how a and δ affect the figures of merit. Increase both variables decreases f_{op}. Increasing δ has more of an effect on v_g, which is optimum at small δ and large a. This is because, as dielectric thickness decreases, the waveguide becomes more like a metallic rectangular waveguide, for which $v_p \to c$. V_z and r_s are maximum at $a = 100$ μm in the plots, with V_z maximum at $\delta = 40$ μm and r_s maximum at $\delta = 100$ μm.

The effects of ϵ_r and a are shown in Figure 6.4. f_{op} increases with ϵ_r and a, but v_g is largest for small ϵ_r and large a. Both V_Z and r_s are maximised for small a, with both maximum for $\epsilon_r \approx 4$.

Figure 6.5 shows that f_{op} increases with ϵ_r and w, and v_g is maximum for small ϵ_r and large w. V_z is maximum at $\epsilon_r \approx 8$, $w \approx 1100$ μm, and r_s is maximum at $\epsilon_r \approx 4.5$, $\wedge \approx 1000$ μm. Both are smallest for small values of w.

Figure 6.6 shows the effect of ϵ_r and δ on the figures of merit. f_{op} decreases with increasing ϵ_r and δ, whereas v_g is largest as the two variables tend to zero. V_z peaks at $\epsilon_r \approx 7$, $\delta \approx 60$ μm, but the value is similar over a large range. In the range of the plot, r_s is maximum at $\epsilon_r \approx 4$, $\delta = 100$ μm.

The final plots in Figure 6.7 show the effects of w and δ. f_{op} decreases with increasing w and δ, and v_g is maximum for small δ and large w. V_z peaks at $w \approx 1100$ μm, $\delta \approx 70$ μm. In the range of the plot, r_s is maximum at $w \approx 1200$ μm, $\delta = 100$ μm.

Considering each variable in turn, the effect of increasing a is to decrease f_{op} which is to be expected as, with increasing cross-section, the supported frequencies become lower. v_g increases with increasing a. Both V_z and r_s decrease with increasing a, again to be expected as the axial fields are weaker. Therefore the optimum value for a is unclear; it is dependent on the choice of THz pulse. For a DLW of length 10 mm the required bandwidth for interaction over the entire length of the structure is much lower than that achieved using currently available laser-driven sources (<100 GHz). The effect of increasing w is to decrease f_{op} whilst increasing v_g. There is a maximum

in both V_z and r_s, which occurs at a different value of w dependent on other parameters. Much like with a, choice of THz pulse must be considered, but the compromise between matching v_g and V is not as severe. Increasing ϵ_r and δ have a similar effect to each other; f_{op} and v_g are largest when the two variables are close to zero. There is a maximum in both V_z and r_s, which occurs at different values of ϵ_r and δ dependent on other parameters.

Regarding our preset limitations, $\epsilon_r = 3.75$ and $\delta = 50$ μm, other parameters can also be limited. Only the use of the optimisation in Figure 6.2 was required in this case. One limit is the operating frequency, as it was desirable to use approximately 0.5 THz, corresponding to the peak frequency of the THz source. There is no clear preference considering the individual parameters, as one cannot maximise V_z and r_s without reducing v_g considerably. For continuous interaction over the length of the structure, the aim is to match 'interaction bandwidth', Δf_{int} with the bandwidth of the input pulse. This is achieved by rearranging Equation 4.22, to find the rms bandwidth, σ_0, required for a given DLW length:

$$\sigma_0 = \frac{L\left(\frac{1}{v_g} - \frac{1}{v_e}\right)}{2\sqrt{2x_1}} \ , \tag{6.1}$$

where $x_1 = 4.605$, corresponding to the envelope amplitude at 1% of maximum. This does not include the effect of GVD. For maximum interaction it is desirable for $\Delta f_{int} = \sigma_f = \frac{\sigma_0}{2\pi}$. Considering single-cycle pulses as generated by lithium niobate, $\sigma_f = 0.069$ THz, although a narrowband setup can also be used. For a broadband pulse there is no set of parameters which achieve this bandwidth.

At this point it is therefore sensible to look at the frequency-dependent figures of merit; $V_z(\omega)$ and $r_s(\omega)$, and the integrated values over a given THz pulse bandwidth. This takes into account the effect of decelerating phases within the THz pulse. The transit time factor for a DLW of length 10 mm with parameters as given in Table 6.1 is shown in Figure 6.8. The transit time factor peaks at the matched frequency, and then oscillates on either side. By finding the points at which the transit time factor falls to zero on either side of the maximum, a new definition of bandwidth is obtained. For these parameters, it is calculated that $\Delta f_{int} = 0.024$ THz. The bandwidth given by the transit time factor is 0.048 THz total, or $\sigma_f = 0.016$ THz.

The frequency dependence of the transit time factor is understood by considering the form of $\beta(\omega)$. Figure 6.9 shows the dispersion relation for the DLW, along with first order and second order dispersive terms. Below cut-off frequency, there is no propagating wave and so the transit time factor is also zero. From cut-off up to

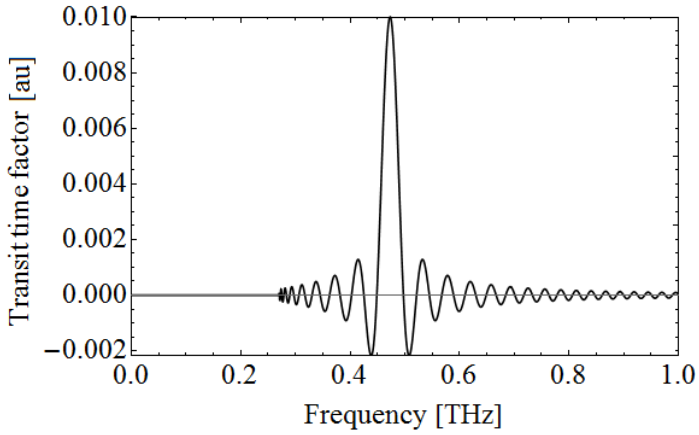

Figure 6.8: The transit time factor as a function of frequency. It is maximum at the matched frequency and oscillates about this point.

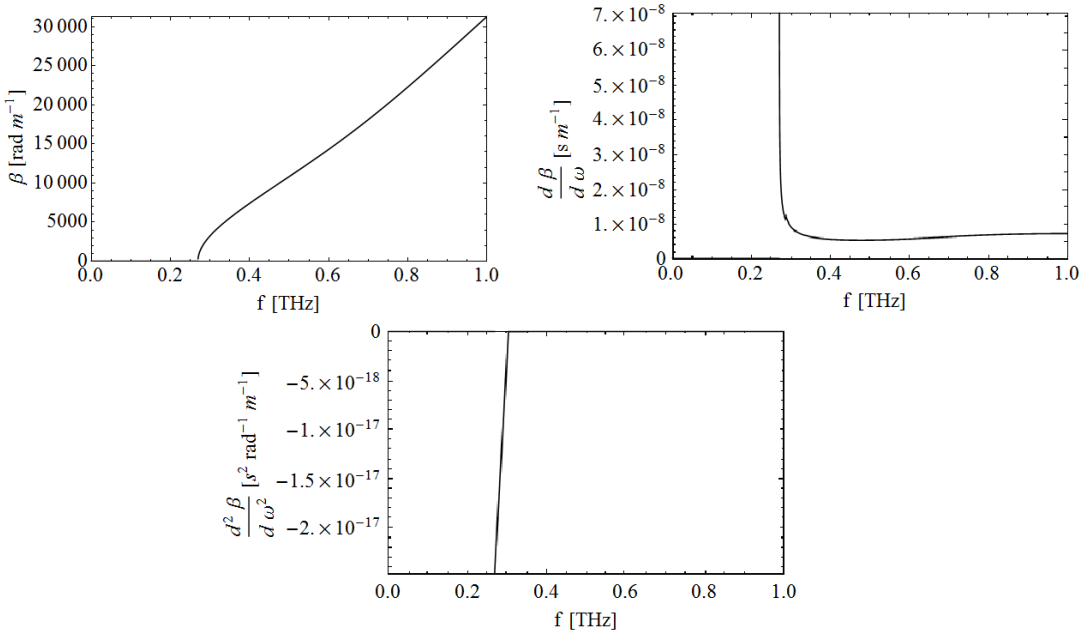

Figure 6.9: L-R: dispersion β, first order dispersion β', second order dispersion β'', each as a function of frequency.

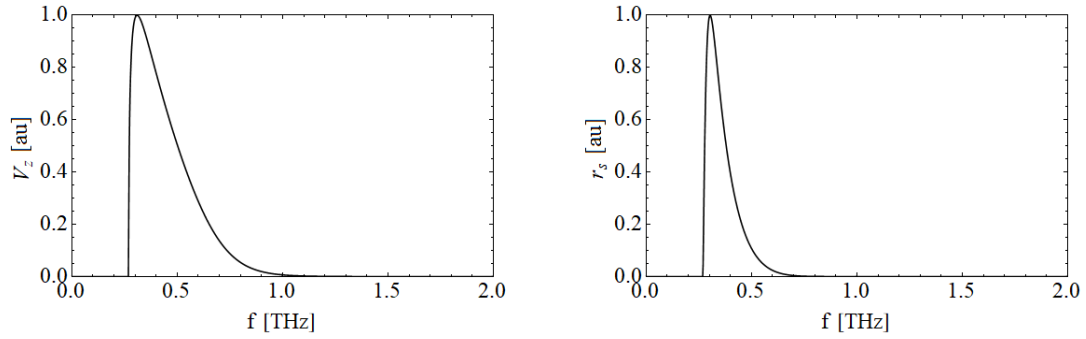

Figure 6.10: Frequency dependence of V_z and r_s.

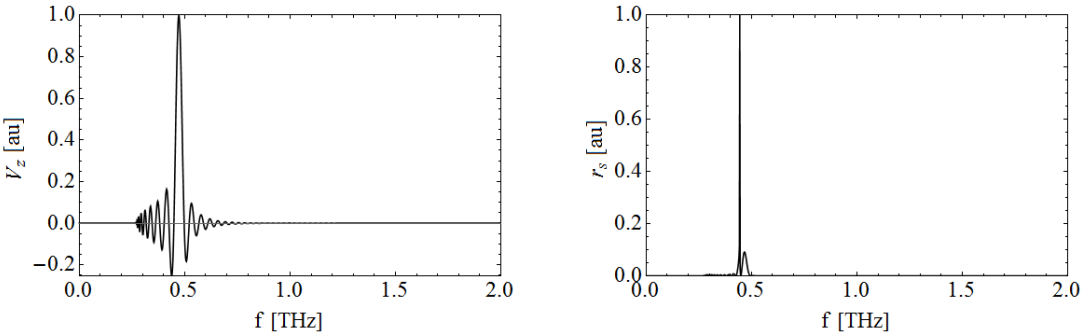

Figure 6.11: Frequency dependence of normalised V_z and r_s, after application of the transit time factor.

the operating frequency β is non-linear, as confirmed by the plot of β'. This is demonstrated in the transit time factor by the decreasing rate of oscillation up to f_{op}. Beyond this, the rate of oscillation increases slightly again before become constant. This results from the non-linear region of β just after f_{op}, which then become linear with increasing f. The form of β'' shows why the two sides of f_{op} differ; it is only significant close to cut-off frequency.

Neglecting for a moment the transit time factor, the fields and corresponding figures of merit still have an associated frequency dependence. Figure 6.10 shows V_z and r_s as a function of frequency. Both peak at approximately 0.3 THz rather than f_{op}. r_s also falls to zero at a faster rate. Although the peak can be found by finding the frequency at which $\frac{\mathrm{d}E_z}{\mathrm{d}\omega} = 0$, in practice this produces a cumbersome equation which must be solved numerically. The plots show that there is a limit to the interacting range of frequencies; as expected there is no V_z or r_s below f_c, but their magnitudes also decrease with increasing frequency.

V_z and r_s are multiplied by the transit time factor in Figure 6.11. The peak of $V_z(\omega)$ is now at f_{op}, and higher frequencies are effectively zero. However this does not

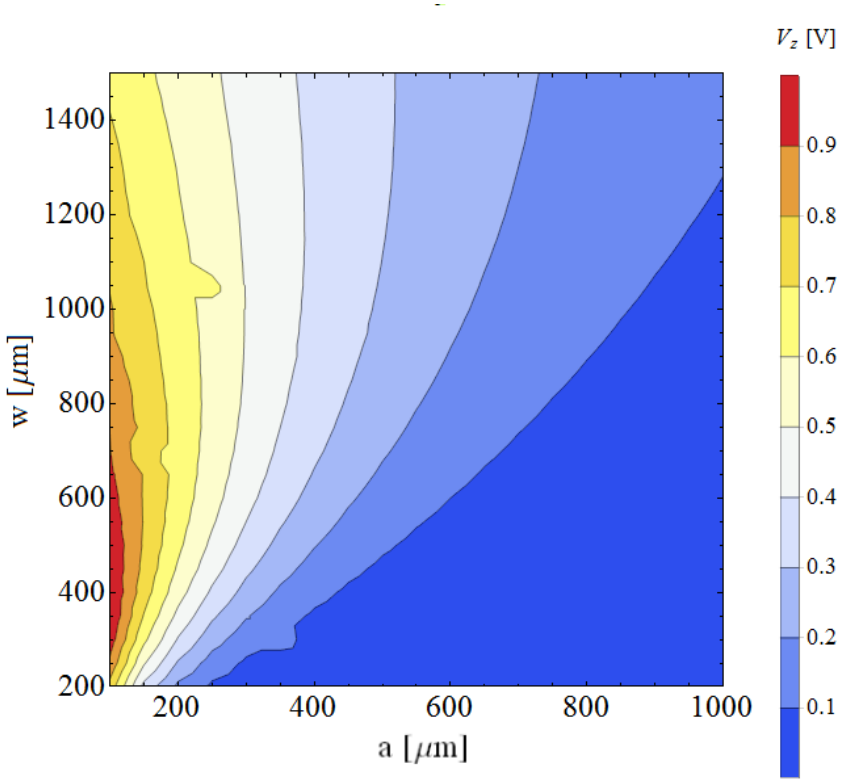

Figure 6.12: Effect of a and w on normalised integrated $V_z(\omega)$ using the modified Gaussian pulse.

provide the full solution as the form of the frequency spectrum has not been taken into account; it is not constant with frequency. To find the total interaction, V_z and r_s are integrated over frequency after being multiplied by the transit time factor and the pulse spectrum. Two forms of THz pulse are considered, giving the integrated voltage as

$$V_{z,int} = \int_{\omega_1}^{\omega_2} V_z(\omega) \exp\left[-\frac{(\omega-\omega_0)^2}{2\sigma^2}\right] \mathrm{d}\omega \ , \tag{6.2}$$

for a Gaussian pulse, and

$$V_{z,int} = \int_{-\infty}^{+\infty} V_z(\omega) \exp\left[-\frac{\omega^2}{\omega_0^2}\right] \mathrm{d}\omega \ , \tag{6.3}$$

for a modified Gaussian (ultrashort) pulse. The V_z calculation from Figure 6.2 is repeated with the modified Gaussian pulse spectrum; this is shown in Figure 6.12. This plot does not reveal an optimum set of parameters; it only suggests that a smaller value of a is ideal. Fixing $\delta = 50$ μm and $\epsilon_r = 3.75$, it is preferable to use a large w and small a as this maximises integrated voltage. The values $a = 250$ μm and

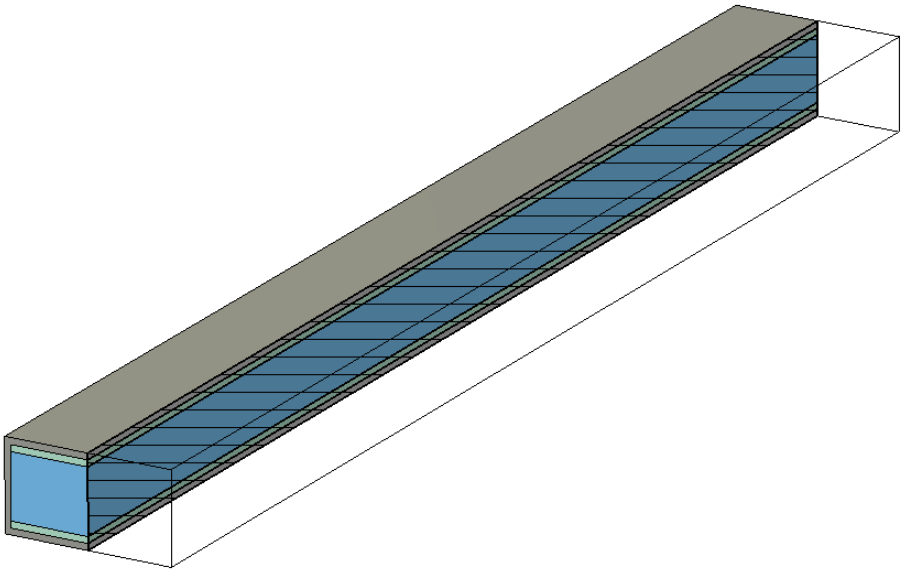

Figure 6.13: CST model of a DLW of length 10 mm. The structure is cut down the middle to show the vacuum (blue) and dielectric (green) components. The structure is enclosed in the transverse planes by a perfect electrical conductor.

$w = 1200$ μm were chosen, which when substituted into the dispersion relation give $f_{op} = 0.472$ THz.

6.2 Pulse propagation studies

The propagation of the pulse through the DLW was modelled both in CST and using Mathematica. In both cases it is assumed that there is no mode conversion inside the waveguide and so only the LSM_{11} mode propagates. A range of input THz pulses were used; $\sigma_f = 0.023$ THz, $\sigma_f = 0.069$ THz (single-cycle), and a modified Gaussian (ultrashort). The single cycle and ultrashort pulses include frequencies below the cut-off frequency of the DLW. Pulse propagation was demonstrated in Chapter 5 for the optimised DLW design, with a focus on the effect of solver settings. The 'correct' settings are used as standard throughout this chapter. The CST model is shown in Figure 6.13, which uses the optimised parameters and a DLW length of 10 mm. The pulse propagation in the DLW is shown in Figures 5.3, 5.5, and 5.6 using Mathematica, and Figures 5.7, 5.11 using CST.

6.3 Coupler design

The coupler is simplified by only considering a rectangular horn design, as discussed in Chaper 4. Any added complexities result in further manufacturing time and increase the potential for errors. The coupler optimisation process itself was straightforward; the THz source was fixed to be a transverse circular Gaussian, which

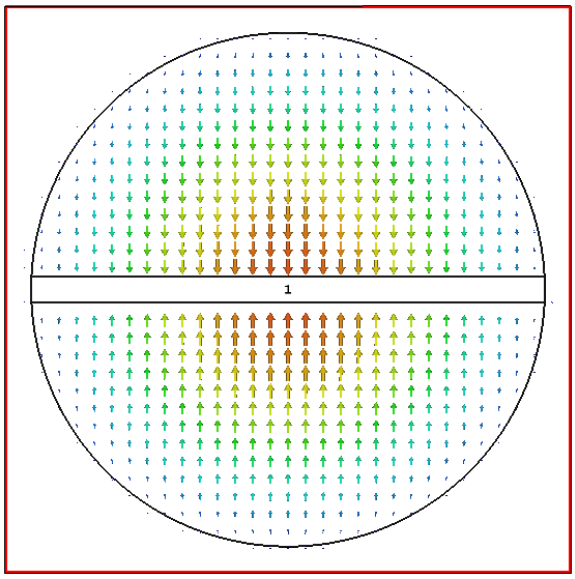

Figure 6.14: Approximation of the transverse profile of the THz source using a single port mode. A circle of dielectric surrounded by vacuum is split by a metal rectangle.

could be focussed into the horn. Therefore the input aperture was square to maximise THz collection. The length of the coupler was then varied to maximise transmission into the LSM_{11} mode over a wide bandwidth. Only CST was used for this process due to its efficiency in handling large simulation domains with multiple modes.

Modelling only the horn neglects the other parts of the coupling system. The THz source was not a standard mode, and so had to be generated artificially in CST. Furthermore, the horn collected the THz in the longitudinal direction, whereas it had to be generated transverse to electron propagation. This was addressed with the use of a mirror with a small aperture, which was also modelled to investigate any associated diffraction effects.

6.3.1 THz source

It was assumed that the transverse profile of the THz source was Gaussian and circular and that the top and bottom halves were symmetric about the transverse axes, based on discussions with the THz group and on the profile obtained by Cliffe *et al* [89]. This is not a standard port mode and therefore modelling in CST required a custom definition. A thin dielectric cylinder with a rectangular metallic insert along the centre, produced the desired mode, as shown in Figure 6.14. There is no longitudinal field component in the centre; it is instead generated as the THz pulse starts to propagate. Any real source will also have a finite gap between the two components. For example, a source setup similar to [89] uses two crystals stacked on top of each other; the gap is non-zero as a result.

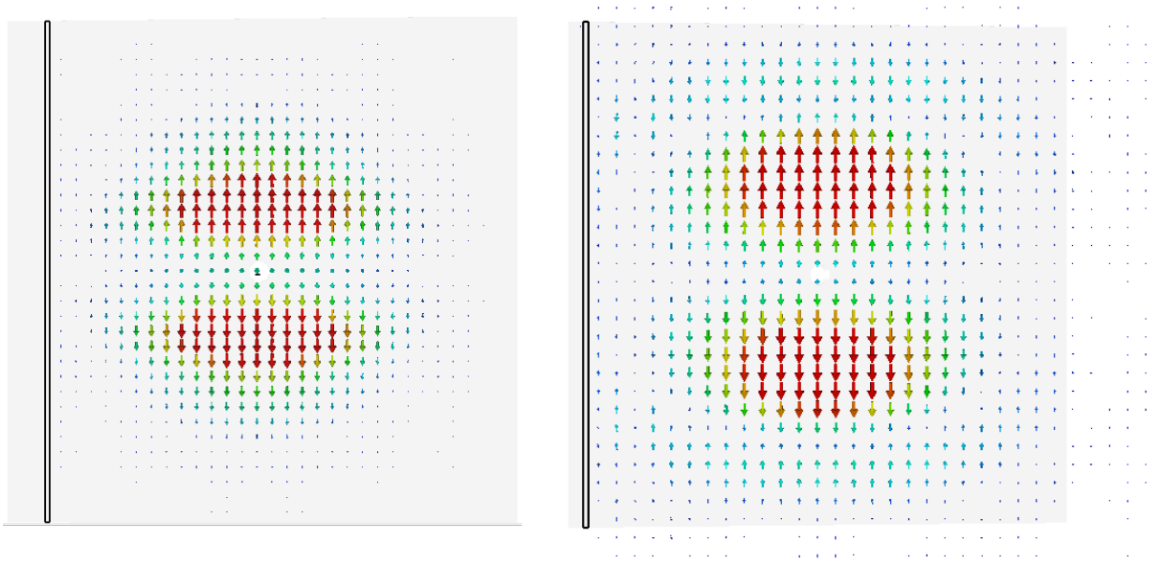

Figure 6.15: Left: THz field after propagating a short distance from the port. Right: THz field after reflecting from the 45° mirror. The ring around the main pulse is an effect of pulse propagation, not the mirror.

The mirror with aperture was also modelled in CST; a circular aperture in the centre of the mirror was required to allow for electron propagation. This was set to be 400 μm diameter so as to allow electrons through the DLW channel without passing directly next to the walls. The effect of the mirror is shown in Figure 6.15. A circular source with radius 5 mm was used in this simulation. There was no observed diffraction from the aperture in the mirror that was visible after the pulse had fully reflected off the mirror. The pulse is unchanged, except for the addition of a ring around the main pulse. It is not clear if this is a result of the simulation or a real effect.

6.3.2 Horn

The choice of THz source evolved whilst the coupler design was being performed. Initially the source was a square crystal of area 4 inch×4 inch (101.6 mm × 101.6 mm). This is oversized compared to the structure, which makes simulation computationally intensive as the large simulation area results in an unreasonably high mesh. Using 10 *cpw* a cross-sectional mesh of approximately 3 million cells is generated, corresponding to billions of cells once length is taken into account. The crystal face was later decreased to an area of 10 mm× 10 mm, illuminated by a laser with a transverse profile of 5 mm radius. This area was still large compared to the waveguide aperture. It was decided to scale down the horn entrance aperture to a square of area 3.175 mm × 3.175 mm. Discussions with the THz source group confirmed that focussing to a

beam waist smaller than this was possible, and so the THz would continue focussing down the horn.

The coupler was modelled assuming a collimated THz pulse due to limitations within CST. It is common in parallel plate waveguides (PPWGs) to use a focussed THz beam and place the PPWG at the beam waist [108, 113, 112], although the situation differs as confinement is in one transverse dimension and the mode of interest is TEM. It was decided to follow the procedure detailed in [134], which details the coupler design used for the acceleration of 60 keV electrons [12]. Discussion with manufacturers revealed some limitations; tapering the thickness of the dielectric is difficult, extending dielectric into the horn is only possible for short lengths, and a linear taper reduces uncertainties in the manufactured structure.

With horn apertures fixed, the only variable was length. A sequential change was performed, starting with a 10 mm long horn and adding 5 mm up to 25 mm. As the opening aperture is square and the DLW aperture is rectangular, the opening angle is different in each transverse dimension;

$$\theta_1 = \arctan\left[\frac{w_c - w}{2L_c}\right] , \tag{6.4}$$

$$\theta_2 = \arctan\left[\frac{w_c - 2(a+\delta)}{2L_c}\right] , \tag{6.5}$$

where the dimensions are shown in Figure 6.16. The horn simulations were performed without the inclusion of the mirror; instead the port was located directly in front of the horn. This allowed for faster simulations and earlier studies had showed that, for a mirror with 100% reflectivity, there was little change in the THz pulse.

Pulse propagation through the horn and a short section of DLW was performed using CST Time Domain Solver. The solver time was set such that the main pulse propagated through the longest simulated structure. This meant that steady state was not achieved in any case, and so the transmission parameter s_{21} was not a steady state quantity. The time range of the simulation was finite, and so there was a maximum time after which the simulation stopped; this led to a windowing of the signals. A further window was applied after individual simulations to only consider the main pulse. This is the windowed transmission parameter, $s_{21,w}$. A rectangular window was used to avoid losses in transmission. For long horns this did not cause any deleterious effects as reflections were well separated from each other. However, for short horns, where reflections propagated within the main pulse, the reflections were not removed by the rectangular window. The signals in the time domain for a

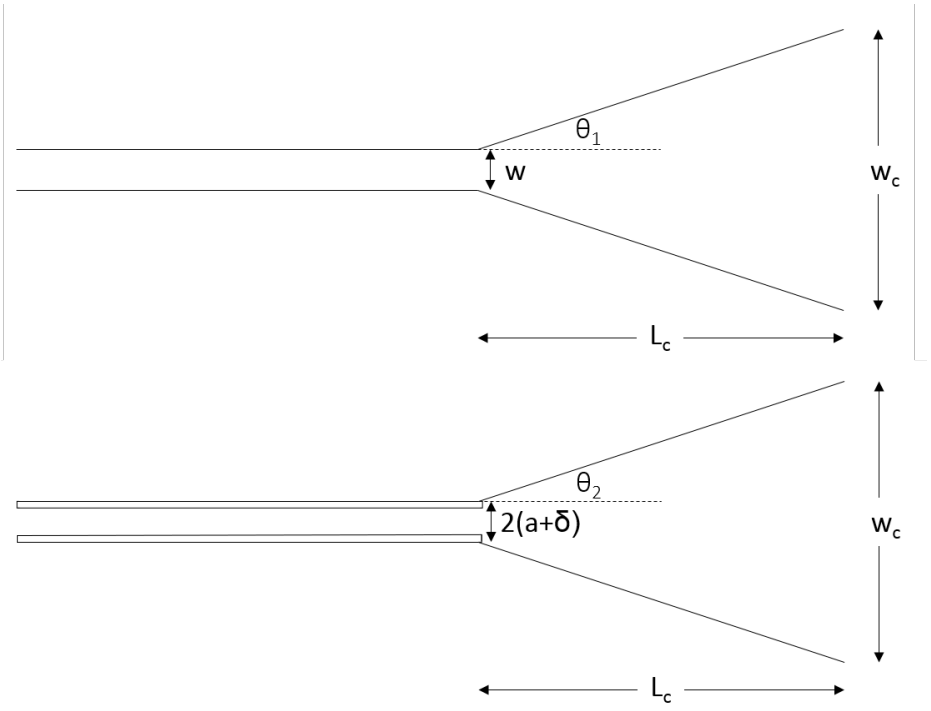

Figure 6.16: Side views of the DLW and coupler with dimensions.

selection of coupler lengths are shown in Figure 6.17. The pulse is broadened more for longer horns, but reflections are no visible. For a short coupler, for example the 5 mm horn, reflections are visible within the tail of the pulse. The windowing was performed over the time periods shown in the figures. The effect of horn length on the transmission parameter $s_{21,w}$ is shown over a wide frequency range in Figure 6.18, with ringing visible for horns of length 5 mm and 10 mm, as the pulse had not decayed to zero by the end of the simulation.

A short horn is generally less effective; however, simply increasing the horn length does not increase transmission. There are two regions of interest. Firstly, up to approximately 0.6 THz the transmission stays constant when horn length is changed (beyond 10 mm). Beyond this, transmission varies greatly with frequency. The low transmission is due to the mismatch in field configuration between the input mode and the LSM mode. Focussing on the 20-25 mm range in Figure 6.19,the effect of changing by 1 mm is significant for broadband pulses; the transmission shifts in frequency. $s_{21,w}$ is smoothest for a coupler of length 23 mm.

For narrowband pulses, centred on $f = 0.5$ THz, there is little change in $s_{21,w}$ between 0.35 THz and 0.65 THz. The position of the small dips in transmission shifts with horn length. For this reason, a 23 mm horn was chosen to correspond to a small peak lying on 0.5 THz. Around this region approximately 30% transmission to the

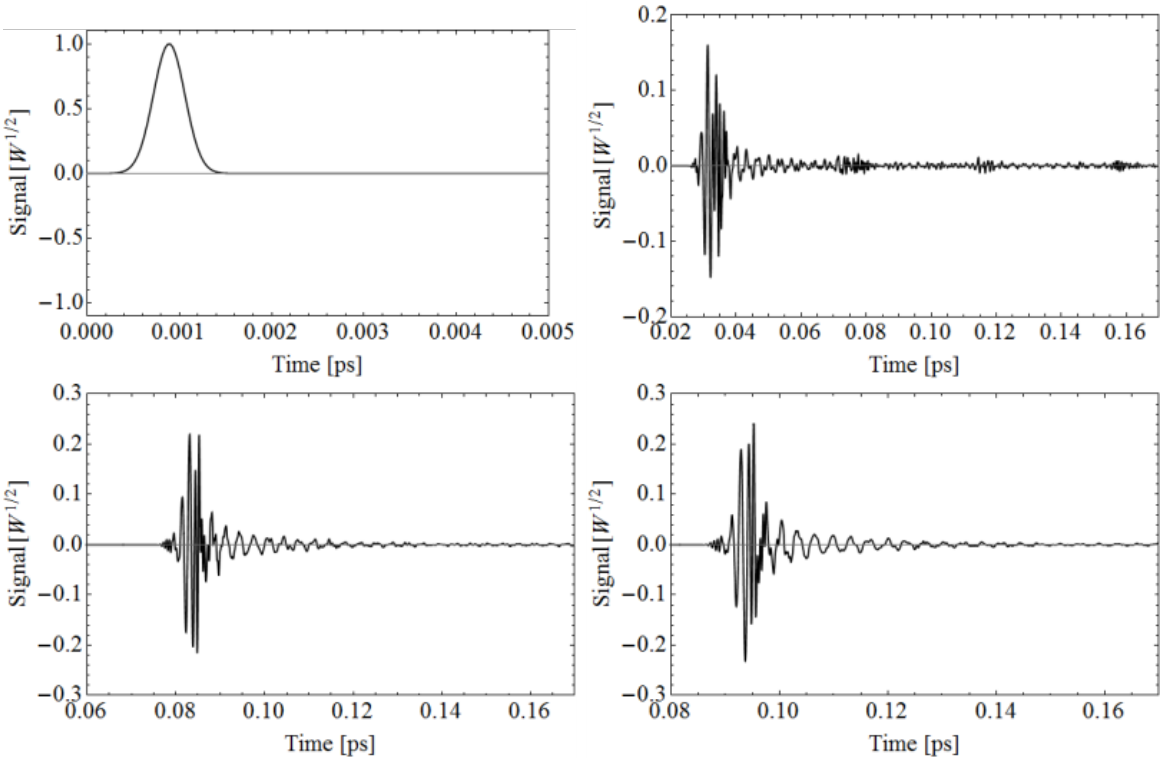

Figure 6.17: Signals from time domain simulations, used to calculate $s_{21,w}$. From left to right, top to bottom: input signal used in each case, signal after propagating through 5 mm horn, 20 mm horn, and 23 mm horn.

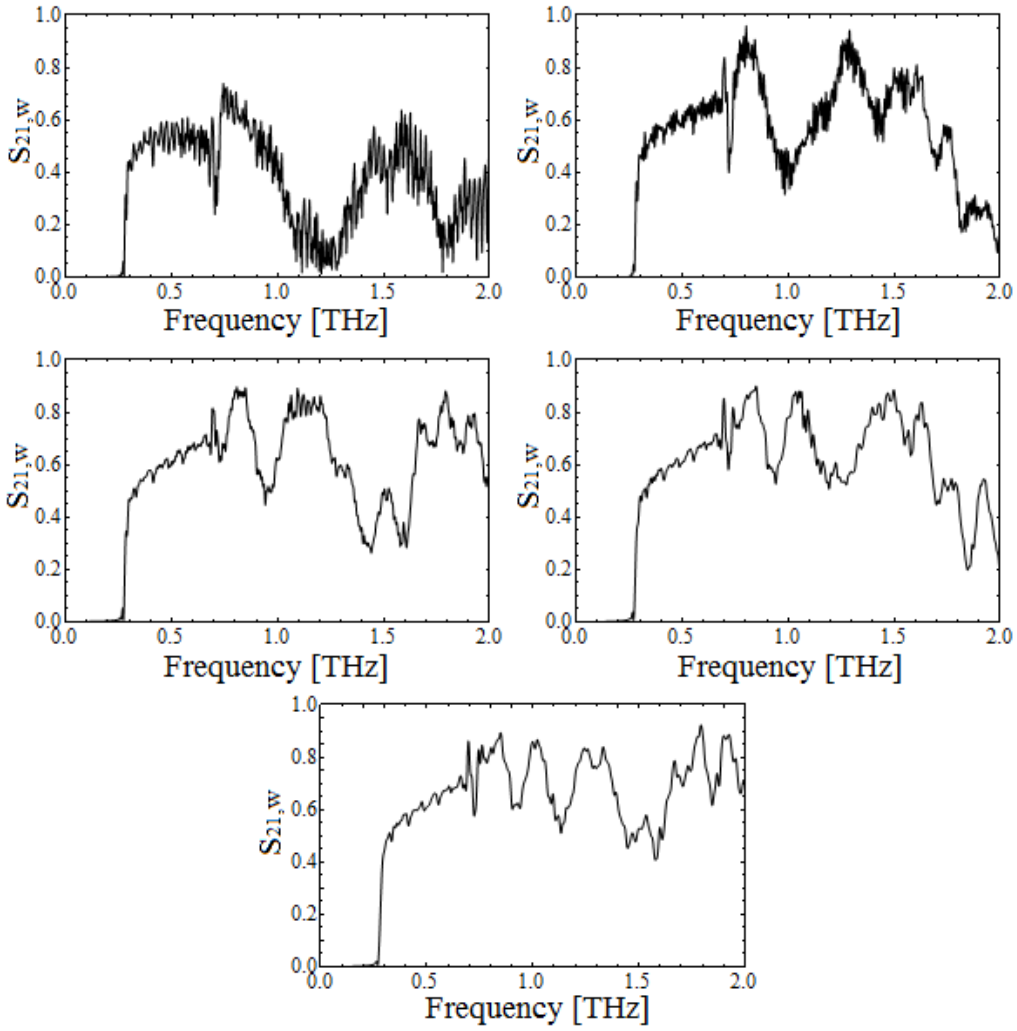

Figure 6.18: Scattering parameter $s_{21,w}$ for varying horn length. From left to right, top to bottom: 5 mm, 10 mm, 15 mm, 20 mm, 25 mm.

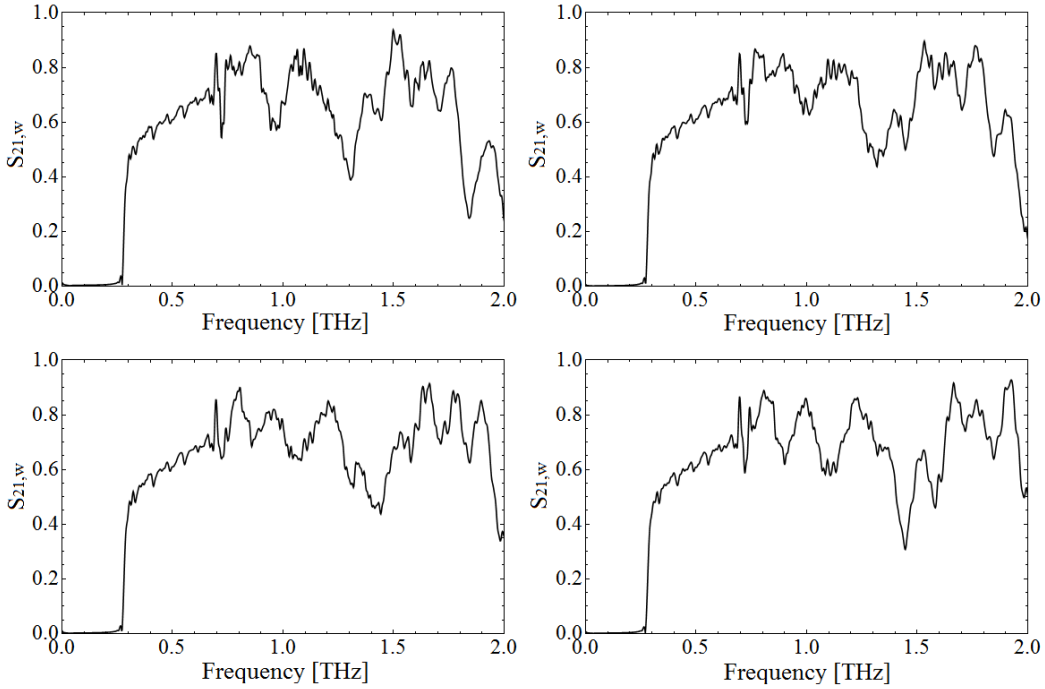

Figure 6.19: Scattering parameter $s_{21,w}$ for varying horn length. From left to right, top to bottom: 21 mm, 22 mm, 23 mm, 24 mm.

LSM_{11} mode was expected.

6.3.3 Pulse propagation

A time domain simulation of the full structure was performed using the chosen coupler design. This was simulated in CST for THz pulses with $\sigma_f = 0.023$ THz and $\sigma_f = 0.069$ THz, as shown in Figure 5.12 and 5.14 respectively. The coupler dispersed the pulse and there was generation of higher order modes in both cases.

6.4 THz-electron interaction

The electron energy gain as a function of delay time was discussed in Chapter 5. Figures 5.15 and 5.16 show the normalised energy gain for a THz pulse with $\sigma_f = 0.023$ THz and $\sigma_f = 0.069$ THz respectively, as calculated using *Mathematica* for the DLW with no coupler. The same simulation in CST produced near identical results. The coupler was added and the same THz pulses used again in CST, with normalised energy gain shown in Figure 5.17 and 5.19. In this chapter the effect of bandwidth on final energy gain is now considered and so the normalisation is removed.

For an input THz pulse of bandwidth $\sigma_f = 0.023$ THz, with longitudinal field amplitude 1 MV/m at the start of the coupler, the field component was enhanced to 7.88 MV/m in the DLW. The resulting energy gain was 75.4 keV. To calculate the accelerating gradient a single electron was tracked along the DLW and the energy

gain as a function of distance was measured. The accelerating gradient is therefore the final energy gain divided by the interaction length. A simpler method is to divide final energy gain by the length of the DLW, giving an average accelerating gradient of 2.51 MV/m. However this is an underestimate as the DLW was deliberately longer than the interaction length so as to maximise the range of the time delay. An electron passes through the THz pulse completely, ending interaction after 15 mm, and so the accelerating gradient over interaction length was 5.02 MV/m.

For $\sigma_f = 0.069$ THz, starting again with 1 MV/m longitudinal field amplitude at the start of the coupler, the field component was enhanced to 7.64 MV/m in the DLW. The energy gain was 27.1 keV. The final accelerating gradient for the full structure was 0.90 MV/m. The full interaction length was 8.1 mm and so the accelerating gradient over this length was 3.33 MV/m.

The effect of variation of the form of the input THz pulse was also simulated to investigate how this affected the observed energy gain. Both bandwidth and centre frequency were varied. A quasi-infinitely long electron beam, with zero radius and zero emittance was used. The energy gain after propagating through a 30 mm DLW with no coupler was used. The effect of different centre frequency for $\sigma_f = 0.023$ THz, $\sigma_f = 0.069$ THz, and a modified Gaussian was then investigated. The energy of the input THz pulse was the same in each case.

6.4.1 Effect of bandwidth

Figure 6.20 shows the maximum energy gain as a function of bandwidth of the input THz pulse. The energy gain is larger for smaller bandwidths except for $\sigma_f =$ 0.01 THz. This is because the interaction length is longer than the length of the structure and so maximum energy gain has not been achieved.

6.4.2 Effect of centre frequency of THz pulse

It was expected that the centre frequency of the THz pulse would not be exactly at f_{op}. To provide a direct comparison it was assumed that the energy of the pulse was the same in each case, and so the energy gain is normalised to the maximum when using $\sigma_f = 0.023$ THz. The effect of THz pulse frequency on maximum energy change is shown in Figure 6.21 for $\sigma_f = 0.023$ THz and Figure 6.22 for $\sigma_f = 0.069$ THz. A modified Gaussian can also be used, the effect of which is shown in Figure 6.23. In each case the final energy gain was calculated using *Mathematica*.

Maximum interaction occurs when the operating frequency and THz centre frequency are the same. The effect of changing centre frequency is more pronounced for a narrowband pulse; for the modified Gaussian pulse the variation of centre frequency does not result in large changes in energy gain.

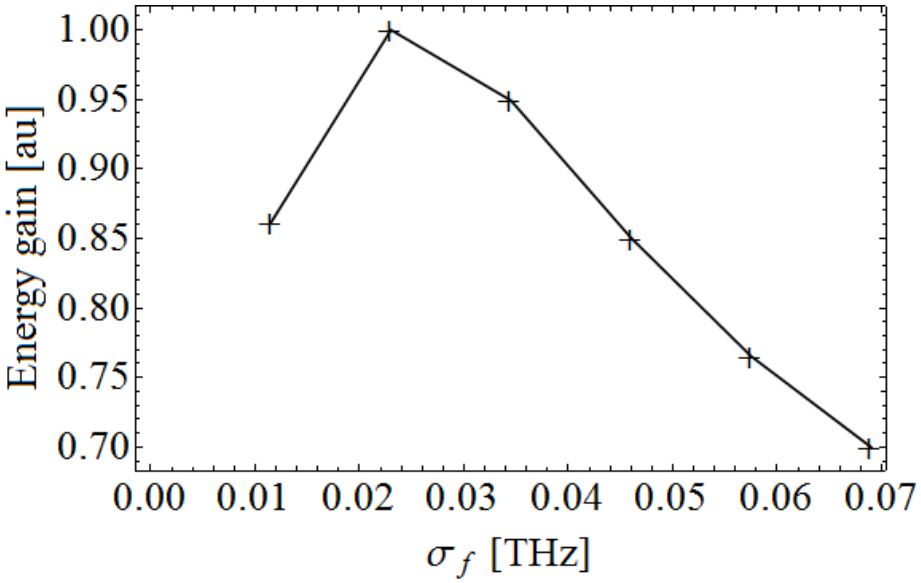

Figure 6.20: Effect of bandwidth on THz-electron interaction through a 10 mm DLW, with no coupler included in the simulation. The energy of the THz pulse is the same in each case.

6.4.3 Addition of the coupler

Within CST it was possible to analyse how the coupler affected THz-electron interaction. It was assumed that broadband pulses would disperse more before entering the DLW, thus reducing interaction. In each case a 30 mm DLW was used. The effect of bandwidth for $f_c = f_{op}$ is shown in Figure 6.24. Energy gain is larger for narrowband pulses. For more broadband pulses, it is preferred to use a shorter waveguide so that the useful length of the structure is maximised. Keeping bandwidth constant and changing centre frequency is shown in Figure 6.25. The final energy gain was calculated using CSt in each case. As with the results from *Mathematica*, the magnitude of interaction is more strongly dependent on centre frequency with decreasing bandwidth. Not shown in *Mathematica* is that there is interaction in the coupler. This tends to cancel due to the phase velocity mismatch, but for large centre frequencies this interaction was significantly larger that that in the DLW (but then cancels due to the mismatch).

6.4.4 Effect of time delay

It was established in Chapter 5 that, for a long structure and THz pulse with $f_c = f_{op}$, the energy gain saturates and becomes sinusoidal as a function of time delay. The periodicity of these oscillations is defined as the modulation frequency. The frequency of modulation for a range of centre frequencies is shown in Figure 6.26

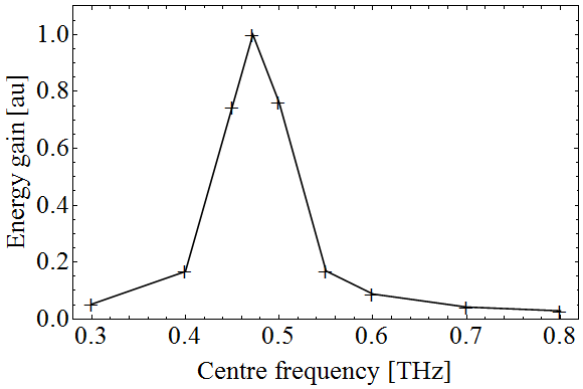

Figure 6.21: Effect of centre frequency of a Gaussian THz pulse with $\sigma_f = 0.023$ THz on maximum energy gain of electron. The energy of the THz pulse is the same in each case.

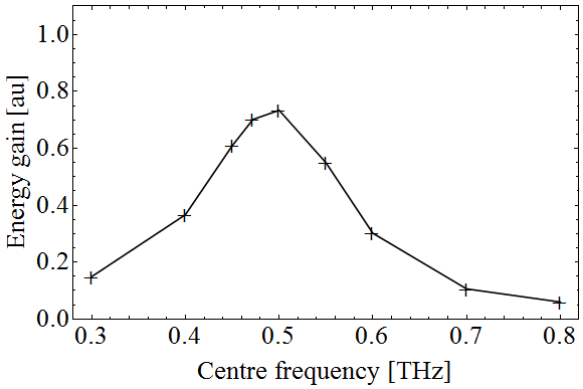

Figure 6.22: Effect of centre frequency of a Gaussian THz pulse with $\sigma_f = 0.069$ THz on maximum energy gain of electron. The energy of the THz pulse is the same in each case.

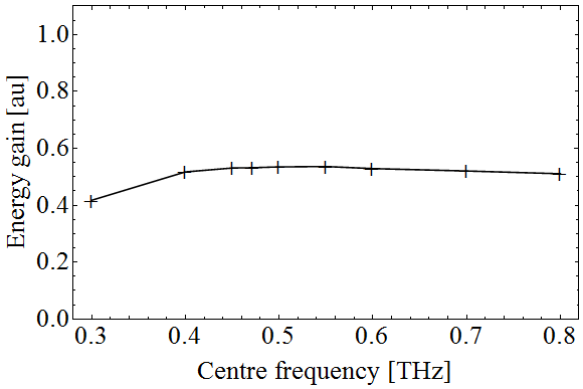

Figure 6.23: Effect of centre frequency of a modified Gaussian THz pulse on maximum energy gain of electron. The energy of the THz pulse is the same in each case.

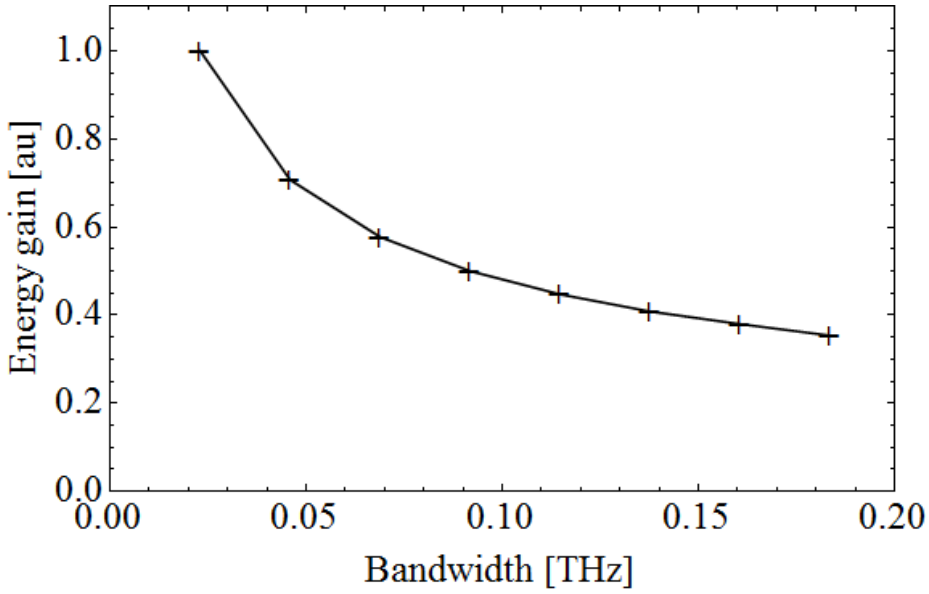

Figure 6.24: Effect of bandwidth on maximum energy gain for a 30 mm DLW with coupler included. The THz pulse has the same energy in each case.

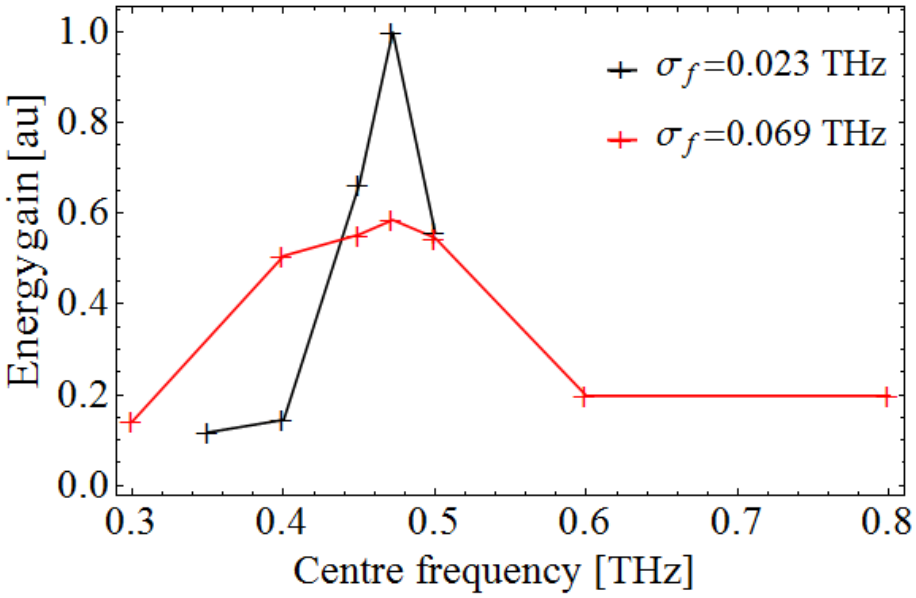

Figure 6.25: Effect of centre frequency on maximum energy gain for a 30 mm DLW with coupler included. The THz pulse has the same energy in each case.

for $\sigma_f = 0.023$ THz, and Figure 6.27 for $\sigma_f = 0.069$ THz. Figure 6.28 shows the effect of a modified Gaussian pulse on the modulation frequency. The maximum energy change is defined at 'Peak 0' in each case and the full structure was simulated.

The periodicity of the oscillation is dependent on delay; as discussed in Chapter 4, a THz pulse with non-zero bandwidth suffers from dispersion, and this is imparted upon the electrons. For $\sigma_f = 0.023$ THz, the dispersion is minimal when $f_c = f_{op}$ and so modulation frequency remains constantly equal to f_c. As the difference between f_c and f_{op} increases, the modulation is no longer constant. It is approximately equal to f_c except for when the centre frequency is far from f_{op}. In this case there are also some peaks where modulation frequency changes more rapidly. This is due to splitting of the interaction, as demonstrated in Figure 6.29. This splitting is due to phase velocity mismatch; an electron will propagate through the pulse, experiencing an oscillation in the interaction. This accounts for both the splitting and the reduced energy change.

Moving to $\sigma_f = 0.069$ THz, the modulation frequency is a function of peak number, or time delay, for all f_c. There is now significant dispersion of the pulse, and so the modulation frequency also varies with peak position at $f_c = f_{op}$. Taking the average of this oscillation gives f_c; however this is not the case for each centre frequency. For example, the average modulation frequency for $f_c = 0.3$ THz is 0.35 THz. This is due to splitting of the interaction, shown in Figure 6.30. Again the splitting is due to phase velocity mismatch, but as the velocity of the peaks changes with position in the structure, the oscillating interaction also changes over the length of the structure.

6.4.5 Summary

The effect of THz pulse bandwidth is to change both the magnitude and form of the interaction. For a narrowband pulse (e.g., $\sigma_f = 0.023$ THz) with $f_c = f_{op}$, energy change of a long electron bunch is sinusoidal. This modulation frequency can be used directly to calculate pulse length provided $f_c \approx f_{op}$ as the modulation frequency is equal to f_c. This is useful as a bunch length diagnostic. The final energy change is strongly dependent on the mismatch. This itself is useful to confirm the operating frequency of the DLW; by varying f_c the manufactured DLW is compared to the design. A larger bandwidth reduces the accuracy of any bunch length calculation. When using a modified Gaussian to describe the THz pulse the modulation frequency appears to be independent of f_c; interaction is therefore less sensitive to the THz pulse centre, which is useful if the THz pulse is not easily changed.

As noted when considering the effect of the THz pulse bandwidth, narrowband pulses require longer DLWs to fully interact, otherwise a broadband pulse is prefer-

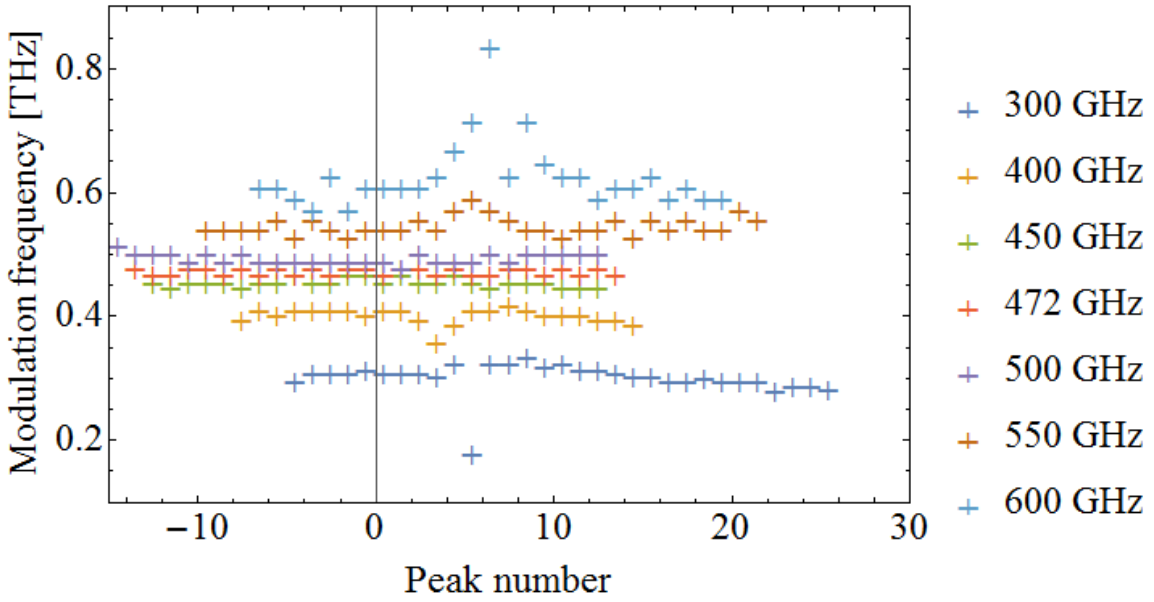

Figure 6.26: Change in frequency of modulation along a long electron train as a function of position for a THz pulse bandwidth $\sigma_f = 0.023$ THz. The effect is shown for a range of THz centre frequencies and THz pulse energy is constant.

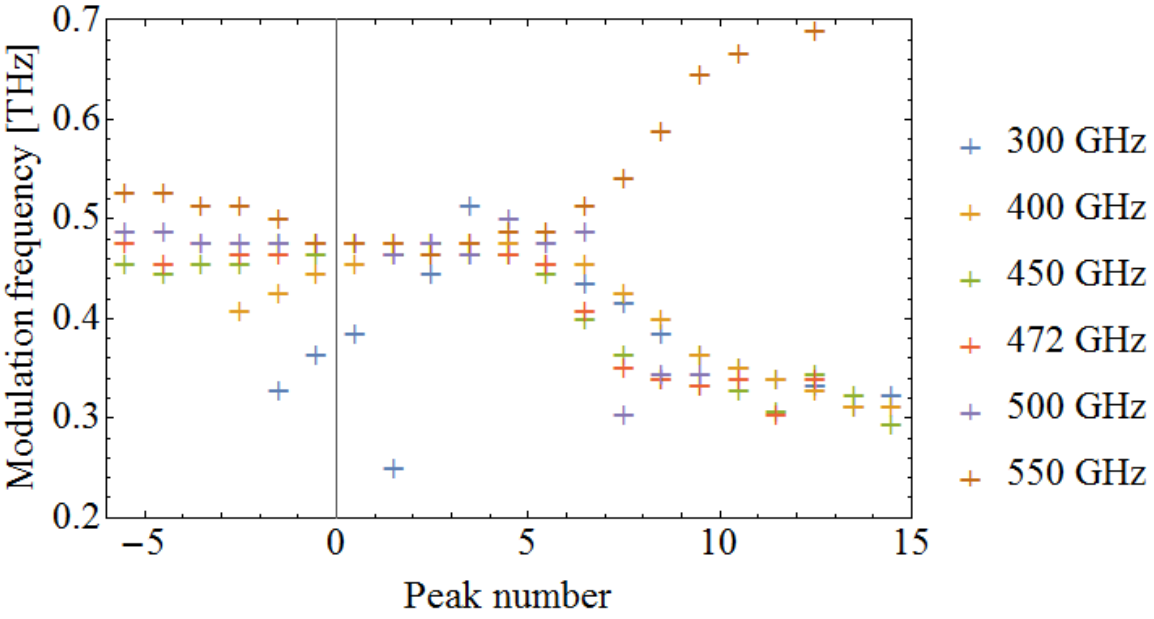

Figure 6.27: Change in frequency of modulation along a long electron train as a function of position for a THz pulse bandwidth $\sigma_f = 0.069$ THz. The effect is shown for a range of THz centre frequencies and THz pulse energy is constant.

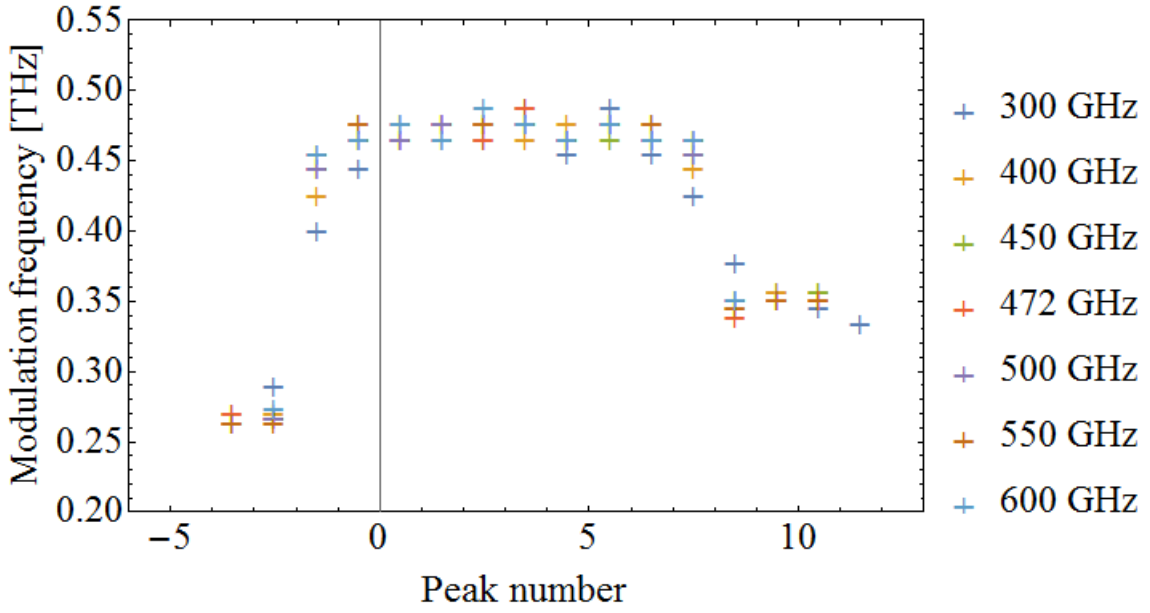

Figure 6.28: Change in frequency of modulation along a long electron train as a function of position for a THz pulse described by a modified Gaussian. The effect is shown for a range of THz centre frequencies.

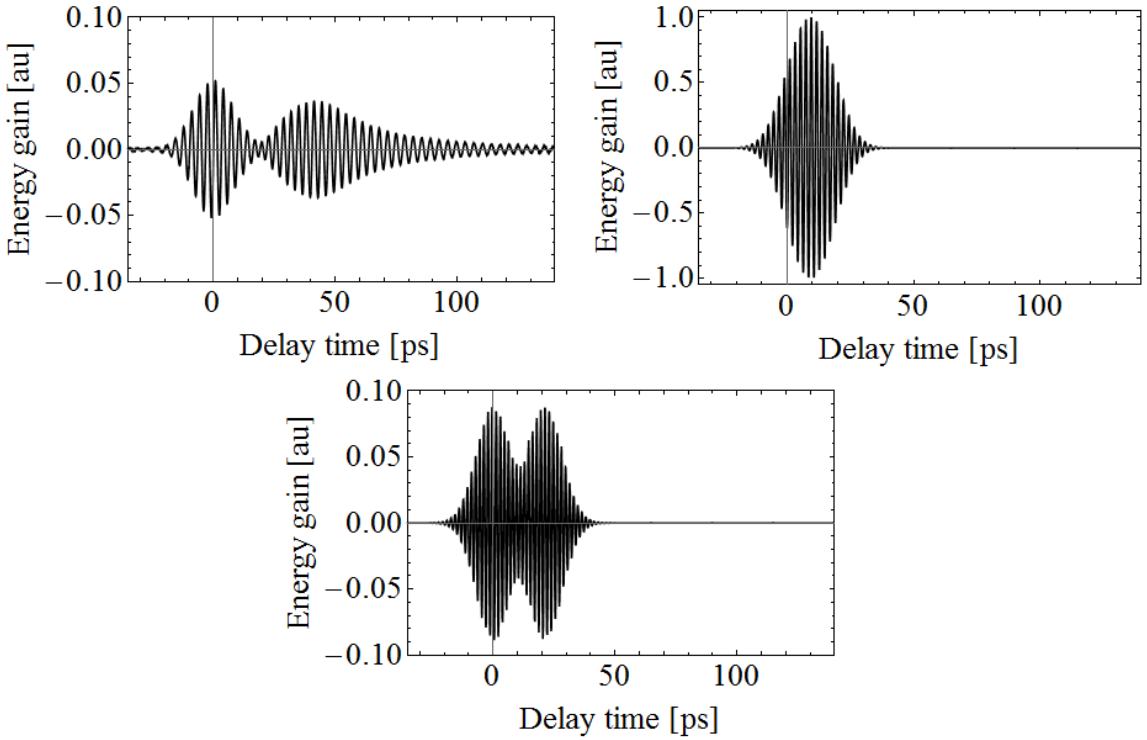

Figure 6.29: Energy change of a long train of electrons as a function of time delay with respect to the THz pulse, with $\sigma_f = 0.023$ THz. Shown are $f_c = 0.3,\ 0.472,\ 0.6$ THz, clockwise from left.

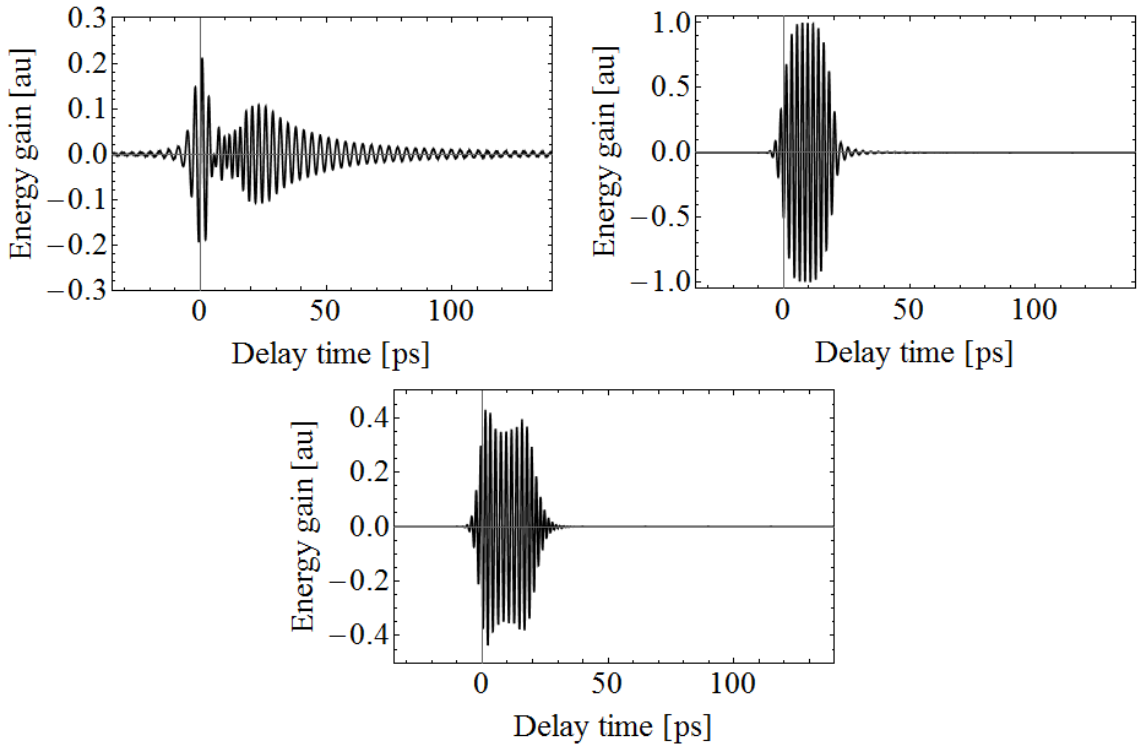

Figure 6.30: Energy change of a long train of electrons as a function of time delay with respect to the THz pulse, with $\sigma_f = 0.069$ THz. Shown are $f_c = 0.3,\ 0.472,\ 0.6$ THz, clockwise from left.

Table 6.3: Electron bunch parameters corresponding to each figure.

Figure number	σ_t [ps]	δE_{corr} [MeV]	δE_{rand} [MeV]	ϕ
6.31	3	0.5	0	0
6.34	3	0.5	0.05	0
6.35	2	0.5	0	0
6.36	0.5	0.5	0	0
6.37	0.2	0.5	0	-0.2 π
6.38	3	0	0.05	0
6.39	0.5	0	0.05	0

able. By using a 30 mm DLW instead of 10 mm it is easier ascertain the effect of bandwidth on magnitude of energy change. It was observed that a narrowband pulse was preferable to maximise energy change. There is the added benefit of use as a bunch length diagnostic. It was decided to use a narrowband pulse for both of these reasons. Additionally simulation of the interaction can be simplified; it can be modelled as a sinusoidal variation provided the 30 mm DLW is used.

6.5 Effect of bunch properties on interaction

A simple method to estimate observed energy change is to create a bunch with variable correlated and uncorrelated energy spread, bunch length, and temporal shape. Correlated energy spread is related to the longitudinal position in the bunch. It is also known as chirp. Uncorrelated energy spread is considered here to be purely random, and so affects the overall emittance of the bunch. The interaction is modelled as a sinusoidal energy change. The different bunch settings, THz amplitude and phase are recorded in Table 6.3, with the corresponding figure name. Unless otherwise stated, in each case the maximum energy gain from the THz is $A_0 = 0.01,\ 0.05,\ 0.1,\ 0.2$ MeV. In each case the interaction is observed in terms of the energy spectrum; it is assumed that the only available diagnostic is a dipole spectrometer.

6.5.1 Linear energy chirp

A linear energy chirp was added by making correlated energy spread, δE_{corr}, non-zero. Initially no additional energy spread is included, $\delta E_{rand} = 0$. Considering a purely Gaussian bunch profile, the centre of which overlaps with a peak energy change, results in an energy spectrum as shown in Figure 6.31. The correlated energy spread is the same in each case, but the amplitude of the energy change is given as $A_0 = 0.01,\ 0.05,\ 0.1,\ 0.2$ MeV. It is of note that increasing field amplitude does not increase the depth of modulation. A fivefold increase in THz amplitude results in a weaker modulation. This is because 'overmodulation' is occurring, where the

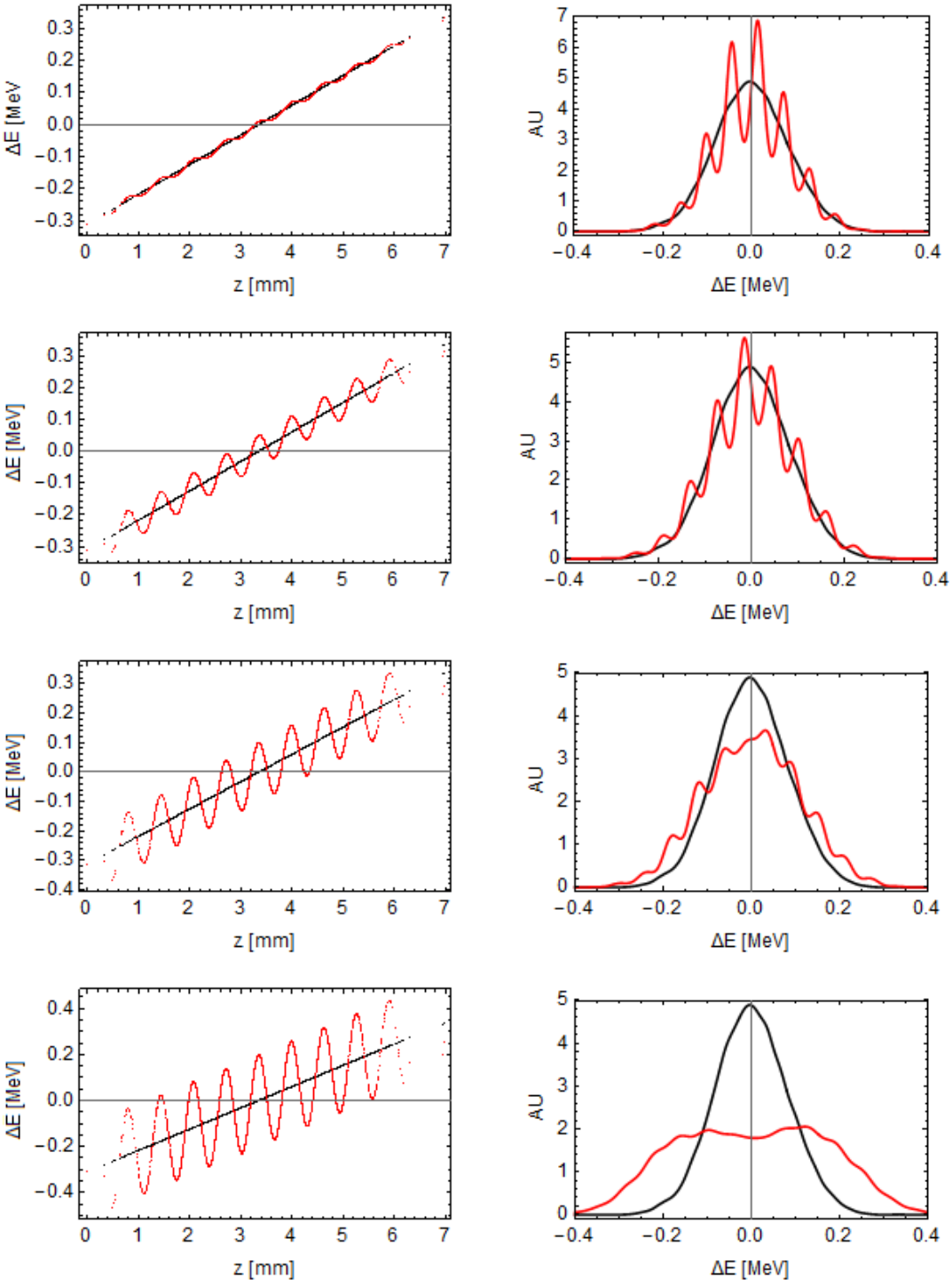

Figure 6.31: Effect of correlated energy spread on THz-electron interaction of a bunch with $\sigma_t = 3$ ps. Top to bottom: amplitude of the THz field is $A_0 = 0.01,\ 0.05,\ 0.1,\ 0.2$. In each case, the left plot shows the longitudinal energy spread of bunch before (black) and after (red) THz interaction. On the right the energy spectrum of the entire bunch is shown.

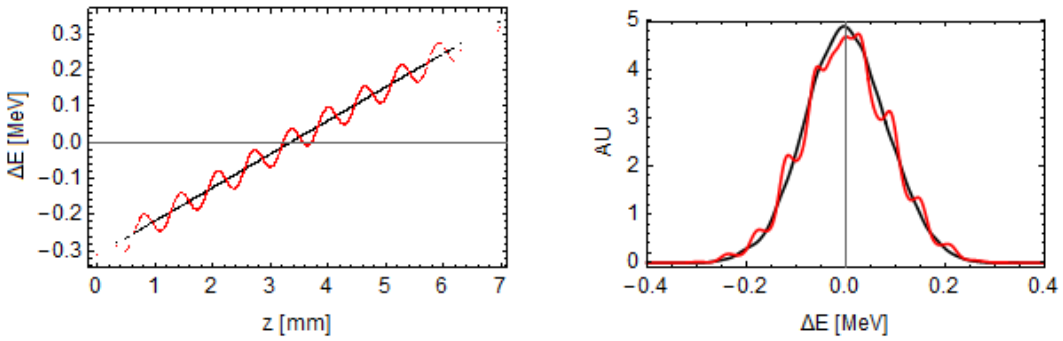

Figure 6.32: Effect of correlated energy spread of a bunch with $\sigma_t = 3$ ps on THz-electron interaction for THz amplitude $A_0 = 0.037$, corresponding to the 'switching point where 'overmodulation' starts to occur. The left plot shows the longitudinal energy spread of bunch before (black) and after (red) THz interaction, and the right plot shows the energy spectrum.

interaction transitions from a 'staircase'-like energy change, to the peaks and troughs overlapping. This means that the intensity of the modulations appear lower, which can be seen in Figure 6.32, where the modulation 'switches' into peaks with a π phase shift. As A_0 is increased further, the energy change is significant enough that an energy spread is introduced, and the observed modulation decreases. This regime is particularly useful for bunch length measurements. The modulations at low THz field amplitude in the energy spectrum are directly related to those in the time domain, for a completely linear chirp. By establishing the number of modulations in the energy spectrum, and converting to time domain, both the linear chirp and the bunch length are derived. The effect of amplitude on the depth of modulations, the ratio between peak and trough, in the energy spectrum is shown in Figure 6.33. The effect of A_0 on modulation depth appears sinusoidal, but with a decreasing amplitude. This cannot be used to determine the THz field amplitude or electron energy gain, as there are multiple possible bunch parameters possible for each observed modulation. Any shift in phase can also be a result of change in timing between THz and electrons.

Uncorrelated energy spread is added in Figure 6.34. The observed modulation is decreased and for this set of bunch parameters interaction is only easily observed once 'overmodulation' is achieved and the energy spread increases. This is a useful indicator for experimental results that, if modulation is to be observed, energy spread must be dominated by the correlated part.

Reducing the bunch length to $\sigma_t = 2$ ps, as in Figure 6.35, shows a different form of modulation. The observed effect changes with increasing THz amplitude. As peaks and troughs at different times overlap in energy, a phase shift is not observed,

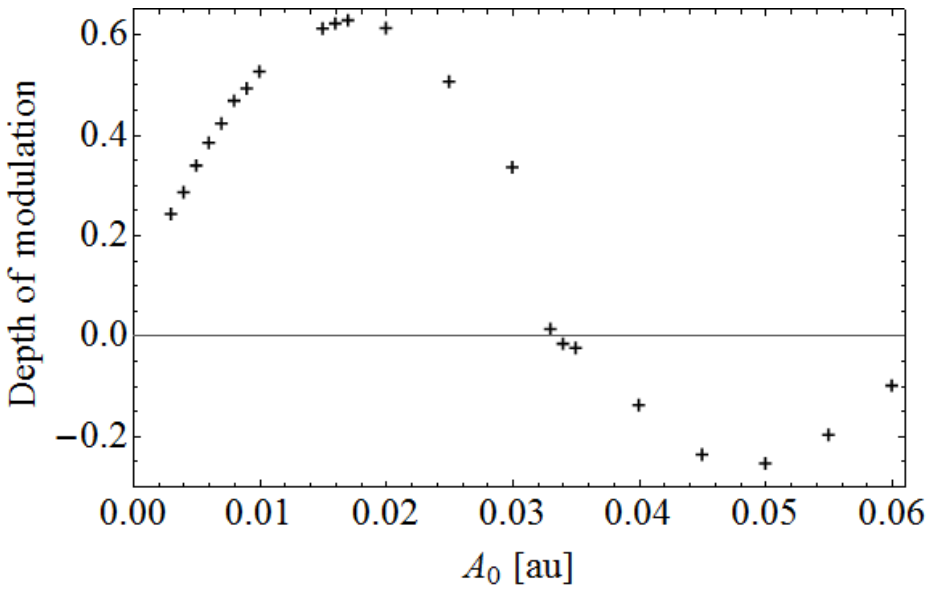

Figure 6.33: Effect of A_0 on depth of modulation of a long chirped bunch.

but instead the modulation is of the form $\sin(mx) + \sin(nx)$, where m and n are different integers. Increasing THz amplitude further leads to the expected energy spread increase, but with modulation still visible in the spectrum. Therefore the length of the bunch has a significant effect on the modulation, and the number of periods does not simply decrease. It is still possible to make an estimate of the bunch length for small THz interaction, as the number of peaks in the energy spectrum does correspond to the number of THz periods that the bunch is overlaid upon.

Decreasing the bunch length further, to $\sigma_t = 0.5$ ps, the interaction is again modelled, as shown in Figure 6.36. Here the interaction is characterised by a change in energy spread rather than a modulation. The bunch is not held within one THz wavelength, and so energy spread is not symmetric; it is instead dependent on the phase of the THz. Interaction is characterised by an energy spread increase. At the phase shown here, only a single peak exists at low THz amplitude on one side of the spectrum, corresponding to deceleration, but there is also observable acceleration. This 'decelerated' edge also includes accelerated electrons as the lowest energy electrons have gained energy. Increasing amplitude results in the accelerated edge also peaking, and then an energy spread increase as the imparted energy exceeds the correlated energy of the bunch. The effect of changing phase of the sinusoid is to shift the relative intensities of the peaks.

When $\sigma_t = 0.2$ ps, nearly all of the bunch is encapsulated within half a wavelength, allowing for acceleration of all electrons. Figure 6.37 shows the resulting THz-electron interaction. Although all electrons gain energy, the energy gain is dependent on

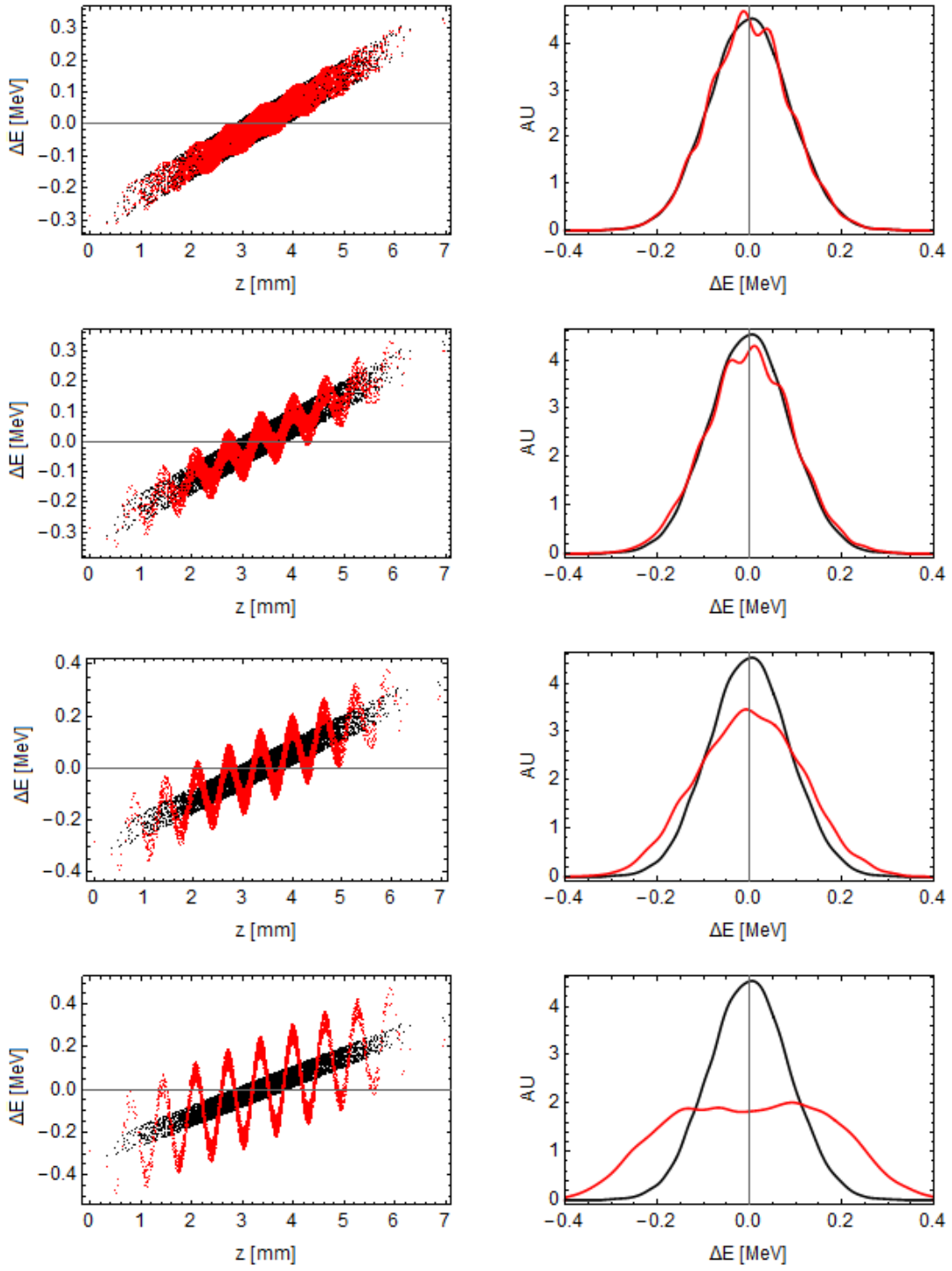

Figure 6.34: Effect of correlated energy spread on THz-electron interaction of a bunch with $\sigma_t = 3$ ps and $\delta E_{rand} = 0.05$. Top to bottom: amplitude of the THz field is $A_0 = 0.01,\ 0.05,\ 0.1,\ 0.2$. In each case, the left plot shows the longitudinal energy spread of bunch before (black) and after (red) THz interaction. On the right the energy spectrum of the entire bunch is shown.

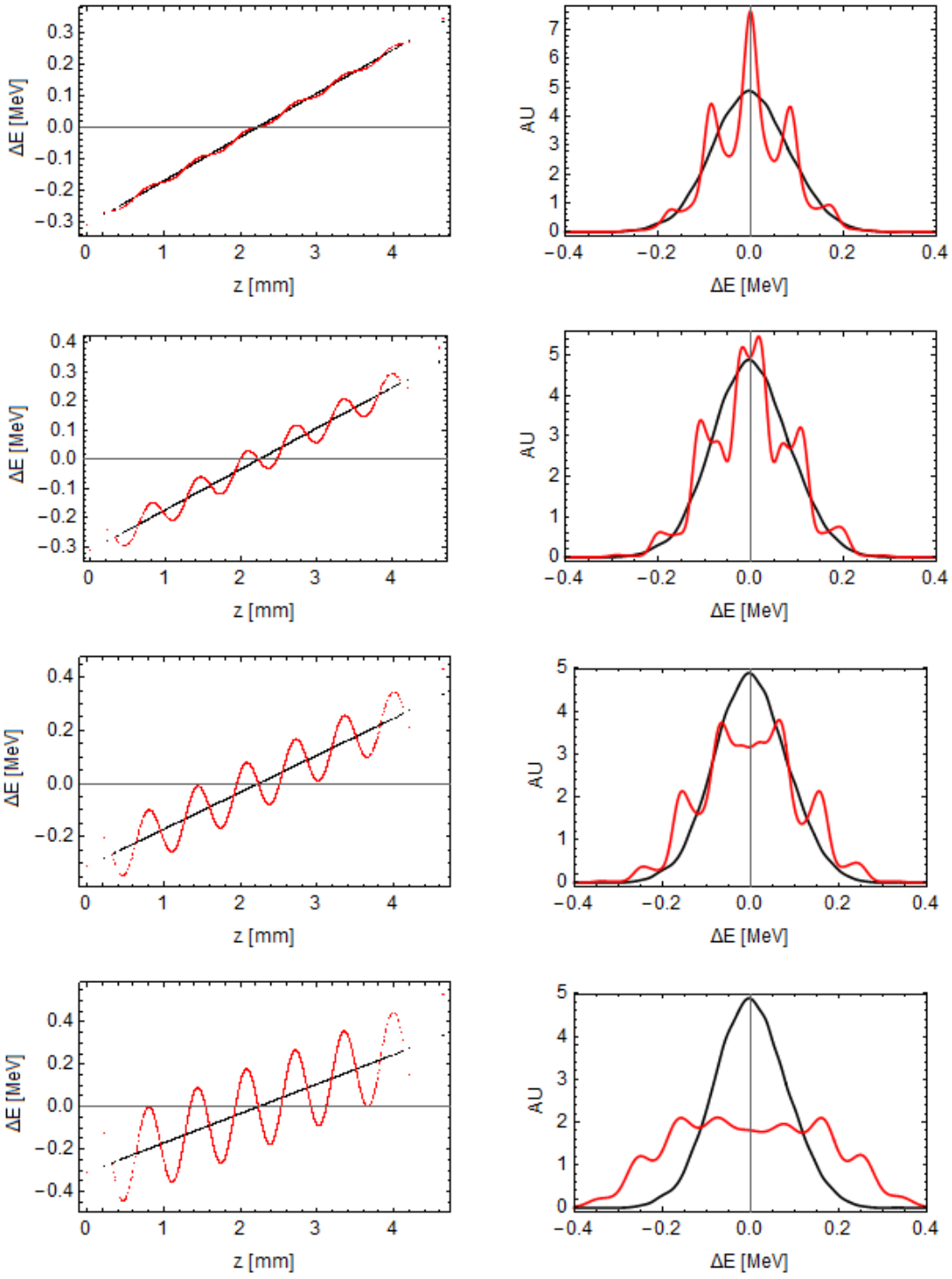

Figure 6.35: Effect of correlated energy spread on THz-electron interaction of a bunch with $\sigma_t = 2$ ps. Top to bottom: amplitude of the THz field is $A_0 = 0.01,\ 0.05,\ 0.1,\ 0.2$. In each case, the left plot shows the longitudinal energy spread of bunch before (black) and after (red) THz interaction. On the right the energy spectrum of the entire bunch is shown.

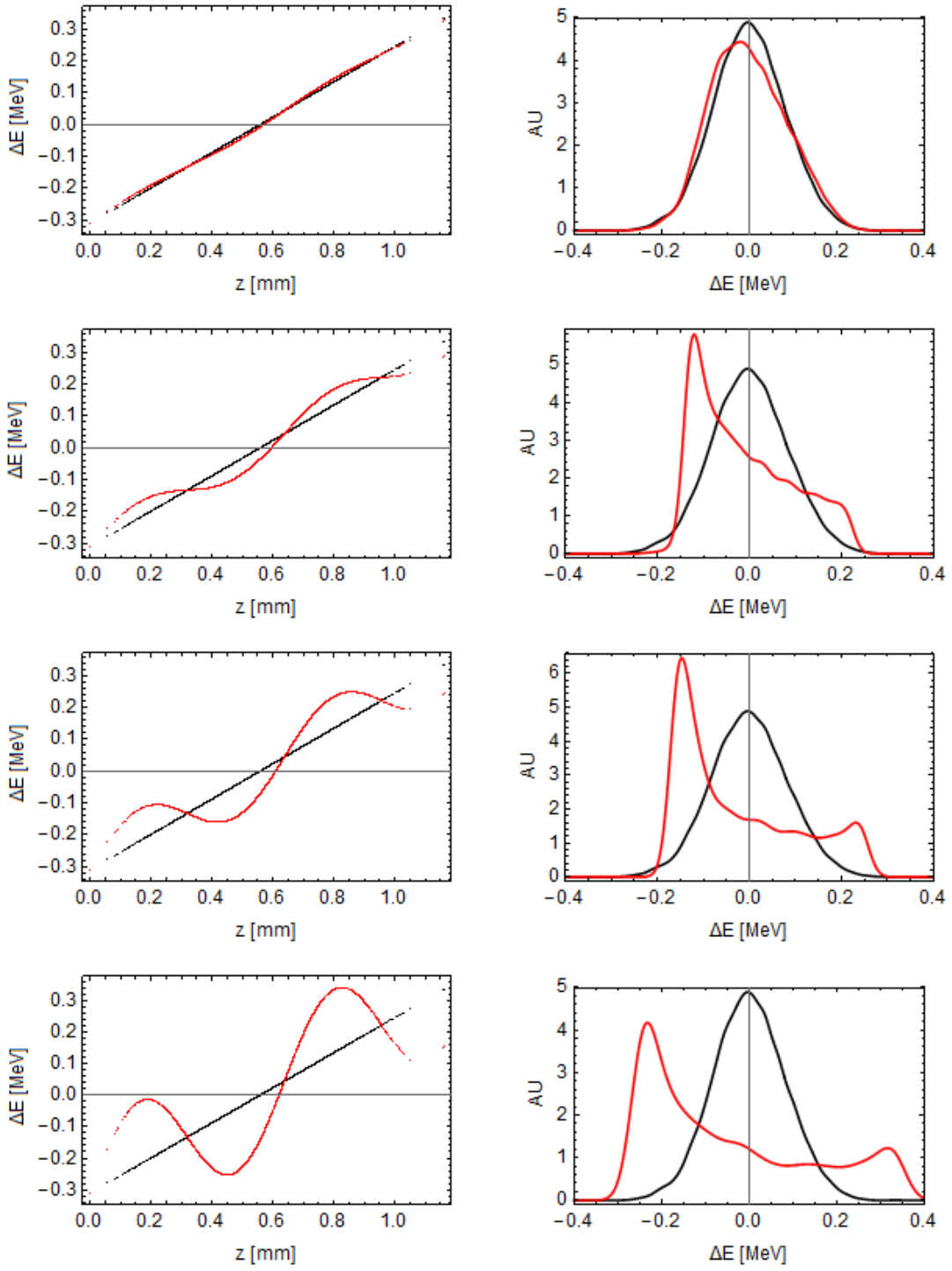

Figure 6.36: Effect of correlated energy spread on THz-electron interaction of a bunch with $\sigma_t = 0.5$ ps. Top to bottom: amplitude of the THz field is $A_0 = 0.01,\ 0.05,\ 0.1,\ 0.2$. In each case, the left plot shows the longitudinal energy spread of bunch before (black) and after (red) THz interaction. On the right the energy spectrum of the entire bunch is shown.

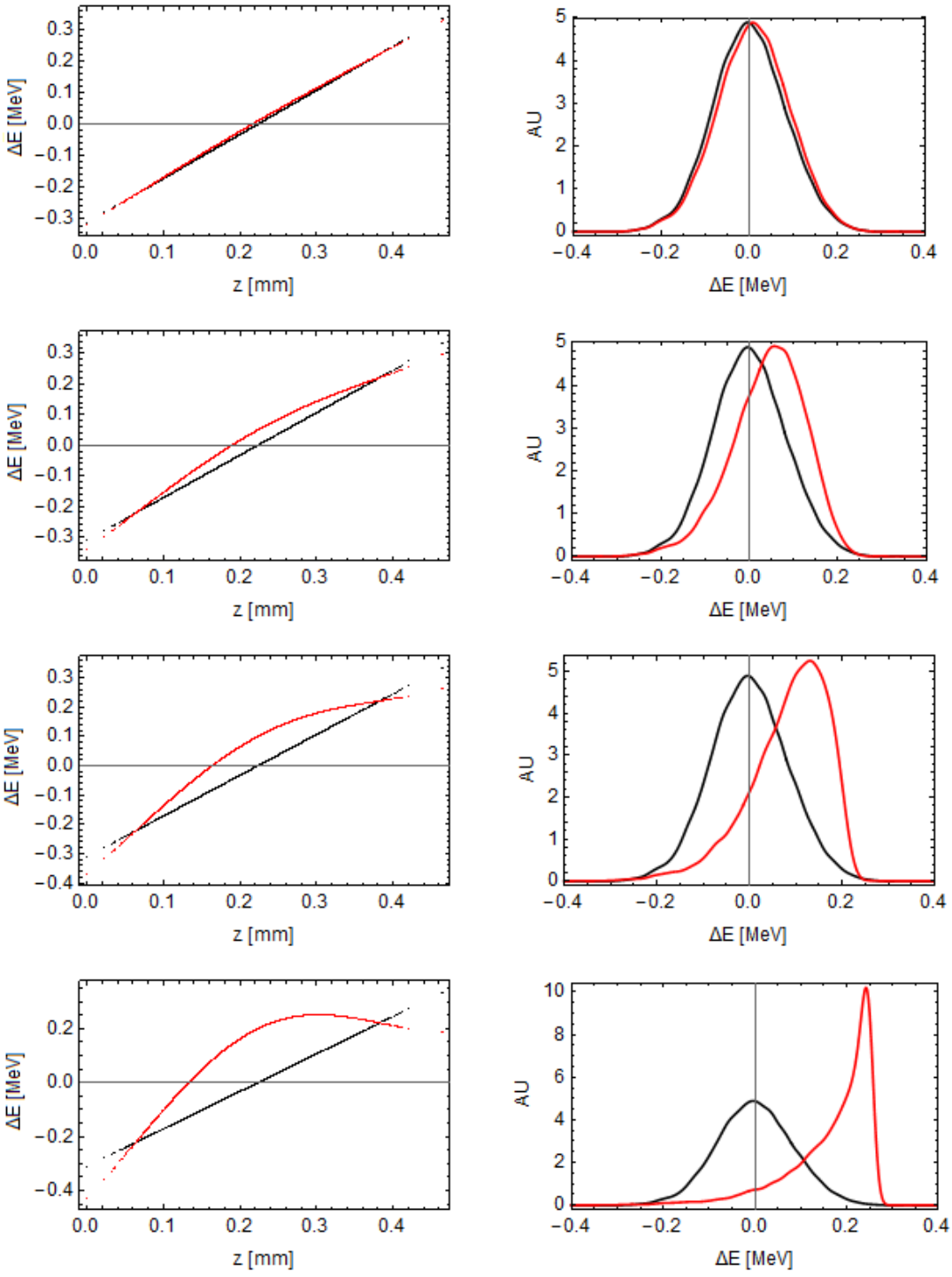

Figure 6.37: Effect of correlated energy spread on THz-electron interaction of a bunch with $\sigma_t = 0.2$ ps. Top to bottom: amplitude of the THz field is $A_0 = 0.01,\ 0.05,\ 0.1,\ 0.2$. In each case, the left plot shows the longitudinal energy spread of bunch before (black) and after (red) THz interaction. On the right the energy spectrum of the entire bunch is shown. The phase has been shifted by -0.2 to overlap the peak THz amplitude with the centre of the bunch.

longitudinal position and so there is also a change in the profile of the energy spectrum. This leads to the creation of a spike with a long tail as A_0 increases. With change in phase, the position of this peak shifts along the spectrum. There are two phases at which the sinusoid is zero at the centre of the bunch. At one, the modulation cancels out the chirp, resulting in an energy spread decrease with the spectrum peaked at $\Delta E = 0$, the other enhances the chirp and increases energy spread, again with the spectrum peaked at $\Delta E = 0$. Maximum energy change is found when the centre of a peak of the sinusoid matches the centre of the pulse.

In summary, modulation of the energy spectrum is easily observed for an electron bunch with a correlated energy spread. The effect is observed at lower THz field amplitudes, and can be used to make an estimate of bunch length. As THz field increases, there is instead an increase in energy spread. The effect of uncorrelated energy spread is to reduce observability of modulation, but not of the energy spread associated with larger field amplitudes. With a short electron bunch (longer than a wavelength), energy spread is observed in the form of splitting into two peaks with hard edges, which then become less well defined with increasing amplitude. Decreasing the bunch length to less than half a wavelength, full acceleration is seen as a shift, which becomes a hard edge with a lower energy tail as amplitude increases. In the spatial domain, the maximum energy is relatively flat with position, causing the hard edge. Increasing amplitude beyond this would result in a defined edge with higher maximum energy, but decreased spectral amplitude. This is because the longitudinal energy spread after THz interaction for $A_0 = 0.2$ MeV has a flat top which is no longer present when the amplitude increases, as can be seen in Figure 6.37. The THz amplitude required for this flat top depends on the initial bunch settings, primarily chirp and length.

6.5.2 Flat longitudinal phase space

Setting $\delta E_{corr} = 0$, the observed interaction is a spreading of the energy spectrum into two distinct peaks. The spectrum is unrealistic; some degree of δE_{rand} must be added, as shown in Figure 6.38 for a bunch with $\sigma_t = 3$ ps. A small THz amplitude has little effect; it is characterised by a change in the intensity profile shape. The energy spread increases with increasing A_0, but does not split into two peaks until energy change exceeds the initial energy spread. The effect of the sinusoid phase is negligible for this bunch length as the proportion of acceleration to deceleration does not vary greatly. An estimate of energy gain is obtained by comparing the energy spread of the bunch with that before interaction and taking the difference divided by two. With a long bunch, the sinusoid phase is inconsequential as the proportion of

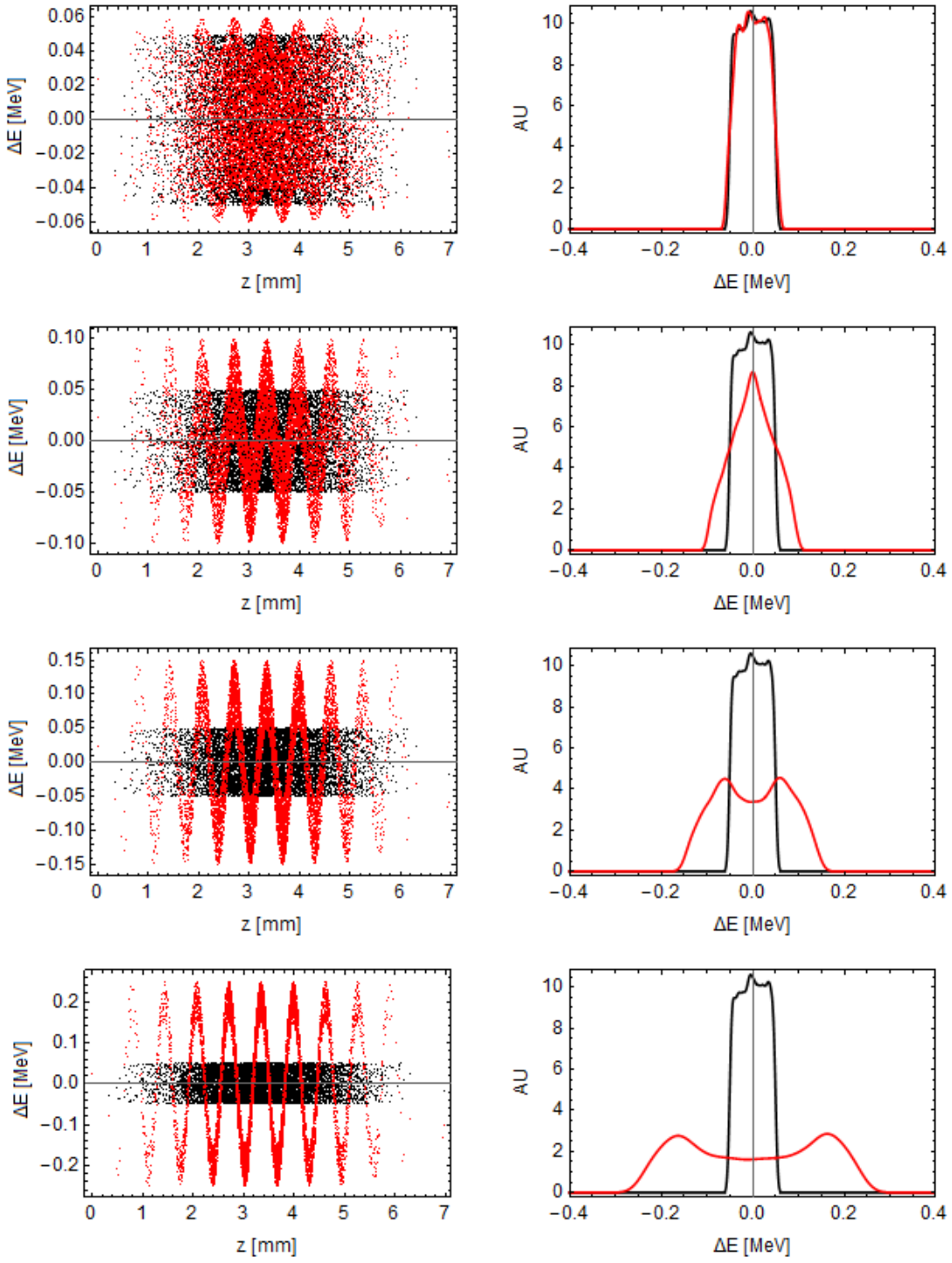

Figure 6.38: THz-electron interaction of a bunch with $\sigma_t = 3$ ps and $\delta E_{corr} = 0$. Some random energy spread has been added ($\delta E_{rand} = 0.05$). Top to bottom: amplitude of the THz field is $A_0 = 0.01,\ 0.05,\ 0.1,\ 0.2$. In each case, the left plot shows the longitudinal energy spread of bunch before (black) and after (red) THz interaction. On the right the energy spectrum of the entire bunch is shown.

acceleration to deceleration does not vary greatly.

Setting $\sigma_t = 0.5$ ps, shown in Figure 6.39, there is again an energy spread, but it is now asymmetric due to the THz phase. This is the main difference between $\sigma_t = 3$ ps and $\sigma_t = 0.5$ ps; it is not possible to measure bunch length to make a better estimate of energy gain with only an energy spectrometer. At this value of σ_t, the bunch is not short enough to see pure acceleration or deceleration.

Reducing to $\sigma_t = 0.2$ ps, with zero correlated energy the interaction depends strongly on phase of the THz with respect to the bunch. Figure 6.40 shows the effect of phase when $A_0 = 0.2$. For maximum acceleration, there is a hard edge with long tail, whereas equal acceleration and deceleration is characterised by symmetric energy spread. The energy change can be easily determined at this bunch length.

In summary, for a flat longitudinal energy spread, it is possible to approximate the magnitude of acceleration, but only with a short bunch can the exact value be found. It is not possible to make a bunch length estimate, except to say that the bunch is less than half a wavelength, approximately one wavelength, or multiple wavelengths, based on the asymmetry of the energy spectrum after interaction.

6.6 Conclusion

A dielectric-lined waveguide has been designed to maximise the accelerating voltage, including the effect of group velocity mismatch. A rectangular coupler with a square aperture has been designed to maximise the transmission to the LSM_{11} mode, although it must be noted that at f_{op} there is little variation in transmission with coupler length. It has been verified in simulation that the use of a mirror with a hole to allow for electron bunch transmission does not noticeably effect the pulse propagation. THz-electron interaction for both the DLW only and the full structure has been investigated. It has been ascertained that, for a long bunch, there is a modulation of the energy. The form of this modulation depends on pulse bandwidth and centre frequency. For narrowband pulses the interaction is sinusoidal with time delay. Therefore the specific case of $\sigma_f = 0.023$ THz was considered, with $f_c = f_{op}$, and the effect of bunch properties; bunch length, energy chirp, and uncorrelated energy spread, analysed. Only the effect on the energy spectrum was considered so as to replicate the observables of the experiment. The amplitude of the THz pulse was varied, demonstrating that for a long, linear chirped bunch, as amplitude increases the modulation depth varies, until an energy spread instead is observed. It was also found that for THz field amplitudes at which modulation is observed, acceleration is very small. To observe acceleration of a full bunch, it must be maximum of half a wavelength, and the field amplitude must be significantly larger. In these cases, the

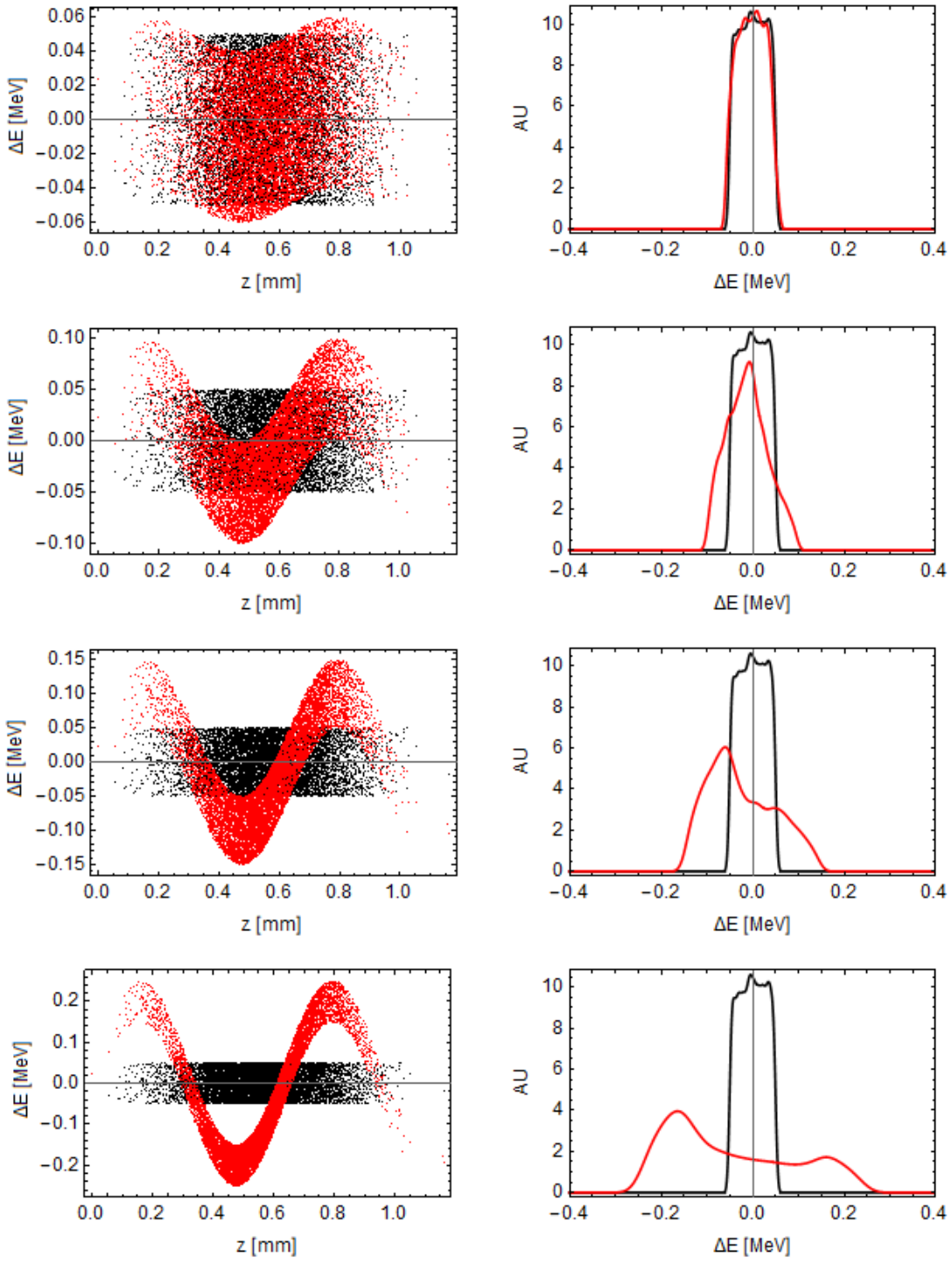

Figure 6.39: Effect of correlated energy spread on THz-electron interaction of a bunch with $\sigma_t = 0.5$ ps. Some random energy spread has been added ($\delta E_{rand} = 0.05$). Top to bottom: amplitude of the THz field is $A_0 = 0.01,\ 0.05,\ 0.1,\ 0.2$. In each case, the left plot shows the longitudinal energy spread of bunch before (black) and after (red) THz interaction. On the right the energy spectrum of the entire bunch is shown.

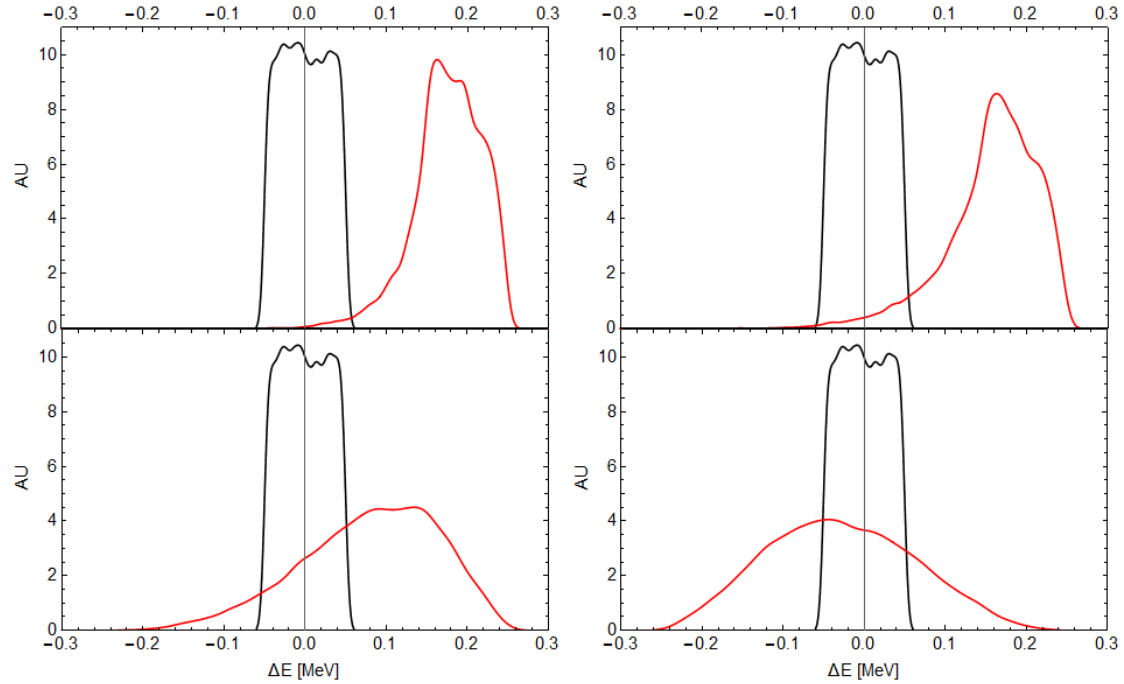

Figure 6.40: Effect of phase between THz and electrons on final energy spectrum for THz amplitude $A_0 = 0.2$ and electron bunch length $\sigma_t = 0.2$ ps. Top left shows maximum acceleration, and all others are at phases giving some acceleration and deceleration. In each case the black plot shows THz off, and red shows THz on.

nominal amplitude, A_0, was used to define relative amplitude. For a chirped bunch with $\sigma_t = 3\ ps$, $A_0 = 0.01$ was preferable for demonstration of modulation. For acceleration of a $\sigma_t = 0.2$ ps bunch, A_0 is increased to 0.2.

Chapter 7

Testing of manufactured structures

The manufactured structures were made by the MMT group, part of RAL Space, who have experience in machining of sub-millimetre components. Two structures were manufactured; one for the deflection of 100 keV electrons, and the other for acceleration of 35 MeV electrons. The parameters of the waveguides are given in Table 2.1. The manufacturing process was similar in the two cases. The structure was produced in two halves, split along the horizontal axis with the dielectric on the top and bottom faces. Copper blocks were milled with the coupler incorporated in the block, and the dielectric then bonded to the coupler before the two halves were bolted together. The manufactured structure as designed for deflection of 100 keV electrons is shown in Figure 7.1. The coupler was 44 mm long with an input aperture of area 5 mm $\times$ 10 mm, the same as the area of the output face of the non-linear crystal used for THz generation. A separate shelf held an aluminium mirror, which had an aperture allowing electrons to propagate down the structure. The DLW itself was 5 mm long; a separate structure with a 10 mm DLW was also manufactured.

The choice of bonding agent was originally a wax for the deflecting structure as this was recommended by the manufacturer to simplify the bonding process. This was a non-permanent solution as this wax melts at 60°. This was changed to an epoxy resin, a permanent bonding agent, for the accelerating structure due to heating concerns. An early problem encountered was poor bonding of the dielectric layers, which meant that one dielectric slab from a 100 keV deflection structure was lost during testing. The reason for this was not clear as the testing only involved propagation of a low power THz pulse through the structure and so heating was not expected. It was suggested that the wax layer was too thin, and so the dielectric was re-bonded with a larger amount of wax, after which no further problems were encountered. However, this experience also contributed to the decision to use epoxy resin in the future.

Figure 7.1: Manufactured structure designed for deflection of 100 keV electrons. Left: full structure bolted together. Right: bottom half of the structure. The DLW and coupler are milled from the same copper block, with a separate shelf which holds a mirror for reflection of THz pulses into the structure. The mirror mas a small aperture in the direction of electron propagation. The shelf also has space for a THz crystal to be mounted.

Table 7.1: Effect of errors in manufacturing on the operating frequency.

δ [μm]	a [μm]	f_{op} [THz]
40	260	0.534
50	250	0.473
60	240	0.428

Two main tests were performed on the manufactured structures; THz time domain spectroscopy (THz-TDS) and microscopic analysis of the structure dimensions. THz-TDS was used for measuring dispersion; the example provided here is a structure used for deflection of 100 keV electrons. Microscopic analysis, in particular of the cross-section, was required to finalise the choice of centre frequency of the THz source. It had been highlighted by the manufacturer that the dielectric thickness had an error ± 10 μm, or 20% of the finalised value. As the copper was milled to incorporate the dielectric, the full aperture was 600 μm, and so change in the dielectric thickness also affected the vacuum aperture. The dispersion relation for $a = 240$ μm and $\delta = 60$ μm is plotted in Figure 7.2, along with $a = 260$ μm and $\delta = 40$ μm, and compared to the dispersion relation of the design dimensions. Increasing the dielectric thickness shifts the dispersion relation function down in frequency; however there is also an associated change in its form. A thicker dielectric (and smaller a) means that β becomes linear at a smaller frequency. The operation frequency also decreases with increasing dielectric thickness; the values are found in Table 7.1. The difference in THz frequency is large enough that there would be an effect on the electron energy gain and the modulation period if the wrong operating frequency is used.

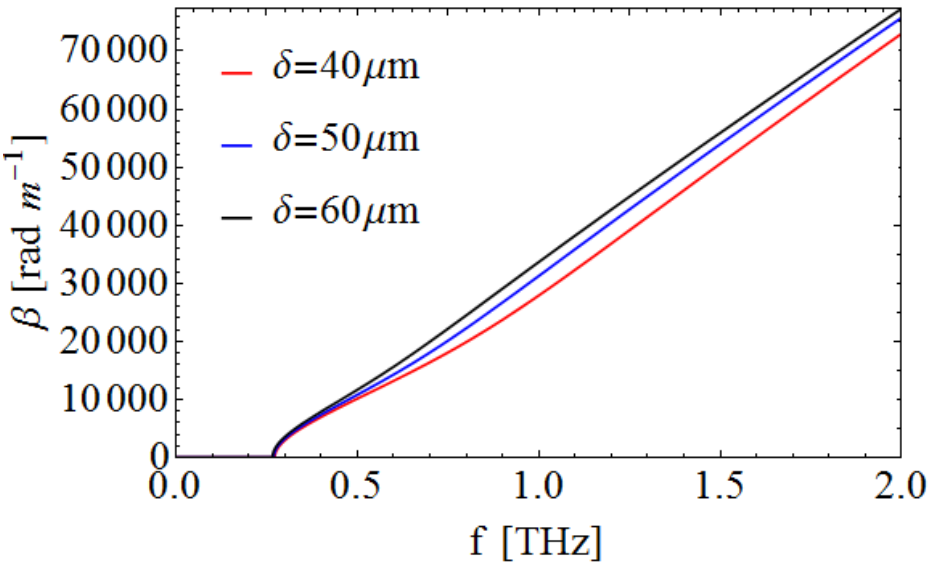

Figure 7.2: Effect of errors in the dielectric thickness on the dispersion relation.

7.1 Determination of the dispersion relation of a structure

The structure analysed here was designed for the deflection of 100 keV electrons in an upcoming experiment as part of a THz exploitation programme. The design followed the same procedure as in Chapter 6, giving waveguide parameters: a = 100 μm, w = 1000 μm, δ = 240 μm and quartz used as the dielectric (ϵ_r=3.75). The DLW was 10 mm long and the coupler was 44 mm long, with input aperture with sides of 10 mm by 5 mm.

7.1.1 Principles of THz-TDS

Using THz-TDS allows for determination of both amplitude and phase of an electric field, thus allowing for determination of absorption and refraction of a sample. It has been used for a variety of applications, for example chemical analysis [135], investigation of biological tissues [136], and determination of charge carrier behaviour in semiconductors [137]. A broadband THz source is used, and typically detected using free-space electro-optic sampling. The principle of electro-optic sampling has been detailed comprehensively elsewhere [138, 139]. A non-linear crystal such as zinc telluride (ZnTe) is illuminated with a THz pulse which has been passed through a sample, along with an optical probe pulse. The crystal is birefringent, meaning that the refractive index depends on the polarisation of the input field. As a result of the Pockels effect this birefringence is dependent on the applied electric field. The THz pulse induces birefringence proportional to its amplitude, and so the polarisation of

the optical pulse is rotated dependent on this amplitude. Therefore with the use of a delay stage, the amplitude of the THz pulse is scanned in time. As the aim is then to use this data to find the properties of the material it is common to purge the system of air using dry nitrogen. Without this, the absorption from water vapour is also included in the result.

7.1.2 Terahertz time domain spectroscopy of structure

Measurements of the transmission of THz radiation through the DLW were performed using the THz time-domain spectrometer (THz-TDS) setup [133] described in Figure 7.3. The THz-TDS used a chirped-pulse amplification based laser system;

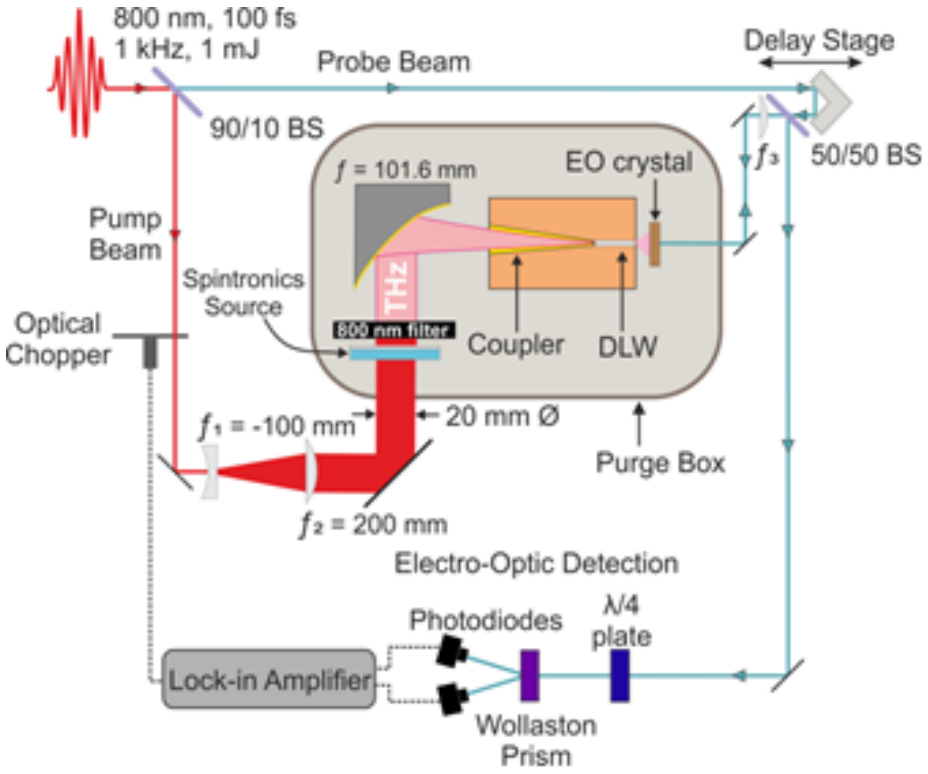

Figure 7.3: Schematic diagram of the experimental THz-TDS setup showing the generation and coupling of the THz radiation into the DLW structure. The transmitted THz radiation is measured using an electro-optic (EO) crystal in a back-reflection geometry. Image courtesy of V. Georgiadis.

a self-mode-locked Ti:sapphire laser oscillator generated pulses with 100 fs duration and central wavelength of 800 nm, and a regenerative amplifier system amplified the pulses to approximately 1 mJ at a repetition rate of 1 kHz. The output from the laser was split into the pump and probe beam respectively using a 90:10 beamsplitter. For the generation process the pump beam was expanded to a beam diameter of 20 mm and used to excite a 25 mm^2 spintronic source. There was some residual transmitted

800 nm radiation which was blocked by a filter. Two neodymium disc magnets of 25 mm diameter were aligned with opposite edges of the source, producing horizontal magnetic field lines across the surface. The THz emission is controlled by the magnetic field orientation; a vertically polarised pulse is generated [140]. The THz pulse was then focused into the coupler by a 90° off-axis parabolic mirror. The transmitted THz radiation was then measured using a 2 mm thick (110)-cut ZnTe crystal placed at the exit of the DLW. All the measurements were performed at room temperature and at a relative humidity of 5-6 %.

The time-dependent field amplitude was directly measured. By performing a Fourier transform both phase and frequency-dependent amplitude were obtained. The THz pulse generated using a spintronic source, after propagating a distance z, is described in the frequency domain as

$$E(\omega, z) = E_0 \omega^2 \exp\left[-\frac{\omega^2}{2\sigma^2} - i\beta(\omega)z\right] , \tag{7.1}$$

where σ controls the width of the pulse. However the signal also contains reflections due to the 500 μm magnesium oxide substrate upon which the source structure was deposited. In the case of a single reflection, the measured signal is given as

$$s(t) = E(t) + rE(t - \tau) , \tag{7.2}$$

where r is an attenuation coefficient and τ is the time delay of the reflection. By the convolution theorem,

$$s(\omega) = E(\omega)(1 + r \exp\left[-i\omega\tau\right]) . \tag{7.3}$$

For multiple reflections,

$$s(t) = E(t) + \sum_{N}^{n=1} r_n E(t - \tau_n) . \tag{7.4}$$

The values of r_n and τ_n were measured from the free space pulse and then applied to the dispersed signals from the waveguides, removing the oscillations from the signal. The corrected field $E(t)$ as measured at the end of the waveguides included the effect of free space, the coupler, and the waveguide. Two structures were used, both with the same coupler but different lengths of DLW (10 mm and 5 mm). The dispersion of the DLW was calculated from the time domain signals obtained from both structures.

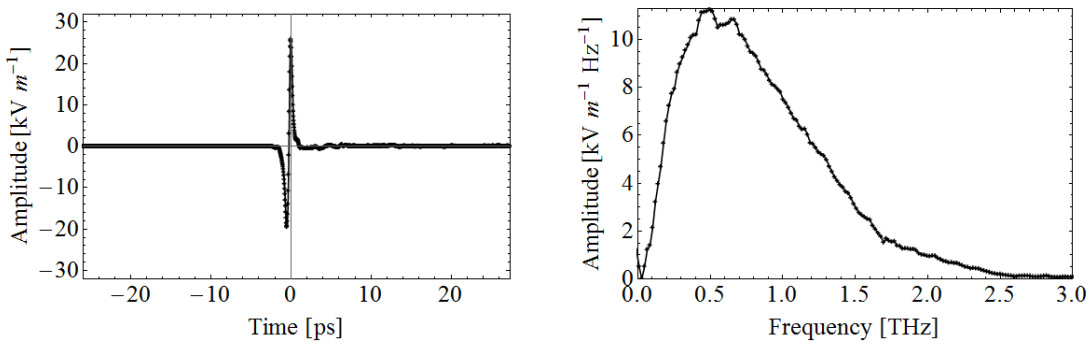

Figure 7.4: Electric field amplitude of a THz pulse after propagating through free space [141]. Shown is the measured time domain data and the Fourier transform.

The dispersive term $\beta(\omega)$ is split into the effects of free space, coupler, and DLW:

$$E(\omega) = E(0)\omega^2 \exp\left[-\frac{\omega^2}{2\sigma^2}\right] \exp\left[-i\left(\beta(\omega)_{fs}L_{fs} + \beta_c(\omega)L_c + \beta_{wg}(\omega)L_{wg}\right)\right] \ , \qquad (7.5)$$

where the subscripts fs, c and wg represent free space, coupler, and DLW dispersion respectively. For two structures, where the detection crystal is directly after the structure, the difference in field amplitudes is given as

$$\frac{E(\omega)_{wg,2}}{E(\omega)_{wg,1}} = \exp\left[-i\beta_{wg}(\omega)\left(L_{wg,2} - L_{wg,1}\right)\right] \ , \qquad (7.6)$$

where $\beta_{wg}(\omega)\left(L_{wg,2} - L_{wg,1}\right)$ is the phase difference, ϕ. The dispersion relation is calculated as

$$\beta(\omega) = -\frac{i}{L_{wg,2} - L_{wg,1}} \ln\left[\frac{E(\omega)_{wg,2}}{E(\omega)_{wg,1}}\right] \ . \qquad (7.7)$$

However as ϕ only exists between $\pm\pi$ it must be unwrapped before calculating $\beta(\omega)$. This is the addition of 2π when the phase jumps by more than $\pm\pi$.

The pulse after propagating through free space is shown in Figure 7.4, along with the frequency domain as calculated via a Fourier transform. There are no sharp drops in the frequency domain, which confirms that the water vapour was significantly reduced due to the nitrogen purge. The fields in the time domain with the structures inserted into the THz path are shown Figure 7.5. The pulse is delayed after propagating through the further 5 mm of waveguide for the 10 mm structure, which is to be expected as the total distance travelled is longer. The amplitude is also decreased as the pulse has stretched in time. The pulses in the frequency domain are shown in Figure 7.6. The cut-off frequency is clear in both cases. In addition, there are sharp drops in spectral amplitude which can be compared to the absorption lines of water

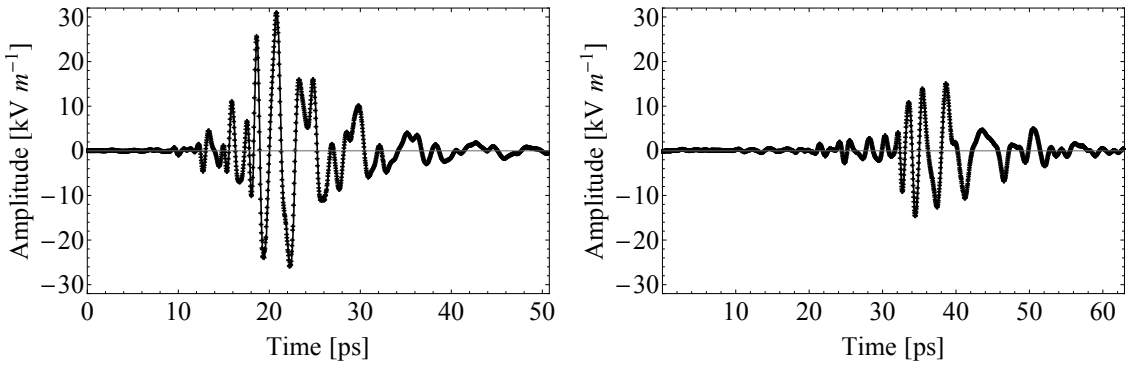

Figure 7.5: Fields in the time domain as measured using a ZnTe crystal butted up to the end of the DLW [141]. Left: 5 mm DLW, right: 10 mm DLW.

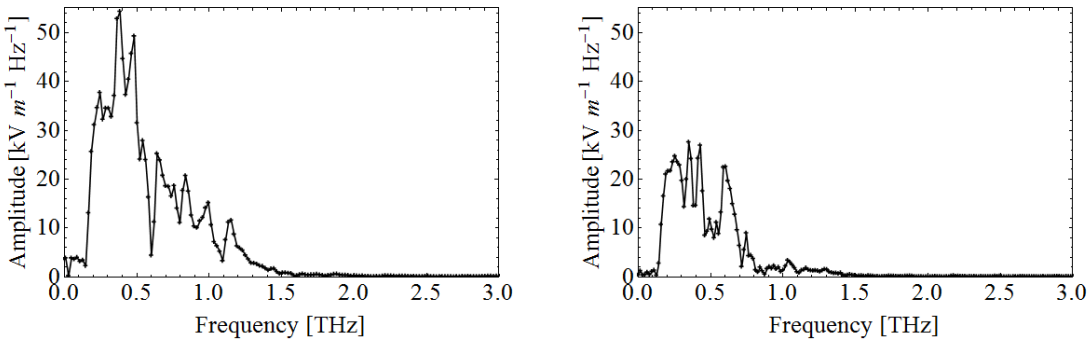

Figure 7.6: Fields in the frequency domain as measured using a ZnTe crystal butted up to the end of the DLW. Left: 5 mm DLW, right: 10 mm DLW.

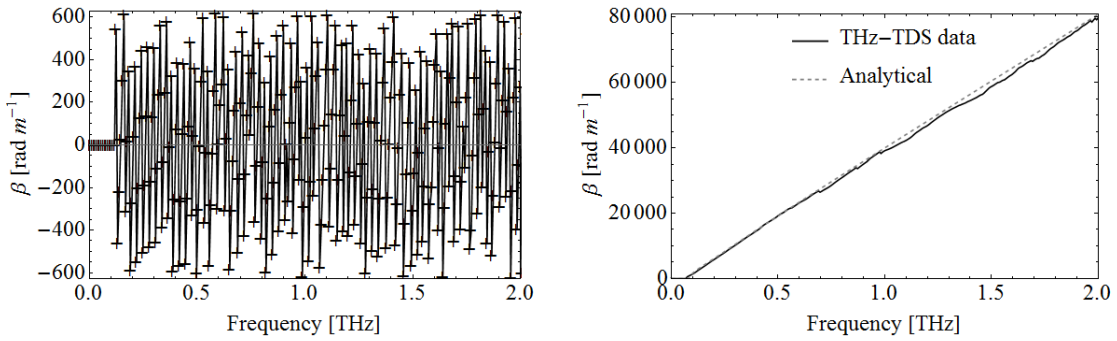

Figure 7.7: $\beta(\omega)$ as calculated from Equation 7.7, using the spectra for the 5 mm and 10 mm DLWs. Left: wrapped data taken from the phase difference between the spectra. Right: unwrapped data showing the dispersion relation, with the analytical solution shown for comparison.

vapour, examples of which occur at 0.557 THz, 0.752 THz and 0.988 THz [142, 143]. It is not clear within the spectra if they are present as the minima of the drops do not correspond exactly to these absorption lines; either the humidity was sufficiently low or the resolution was not high enough to resolve the absorption.

The dispersion relation as calculated from Equation (7.7) is shown in Figure 7.7. The wrapped phase calculated from the raw data is shown along with the unwrapped data. The interpolated dispersion relation function, as calculated from Equation (2.76), is also included in the figure for comparison. The general form of $\beta(\omega)$ is correct, but close to cut-off the non-linearities of the dispersion relation are not well replicated. There are also discontinuous jumps in the data which have not been removed by the unwrapping routine. The phase velocity was directly calculated from $\beta(\omega)$; it is shown in Figure 7.8. $v_p(\omega)$ as calculated using the interpolated form of $\beta(\omega)$ is also plotted; the higher frequencies are again better replicated than lower frequencies. The operating frequency of the structure is found from the data. For 100 keV electrons, $v_e = 0.54822\ c$, which corresponds to $f_{op} = 0.503$ THz for the analytical dispersion relation. From the data, this corresponds to 0.59 THz; however as the curve is discontinuous this cannot be determined accurately. Due to these discontinuities the group velocity is poorly characterised. Shown in Figure 7.9 is $v_g(\omega)$ calculated from both the raw data and a fit applied to the raw data. From this analysis it is apparent that THz-TDS is useful to give a rough estimate of the dispersion relation. It is however necessary to use a higher resolution; the frequency resolution is 7 GHz in this study. An increase in resolution is achieved by scanning over a larger delay stage (and thus time range); in Figure 7.5 the signals in the time domain have not decayed to zero.

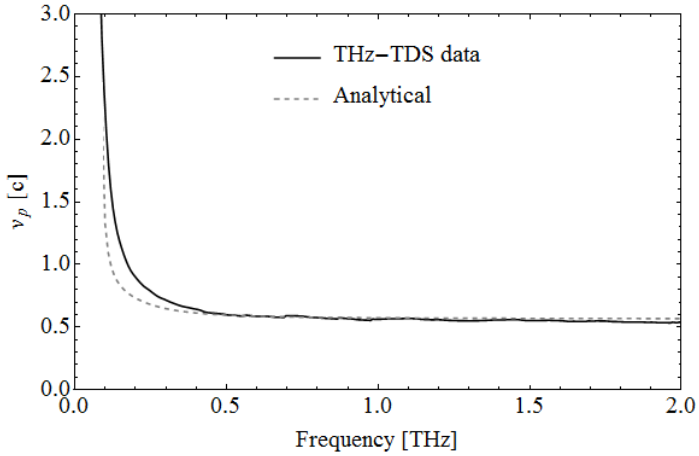

Figure 7.8: Phase velocity as calculated for a DLW designed for deflection of 100 keV electrons, as measured using THz-TDS.

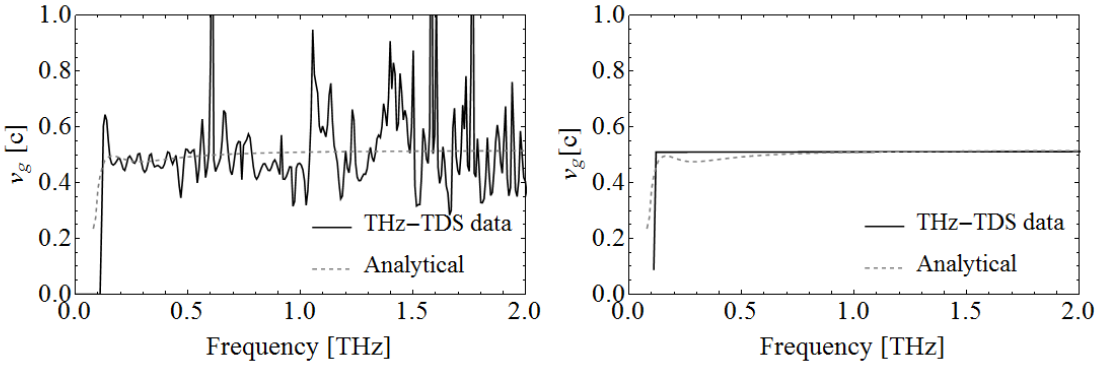

Figure 7.9: Group velocity as calculated for a DLW designed for deflection of 100 keV electrons, as measured using THz-TDS.

It is useful to establish another method of finding the phase and group velocity; one such example is time-frequency analysis via the short-time Fourier-transform (STFT). A window function, which is zero except for a short time period, $w(t-\tau)$, is swept across the analytical signal, $x(t)$;

$$X(t,\omega) = \int_{-\infty}^{\infty} x(t)w(t-\tau)\exp\left[-i\omega t\right]\mathrm{d}\omega \ . \tag{7.8}$$

$w(t-\tau)$ must be carefully selected so as not to cause ringing in the frequency domain. This allows for localisation of the frequencies to within this window. A narrower window improves the time resolution, but the smaller number of points reduces frequency resolution. This is due to the Gabor limit; one cannot simultaneously achieve high time domain and frequency domain resolution of a signal [144]:

$$\sigma_t\sigma_f \leq \frac{1}{4\pi} \ . \tag{7.9}$$

This is not a hard limit provided other analysis methods are used [145]. One such example is the Wigner-Ville distribution [146], defined as:

$$W_x(t,\omega) = \int_{-\infty}^{\infty} x\left(t+\frac{\tau}{2}\right)x^*\left(t-\frac{\tau}{2}\right)\exp\left[-i\omega\tau\right]\mathrm{d}\tau \ . \tag{7.10}$$

this allows for calculation of both instantaneous frequency and group delay. Instantaneous frequency can be calculated from [147]:

$$f_x(t) = \frac{\int_{-\infty}^{\infty}\omega W_x(t,\omega)\mathrm{d}\omega}{\int_{-\infty}^{\infty}W_x(t,\omega)\mathrm{d}\omega} \ , \tag{7.11}$$

and group delay of the analytic signal x is calculated from [148]:

$$t_x(\omega) = \frac{\int_{-\infty}^{\infty} tW_x(t,\omega)\mathrm{d}t}{\int_{-\infty}^{\infty}W_x(t,\omega)\mathrm{d}t} \ . \tag{7.12}$$

However the WVD is also limited due to the presence of interference terms. These can overlap with the signal terms, making results difficult to interpret. Negative values can be produced, which correspond to a negative energy and are therefore unphysical. The WVD plots are shown in 7.10 and 7.11. In both figures the interference terms are clearly visible, implying non-physical negative energy components. In Figure 7.11 the main curve is easy to track as there are no interference offshoots. This is not the case with the 5 mm DLW structure in Figure 7.10. In both cases, the cut-off frequency

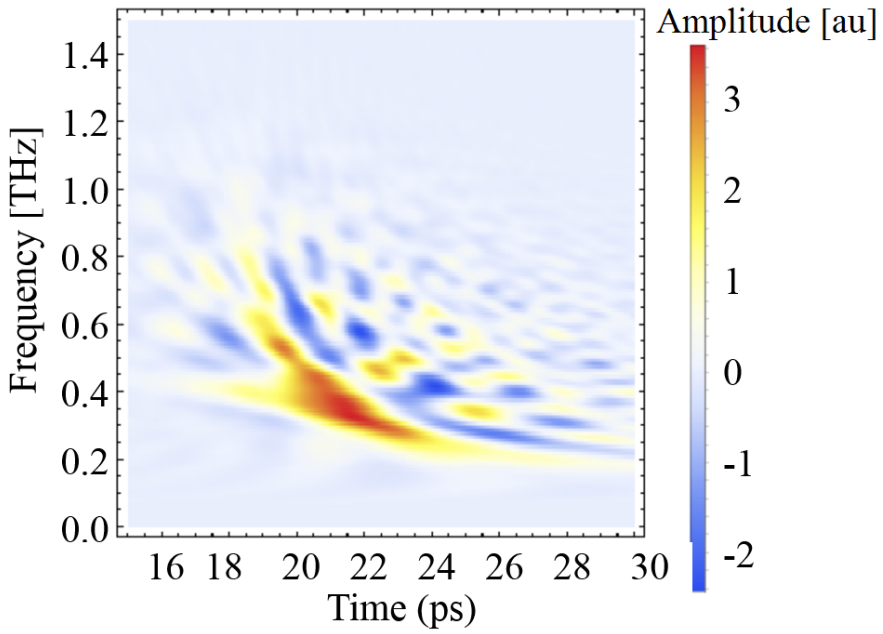

Figure 7.10: Time-frequency plot of the broadband THz pulse as measured at the end of the 5 mm DLW structure, calculated using the WVD.

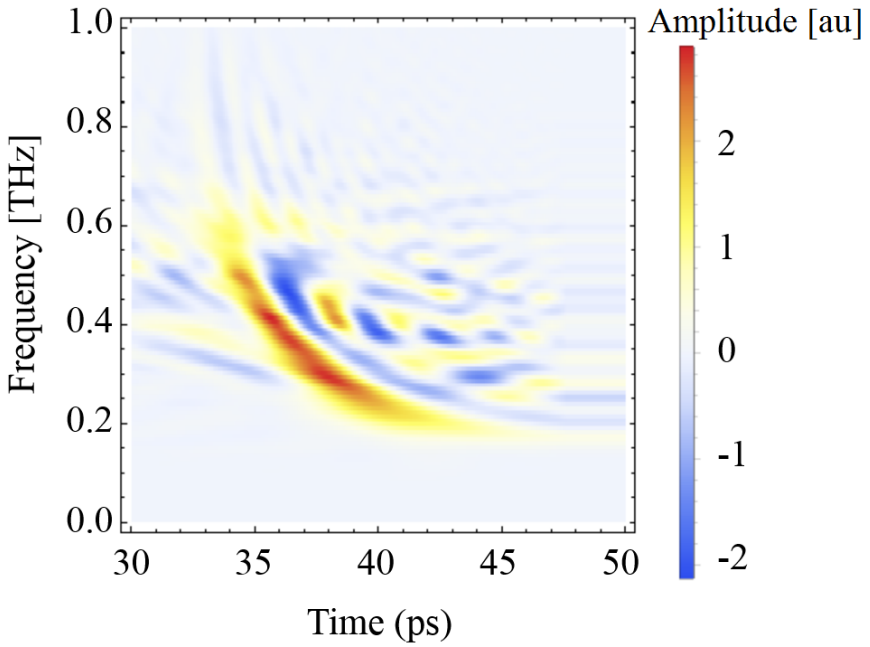

Figure 7.11: Time-frequency plot of the broadband THz pulse as measured at the end of the 10 mm DLW structure, calculated using the WVD.

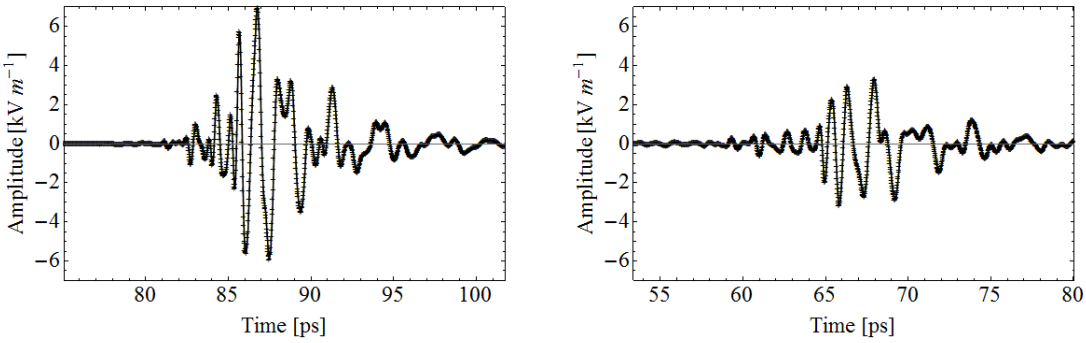

Figure 7.12: Fields in the time domain as measured using a ZnTe crystal butted up to the end of the DLW [141]. Left: 5 mm DLW, right: 10 mm DLW. These measurements were taken before that in Figure 7.5.

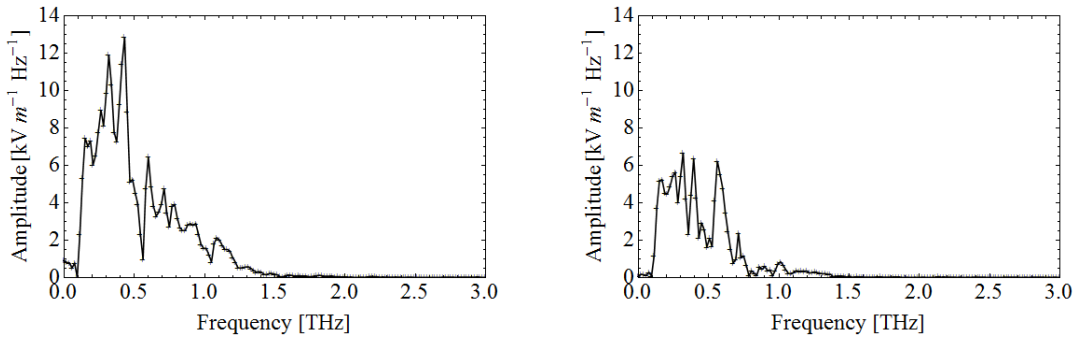

Figure 7.13: Fields in the frequency domain as measured using a ZnTe crystal butted up to the end of the DLW. Left: 5 mm DLW, right: 10 mm DLW. These measurements were taken before that in Figure 7.6.

is that at which the curves flatten out. However this appears to be approximately 0.2 THz which is incorrect; this is due to the low signal for lower frequencies which means that the curve becomes inaccurate. This suggests that there are not enough data points in either the time or frequency domain to accurately resolve the group velocity. Considering Figure 7.6 it can be seen that the full pulses have not been recorded; this was due to the limited length of the scanning delay stage.

It is important to note that the signals recorded in the time domain were strongly dependent on the position of the waveguide structure and changes to the optics line over time, due to shifting of components. Examples of the THz pulse in the time domain after propagating through the 5 mm and 10 mm structures, taken at a time before those in Figure 7.5, are shown in Figure 7.12, with the corresponding frequency domain in 7.13. The amplitude of the THz pulse was smaller due to lower laser energy. Comparing the pulses in the time domain to those in Figure 7.5, the forms are similar. Looking instead at the frequency domain and comparing to Figure 7.6, the spectra

of the 5 mm structure have the same drops at approximately 0.6 THz and 1.1 THz. The spectra of the two datasets differ most at low frequencies, around 0.2-0.4 THz. However, the cut-off frequency is the same for both datasets. For the 10 mm structure, the drops at approximately 0.5 THz and 0.7 THz appear in both Figures 7.6 and 7.13. Again, the lower frequencies of the spectra differ for the two datasets, but the cut-off frequency is the same. The differences are likely a result of slight misalignment of the structure; a five-axis stage was used to adjust the position of the structures but alignment was done by eye using a level. This means that the vertically-polarised THz pulses were entering at a slight angle with respect to the input face of the structure, and the structure itself was offset with respect to the centre of the transverse pulse profile.

In summary, a DLW structure has been analysed using THz time-domain spectroscopy to calculate the dispersion relation of only the DLW. Two structures were used; the coupler was the same in both cases and the only DLW parameter which varied was the length. By measuring the electric field amplitude at the end of two structures the frequency domain was compared to produce the dispersion relation of the DLW. As the delay stage was too short to measure the full THz pulse, frequency domain information was lacking which reduced resolution. The low frequency components, which are more non-linear, were therefore less well characterised. However it was possible to establish the cut-off frequency and estimate the operating frequency, making the technique useful in determining that the manufactured structure does not differ significantly from the design.

7.2 Measurement of structure dimensions

Although THz-TDS allows for determination of the dispersion relation and therefore highlights the existence of any differences in the structure parameters between the designed and manufactured structures, it does not allow for explicit determination of where the errors lie. The most direct method is to measure the dimensions of the input and output apertures of the structure. There are also limitations here; without destroying the structure it is only possible to analyse faces.

This method was used to measure the dimensions of the structure designed for acceleration of 35 MeV electrons, with parameters $a = 250$ μm, $w = 1200$ μm, $\delta = 50$ μm and $\epsilon_r = 3.75$ for a DLW length 30 mm. The coupler aperture is a square with sides of length 3.175 mm. Using a microscope camera, images were taken of the coupler aperture face and output face. These are shown in Figure 7.14. A zoomed image of the output aperture is shown in Figure 7.15, with a drawing of the imaged aperture and measured dimensions to highlight the changes in dielectric thickness.

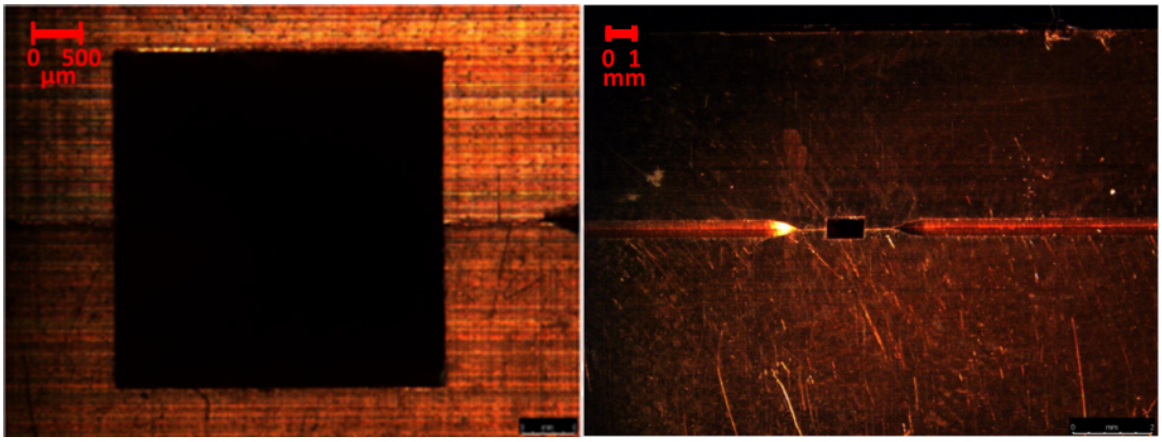

Figure 7.14: Images of the coupler input (left) and DLW output (right) apertures taken using a microscope [141].

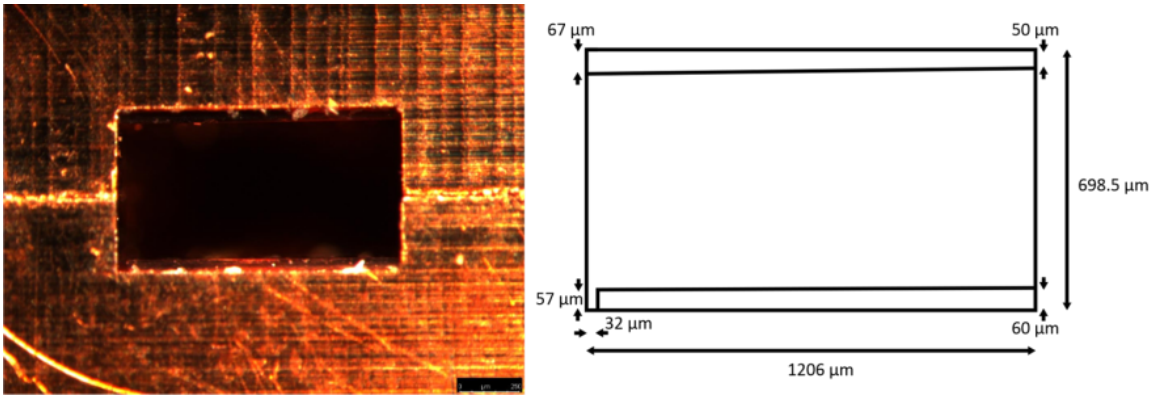

Figure 7.15: Left: Microscope image of the output DLW aperture, showing the dielectric. Right: dimensions of this aperture [141].

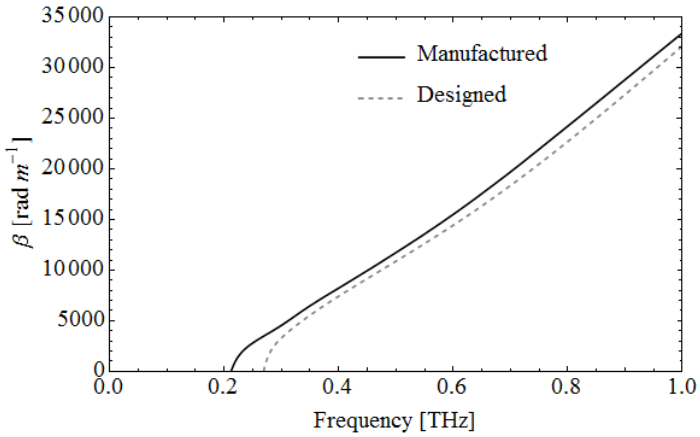

Figure 7.16: The dispersion relation of the manufactured structure compared to the design.

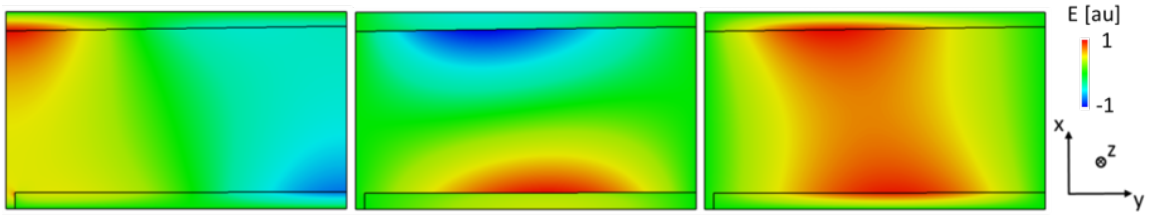

Figure 7.17: Normalised electric field profiles for the manufactured structure, as measured at the operating frequency, 0.411 THz. From left to right: E_x, E_y and E_z.

This analysis highlighted several discrepancies. Firstly, the vacuum aperture is larger than designed by nearly 100 μm. Secondly, the dielectric is thicker than design. This in itself is not unexpected as tolerances on the thickness were ± 10 μm. However it was expected that the variation across a dielectric tile would be less than 1 μm. Assuming that this is the case, the change in thickness may instead be due to the epoxy resin used for affixing dielectric to metal. The permittivity of this resin is unknown.

The dispersion relation for the manufactured structure has no analytical solution due to the inhomogeneity of the cross-section. CST is used instead to calculate β, which is shown in Figure 7.16. The cut-off frequency is 0.212 THz, which is smaller that the design value of 0.269 THz. The operating frequency is calculated to be 0.411 THz, which is considerably smaller than the design value (0.473 THz). This is explained almost completely by the change in aperture. It is also useful to observe the field profile, which is expected to no longer be exactly the LSM_{11} mode; the normalised electric field components are shown in Figure 7.17. There is a change in the field pattern which is a result of the tilted dielectric surface. This does not

Figure 7.18: Local maximum of the transverse electric field on the corner of the dielectric slab in the bottom left of the DLW.

have a large effect on the axial electric field and so was not expected to impact the experiment.

The small gap between dielectric and copper leads to a local maximum of the transverse electric field which is shown in more detail in Figure 7.18. This is a concern for high field strengths as it is a place where electrical breakdowns can occur. However as this field is primarily due to the E_x component, this is approximately a fifth of the magnitude of the E_y field on the dielectric surface.

7.3 Summary

Two methods of analysing the DLW structures have been investigated; THz time-domain spectroscopy and measuring the dimensions using a microscope camera. Ideally both would be used in conjunction; using the images of the apertures to correct the design parameters in simulation and the THz-TDS to then confirm that the simulated dispersion relation matches the measurement. For example, it was possible to ascertain that the accelerating structure was manufactured incorrectly; discussions with the manufacturer confirmed that there had indeed been a mistake in machining. This meant that the THz centre frequency for the experimental work into acceleration of 35 MeV electrons had to be shifted.

7.4 Acknowledgements

THz-TDS was performed in conjunction with V. Georgiadis and M. Hibberd, who built and operated the setup. Data collection was performed in conjunction with V. Georgiadis. Images from the microscopic analysis were taken by V. Georgiadis. The waveguide structures were manufactured by P. Huggard and B. Alderman of the MMT group, part of RAL Space.

Chapter 8

Experimental demonstration of THz-driven electron bunch manipulation using a dielectric-lined waveguide

Experimental demonstration of electron bunch manipulation was performed at the CLARA/VELA facility at Daresbury Laboratory [149]. CLARA (Compact Linear Accelerator for Research and Applications) provided electron bunches with energy 35 MeV. A terawatt laser laboratory is housed within the facility; this was necessary for generating the THz pulses required. CLARA features an experimental area, Beam Area 1 (BA1), which contains a vacuum chamber and necessary beam diagnostics. An image of BA1 is shown in Figure 8.1. At the time of the experiments, performed in January 2019, CLARA was between stages of development and so the beam properties were not optimised.

This chapter includes a description of the experimental setup, namely the development of custom diagnostics, placement of existing equipment, and an overview of the THz source and optics. The electron bunch properties are discussed with an emphasis on the effect of the RF phase of the linac. The results obtained at a range of linac phases, at which the bunches had different bunch length and energy spread, are then presented.

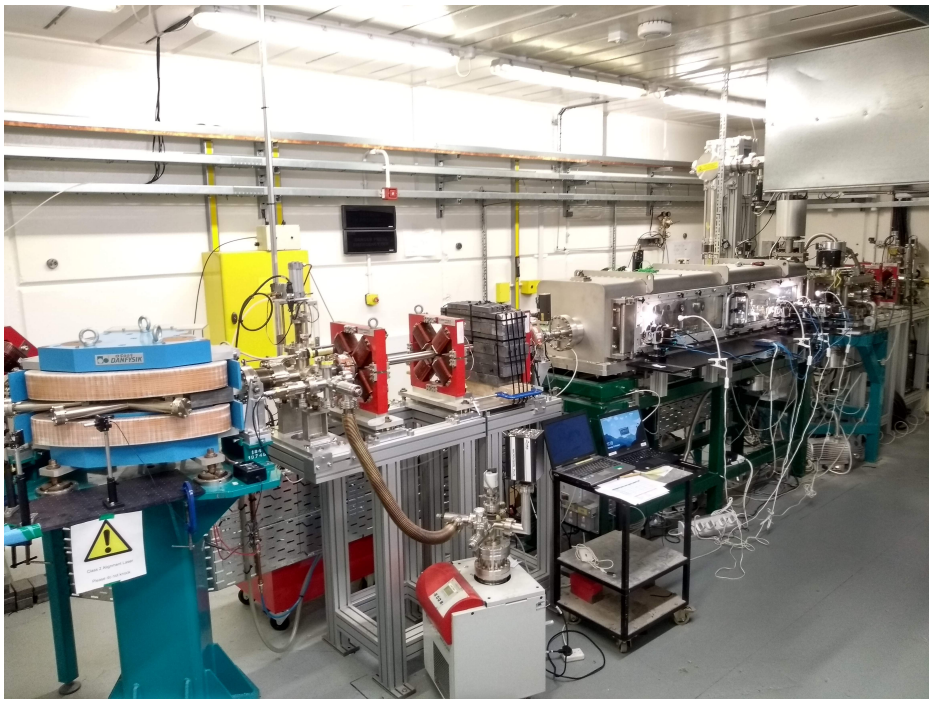

Figure 8.1: Image of Beam Area 1. The vacuum chamber is shown from the access side. The cameras and lights used for imaging are mounted on a shelf. After passing through this chamber, electron bunches are then transported to the final Faraday cup through a quadrupole triplet. The dipole is part of the energy spectrometer.

8.1 Accelerator and laser layout

8.1.1 THz beamline

The terawatt laser is housed separately from BA1 and the laser is fed through to the experimental chamber under vacuum. It produces 60 fs pulses with centre wavelength 800 nm of energy up to 800 mJ and repetition rate 10 Hz. The system features an initial Ti:sapphire oscillator which produces 30 fs, 4 nJ pulses centred on 800 nm at a repetition rate 83 MHz. This seeds a Ti:sapphire regenerative amplifier, which provides 50 fs, 1 mJ, 800 nm pulses at a 1 kHz repetition rate. This then feeds a multi-pass Ti:sapphire amplifier producing the final output laser with centre wavelength 535 nm, length 10 ns, 1.5 J energy and repetition rate 10 Hz. The maximum achievable energy was not available for the experiment; only 100 mJ was used which resulted in 50 mJ after beam transport to the experimental chamber. This loss arises due to optical components along the laser line.

Narrowband THz pulses were generated using a chirped-pulse beating scheme [150, 84]. The input laser pulse was chirped by use of the grating-pair compressor on the TW system. The laser beam was then split using a beam splitter and a Michelson interferometer used to add a variable phase delay. Changing the length of one of the paths allows for variation of the THz centre frequency. The input laser pulse was 12 ps, and tilting of the pulse front was achieved using a diffraction grating. Linearly polarised THz was generated via illumination of a magnesium oxide doped $LiNbO_3$ crystal using this recombined laser pulse, with FWHM bandwidth of 50 GHz, and centre frequency set by the Michelson arms. The accelerating mode was then created using a segmented polytetrafluoroethylene (PTFE) waveplate. There was a step change in thickness across the vertical dimension, resulting in half of the pulse being delayed by half a wavelength. The thickness of each segment was accurate to within 100 μm.

Although the laser beam was transported into the beam area under vacuum, it then exited through a Z-cut quartz window to air. The optical setup for THz generation and measurement was built outside of the vacuum chamber and then fed into the interaction chamber. The optical setup was constructed in advance on separate boards, which were then put back together on top of the 'breadboard'. This setup is shown in Figure 8.2. The chirped laser was first sent to a delay stage to change the time of arrival (TOA) of the THz, necessary for synchronisation. The pump laser was then guided to the Michelson interferometer before application of a phase front tilt. The THz radiation, once generated, was collected by an off-axis parabolic (OAP)

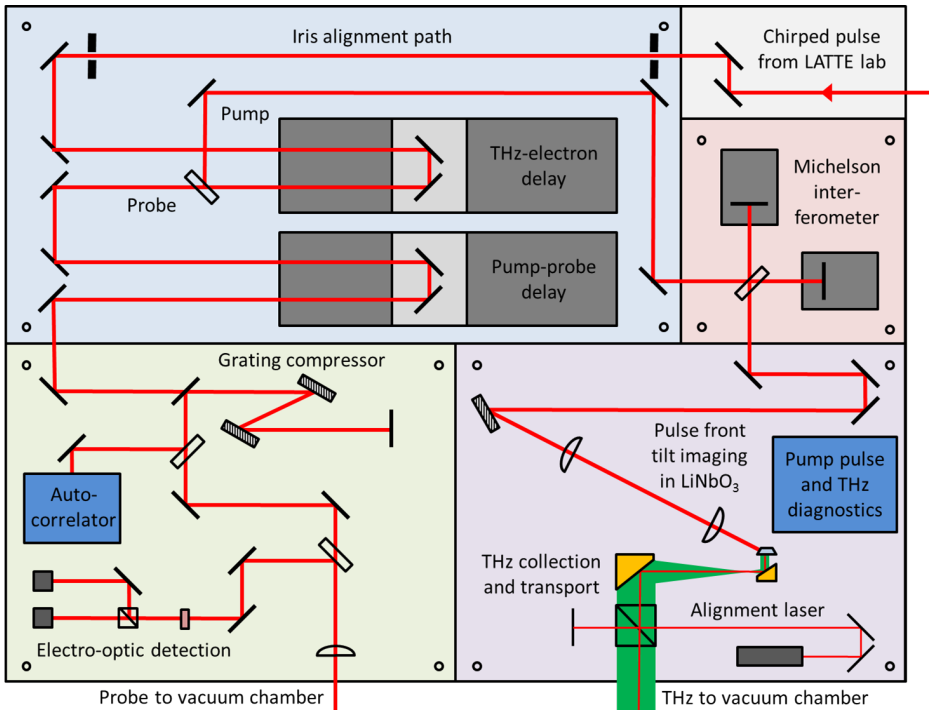

Figure 8.2: Optical setup leading to the THz source. The red path signifies the 800 nm laser, and green represents THz. The thicknesses of the lines are a guide to the transverse size, but not to scale. Figure courtesy of M. Hibberd.

mirror and guided into the experimental vacuum chamber using silver mirrors. The pulse was focussed down to a spot size with $\sigma = 750$ μm onto the entrance of the coupler, as this allowed for maximum transmission through the DLW structure.

The THz inside the experimental chamber could be sampled using an electro-optic setup. The laser pulse was split into pump and probe beams. The probe beam was recompressed to 6 fs using another grating-pair compressor, and focussed onto a 500 μm thick (110)-cut zinc telluride crystal. Time-domain measurements of the THz pulse were performed by use of a delay stage for the probe beam.

A pyroelectric detector was used to perform measurements directly after THz generation, but was not suitable for use in vacuum. When the experimental chamber was at atmospheric pressure (with no electron beam) the pyroelectric detector was also used to perform energy readings at the end of the structure. Due to the lack of output coupler the THz was emitted from the exit of the DLW with a wide angle. This is demonstrated in Figure 8.3, which shows the magnitude of the simulated electric field after exiting the DLW, as modelled using the time domain solver in CST. The THz is emitted as two lobes with minimal field on axis. Therefore a detector placed directly after the waveguide requires a large acceptance angle.

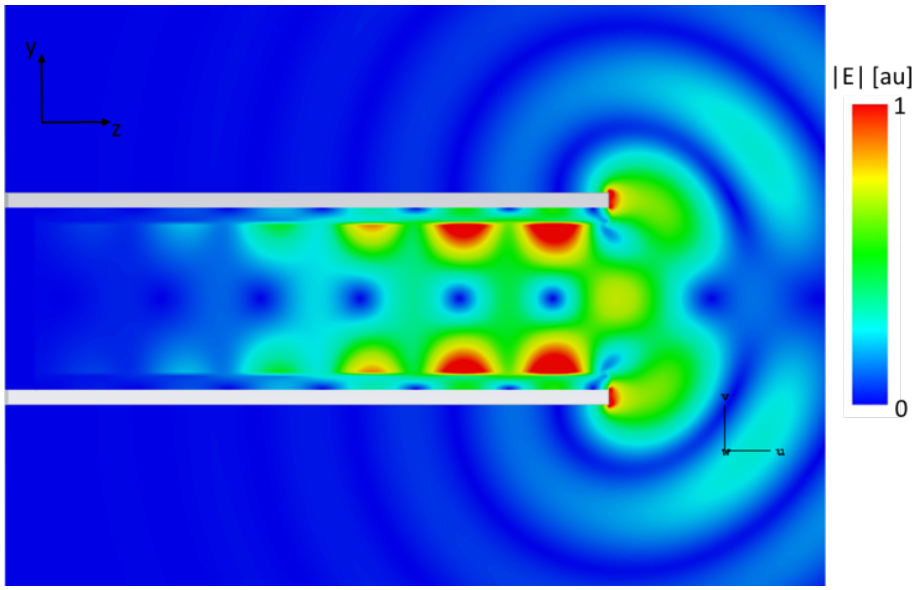

Figure 8.3: Cross-section view of the magnitude of the electric field of a THz pulse exiting the DLW, simulated using the time domain solver in CST.

Using the electro-optic setup the THz field was measured in the time domain at atmosphere. Electro-optic modulation has been discussed comprehensively elsewhere in [138], with an overview provided in Section 7.1.2. In summary, a birefringent crystal, ZnTe in this case, was illuminated with an electric field which modulates the birefringence proportional to the field amplitude. A near-infrared probe laser, which was directed onto the back of the crystal, reflected back onto a photodiode. A change in birefringence modifies the polarisation of the probe laser and so the electric field of, for example, a THz pulse, can be mapped as a function of change in polarisation of the probe with time. The EO detection scheme could not be used under vacuum as vacuum-compatible components were not available. As a result THz time-domain measurements were not performed in conjunction with interaction measurements.

THz pulses measured both in free space and after propagation through the waveguide are shown in Figure 8.4. The data showing THz propagation through the structure was not taken with the ZnTe crystal pushed up against the output aperture, and so the field was weak and poorly characterised due to the wide angle of the THz output from the waveguide, as shown in Figure 8.3. The profiles show a double pulse due to reflections and the measurement duration was not long enough to record the whole pulse. Therefore the data in Figure 8.4 cannot be used to quantify THz transmission through the DLW structure, the design of which is discussed in Chapter 6. Figure 8.5 shows the field amplitude in the frequency domain. The pulse is centred on 0.39 THz with a bandwidth $\sigma_f = 0.042$ THz.

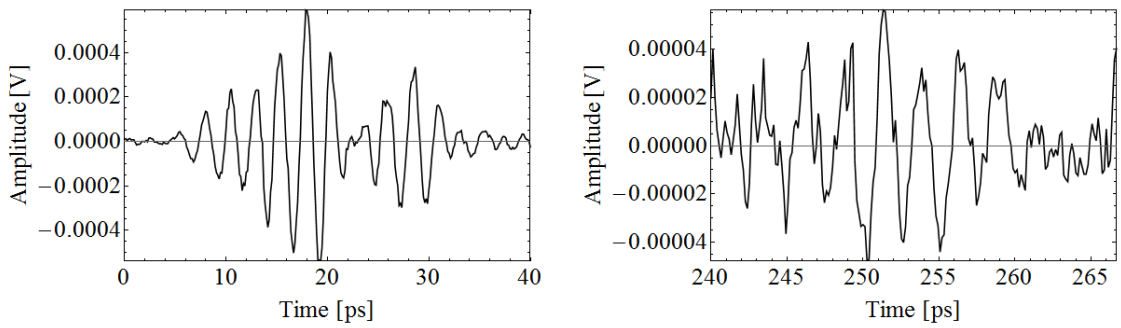

Figure 8.4: THz field amplitude as a function of time. Left: after propagation through free space, right: after propagation through the DLW structure. Data courtesy of M. Hibberd, D. Lake, and V. Georgiadis.

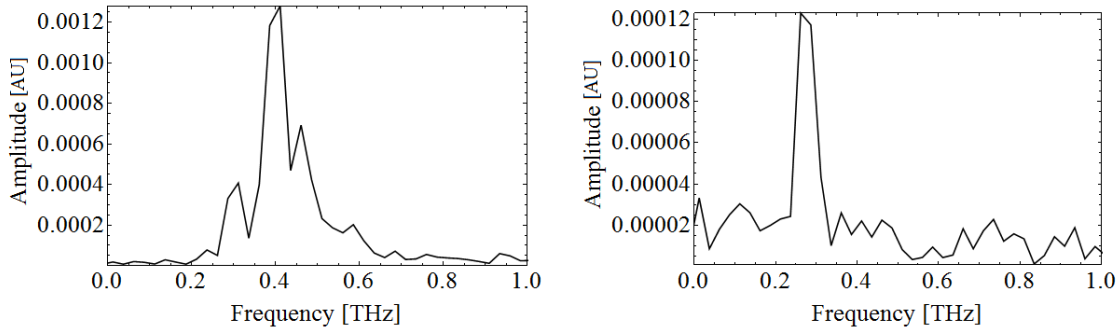

Figure 8.5: THz field amplitude as a function of time. Left: after propagation through free space, right: after propagation through the DLW structure. Data courtesy of M. Hibberd, D. Lake, and V. Georgiadis.

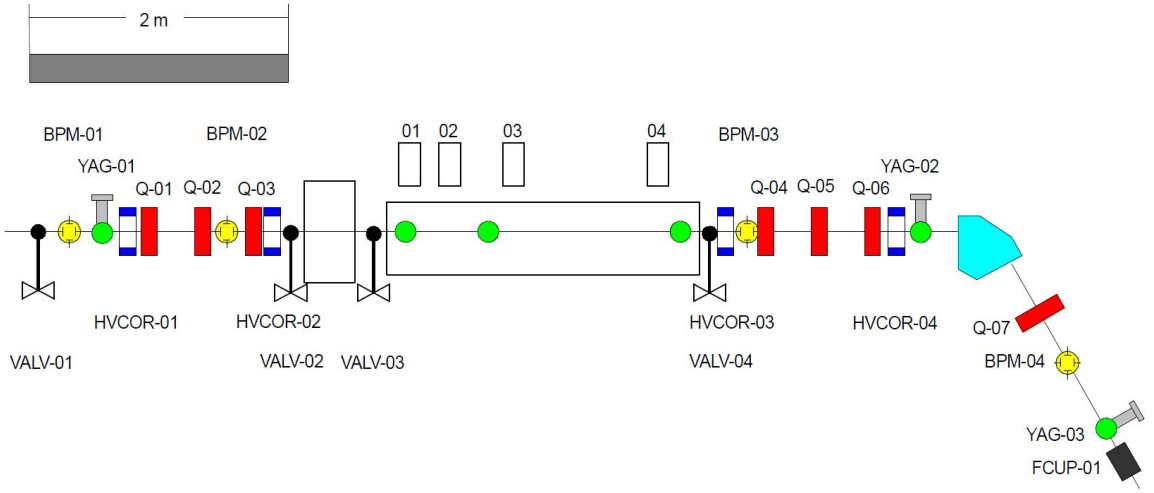

Figure 8.6: Schematic diagram of CLARA BA1. The magnets, valves, and diagnostics positions are shown.

8.1.2 Electron beamline

Only the electron optics inside the beam area are considered here. The optics of the preceding beamline followed a standard setup procedure which had been developed to maximise charge transport to BA1. The key components of the accelerator are briefly described below.

Electrons are generated in a radio frequency (RF) gun using a copper cathode illuminated by a UV photo injector (PI) laser. The electrons are first accelerated to approximately 5 MeV with a field gradient of approximately 70 MV/m. The electron bunch exits the gun with a positive longitudinal energy spread, or chirp. 'Positive' chirp is defined such that the head of the bunch has higher energy than the tail.

The bunch then enters the linac which accelerates the electrons to their final energy of 35 MeV. The RF phase of the linac affects the energy chirp of the bunch. The beam is then transported to the dogleg. The longitudinal phase space at the exit of this dogleg is dependent on the RF phase of the linac, ranging from decompression, compression, to over-compression.

The beam is finally transported to BA1, which is isolated from the rest of the machine by a concrete shield wall. Figure 8.6 shows a schematic diagram of the beamline in BA1. For the purposes of these experiments, only the cameras and YAG screens of the vacuum chamber and the energy spectrometer are considered. The energy spectrometer consists of the dipole, final quadrupole (Q-07) and YAG-03. The quadrupole is used to set the dispersion such that the full energy spread is imaged on the YAG screen.

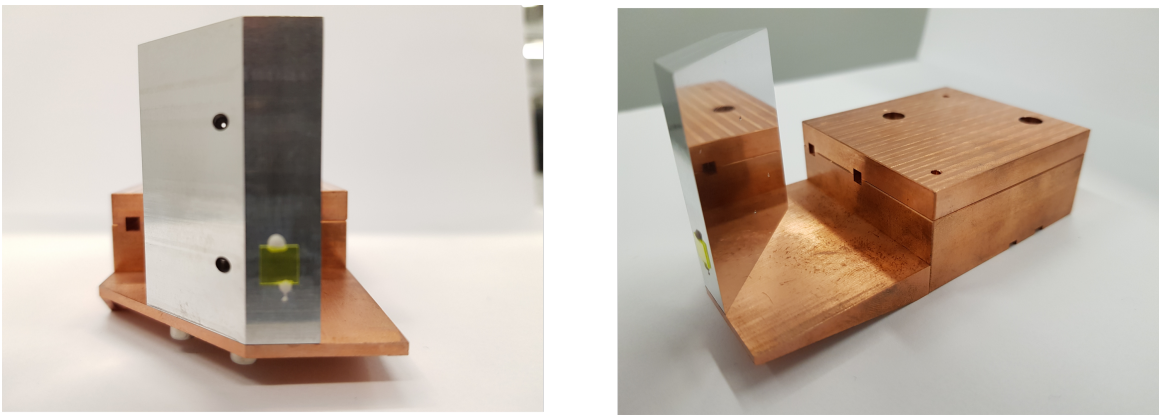

Figure 8.7: Images of the DLW structure showing the surface to which the YAG was glued. Left: front view. The YAG is on the front flat surface. To the left is a 2 mm aperture for electron propagation. Above this is a second aperture used for synchronisation measurements. Right: orthogonal view showing mirror. The 400 μm apertures on the mirror are not resolvable.

8.1.3 Interaction chamber

The vacuum chamber itself is 0.5 m wide, 2 m long, and approximately 0.5 m tall. Motorised stages are used for transverse position variation. Optical breadboards are mounted on the base for this purpose. On one of the long sides are the two quartz windows used for THz and laser transport. The other side consists of two large doors, made of glass and perspex. These doors allow access and enable imaging of the interior of the chamber.

Inside the chamber, positioning of equipment with respect to the electron beam used an alignment laser which counter-propagated with the beam. Two 1-inch YAG screens mounted on translation stages were orientated at 45° to the beam path. One YAG was placed at the start of the chamber, and the other close to the end. A third delay stage, positioned next to the large quartz window, held a vertical delay stage used for THz pulse measurement. A Newport five-axis tip-tilt stage, model 90782-V-M, was mounted onto this and the DLW structure was then affixed on top. The five-axis stage was controlled using unencoded picomotors. However all other motorised stages were repeatable to 1 μm accuracy.

A 5 mm^2 YAG was affixed to the front of the structure, as shown in Figure 8.7, approximately 8 mm in front of the centre of the input mirror aperture. The structure front as imaged in the vacuum chamber is shown in Figure 8.8. The blurred image of the aperture is due to the low depth of focus of the camera lens, and so this uncertainty of input aperture was taken into account during alignment.

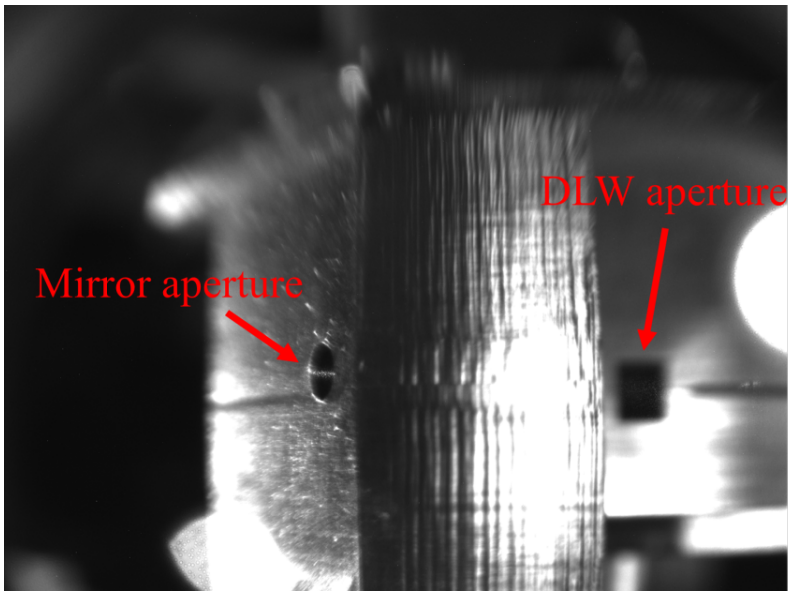

Figure 8.8: Image of the front of the DLW structure as seen in the beamline. The mirror aperture and DLW input aperture appear to be misaligned due to the lens used in imaging.

8.1.4 Synchronisation

In order to synchronise the THz pulses and electron bunches, the time of arrival of the two was measured. Coherent transition radiation (CTR) is emitted when a charged particles passes from vacuum into metal [151, 152]. The frequency is in the sub-THz range for bunches of order ps in length, and so the two signals can be measured using the same sensor.

A target was mounted on top of the DLW structure; this was a gold-coated prism mirror chosen so as to also reflect the THz pulses. Electrons propagated through an aperture in this mirror. The CTR target itself was angled at 45° to the beam path and placed directly above the entrance of the DLW, as this was the intended focal point of the THz. The CTR and the THz pulses were then collected using an OAP mirror with focal length 2 inches and directed to a Schottky diode. A description of this diode and the manufacturing process detailed in [153]. The Schottky diode was connected to a DPO70604 oscilloscope with a 6 GHz bandwidth. The diode had a minimum rise time of 10 ps, but the oscilloscope was limited to about 60 ps by the bandwidth. For synchronisation only the relative time of arrival of the CTR and THz pulse signals was required, although differences between the profiles makes it simple to distinguish the two. Example signals as displayed on the oscilloscope are shown in Figure 8.9.

The time of arrival of the THz pulse was first adjusted by delaying the Terawatt

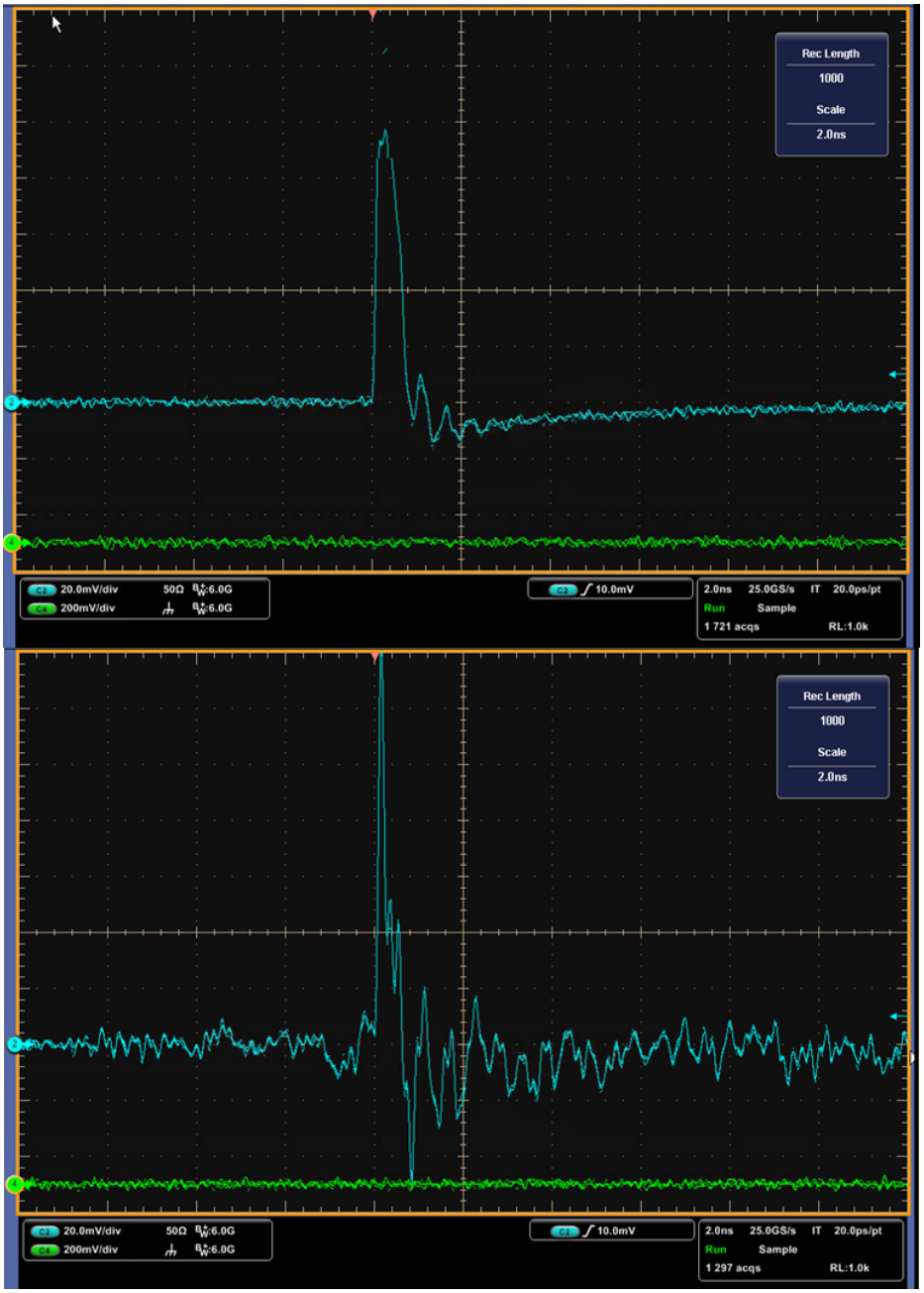

Figure 8.9: Example signals from the oscilloscope. Top: THz signal. Bottom: CTR signal from electron bunch.

laser. This resulted in synchronisation to within 12 ns, sufficient to overlap the signals on the oscilloscope. The structure was translated vertically so that the electron bunch and THz pulse propagated through the DLW. The THz-electron delay stage was then moved in steps of 10 ps to scan over a 2 ns range, observing the energy spectrum of the bunch.

Timing jitter was present for both the terawatt laser and the electron bunches. Jitter was expected to be approximately 500 fs, which is approximately a quarter of a period of the THz pulse. It was therefore expected that observed interaction would vary with each shot; for single bucket acceleration this would range from acceleration to energy spread increase. The electron bunches jitter in terms of both mean energy and energy spread. A change in mean energy is due to both amplitude and phase jitter of the linac, and results in variation of the TOA of the bunches.

8.2 Longitudinal dynamics of the electron bunches

The longitudinal bunch properties are strongly dependent on the RF phase of the linac. Shown in Figure 8.10 is the energy spread as a function of linac off-crest phase as measured on the final YAG screen in BA1, YAG-03. Starting from the most

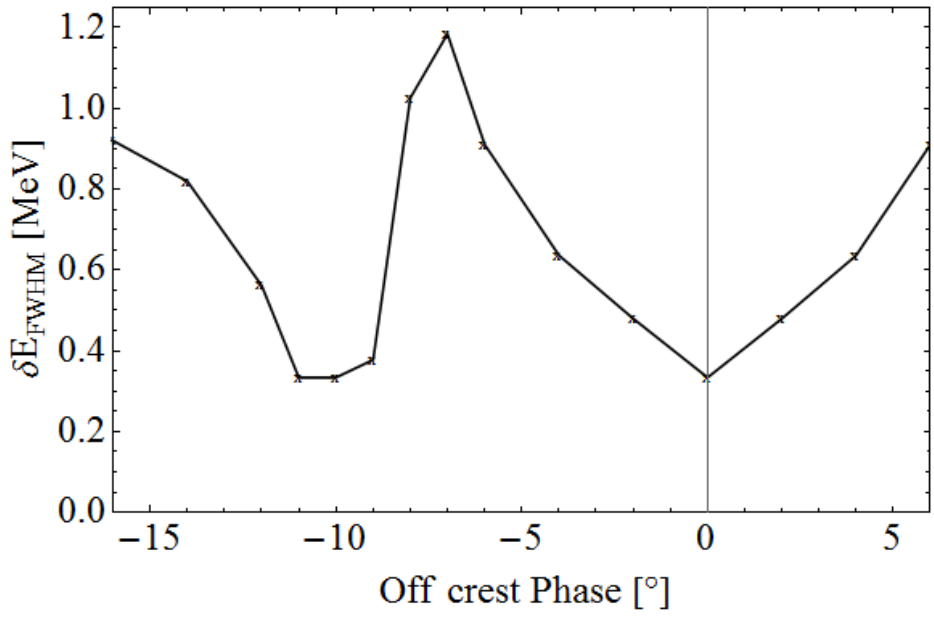

Figure 8.10: Example phase scan showing the FWHM energy spread. The energy spread is minimum at a linac phase of +4°, with another minimum at −10°.

positive linac phase, the bunch first has minimum energy spread at +4°. This is where the chirp introduced in the RF gun cancels with that from the linac. The bunch is at maximum compression at approximately −7°, which is a result of the dogleg. Beyond this the bunch is 'over-compressed', and so the chirp is negative. However the effect at

approximately $-10°$ is to reduce the energy spread whilst maintaining a short bunch length. This has been suggested to be an effect of space charge on the bunch.

The intensity profiles of consecutive shots at a range of phases are plotted as a function of energy in Figure 8.11 to show the shot-to-shot jitter. The same profiles are shown in Figure 8.12 with the peak intensity shifted to zero, showing the change in the energy spectra. The effect of the jitter on the peak energy, mean energy, and energy spread are detailed in Table 8.1. At a linac phase of $+15°$ the shot-to-shot jitter of

Table 8.1: The peak and mean energy, and energy spread, using the twenty shots taken at each RF phase of the linac, as seen in Figure 8.11. The standard error is given for each. In the case of $-7°$, the full-width at 10% of the maximum intensity (FWTM) energy spread is used, as FWHM gives a small energy spread due to the sharp peaks. Peak and mean energy are relative to the centre of the energy range.

Phase [°]	Peak energy [keV]	Mean energy [keV]	Energy spread [keV]
+15	52.4 ± 29.6	5.4 ± 6.0	552.2 ± 2.5 (FWHM)
+4	-99.0 ± 6.3	71.0 ± 6.5	122.2 ± 0.3 (FWHM)
0	-149.0 ± 10.5	-46.3 ± 6.2	287.9 ± 1.3 (FWHM)
-7	-602.7 ± 15.3	9.1 ± 4.4	1369.7 ± 26.8 (FWTM)
-10	15.3 ± 69.1	11.3 ± 5.3	270.7 ± 7.4 (FWHM)

the peak and mean energy is small and the energy spread is consistent. Energy chirp is approximately linear and so it is suitable for demonstration of energy modulation. The energy spread and its error are minimised at $+4°$; the mean and peak energy shift with each shot, but this variation is smaller than at $+15°$. This linac phase is suitable for demonstration of change in energy spread as the longitudinal phase space is flattest and the bunch is longer than a THz pulse wavelength. At this linac phase the uncorrelated energy spread dominates. Moving to a linac phase of $-7°$, the bunch is close to maximum compression and so it is suitable to investigate single bucket acceleration. However, the error on the energy spread is large and the profile of the spectrum varies greatly on a shot-to-shot basis; it was chosen to instead use a linac phase of $-10°$, where the bunch is longer but jitter is reduced. Figure 8.13 shows the mean profile with the standard deviation at linac phases $-7°$ and $-10°$, highlighting the relative stability of the latter. CTR measurements performed in a separate experiment [154] found the RMS bunch length to be $\sigma = 0.3 \pm 0.1$ ps at $-10°$. This is sufficiently smaller than one THz wavelength and so the phase is also suitable for demonstration of acceleration, and so the use of an rf phase of $-10°$ is acceptable.

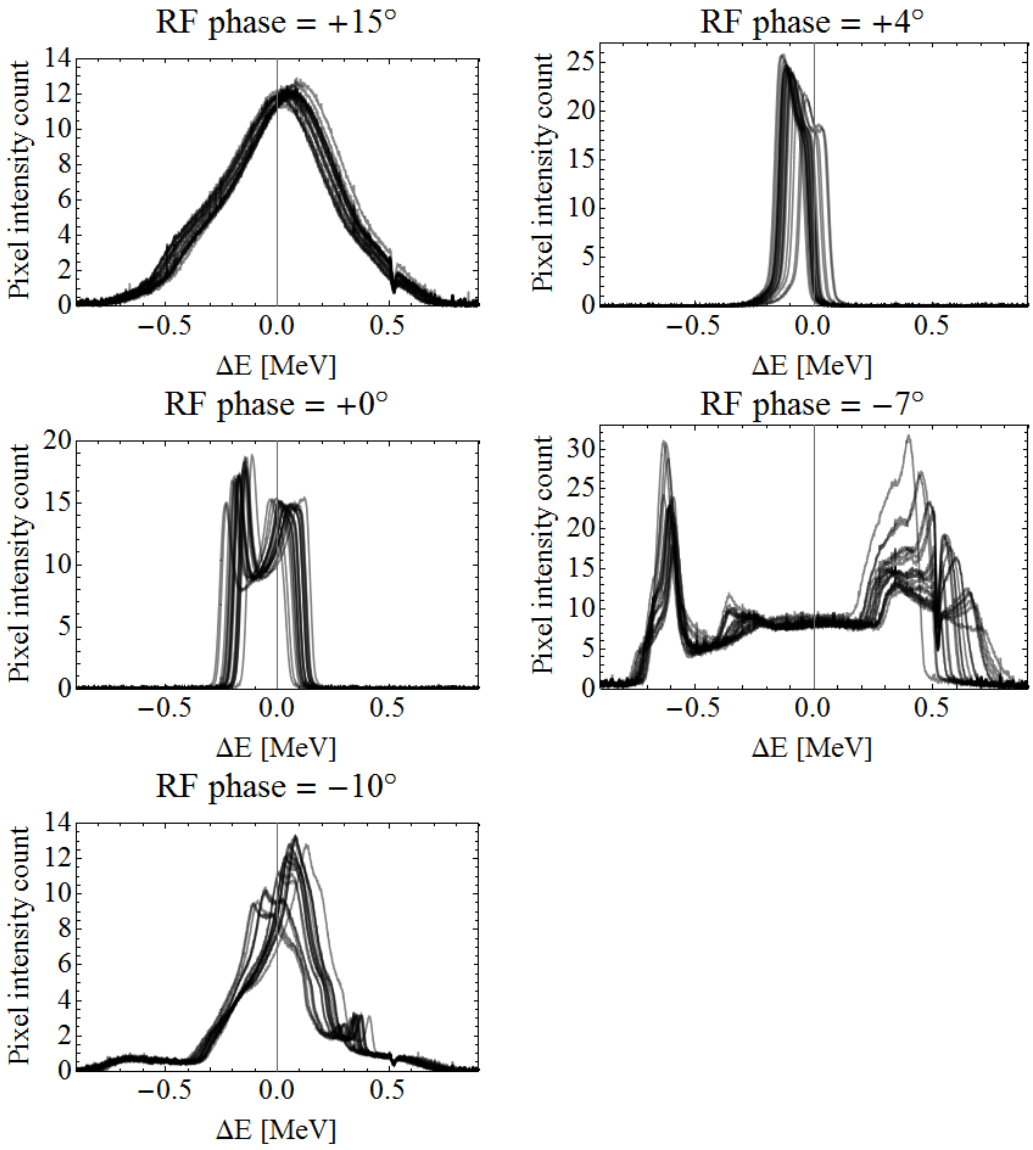

Figure 8.11: Intensity profiles of the electron bunch energy spread, taken on YAG-03. Each consists of 20 images, taken consecutively. The effect of RF phase (written above each plot) is to change both energy spread and the jitter. Dips at $\Delta E \approx 0.5$ MeV are due to an alignment mark on the YAG and are not present in the bunch energy spread itself.

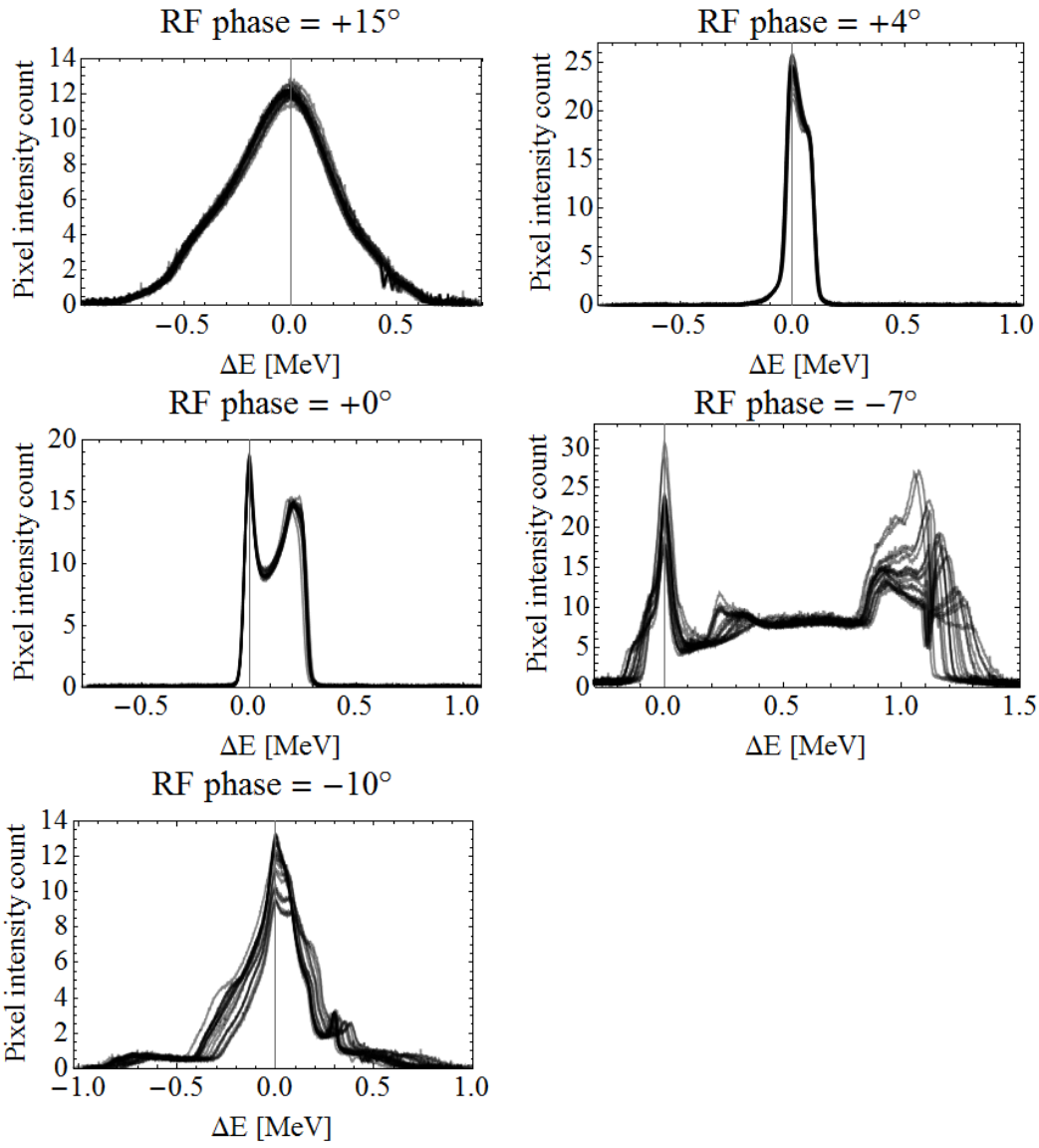

Figure 8.12: Intensity profiles of the electron bunch energy spread from Figure 8.11, taken on YAG-03, at different rf phase values and peaks shifted to zero energy.

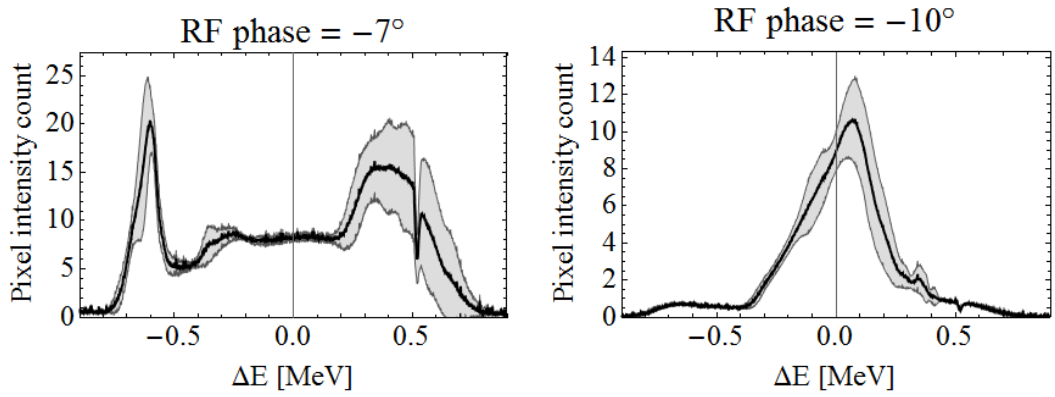

Figure 8.13: Mean and standard deviation of the intensity profiles of the electron bunch energy spread from Figure 8.11, taken on YAG-03, at rf phases of −7° and −10°.

8.3 Experimental results

The experiment was performed in three different longitudinal phase space regimes. Firstly the linac phase was set such that the electron bunches were decompressed with a linear energy chirp, more precisely this was at linac off-crest phases of +10° and +15°. The form of the interaction depends on available THz pulse energy. Figure 6.31 shows that low field strengths result in observed modulation, and a significantly higher amplitude is required for increase in the energy spread.

For bunches with minimal chirp, as at a linac phase of +4°, the energy spread will increase due to THz interaction, as shown in Figure 6.38. With higher field strength the observed interaction varies from an increase in energy spread and reduced intensity of the peak energy, to splitting into two distinct peaks with increasing energy separation.

Observed interaction in these two regimes does not mean that single-bucket acceleration is observable. A compressed bunch with minimal energy jitter is required; this corresponds to a linac phase −10° as discussed in Section 8.2. The modelled interaction in Figure 6.40 shows that it is necessary to have a large field strength for definitive acceleration, similar to that required for peak splitting of a minimally chirped bunch. However the larger jitter at this linac phase means that energy gain must be larger still to be observed.

8.3.1 Bunch energy modulation

Without longitudinal diagnostics it was only possible to demonstrate energy modulation by imparting a change upon an electron bunch with linear chirp. An example electron bunch energy spread, as seen on the YAG screen at the end of the beam area,

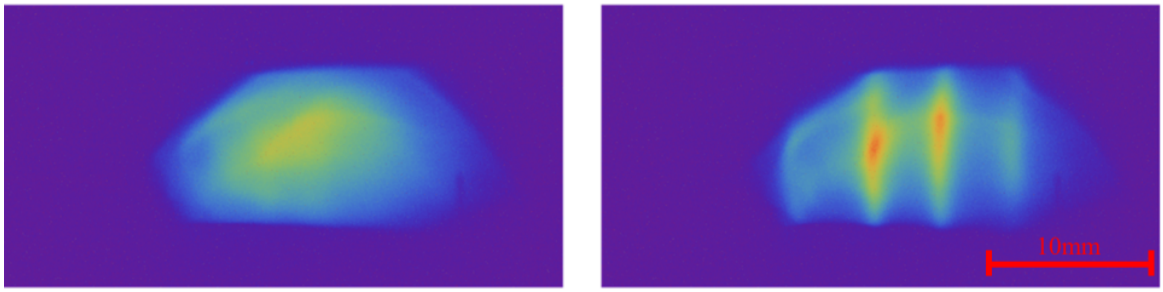

Figure 8.14: Example of a single shot of the bunch at linac phase +10°, as imaged on the YAG-03. The final quadrupole current was set to 0 A. Left: THz off, right: THz on. Modulations in the energy are observable.

is shown in Figure 8.14 with THz off and on for a linac phase +10°. The intensity profiles at linac phase +10° and +15° are compared in Figure 8.15. The bunches at phase +15° have larger energy spread as expected. By taking the difference between THz on and THz off, the periodicity of the modulations is easily observable. There are more periods at linac phase +15°; the bunch is longer and the energy spread is greater.

Figure 8.16 shows the profiles of ten shots at linac phases of +10° and +15°. The peak and mean energies and the energy spread at both rf phases, with THz off and THz on, are given in Table 8.2. The mean energy is consistent with THz on and off, which

Table 8.2: The peak and mean energy, and energy spread, using the 100 shots taken at RF phase of +10° and 15°. FWTM is used to avoid uncertainty in the energy spread due to modulations. The energy profiles when THz is off and on are both analysed.

Phase [°]	+10		+15	
	THz off	THz on	THz off	THz on
Peak energy [keV]	-63.6 ± 1.7	-61.3 ± 3.7	122.1 ± 2.9	103.3 ± 5.0
Mean energy [keV]	-78.1 ± 2.0	-82.4 ± 2.0	31.3 ± 1.8	32.4 ± 1.6
FWTM energy spread [keV]	545.2 ± 5.5	507.9 ± 5.4	756.6 ± 7.7	732.1 ± 1.9

is expected for energy modulation. The peak energy varies on a shot-to-shot basis with THz on, with a standard error larger than that with the THz off, suggesting that there is both jitter on the electron beam and timing jitter of the THz time of arrival. There is some change between THz on and THz off of the FWTM energy spread, which is more significant at +10°. As the phase of the energy modulation varied on a shot-to-shot basis the profiles were analysed individually to measure the periodicity of these modulations and the predicted bunch length. To predict the bunch length the chirp must be assumed to be linear; otherwise the periodicity in the time domain

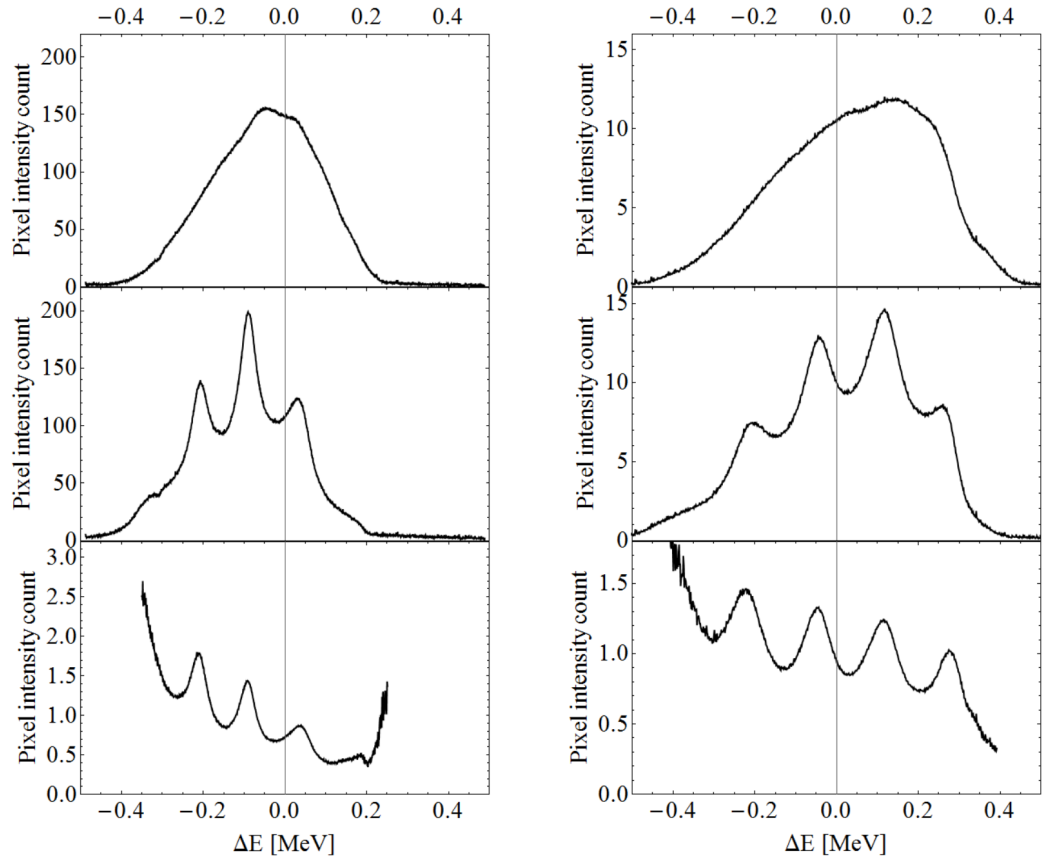

Figure 8.15: Example energy spectra of single shots, imaged on YAG-03. From top to bottom: THz off, THz on, and the ratio. Left: an RF phase of +10°, right: an RF phase of +15°.

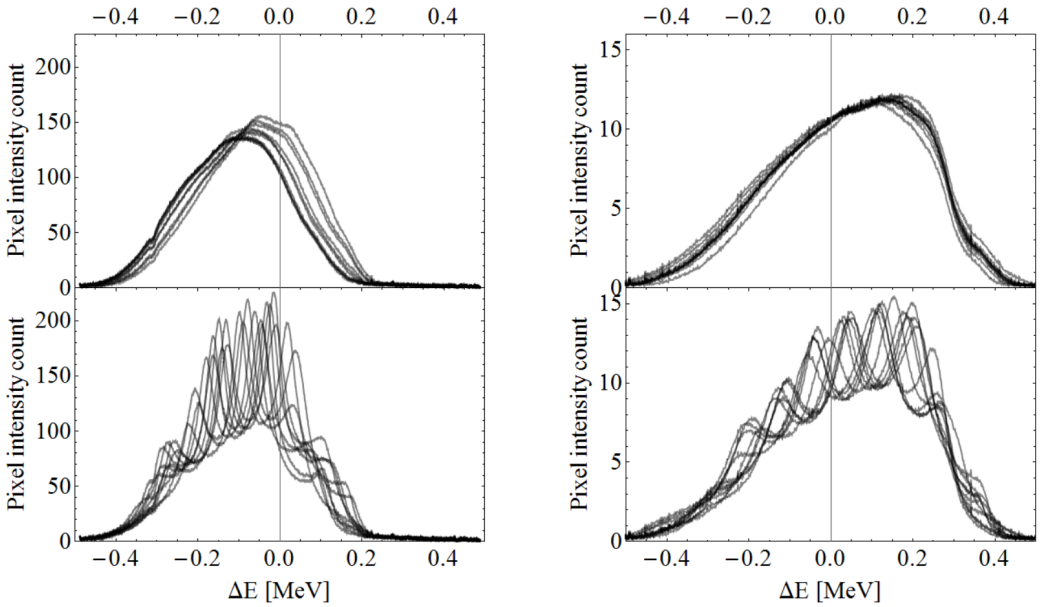

Figure 8.16: Profiles of 10 shots, imaged on the final YAG in the beamline. Top: THz off, bottom: THz on. Left: intensity profiles at linac phase +10°, right: profiles at linac phase +15°.

cannot be translated into the energy spectrum. Assuming a THz centre frequency of 0.39 THz, as discussed in Section 8.4, a single modulation has period 2.56 ps. The period of a modulation in the energy spectrum is defined as δE_{mod}, which is shown in Figure 8.17. The mean modulation period of one shot was calculated by using all modulations that were above the noise of the data, and the standard error on this mean calculated using the number of modulation periods per shot. This is shown in Figure 8.18 for all 100 shots (for both THz on and THz off) to show that the mean modulation period varied randomly for each shot. The mean and standard error on

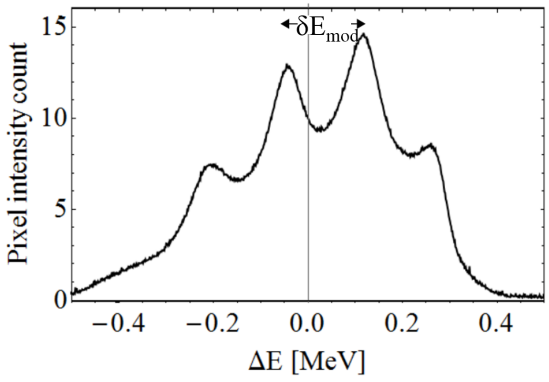

Figure 8.17: Definition of δE_{mod}, the periodicity of energy modulation.

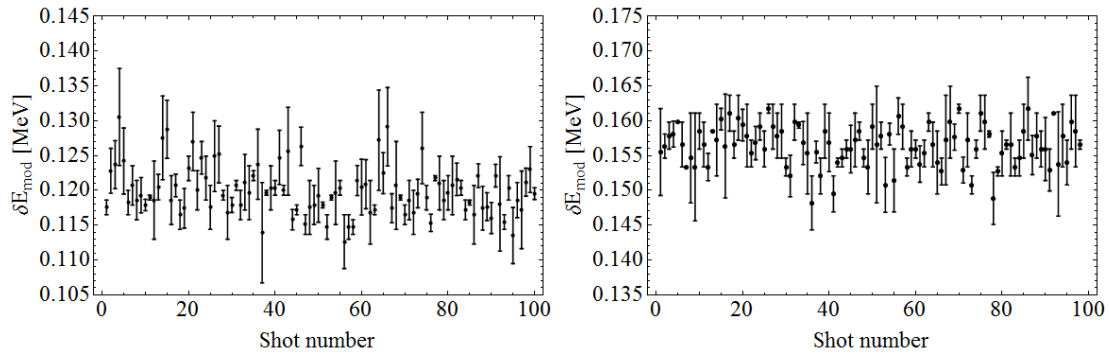

Figure 8.18: Mean peak-to-peak energy spread as a function of shot number. Mean and standard error were calculated using all modulations of each shot. Left: linac phase of +10°, right: +15°.

these data points is given in Table 8.3, along with the chirp and an estimate of the RMS bunch length. The average chirp, given in keV/ps, was found by dividing δE_{mod}

Table 8.3: The mean and standard error of the peak-to-peak energy spread, and the resulting chirp and RMS bunch length, for 100 shots taken at an RF phase of +10° and +15°, with THz on.

Phase	δE_{mod} [keV]	Chirp [keV/ps]	RMS bunch length [ps]
+10°	120.0 ± 5.7	46.8 ± 2.2	3.0 ± 0.1
+15°	156.4 ± 5.2	61.0 ± 2.0	3.3 ± 0.2

by the period of a single modulation. RMS bunch length of each shot was calculated by finding σ_E, the RMS energy spread, and dividing by the average chirp across the bunch. Taking the mean peak-to-peak energy spread of all shots gives a chirp at linac phase +15° of 61 ± 2 keV/ps. At +10° the chirp was calculated to be 47 ± 2 keV/ps. The RMS bunch length was calculated as $\sigma = 3.3 \pm 0.2$ ps for a linac phase of +15°, and $\sigma = 3.0 \pm 0.1$ ps at +10° [155].

Chirp was assumed to be linear across the bunch; however simulations have shown that this is only an approximation. The energy spread at the head and tail of the bunch were shown to be non-linear with respect to time. However this is a small effect and the central part of the bunch has an approximately linear chirp [156]. The RMS bunch lengths from these simulations are approximately 3.2 ps and 3.7 ps at RF phases of +10° and +15° respectively. Figure 8.19 shows the peak and trough separation as a function of position of the peaks in the spectrum at linac phases +10° and +15°. The energy spread modulation is not constant across the energy spectrum, which is to be expected due to the non-linear terms in the chirp. The uncertainty is higher at the minimum and maximum energy, which is due to the lower signal-to-noise

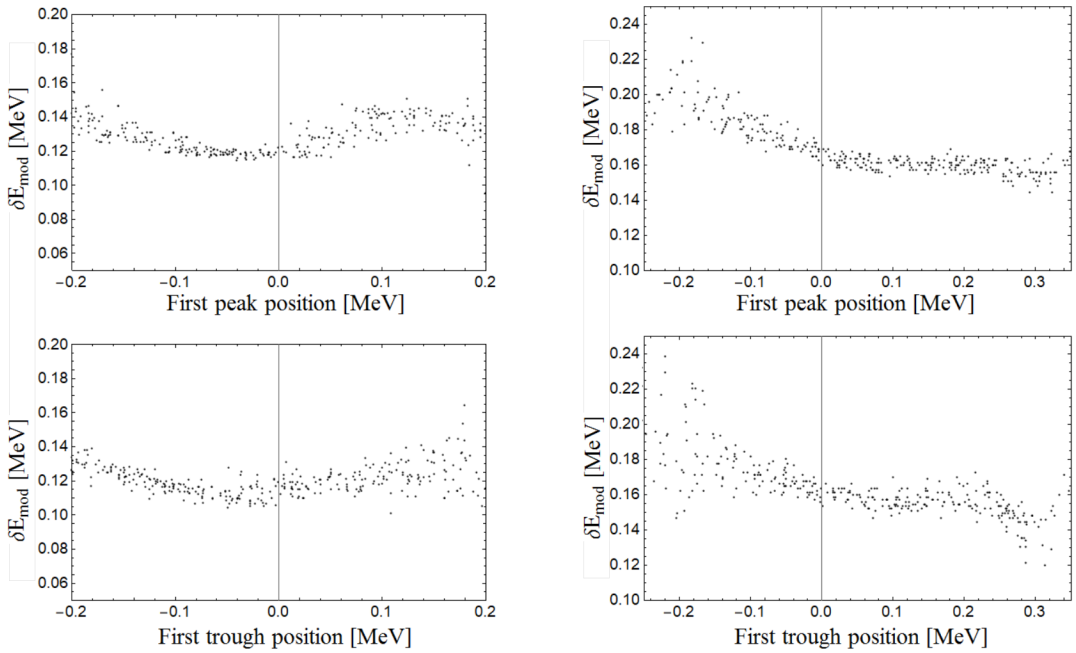

Figure 8.19: Magnitude of peak separation along the energy profile. Top: peak separation as a function of energy of the peaks. Bottom: trough separation as a function of energy of the peaks. Left: linac phase of +10°, right: +15° [155].

ratio at smaller intensities. In both cases the modulations around the peaks of the spectra are approximately linear.

8.3.2 Increase in energy spread

At a linac phase of +4° the bunch has the lowest possible chirp. Any energy change imparted was expected to result in an increase in spread. The exact bunch length was unknown, although it is less than that calculated at linac phase +10° and was of order multiple wavelengths. Simulations had been performed which gave a RMS bunch length of $\sigma \approx 2.3$ ps, with a RMS energy spread of approximately 40 keV [156]. The results of simulations discussed in Chapter 6 showed that a bunch of this length will demonstrate an energy spread after interaction.

Multiple sets of images were taken for different bunch charges, and at different times during the beam run; this meant that the bunch properties varied. Figure 8.20 shows example shots with THz on and off for an estimated bunch charge of 20 pC. The RF amplitude jitter meant that the profiles jitter in energy on a shot-to-shot basis. Figure 8.21 shows the profiles for both THz on and THz off. Also shown are the profiles such that their mean energy is shifted to $\Delta E = 0$; this highlights the clear interaction between THz pulses and electron bunches. Interaction did not

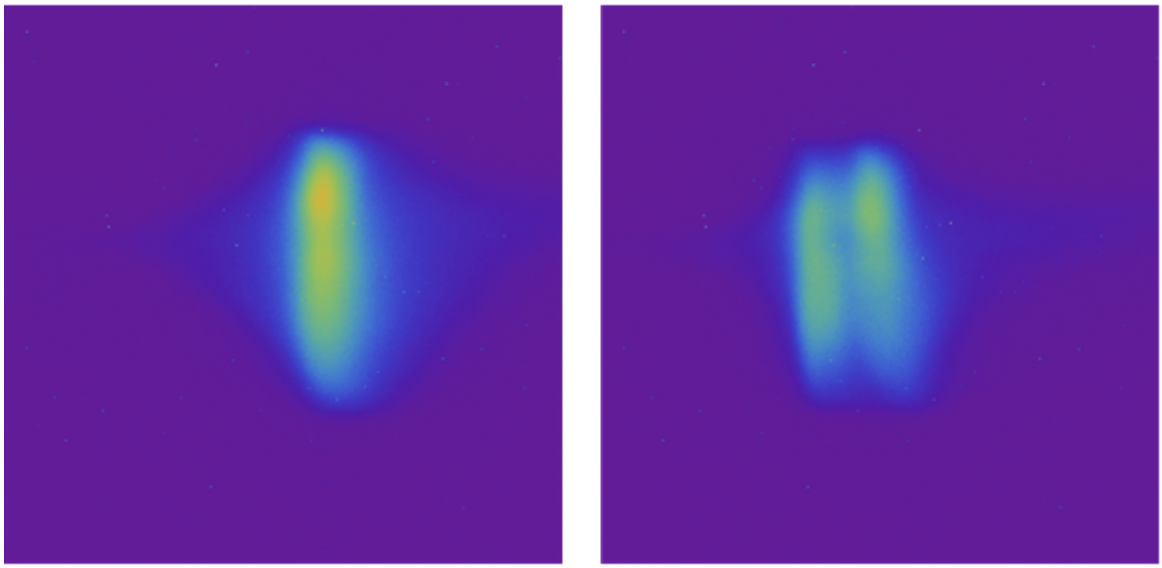

Figure 8.20: Example of a single shot of the bunch at linac off-crest phase +4°, as imaged on the final YAG in the beamline. Left: THz off, right: THz on. Peak splitting is observed.

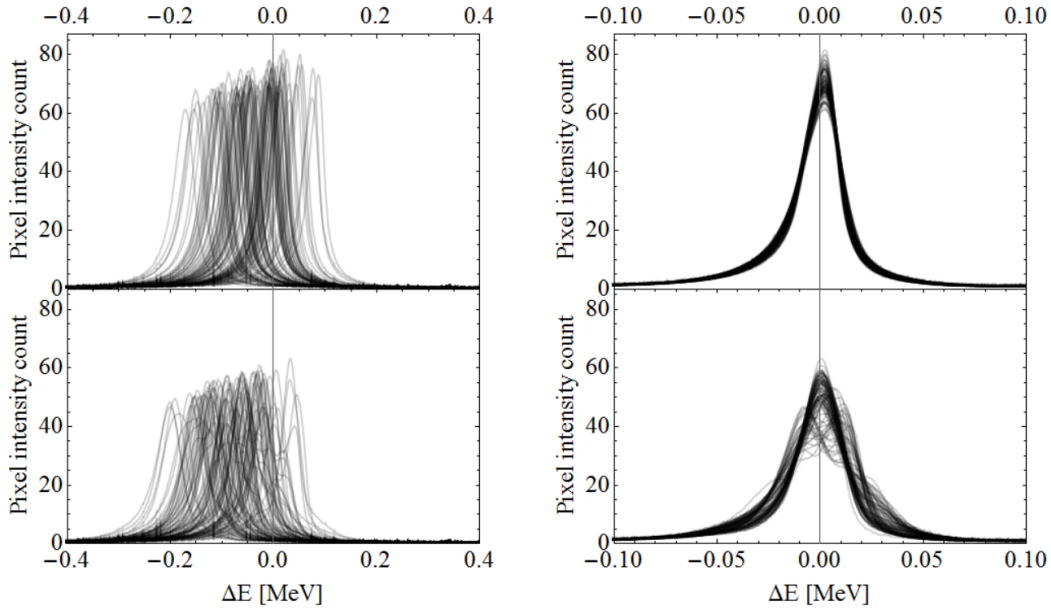

Figure 8.21: Profiles of 100 shots of the bunch at linac phase +4°, as imaged on the final YAG in the beamline. Left shows shots as appeared on the screen, right shows shots with centre of energy distribution moved to $\Delta E = 0$. Top: THz off, bottom: THz on.

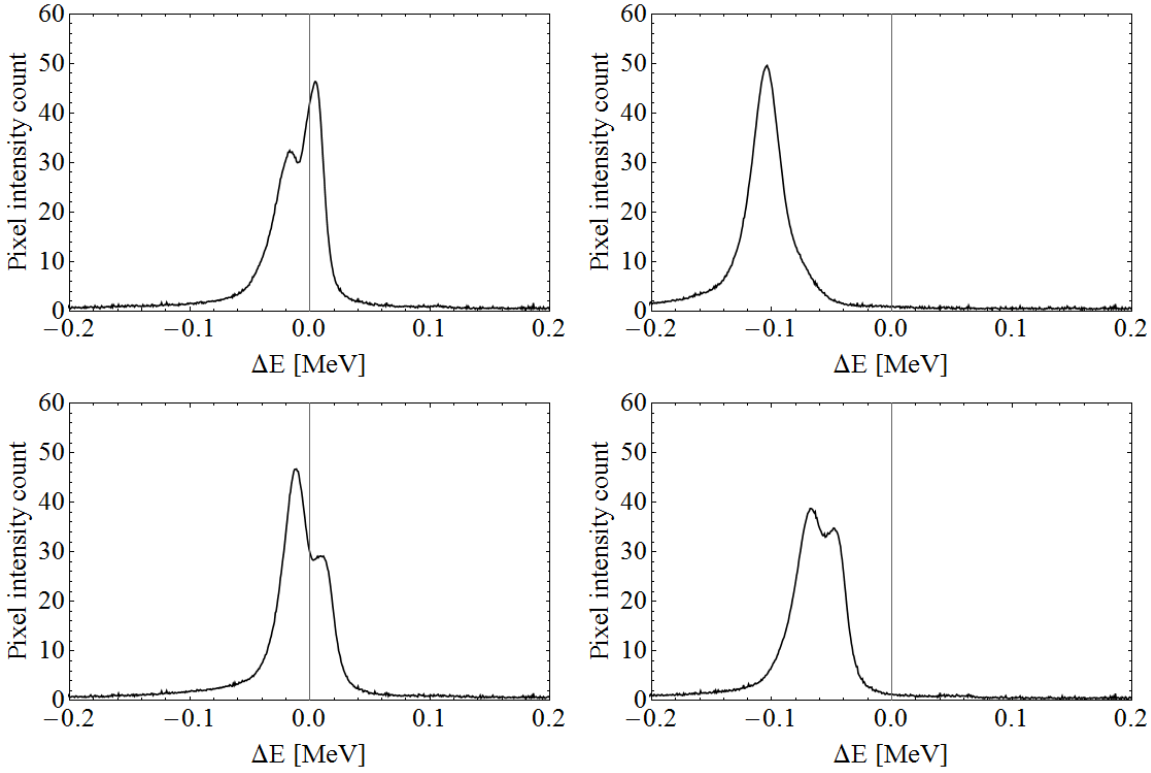

Figure 8.22: Examples of the different energy spectra of the bunch after THz-electron interaction at linac phase +4°. Change in position in the energy spectrum is due to jitter and not an effect of THz interaction.

always result in a clear peak splitting; Figure 8.22 shows four distinct examples of interaction. The peak and mean energy and the FWQM energy spread calculated from the 100 shots in Figure 8.21 are given in Table 8.4 for THz off and THz on. Histograms of the mean energy, ΔE_{mean}, and full width half max (FWHM) energy

Table 8.4: The peak and mean energy, and energy spread, using the 100 shots taken at RF phase of +4°. FWQM is used to avoid uncertainty in the energy spread due to peak spreading when THz interaction takes places, but FWHM is also calculated. The energy profiles when THz is off and on are both analysed.

Phase	+4°	
	THz off	THz on
Peak energy [keV]	-20.7 ± 3.0	-31.2 ± 3.2
Mean energy [keV]	-25.6 ± 2.4	-34.2 ± 2.5
FWQM energy spread [keV]	36.4 ± 0.4	48.1 ± 0.6
FWHM energy spread [keV]	22.1 ± 0.2	30.4 ± 0.6

spread, δE_{FWHM}, are also shown in Figure 8.23. Here there are 100 shots for THz off, and 500 shots for THz on. There is no clear change in the mean energy when

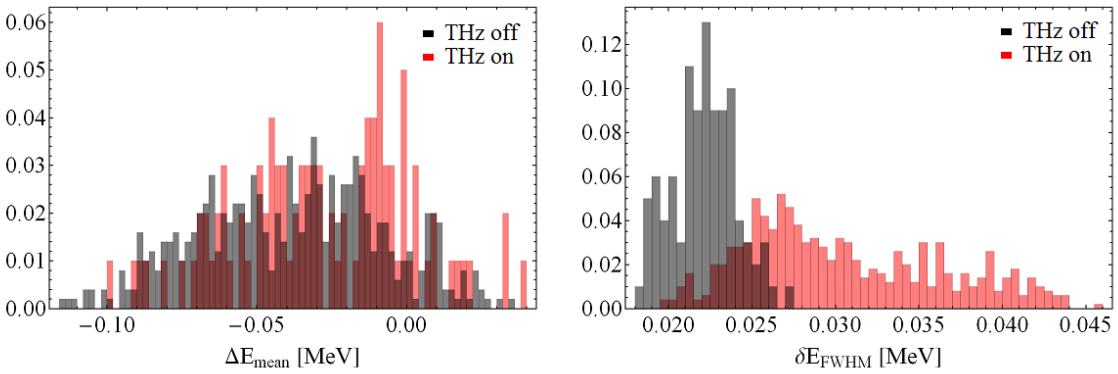

Figure 8.23: Histograms showing the properties of the energy profiles of the bunch at linac phase +4°. Left: histogram showing distributions of the mean energy of electron bunch with THz on and THz off. Right: histogram showing FWHM energy spread of electron bunch with and without THz interaction. 100 shots are shown for THz off, and 500 shots for THz on.

interaction occurs. With THz off, the mean FWHM energy spread over all shots is $\delta E_{\mathrm{FWHM}} = 22.1 \pm 0.2$ keV. After interaction with the THz, the mean FWHM energy spread over all shots is $\delta E_{\mathrm{FWHM}} = 30.4 \pm 0.2$ keV. The standard error is smaller than that given in Table 8.4 due to the increased number of shots. Therefore the average increase in FWHM energy spread is 8.3 ± 0.3 keV.

The accelerating gradient can be estimated from this energy spread increase. Dividing the change in energy spread by two and then by the length of the DLW gives 0.14 ± 0.01 MV/m. The accelerating gradient over the interaction length is 0.28 ± 0.03 MV/m. The E_z field at the start of the DLW is therefore estimated to be 0.060 ± 0.004 MV/m.

Due to misalignment of the DLW structure with respect to the electron beam there was loss of bunch charge. The area under each profile is plotted as a function of FWHM energy spread in Figure 8.24 in order to compare the bunch intensity for each shot. It was assumed that the YAG screen response is linear with charge. The range of magnitudes for the integrated profile is the same for THz on and THz off; there are no losses associated with interaction.

Energy spread decrease

The data in Figure 8.21 was taken at a charge of 20 pC. Another set of data was taken at the same charge after adjusting the downstream magnets to improve charge transport through BA1. The energy spread of the bunch as a function of mean energy, peak energy, and peak intensity are shown in Figure 8.25 for this dataset. In some cases the energy spread of the bunch is decreased. There does not appear to be any

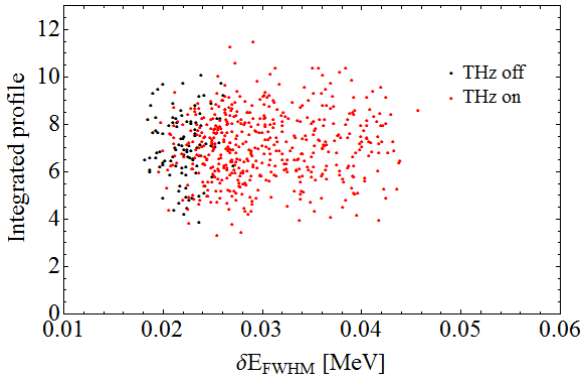

Figure 8.24: Integrated profile of all shots as a function of FWHM energy spread.

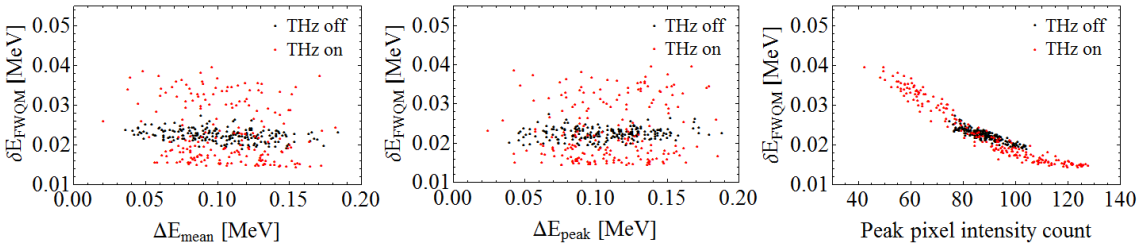

Figure 8.25: Energy spread of the bunch at linac phase +4°, as imaged on the final YAG in the beamline. From left to right: energy spread as a function of mean energy, peak energy, and peak intensity.

correlation with the jitter of the bunch. There is insufficient information about the bunch to explain why the spectra in Figure 8.21 does not demonstrate a decrease in energy spread. However it can be assumed that part of the bunch was lost whilst propagating through the structure. Simulations of beam propagation in BA1 had demonstrated a small non-linear component of the longitudinal energy dependence. This was not included in the original simulations in Chapter 6.

The accelerating gradient is again estimated from δE_{FWQM} of the data in Figure 8.25. With THz on, $\delta E_{FWQM} = 31.5 \pm 7.6$ MeV and with THz off, $\delta E_{FWQM} = 29.8 \pm 1.7$ MeV. Therefore the difference is 1.6 ± 7.8 MeV, corresponding to an average accelerating gradient over the 30 mm DLW of 0.03 ± 0.13 MV/m. The standard deviation is large due to the large range of energy spreads.

Effect of charge

An investigation into the effect of charge was also performed. Histograms of the energy spread are shown in Figure 8.26. The full width quarter maximum (FWQM) energy spread was used as this avoids the effect of peak splitting.

At 10 pC there are more instances of energy spread decrease, and in general the magnitude of δE_{FWQM} is larger than at 20 pC and 45 pC. With higher bunch charge

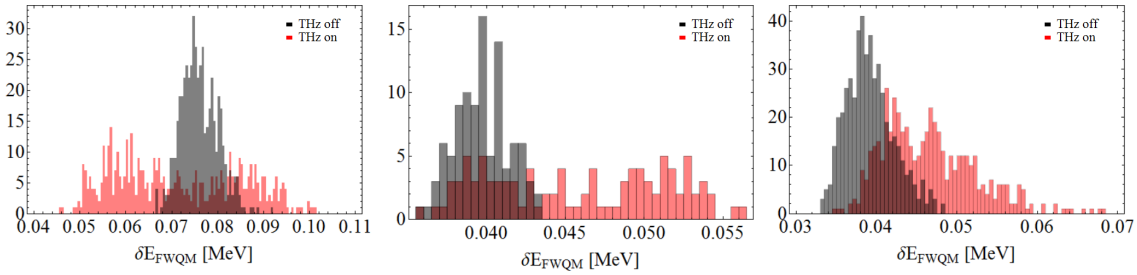

Figure 8.26: Histograms of the energy spread of the bunch at linac phase +4° at different bunch charge, as imaged on the final YAG in the beamline. From left to right: 10 pC, 20 pC, and 45 pC.

there is a greater proportion of shots showing an increase in δE_{FWQM}. Assuming that the longitudinal energy dependence contains non-linear components which are larger at the head and tail of the bunch, the longitudinal charge distribution must also be considered. The form of this distribution is unknown. If it is non-Gaussian and charge dependent, the distribution may be such that the population at the head and tail of the bunch changes with charge. This would account for the larger energy spread at low charge [157]. Therefore interaction between THz and electrons no longer presents purely as an energy spread increase and there would also be a dependence on the jitter of the TOA of the THz pulse.

Table 8.5 shows δE_{FWQM} for each set of data in Figure 8.26. In each case the

Table 8.5: Effect of charge on the energy spread change between THz on and THz off at a linac phase +4°. The average accelerating gradient, $E_{z,acc}$ is calculated from the energy spread change for a 30 mm DLW. The standard error on the mean is included in each case, and so the number of shots are also provided.

Charge	δE_{FWQM} THz off [keV]	δE_{FWQM} THz on [keV]	δE_{FWQM} change [keV]	$E_{z,acc}$ [MV/m]	No. shots
10 pC	75.8 ± 0.2	71.0 ± 0.6	-4.8 ± 0.7	0.08 ± 0.01	500
20 pC	39.7 ± 0.2	45.8 ± 0.6	6.1 ± 0.6	0.10 ± 0.01	100
45 pC	39.1 ± 0.1	46.5 ± 0.3	7.3 ± 0.3	0.12 ± 0.01	500

average accelerating gradient was around 0.1 MV/m, but the uncertainty was fairly large due to the wide range of final energy spreads after interaction.

8.3.3 Energy spread change using the on-crest linac phase

Selecting only images taken when the linac phase was 0°, corresponding to the RF operating on-crest, it was expected that any interaction would result in a change of energy spread. An example data set in Figure 8.27 shows the energy profiles of 100 shots with THz on and off, along with profiles shifted such that the maximum peak is

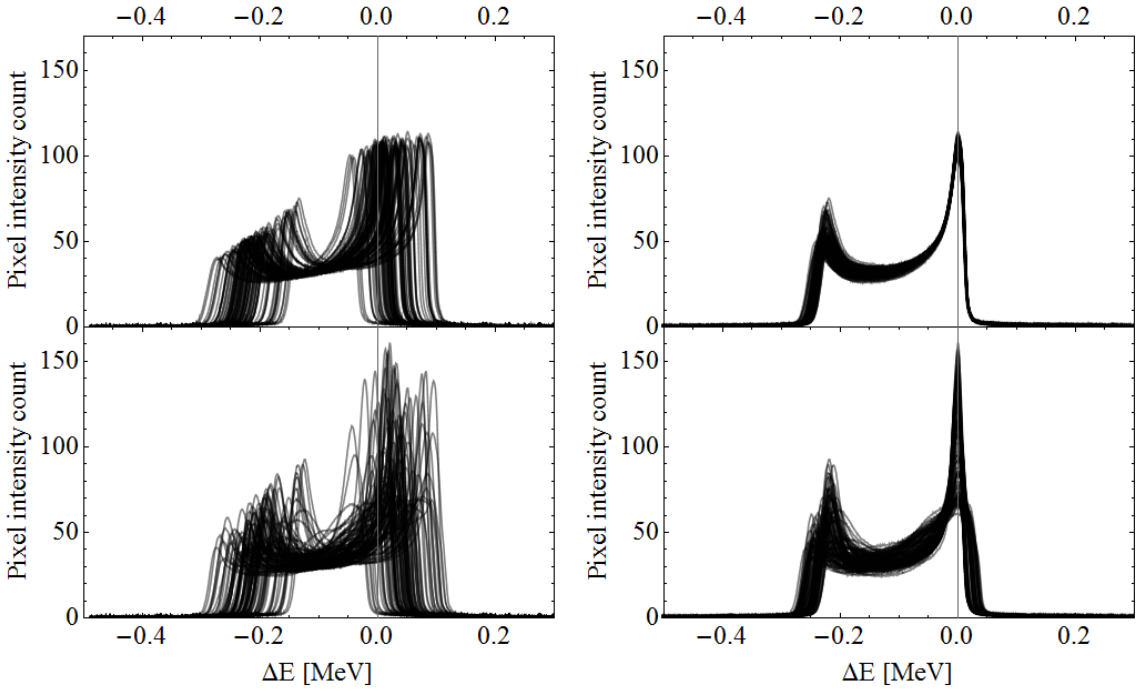

Figure 8.27: Left: intensity profiles of images taken of the final YAG for the linac operated on-crest. Each contains 100 shots. Right: the same shots, but all with the second peak shifted to zero. Top: THz off, bottom: THz on.

at 'zero' energy. The mean profiles and their standard deviations for THz off and on are shown in Figure 8.28. There is a small shift of the main peak of the mean energy spectrum, but otherwise any interaction is not clearly observed. The peak and mean energy and the FWQM energy spread are given in Table 8.6 for THz off and THz on. Histograms of the mean energy and energy spread are shown in Figure 8.29.

Table 8.6: The peak and mean energy, and energy spread, and their standard errors, using the energy spectra of the shots shown in Figure 8.27. FWQM is used to avoid uncertainty in the energy spread due to peak spreading when THz interaction takes places, but FWHM is also calculated. The energy profiles when THz is off and on are both analysed.

Phase	+0°	
	THz off	THz on
Peak energy [keV]	19.7 ± 3.0	28.0 ± 3.0
Mean energy [keV]	-73.4 ± 2.6	-66.5 ± 2.6
FWQM energy spread [keV]	256.2 ± 0.5	264.8 ± 1.3
FWHM energy spread [keV]	110.0 ± 9.5	183.1 ± 10.6

There is a small increase in mean energy after THz interaction, but the range of δE_{FWQM} has clearly increased. Considering the shape of the profiles, there are some

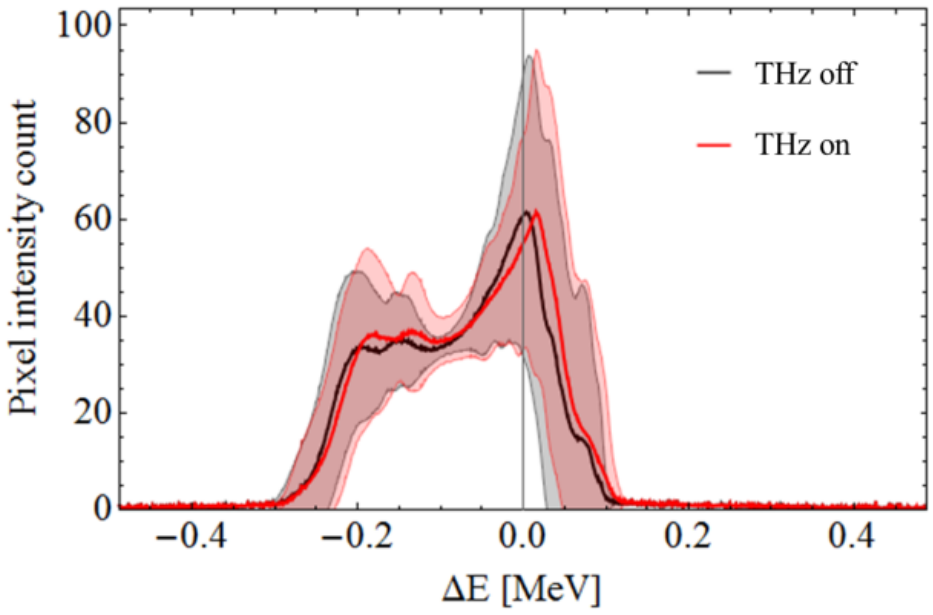

Figure 8.28: Mean and standard deviation of the intensity profiles of the electron bunch energy spread from Figure 8.27, taken on YAG-03, at on-crest rf phase, with THz off and THz on.

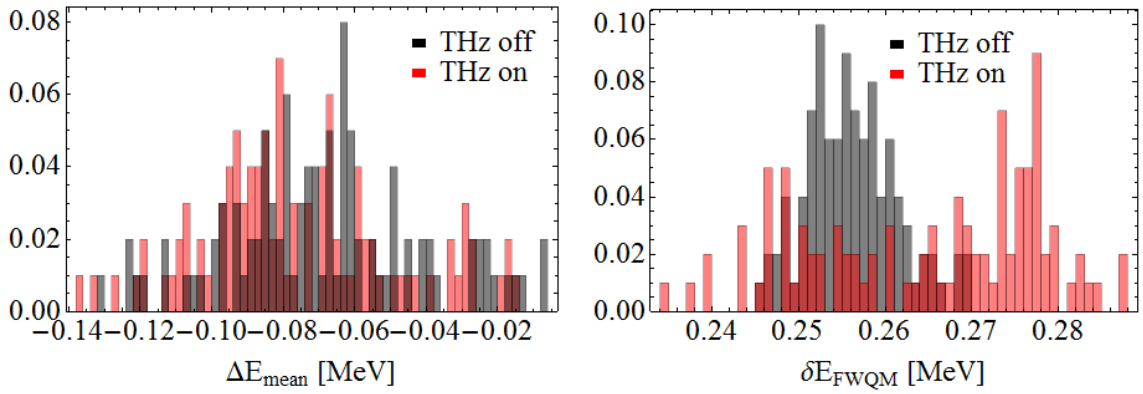

Figure 8.29: Histograms showing mean energy (left) and FWQM energy spread (right) of the profiles in Figure 8.27, for the linac operated on-crest. Black: THz off, red: THz on. There are 100 shots for both THz off and THz on.

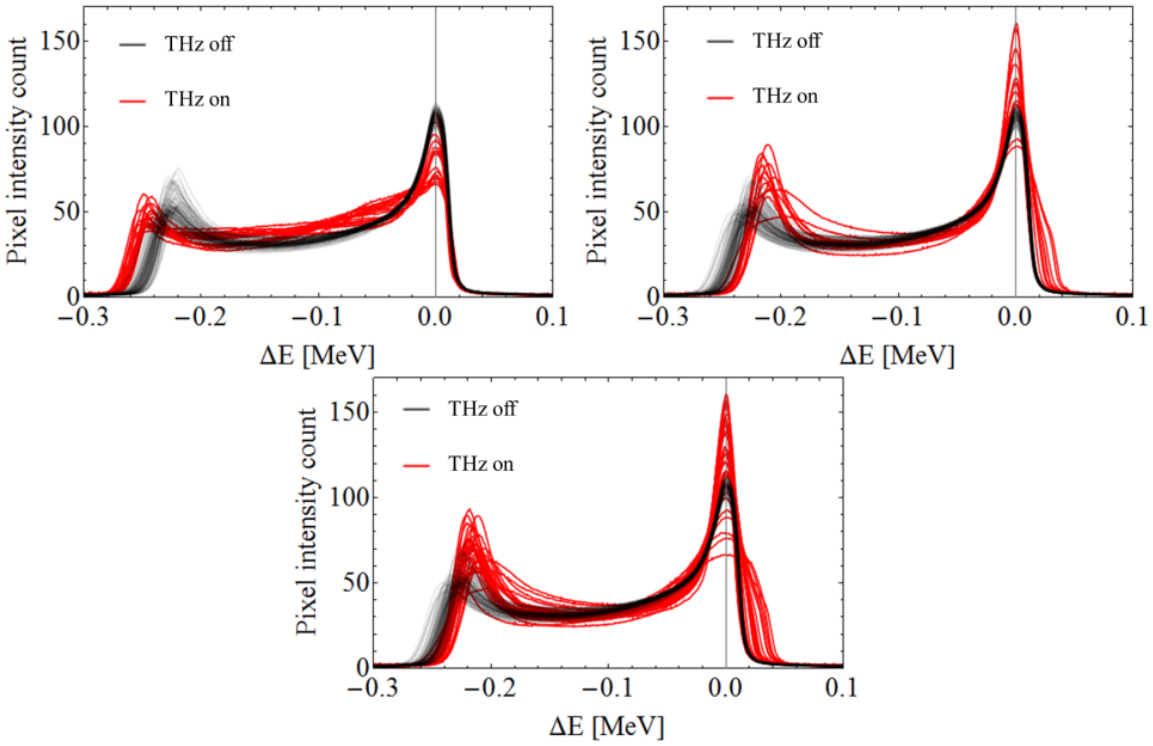

Figure 8.30: Intensity profiles of all 'THz off' shots, and shots from 'THz on' which show different observed interaction, with the linac operated on-crest. Clockwise from top left: deceleration beyond the minor peak, acceleration of the minor peak, broadening of the major peak. The profiles are shifted such that the major peak has zero relative energy change.

shots which demonstrate an increase in the intensity of the peaks, and the hard edges are less well defined. In order to investigate these changes, the 'THz on' shots are separated into different interaction regimes, using only the shifted plots to make any changes more visible. This is shown in Figure 8.30. The peak shifted to zero is defined as the 'major peak', and the smaller peak as the 'minor peak'. The profiles have been selected based on two observables: deceleration of the minor peak and acceleration of the minor peak. As a comparison, Figure 8.31 shows the same profiles, with no shift of the peak energy.

The first plot in Figures 8.30 and shows shifted profiles which have an apparent deceleration of the minor peak. This is not true deceleration as the peaks are shifted, but represents an energy spread increase. It is notable that all of these profiles, compared to THz off, have a less intense major peak and the plateau in the centre is slightly higher intensity. This is a strong indication of interaction, as this suggests that electrons which had higher energy now populate this central region. In the second plot only profiles which show an acceleration beyond the minor peak are shown. The

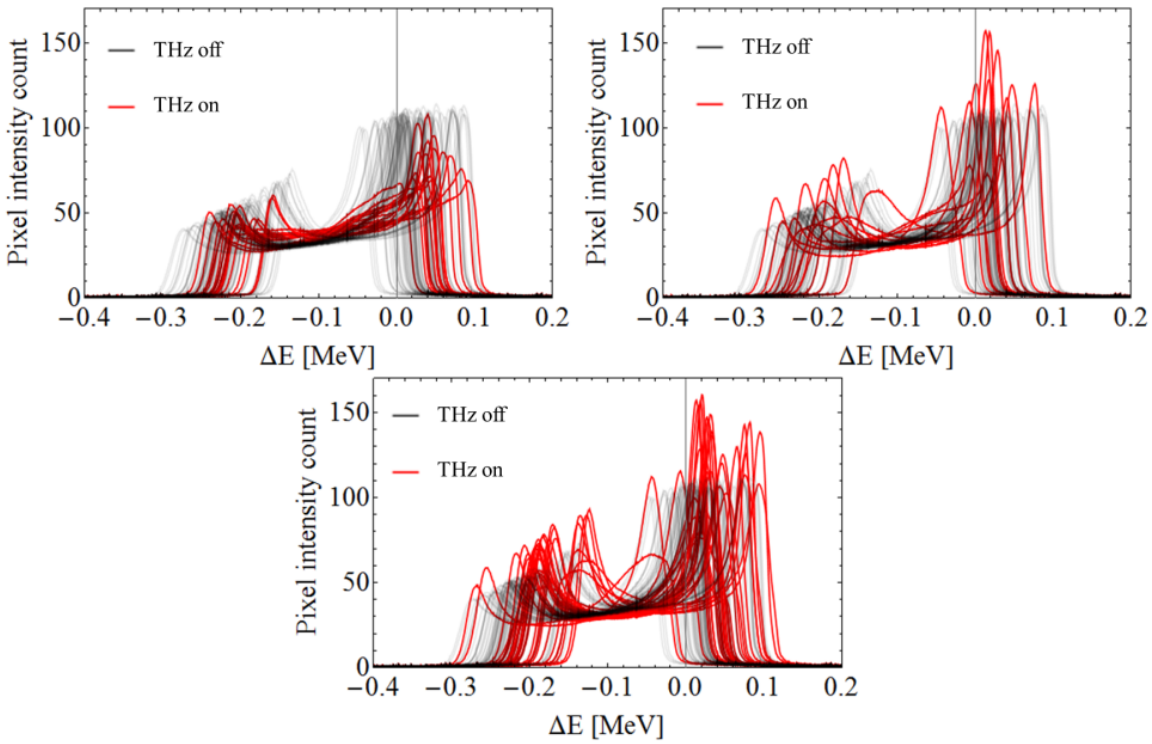

Figure 8.31: Intensity profiles of all 'THz off' shots, and shots from 'THz on' which show different observed interaction, with the linac operated on-crest, also seen in Figure 8.30. Clockwise from top left: deceleration beyond the minor peak, acceleration of the minor peak, broadening of the major peak. The profiles are not shifted.

major peak no longer has a hard edge, showing that some electrons in the bunch have gained energy. The third plot shows profiles which have a clear broadening of the major peak. Table 8.7 gives the peak and mean energy, and energy spread, and their standard errors of each of these plots. Compared to THz off, detailed in Table 8.6,

Table 8.7: The peak and mean energy, and energy spread, and their standard errors, using the energy spectra shown in Figure 8.30, with THz on. Each plot shows a different observed interaction and therefore different properties. Number of shots for each is given. FWQM is used to avoid uncertainty in the energy spread due to peak spreading when THz interaction takes places, but FWHM is also calculated.

Observed interaction	Peak energy [keV]	Mean energy [keV]	δE_{FWQM} [keV]	δE_{FWQM} [keV]	No. shots
Minor peak deceleration	42.8 ± 5.1	-61.9 ± 4.4	275.2 ± 1.1	205.4 ± 23.8	18
Minor peak acceleration	17.5 ± 4.7	-75.7 ± 4.2	259.0 ± 2.2	143.5 ± 17.2	41
Major peak broadening	33.2 ± 5.8	-57.0 ± 4.6	252.6 ± 1.9	180.3 ± 17.7	32

there is an increase in δE_{FWQM} in each case, and there is a change in the position of the peak energy. An estimate of the energy change due to the THz is obtained by finding the mean energy spread of each set of shots. With no THz, the FWQM energy spread is 256.2±0.5 keV, with an increase to 264.8±1.3 keV when THz is on, with 100 shots taken of each. The larger standard deviation is reflective of the increased range of energy spreads. The mean change in FWQM energy spread is therefore 8.6±1.4 keV. The standard error is relatively large due to the wide range of energy spreads after THz interaction. As each shot with THz off features a distinct double peak, and a hard edge at the maximum energy, a maximum energy gain can be estimated. Taking the profiles which demonstrate a blurring of the hard edge of the major peak, up to 20 keV energy gain has been achieved. The average accelerating gradient was calculated to be 0.14 ± 0.02 MV/m, which is higher than that observed at linac phase +4°.

8.3.4 Single-bucket acceleration

Pure acceleration of the entire bunch is only possible if it sits within half of a wavelength of the THz pulse. Unless the bunch is significantly smaller than the wavelength, magnitude of acceleration depends on longitudinal position, and so the bunch would not only shift with respect to energy, but the energy spread would also increase. It has already been ascertained that, because the modulation of linearly-chirped pulses was well defined, the energy change was small compared to the bunch energy. The energy spread increase of the bunches at a linac phase of +4° also suggested an acceleration/deceleration of order 10 keV. The energy jitter of the profiles

at linac phase $-10°$ was therefore greater than the energy change, as visible in Figure 8.11. The data sets taken at this phase are shown in Figure 8.32. Only some shots with THz on differ from those without interaction. The profiles taken with no THz are plotted over the THz on data, so that any variation outside of the jitter is visible. It was expected that each set of data has the same shape when all profiles are plotted together. However, each set was performed with different charge and/or THz-electron delay.

The first set of data, using a bunch of 20 pC, shows potential interaction. The second data set, performed at 70 pC, shows a clear variation with THz on. Set three was performed at approximately 70 pC and was taken after an attempt to optimise phase and charge. There is variation between the THz on and THz off data. Set four again shows potential acceleration. The charge here was dropped to approximately 45 pC. Set five, taken after changing the delay by 800 μm and increasing charge to 60 pC, demonstrates a similar effect as in set two. There is insufficient data to verify if interaction has taken place. The final data set, taken at a charge of 20 pC and moving the delay stage by 1.7 mm, demonstrates potential acceleration of a small number of shots.

The statistical data for the peak and mean energy, and the FWQM and FWHM energy spread, are shown for each set of data in Tables 8.8 and 8.9 for THz on and THz off respectively. There were some differences between the sets for THz on and THz off, but in most cases it is not significant. There are two exceptions. In the

Table 8.8: The peak and mean energy, and energy spread, and their standard errors, using the energy spectra shown in Figure 8.32, with THz on. Each plot shows a different observed interaction and therefore different properties. Number of shots for each is given. FWQM is used to avoid uncertainty in the energy spread due to peak spreading when THz interaction takes places, but FWHM is also calculated.

Charge	Peak energy [keV]	Mean energy [keV]	δE_{FWQM} [keV]	δE_{FWQM} [keV]	No. shots
20 pC	11.0 ± 2.5	19.2 ± 0.1	307.0 ± 2.0	159.3 ± 1.6	500
70 pC	-15.6 ± 3.2	-10.2 ± 1.0	429.5 ± 3.2	240.0 ± 2.4	500
70 pC	-70.7 ± 0.7	-64.0 ± 0.7	531.2 ± 1.6	361.6 ± 2.9	200
45 pC	-111.7 ± 2.8	-90.7 ± 0.8	407.4 ± 2.0	187.5 ± 1.6	500
60 pC	-74.3 ± 1.7	-68.6 ± 0.4	545.6 ± 2.7	371.1 ± 2.7	500
20 pC	-165.3 ± 2.7	-109.9 ± 0.7	326.0 ± 2.4	181.2 ± 1.6	500

second set of data, there is a clear increase in the position of the peak and mean energy of the data with THz on, and a small increase in the energy spread. In the third set of data, there is a change in the position of the peak energy but the mean

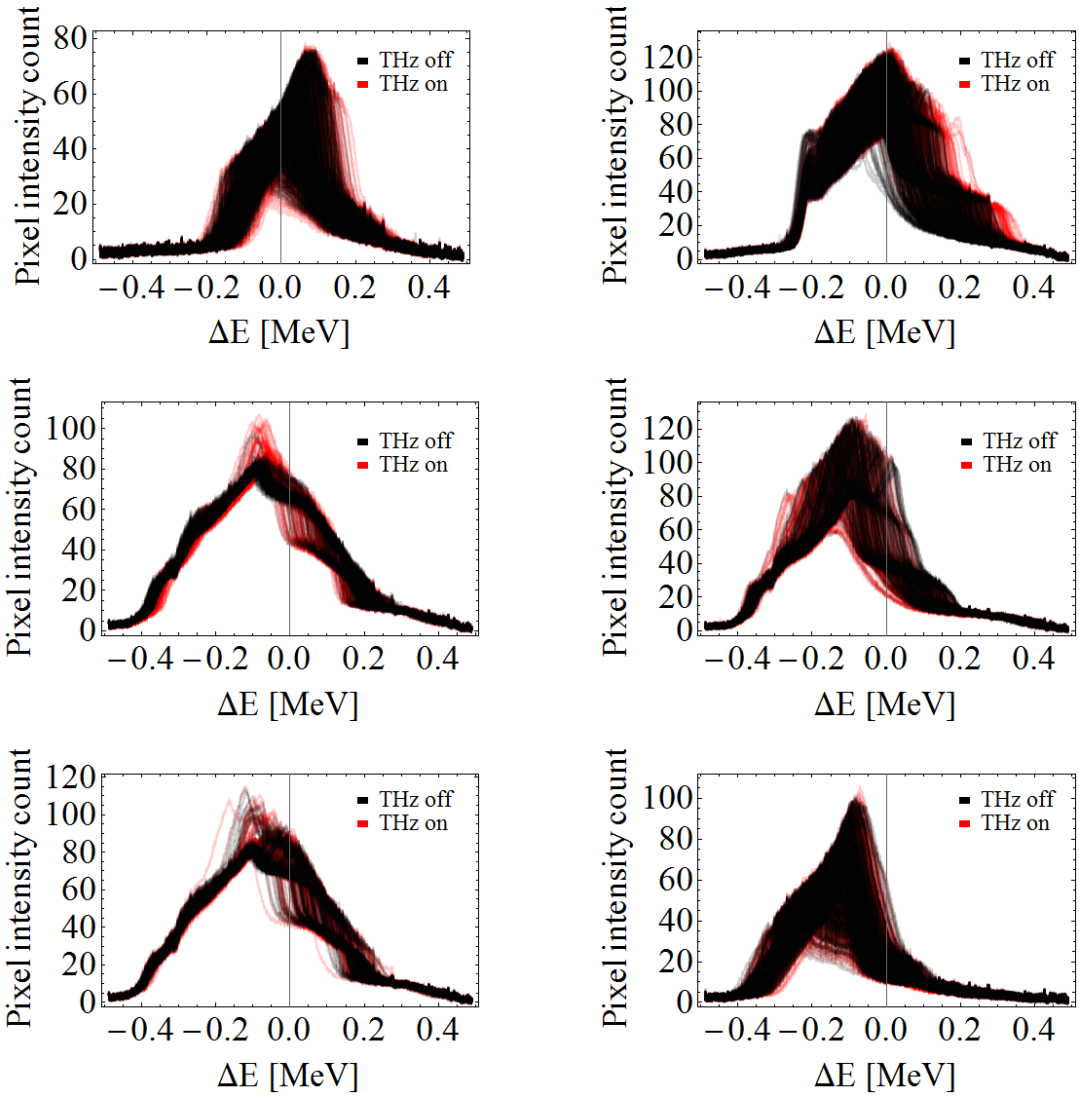

Figure 8.32: Intensity profiles of all shots from six sets of data taken at linac phase $-10°$, as imaged on the final YAG in the beamline. The THz off shots are overlaid on the THz on shots. Charge and machine settings vary for each set.

Table 8.9: The peak and mean energy, and energy spread, and their standard errors, using the energy spectra shown in Figure 8.32, with THz off. Each plot shows a different observed interaction and therefore different properties. Number of shots for each is given. FWQM is used to avoid uncertainty in the energy spread due to peak spreading when THz interaction takes places, but FWHM is also calculated.

Charge	Peak energy [keV]	Mean energy [keV]	δE_{FWQM} [keV]	δE_{FWQM} [keV]	No. shots
20 pC	8.0 ± 2.5	17.1 ± 0.1	303.3 ± 2.1	168.1 ± 1.5	500
70 pC	-40.4 ± 2.9	-19.4 ± 0.1	401.5 ± 2.5	225.9 ± 2.0	500
70 pC	-90.0 ± 0.7	-64.4 ± 0.6	554.3 ± 2.9	399.1 ± 1.8	200
45 pC	-100.0 ± 4.4	-89.6 ± 1.2	416.8 ± 3.0	187.1 ± 2.7	200
60 pC	-71.0 ± 3.2	-70.0 ± 0.7	545.0 ± 5.0	380.4 ± 3.6	200
20 pC	-170.7 ± 2.7	-111.8 ± 0.6	335.6 ± 2.2	188.6 ± 1.6	500

energy is unchanged, and there is a decrease in the energy spread.

The change in profile between each set suggests that charge transport was not well defined, likely due to misalignment of the structure. Additionally each set only demonstrates an apparent energy gain or loss, not both as would be expected due to the timing jitter. Therefore it cannot be conclusively stated that there was an interaction between electron bunches and THz pulses at linac phase $-10°$.

8.3.5 Summary

The THz-electron interaction was investigated experimentally for electron bunches with different longitudinal properties. Modulation of the energy spread of a decompressed chirped bunch and increase in energy spread of a bunch with minimum chirp were both conclusively demonstrated. These were expected from the studies in Chapter 6. It was also confirmed that the THz field amplitude was insufficient to demonstrate conclusive single-bucket acceleration. This was due in part to the energy jitter exceeding the (small) energy gain due to the THz. Additionally the structure was misaligned and so there were charge losses, resulting in incomplete energy spectra of the bunch.

Using a linac phase of $0°$ gave the best estimate of the energy gain due to THz interaction. The increase in δE_{FWQM} was 8.6 ± 1.4 keV, corresponding to an acceleration of 4.3 ± 0.7 keV. The well-defined shape of the energy spectrum meant that, without interaction, there was a well-defined hard edge. This became blurred after interaction which suggested that some electrons had gained up to 20 keV. An estimate of the accelerating gradient in the DLW was therefore 0.14 ± 0.02 MV/m, or 0.28 ± 0.03 MV/m if only considering the interaction length, simulated to be 15 mm.

An energy spread decrease was also observed for minimum chirp. This was unex-

pected for a flat phase space. This is likely due to bunches having non-linear charge distribution and energy spread across the length of the bunch; however the exact form of this is unknown and would require a time-dependent longitudinal diagnostic which was not available at the time of experiments.

Due to the quadrupole-like transverse fields of the LSM_{11} mode, electron bunches experience a transverse force. This effect was not observed during experiments. This was because of both the low field amplitude and unoptimised charge transport.

8.4 Centre frequency

For THz pulses with the same bandwidth but variation in centre frequency, the resulting THz interaction decreases further from the operating frequency of the DLW. This was used as a diagnostic to verify the true operating frequency of the DLW, which had already been established in Chapter 7 to be different from design due to a manufacturing error.

There are two expected differences in observed interaction with change in centre frequency; amplitude and periodicity of modulation. It is simplest to observe these changes when at a linac phase of $+15°$ as there are more periods in the spectrum. The average energy chirp is known and so the periodicity can be directly translated into frequency. For the narrowband pulse considered here, provided the centre frequency is relatively close to the DLW operating frequency, f_{op} and modulation frequency are linearly related.

It was first assumed that f_{op} was unknown, ans so the known chirp of the electron bunch, calculated as 61 ± 2 keV/ps, was used to determine the pulse centre frequency from the energy spectra. The frequency as a function of arm position is shown in Figure 8.33, with a linear fit applied to the data. The studies in Section 8.3.1 were performed with the arm position set to 16.2 μm, which was found to produce THz pulses centred on 0.39 THz. This was deemed to have the highest modulation, which was assessed by comparing the depth of modulations to the mean 'THz off' amplitude at the centre of each modulation, as shown in Figure 8.34. The operating frequency is not that calculated in Chapter 7; however it can be recovered by setting $\epsilon_r = 3.8$. This is not unexpected; the relative permittivity of quartz is not fully characterised in the THz regime [158, 159]. Considering Figures 6.4, 6.5, 6.6, a small change in ϵ_r does not significantly affect figures of merit.

The simulations performed in Section 6.5 demonstrated that an increased energy gain does not always correspond to an increase in the depth of modulations. However as the THz field amplitude regime was low it can be assumed that it is a valid assumption in this case. For higher energy THz pulses the verification of centre frequency

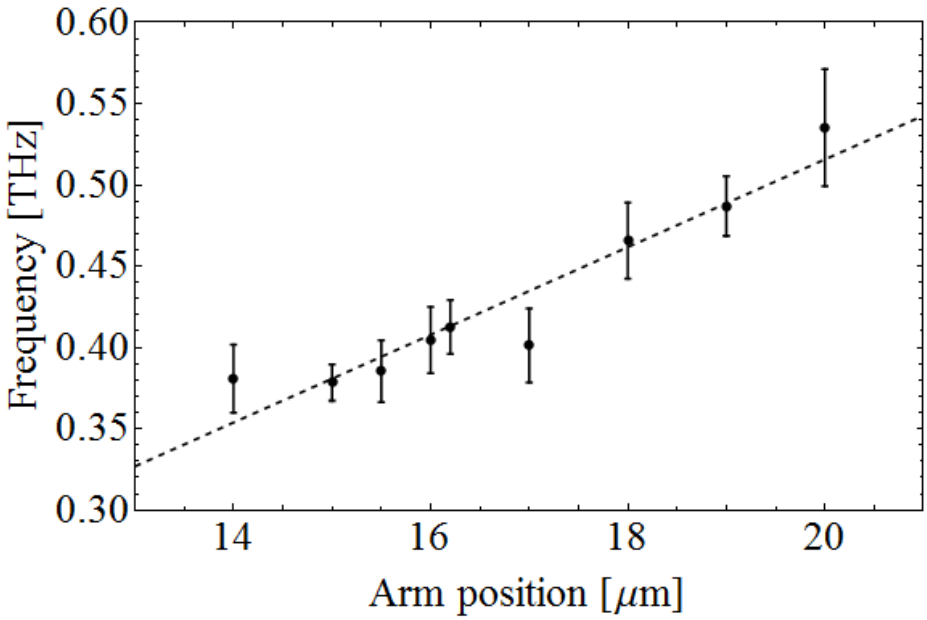

Figure 8.33: Effect of Michelson arm position on frequency of the input THz pulse, as calculated from the δE_{mod} of the electron bunches [155]. The dashed line shows a linear fit applied to the data.

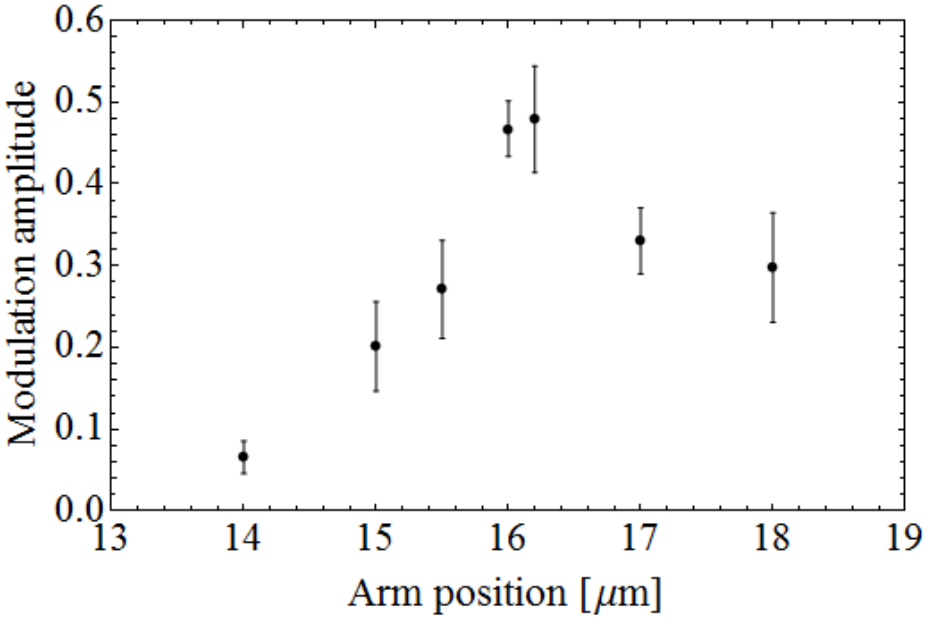

Figure 8.34: Effect of Michelson arm position on amplitude of modulation.

would be performed by finding maximum energy spread at a linac phase +4°.

8.5 Conclusion

Experimental verification of THz-driven modulation of electron bunches has been demonstrated for a low-power narrowband THz source. The use of a Michelson interferometer enabled simple adjustment of the THz centre frequency to maximise interaction. This showed that the operating frequency was 0.39 THz; different to the estimated operating frequency of the manufactured structure. This analysis was performed at a linac phase of +15°, where the chirp was estimated to be 61 ± 2 keV/ps.

Modulation of an electron bunch with a mostly linear chirp was visible after THz interaction, both verifying the energy change and also suggesting that the THz field amplitude was too low for significant acceleration. Energy spread increase was also demonstrated for a bunch with a 'flat' longitudinal energy spread. Due to unoptimised charge transport and a large jitter relative to the energy gain it was not possible to verify if acceleration of short bunches had taken place. The unoptimised charge transport also meant that no transverse effects could be observed.

An unexpected feature observed during experiments was decrease of bunch energy spread in some cases when using the flattest energy spread. This was not observed in the interaction model, and was suggested to be due to non-linear longitudinal charge distribution which also varied with the bunch charge itself.

The energy gain was best estimated at linac phase 0°. The change in energy spread was measured and a final energy gain of 4.3 ± 0.7 keV, corresponding to an accelerating gradient of 0.14 ± 0.02 MV/m. A maximum energy gain of 20 keV was also measured.

8.6 Acknowledgements

The THz optics were set up by D. Walsh, M. Hibberd, D. Lake, V. Georgiadis, S. Mondal and O. Finlay. The waveguide structure and CTR diagnostic were manufactured by P. Huggard and B. Alderman of the MMT group, part of RAL Space. Primary CLARA operators were T. Pacey, Y. Saveliev, and J. Jones. T. Pacey and Y. Saveliev were responsible for development of the beam area diagnostics and characterising the standard machine setup. J. Jones provided the simulations of the CLARA beamline. Calculation of the energy chirp was performed in conjunction with O. Finlay.

Chapter 9

Conclusion

This thesis details the design, manufacture, and experimental verification of a DLW structure used for manipulation of electrons with a co-propagating THz pulse. Approaches to design optimisation in both the time and frequency domain have been considered. Both conventional accelerator design techniques, which are useful for single-frequency analysis, and optical analysis have been used to design the DLW structure. The interaction length between a THz pulse and co-propagating electron in a DLW was studied in detail. By Taylor expanding the dispersion relation, the effect of higher order dispersive terms was applied in turn. It was therefore established that, for longer, narrowband THz pulses, the effect of group velocity dispersion was negligible. With broadband pulses this was no longer the case.

The THz-electron interaction was investigated as a function of time delay for THz pulses with bunch length $\sigma_f = 0.023$ THz and $\sigma_f = 0.069$ THz, using both CST-MWS and purpose-built simulations in *Mathematica*. The effect of the coupler was included in CST-MWS simulations. In both cases the coupler reduced the final energy change of the electrons. It was found that interaction was sinusoidal with a constant periodicity provided a narrowband pulse and long DLW were used. The DLW length was set to 30 mm to ensure that saturation of the energy gain was achieved, which also increased the time range over which interaction was observed. The effect of changing centre frequency was explored and it was again established that this sinusoidal relationship held provided that the centre frequency was close to the operating frequency of the waveguide. A narrowband THz source was used in experiments as a result of these studies. The effect of electron bunch properties was then considered. From this it was established that energy modulation would be observed for low THz field amplitude using a linearly chirped bunch. It was also noted that for full acceleration of a bunch encapsulated within half a cycle of the THz pulse, the required THz amplitude was

approximately 20 times larger.

Energy modulation of chirped electron bunches has been experimentally demonstrated for two different values of chirp. The average chirp was calculated from the periodicity of the energy modulation and used to calculate the centre frequency of the THz pulse. Energy spread increase was also demonstrated for bunches with a longitudinally 'flat' energy distribution. The interaction was strongly dependent on charge, however there was an uncertainty on the actual energy change as charge transport was not optimised. As a result the energy spectrum was missing information. An energy spread decrease was also observed, which was suggested to be a result of a non-linear longitudinal charge distribution. A maximum energy spread of 8.6 ± 1.4 keV was recorded, which corresponds to an average accelerating gradient of 0.14 ± 0.02 MV/m over a 30 mm structure. The field amplitude was insufficient to conclusively demonstrate short-bunch acceleration beyond the energy jitter of the bunch, as was expected from simulation studies.

Further experiments at Daresbury with an upgraded laser system are planned. A significant factor in the low THz pulse energy was the use of chirped pulse beating. Alternatives to the chirped pulse beating include cryogenically cooled periodically-poled $LiNbO_3$, which has produced μJ-level THz pulses with bandwidth 20 GHz [87, 160]. As the energy gain increases it is vital to develop a full understanding of the beam dynamics in the DLW structures, including the effect of wakefields [56]. These were not included in this study as only the effects of the THz interaction in the structure were considered. It is also expected that the transverse force due to the transverse field components of the LSM_{11} mode will be more pronounced with higher THz field amplitude. However the quadrupole-like focussing effect was not observed on the bunches during the experiments discussed here.

To the author's knowledge there has been no published research into the use of terahertz-driven rectangular dielectric-lined waveguides for manipulation of relativistic electrons. In conclusion, the work presented in this thesis has demonstrated the use of THz-driven dielectric-lined waveguides for energy manipulation of relativistic electron bunches. With a low THz field strength of order 0.1 MV/m, energy modulation was easily observed and used to calculate the linear chirp of a long electron bunch. This has use as a bunch length diagnostic as the imparted modulation is directly related to the bunch length. Energy spread increase of bunches was also demonstrated. Simulations of the effect of bunch properties on observed interaction suggested that, with these two effects observed, the THz field amplitude was small and therefore full bunch acceleration would not be observed. This was confirmed in

experiment, as although there were indications of acceleration fo short bunches, poor charge transport through the structure meant that changes in the energy spectra could not be attributed to charge losses.

Bibliography

[1] H. Podlech. "Superconducting versus normal conducting cavities". In: *Contibution to CERN Accelerator School*. 2013.

[2] C. Joshi and V. Malka. "Focus on laser-and beam-driven plasma accelerators". In: *New Journal of Physics* 12.4 (2010), p. 045003.

[3] T. Tajima and J. M. Dawson. "Laser electron accelerator". In: *Physical Review Letters* 43.4 (1979), p. 267.

[4] P. Chen, J. Dawson, R. W. Huff, and T. Katsouleas. "Acceleration of electrons by the interaction of a bunched electron beam with a plasma". In: *Physical Review Letters* 54.7 (1985), p. 693.

[5] B. Hidding et al. "Directions in plasma wakefield acceleration". In: *Philosophical Transactions of the Royal Society A: Mathematical, Physical and Engineering Sciences* (2019).

[6] J. Wang and G. Loew. "RF breakdown studies in copper electron linac structures". In: *Proceedings of the 1989 IEEE Particle Accelerator Conference*. IEEE. 1989, pp. 1137–1139.

[7] J. Hirshfield. "Millimeter-Wave RF Sources for Accelerator Applications". In: *10th Workshop of Advanced Accelerator Concepts*. Vol. 647. 1. AIP. 2002, pp. 29–38.

[8] R. England et al. "Dielectric laser accelerators". In: *Reviews of Modern Physics* 86.4 (2014).

[9] D. Cesar et al. "High-field nonlinear optical response and phase control in a dielectric laser accelerator". In: *Communications Physics* 1.1 (2018), p. 46.

[10] C. Sirtori. "Applied physics: Bridge for the terahertz gap". In: *Nature* 417.6885 (2002), p. 132.

[11] M. Tonouchi. "Cutting-edge terahertz technology". In: *Nature Photonics* 1.2 (2007), p. 97.

[12] E. Nanni et al. "Terahertz-driven linear acceleration". In: *Nature Communications* 6.8486 (2015).

[13] E. Curry et al. "Meter-scale terahertz-driven acceleration of a relativistic beam". In: *Physical Review Letters* 120.9 (2018), p. 094801.

[14] J. Slater. "The design of linear accelerators". In: *Reviews of Modern Physics* 20.3 (1948), p. 473.

[15] E. L. Ginzton, W. W. Hansen, and W. R. Kennedy. "A linear electron accelerator". In: *Review of Scientific Instruments* 19.2 (1948), pp. 89–108.

[16] T. Higo et al. "Advances in X-band TW Accelerator Structures Operating in the 100 MV/m Regime". In: SLAC-PUB-15150 (2012).

[17] A. Grassellino et al. "Unprecedented quality factors at accelerating gradients up to 45 MVm- 1 in niobium superconducting resonators via low temperature nitrogen infusion". In: *Superconductor Science and Technology* 30.9 (2017), p. 094004.

[18] A. Grudiev, S. Calatroni, and W. Wuensch. "New local field quantity describing the high gradient limit of accelerating structures". In: *Physical Review Special Topics-Accelerators and Beams* 12.10 (2009), p. 102001.

[19] V. D. Shiltsev. "Accelerator physics and technology challenges of very high energy hadron colliders". In: *International Journal of Modern Physics A* 30.23 (2015), p. 1544001.

[20] P. Tenenbaum. *A Brief Introduction to RF Power Sources*. Tech. rep.

[21] M. Breidenbach and W. Barletta. *Accelerator Research in the US for High Energy Physics: A biased perspective*. Tech. rep. 2015.

[22] M. Aicheler et al. *A Multi-TeV linear collider based on CLIC technology: CLIC Conceptual Design Report*. Tech. rep. SLAC National Accelerator Lab., Menlo Park, CA (United States), 2014.

[23] A. Nassiri et al. "A 50-MeV mm-wave electron linear accelerator system for production of tunable short wavelength synchrotron radiation". In: *Proceedings of IEEE International Electron Devices Meeting*. IEEE. 1993, pp. 169–172.

[24] P. Chou et al. "Design and fabrication of a traveling-wave muffin-tin accelerating structure at 90 GHz". In: *Proceedings of the 1997 Particle Accelerator Conference*. Vol. 1. IEEE. 1997, pp. 464–466.

[25] P. Chou et al. "Cold test results of a standing wave muffin-tin structure at X-band". In: *7th Workshop of Advanced Accelerator Concepts*. Vol. 398. 1. AIP. 1997, pp. 473–484.

[26] P. Chou et al. "The fabrication of millimeter-wavelength accelerating structures". In: *7th Workshop of Advanced Accelerator Concepts*. Vol. 398. 1. AIP. 1997, pp. 501–517.

[27] M. E. Hill. "Experimental studies of W-band accelerator structures at high field". PhD thesis. Stanford Linear Accelerator Center, Menlo Park, CA (US), 2001.

[28] M. Dal Forno et al. "RF breakdown tests of mm-wave metallic accelerating structures". In: *Physical Review Accelerators and Beams* 19.1 (2016), p. 011301.

[29] E. Nanni et al. "mm-Wave Standing-Wave Accelerating Structures for High-Gradient Tests". In: *Proceedings of IPAC2016*. 2016.

[30] E. Nanni et al. "Toward High-Power High-Gradient Testing of mm-Wave Standing-Wave Accelerating Structures". In: *Proceedings of IPAC2018*. JACOW Publishing, Geneva, Switzerland. 2018, pp. 1224–1227.

[31] K. Shimoda. "Proposal for an electron accelerator using an optical maser". In: *Applied Optics* 1.1 (1962), pp. 33–35.

[32] Y. Takeda and I. Matsui. "Laser linac with grating". In: *Nuclear Instruments and Methods* 62.3 (1968), pp. 306–310.

[33] K. Mizuno, S. Ono, and O. Shimoe. "Interaction between coherent light waves and free electrons with a reflection grating". In: *Nature* 253.5488 (1975), p. 184.

[34] K. Mizuno, J. Pae, T. Nozokido, and K. Furuya. "Experimental evidence of the inverse Smith–Purcell effect". In: *Nature* 328.6125 (1987), p. 45.

[35] M. Lenzner et al. "Femtosecond optical breakdown in dielectrics". In: *Physical Review Letters* 80.18 (1998), p. 4076.

[36] J. Rosenzweig, A. Murokh, and C. Pellegrini. "A proposed dielectric-loaded resonant laser accelerator". In: *Physical Review Letters* 74.13 (1995).

[37] J. Rosenzweig and P. Schoessow. "An optimized slab-symmetric dielectric-based laser accelerator structure". In: *8th Workshop on Advanced Accelerator Concepts*. 1999, pp. 693–700.

[38] T. Plettner, P. Lu, and R. Byer. "Proposed few-optical cycle laser-driven particle accelerator structure". In: *Physical Review Special Topics-Accelerators and Beams* 9.11 (2006), p. 111301.

[39] E. Peralta et al. "Demonstration of electron acceleration in a laser-driven dielectric microstructure". In: *Nature* 503.7474 (2013), pp. 91–94.

[40] P. Yeh and A. Yariv. "Bragg reflection waveguides". In: *Optics Communications* 19.3 (1976), pp. 427–430.

[41] P. Yeh, A. Yariv, and E. Marom. "Theory of Bragg fiber". In: *Journal of Sciences America* 68.9 (1978), pp. 1196–1201.

[42] A.-C. Tien et al. "Short-pulse laser damage in transparent materials as a function of pulse duration". In: *Physical Review Letters* 82.19 (1999), p. 3883.

[43] K. P. Wootton et al. "Demonstration of acceleration of relativistic electrons at a dielectric microstructure using femtosecond laser pulses". In: *Optics Letters* 41.12 (2016), pp. 2696–2699.

[44] K. Soong. "Particle accelerator on a wafer: demonstration of electron acceleration and diagnostics with microstructures". PhD thesis. Stanford University, 2014.

[45] E. Peralta et al. "Fabrication and measurement of dual layer silica grating structures for direct laser acceleration". In: SLAC-PUB-16682 (2016).

[46] M. Hamberg et al. "Dielectric Laser Acceleration Setup Design, Grating Manufacturing and Investigations Into Laser Induced RF Cavity Breakdowns". In: *38th International Free-Electron Laser Conference, Santa Fe, 20-25 Aug.* 2017.

[47] E. Simakov et al. "Possibilities for Fabricating Polymer Dielectric Laser Accelerator Structures with Additive Manufacturing". In: *Proceedings of IPAC2018*. JACOW Publishing, Geneva, Switzerland. 2018, pp. 4671–4674.

[48] R. J. England. "Review of laser-driven photonic structure-based particle acceleration". In: *IEEE Journal of Selected Topics in Quantum Electronics* 22.2 (2015), pp. 171–177.

[49] K. Wootton, J. McNeur, and K. Leedle. "Dielectric laser accelerators: designs, experiments, and applications". In: *Reviews of Accelerator Science and Technology: Volume 9: Technology and Applications of Advanced Accelerator Concepts* (2016), pp. 105–126.

[50] W. Gai et al. "Experimental demonstration of wake-field effects in dielectric structures". In: *Physical Review Letters* 61.24 (1988), p. 2756.

[51] G. Andonian et al. "Dielectric wakefield acceleration of a relativistic electron beam in a slab-symmetric dielectric lined waveguide". In: *Physical Review Letters* 108.24 (2012), p. 244801.

[52] B. O'Shea et al. "Observation of acceleration and deceleration in gigaelectron-volt-per-metre gradient dielectric wakefield accelerators". In: vol. 7. Nature Publishing Group, 2016, p. 12763.

[53] M. Thompson et al. "Ultra-High Gradient Dielectric Wakefield Accelerator Experiments". In: 877.1 (2006), pp. 903–909.

[54] M. Thompson et al. "Breakdown limits on gigavolt-per-meter electron-beam-driven wakefields in dielectric structures". In: *Physical Review Letters* 100.21 (2008), p. 214801.

[55] S. Antipov et al. "Experimental demonstration of energy-chirp compensation by a tunable dielectric-based structure". In: *Physical Review Letters* 112.11 (2014), p. 114801.

[56] T. H. Pacey, Y. Saveliev, G. Xia, and J. Smith. "Simulation studies for dielectric wakefield programme at CLARA facility". In: *Nuclear Instruments and Methods in Physics Research Section A: Accelerators, Spectrometers, Detectors and Associated Equipment* 909 (2018), pp. 261–265.

[57] M. Guetg et al. "Commissioning of the RadiaBeam/SLAC dechirper". In: *Proceedings of IPAC2016*. 2016.

[58] A. A. Lutman et al. "Fresh-slice multicolour X-ray free-electron lasers". In: *Nature Photonics* 10.11 (2016), p. 745.

[59] S. Bettoni, P. Craievich, A. Lutman, and M. Pedrozzi. "Temporal profile measurements of relativistic electron bunch based on wakefield generation". In: *Physical Review Accelerators and Beams* 19.2 (2016), p. 021304.

[60] R. Yoder and J. Rosenzweig. "Side-coupled slab-symmetric structure for high-gradient acceleration using terahertz power". In: *Physical Review Special Topics - Accelerators and Beams* 8.11 (2005).

[61] P. Musumeci et al. "A THz radiation driven IFEL as a phaselocked prebuncher for a Plasma Beat-Wave Accelerator". In: *Proceedings of the International Conference on LASERS*. STS Press. 2001, p. 41.

[62] L. Wong, A. Fallahi, and F. Kärtner. "Compact electron acceleration and bunch compression in THz waveguides". In: *Optics Express* 21.8 (2013), pp. 9792–9806.

[63] D. Zhang et al. "Segmented terahertz electron accelerator and manipulator (STEAM)". In: *Nature Photonics* 12.6 (2018), p. 336.

[64] W. R. Huang et al. "Toward a terahertz-driven electron gun". In: *Scientific Reports* 5 (2015), p. 14899.

[65] W. R. Huang et al. "Terahertz-driven, all-optical electron gun". In: *Optica* 3.11 (2016), pp. 1209–1212.

[66] A. Fallahi et al. "Short electron bunch generation using single-cycle ultrafast electron guns". In: *Physical Review Accelerators and Beams* 19.8 (2016), p. 081302.

[67] M. Fakhari, A. Fallahi, and F. X. Kärtner. "THz cavities and injectors for compact electron acceleration using laser-driven THz sources". In: *Physical Review Accelerators and Beams* 20.4 (2017), p. 041302.

[68] C. Kealhofer et al. "All-optical control and metrology of electron pulses". In: *Science* 352.6284 (2016), pp. 429–433.

[69] E. Curry, S. Fabbri, P. Musumeci, and A. Gover. "THz-driven zero-slippage IFEL scheme for phase space manipulation". In: *New Journal of Physics* 18.11 (2016), p. 113045.

[70] S.-W. Huang et al. "High conversion efficiency, high energy terahertz pulses by optical rectification in cryogenically cooled lithium niobate". In: *Optics Letters* 38.5 (2013), pp. 796–798.

[71] J. Fülöp et al. "Generation of sub-mJ terahertz pulses by optical rectification". In: *Optics letters* 37.4 (2012), pp. 557–559.

[72] F. Ahr et al. "Narrowband terahertz generation with chirped-and-delayed laser pulses in periodically poled lithium niobate". In: *Optics Letters* 42.11 (2017), pp. 2118–2121.

[73] E. Nichols and J. Tear. "Joining the infra-red and electric wave spectra". In: *The Astrophysical Journal* 61 (1925), p. 17.

[74] P. Tan et al. "Terahertz radiation sources based on free electron lasers and their applications". In: *Science China Information Sciences* 55.1 (2012), pp. 1–15.

[75] S. Krishnagopal and V. Kumar. "Free-electron lasers". In: *Radiation Physics and Chemistry* 70.4-5 (2004), pp. 559–569.

[76] S. Casalbuoni et al. "Ultrabroadband terahertz source and beamline based on coherent transition radiation". In: *Physical Review Special Topics-Accelerators and Beams* 12.3 (2009), p. 030705.

[77] Z. Wu et al. "Intense terahertz pulses from SLAC electron beams using coherent transition radiation". In: *Review of Scientific Instruments* 84.2 (2013), p. 022701.

[78] A. Cook et al. "Observation of narrow-band terahertz coherent Cherenkov radiation from a cylindrical dielectric-lined waveguide". In: *Physical Review Letters* 103.9 (2009), p. 095003.

[79] P. Cherenkov. "The Visible Light Emitted by Electrons Moving with Velocities Exceeding that of Light in a Medium". In: *Cr Acad Sci USSR* 14 (1937), pp. 101–105.

[80] M. Bass, P. Franken, J. Ward, and G. Weinreich. "Optical rectification". In: *Physical Review Letters* 9.11 (1962), p. 446.

[81] E. Hecht. *Optics Addison-Wesley Longman*. 1998.

[82] K. Yang, P. Richards, and Y. Shen. "Generation of Far-Infrared Radiation by Picosecond Light Pulses in LiNbO3". In: *Applied Physics Letters* 19.9 (1971), pp. 320–323.

[83] C. Vicario et al. "Broadband and narrowband terahertz source at extreme field strength". In: *CLEO: Science and Innovations* (2017), STu3J–6.

[84] S. Kamada, T. Yoshida, and T. Aoki. "The chirp-control of frequency-tunable narrowband terahertz pulses by nonlinearly chirped laser pulse beating". In: *Applied Physics Letters* 104.10 (2014), p. 101102.

[85] Y.-S. Lee et al. "Generation of narrow-band terahertz radiation via optical rectification of femtosecond pulses in periodically poled lithium niobate". In: *Applied Physics Letters* 76.18 (2000), pp. 2505–2507.

[86] T. Rozzi and M. Farina. *Advanced electromagnetic analysis of passive and active planar structures*. Vol. 46. IET, 1999.

[87] S. Carbajo et al. "Efficient narrowband terahertz generation in cryogenically cooled periodically poled lithium niobate". In: *Optics Letters* 40.24 (2015), pp. 5762–5765.

[88] L. Wang, A. Fallahi, K. Ravi, F. Kä, et al. "Multi-mJ terahertz generation in periodically poled Lithium-Niobate by pulse recycling with dispersion compensation". In: 205 (2019), p. 01016.

[89] M. Cliffe, D. Graham, and S. Jamison. "Longitudinally polarized single-cycle terahertz pulses generated with high electric field strengths". In: *Applied Physics Letters* 108.22 (2016), p. 221102.

[90] D. H. Auston, K. Cheung, J. Valdmanis, and D. Kleinman. "Cherenkov radiation from femtosecond optical pulses in electro-optic media". In: *Physical Review Letters* 53.16 (1984), p. 1555.

[91] M. Cliffe, A. Rodak, D. Graham, and S. Jamison. "Generation of longitudinally polarized terahertz pulses with field amplitudes exceeding 2 kV/cm". In: *Applied Physics Letters* 105.19 (2014), p. 191112.

[92] A. Woldegeorgis et al. "Multi-MV/cm longitudinally polarized terahertz pulses from laser–thin foil interaction". In: *Optica* 5.11 (2018), pp. 1474–1477.

[93] A. Gopal et al. "Observation of energetic terahertz pulses from relativistic solid density plasmas". In: *New Journal of Physics* 14.8 (2012), p. 083012.

[94] T. Seifert et al. "Efficient metallic spintronic emitters of ultrabroadband terahertz radiation". In: *Nature Photonics* 10.7 (2016), p. 483.

[95] M. Hibberd et al. "Magnetic-field patterning of a spintronic source for arbitrary terahertz polarization control". In: *2018 43rd International Conference on Infrared, Millimeter, and Terahertz Waves (IRMMW-THz)*. IEEE. 2018, pp. 1–2.

[96] J. D. Jackson. *Classical electrodynamics*. John Wiley & Sons, 2012.

[97] L. Xiao, W. Gai, and X. Sun. "Field analysis of a dielectric-loaded rectangular waveguide accelerating structure". In: *Physical Review E* 65.1 (2001).

[98] M. Miyagi and S. Nishida. "Pulse spreading in a single-mode fiber due to third-order dispersion". In: *Applied Optics* 18.5 (1979), pp. 678–682.

[99] H. Wiedemann et al. *Particle accelerator physics*. Vol. 314. Springer, 2007.

[100] R. Akre, P. Emma, P. Krejcik, and L. Bentson. "Bunch length measurements using a transverse RF deflecting structure in the SLAC linac". In: *Proceedings of the 8th European Particle Accelerator Conference*. 2002.

[101] P. Krejcik et al. "Commissioning the new LCLS X-band transverse deflecting cavity with femtosecond resolution". In: *Proceedings of IBIC2013, Oxford, UK* (2013).

[102] W. Panofsky and W. Wenzel. "Some considerations concerning the transverse deflection of charged particles in radio-frequency fields". In: *Review of Scientific Instruments* 27.11 (1956), pp. 967–967.

[103] H. Kogelnik and H. Weber. "Rays, stored energy, and power flow in dielectric waveguides". In: *Journal of the Optical Society of America* 64.2 (1974), pp. 174–185.

[104] N. Laman, S. S. Harsha, D. Grischkowsky, and J. S. Melinger. "7 GHz resolution waveguide THz spectroscopy of explosives related solids showing new features". In: *Optics Express* 16.6 (2008), pp. 4094–4105.

[105] R. Mendis and D. Grischkowsky. "Undistorted guided-wave propagation of subpicosecond terahertz pulses". In: *Optics Letters* 26.11 (2001), pp. 846–848.

[106] J. Zhang and D. Grischkowsky. "Waveguide terahertz time-domain spectroscopy of nanometer water layers". In: *Optics Letters* 29.14 (2004), pp. 1617–1619.

[107] J. S. Melinger, N. Laman, S. S. Harsha, and D. Grischkowsky. "Line narrowing of terahertz vibrational modes for organic thin polycrystalline films within a parallel plate waveguide". In: *Applied Physics Letters* 89.25 (2006), p. 251110.

[108] A. J. Shutler and D. Grischkowsky. "Gap independent coupling into parallel plate terahertz waveguides using cylindrical horn antennas". In: *Journal of Applied Physics* 112.7 (2012), p. 073102.

[109] R. Mendis and D. Grischkowsky. "THz interconnect with low-loss and low-group velocity dispersion". In: *IEEE Microwave and Wireless Components Letters* 11.11 (2001), pp. 444–446.

[110] S.-H. Kim, E. Lee, Y. Ji, and T.-I. Jeon. "Improvement of THz coupling using a tapered parallel-plate waveguide". In: *Optics Express* 18.2 (2010), pp. 1289–1295.

[111] M. Theuer, S. S. Harsha, and D. Grischkowsky. "Flare coupled metal parallel-plate waveguides for high resolution terahertz time-domain spectroscopy". In: *Journal of Applied Physics* 108.11 (2010), p. 113105.

[112] M. Gerhard, M. Theuer, and R. Beigang. "Coupling into tapered metal parallel plate waveguides using a focused terahertz beam". In: *Applied Physics Letters* 101.4 (2012), p. 041109.

[113] K. Iwaszczuk et al. "Terahertz field enhancement to the MV/cm regime in a tapered parallel plate waveguide". In: *Optics Express* 20.8 (2012), pp. 8344–8355.

[114] F. Scheiba. "THz coupler design for electron accelerators". MA thesis. University of Oldenburg, 2013.

[115] G. Andonian et al. "Planar-dielectric-wakefield accelerator structure using Bragg-reflector boundaries". In: *Physical Review Letters* 113.26 (2014), p. 264801.

[116] A. Smirnov. "Characterization of coherent Cherenkov radiation source". In: *Nuclear Instruments and Methods in Physics Research Section A: Accelerators, Spectrometers, Detectors and Associated Equipment* 771 (2015), pp. 147–152.

[117] S. Antipov et al. "Efficient extraction of high power THz radiation generated by an ultra-relativistic electron beam in a dielectric loaded waveguide". In: *Applied Physics Letters* 109.14 (2016), p. 142901.

[118] O. Mitrofanov and J. A. Harrington. "Dielectric-lined cylindrical metallic THz waveguides: mode structure and dispersion". In: *Optics Express* 18.3 (2010), pp. 1898–1903.

[119] B. Bowden, J. A. Harrington, and O. Mitrofanov. "Low-loss modes in hollow metallic terahertz waveguides with dielectric coatings". In: *Applied Physics Letters* 93.18 (2008), p. 181104.

[120] J. Breuer and P. Hommelhoff. "Laser-based acceleration of nonrelativistic electrons at a dielectric structure". In: *Physical Review Letters* 111.13 (2013).

[121] F. Aquistapace et al. "Photovariation of grating-assisted coupling of terahertz waves into a silicon waveguide". In: *Journal of Applied Physics* 94.12 (2003), pp. 7888–7891.

[122] Y. Wei et al. "Investigations into dual-grating THz-driven accelerators". In: *Nuclear Instruments and Methods in Physics Research Section A: Accelerators, Spectrometers, Detectors and Associated Equipment* 877 (2018), pp. 173–177.

[123] D. Alesini. *Power coupling*. arXiv preprint arXiv:1112.3201. 2011.

[124] K. Jin et al. "X-band travelling wave accelerator structure R&D". In: *Proceedings of the 2001 Particle Accelerator Conference*. Vol. 5. IEEE. 2001, pp. 4089–4091.

[125] D. M. Pozar. *Microwave engineering*. John Wiley & Sons, 2009.

[126] G. V. Eleftheriades, W. Y. Ali-Ahmad, L. P. Katehi, and G. M. Rebeiz. "Millimeter-wave integrated-horn antennas. I. Theory". In: *Antennas and Propagation, IEEE Transactions on* 39.11 (1991), pp. 1575–1581.

[127] H. Patzelt and F. Arndt. "Double-plane steps in rectangular waveguides and their application for transformers, irises, and filters". In: *IEEE Transactions on Microwave Theory and Techniques* 30.5 (1982), pp. 771–776.

[128] B. M. Cowan et al. "Generalized algorithm for control of numerical dispersion in explicit time-domain electromagnetic simulations". In: *Physical Review Special Topics-Accelerators and Beams* 16.4 (2013), p. 041303.

[129] T.-T. Chia, R. J. Burkholder, and R. Lee. "The application of FDTD in hybrid methods for cavity scattering analysis". In: *IEEE Transactions on Antennas and Propagation* 43.10 (1995), pp. 1082–1090.

[130] T. Shibata and T. Itoh. "Generalized-scattering-matrix modeling of waveguide circuits using FDTD field simulations". In: *IEEE transactions on microwave theory and techniques* 46.11 (1998), pp. 1742–1751.

[131] T. Weiland. "Advances in FIT/FDTD modeling". In: *Proceedings of 18th Annual review of progress in applied computational electromagnetics*. 2002, pp. 1–1.

[132] *Understanding time domain meshing in CST Microwave Studio*. Tech. rep. Computer Simulation Technology.

[133] V. Georgiadis et al. "Characterizing a terahertz-driven dielectric-lined waveguide for electron beam manipulation". In: *2018 43rd International Conference on Infrared, Millimeter, and Terahertz Waves (IRMMW-THz)*. IEEE. 2018, pp. 1–2.

[134] F. Scheiba. "THz coupler design for electron accelerators". MA thesis. 2013.

[135] B. Fischer et al. "Chemical recognition in terahertz time-domain spectroscopy and imaging". In: *Semiconductor Science and Technology* 20.7 (2005), S246.

[136] M. M. Nazarov, A. P. Shkurinov, E. Kuleshov, and V. V. Tuchin. "Terahertz time-domain spectroscopy of biological tissues". In: *Quantum Electronics* 38.7 (2008), p. 647.

[137] R. Ulbricht et al. "Carrier dynamics in semiconductors studied with time-resolved terahertz spectroscopy". In: *Reviews of Modern Physics* 83.2 (2011), p. 543.

[138] A. Yariv. *Quantum Electronics*. John Wiley & Sons, 1967.

[139] C. A. Schmuttenmaer. "Exploring dynamics in the far-infrared with terahertz spectroscopy". In: *Chemical Reviews* 104.4 (2004), pp. 1759–1780.

[140] M. Hibberd et al. "Magnetic-field tailoring of the terahertz polarization emitted from a spintronic source". In: *Applied Physics Letters* 114.3 (2019), p. 031101.

[141] V. Georgiadis. *Private communication.*

[142] M. Van Exter, C. Fattinger, and D. Grischkowsky. "Terahertz time-domain spectroscopy of water vapor". In: *Optics letters* 14.20 (1989), pp. 1128–1130.

[143] X. Xin et al. "Terahertz absorption spectrum of para and ortho water vapors at different humidities at room temperature". In: *Journal of Applied Physics* 100.9 (2006), p. 094905.

[144] D. Gabor. "Theory of communication. Part 1: The analysis of information". In: *Journal of the Institution of Electrical Engineers-Part III: Radio and Communication Engineering* 93.26 (1946), pp. 429–441.

[145] P. M. Oliveira and V. Barroso. "Uncertainty in the time-frequency plane". In: *Proceedings of the Tenth IEEE Workshop on Statistical Signal and Array Processing (Cat. No. 00TH8496)*. IEEE. 2000, pp. 607–611.

[146] T. Claasen and W. Mecklenbrauker. "Time-frequency signal analysis by means of the Wigner distribution". In: *IEEE International Conference on Acoustics, Speech, and Signal Processing*. Vol. 6. IEEE. 1981, pp. 69–72.

[147] L. White and B. Boashash. "On estimating the instantaneous frequency of a Gaussian random signal by use of the Wigner-Ville distribution". In: *IEEE Transactions on Acoustics, Speech, and Signal Processing* 36.3 (1988), pp. 417–420.

[148] R. Latif et al. "Determination of the group and phase velocities from time–frequency representation of Wigner–Ville". In: *NDT & E International* 32.7 (1999), pp. 415–422.

[149] P. McIntosh et al. "The VELA and CLARA test facilities at daresbury laboratory". In: *Proceedings of LINAC2017*. 2017.

[150] A. Weling, B. Hu, N. Froberg, and D. Auston. "Generation of tunable narrow-band THz radiation from large aperture photoconducting antennas". In: *Applied Physics Letters* 64.2 (1994), pp. 137–139.

[151] U. Happek, A. Sievers, and E. Blum. "Observation of coherent transition radiation". In: *Physical Review Letters* 67.21 (1991), p. 2962.

[152] B. Schmidt et al. "Longitudinal bunch diagnostics using coherent transition radiation spectroscopy. Physical principles, multichannel spectrometer, experimental results, mathematical methods". In: *Technical Report, Deutsches Elektronen-Synchrotron (DESY)* (2018).

[153] N. Daghestani et al. "Room temperature ultrafast InGaAs Schottky diode based detectors for terahertz spectroscopy". In: *Infrared Physics & Technology* (2019).

[154] T. Pacey. Private communication.

[155] O. Finlay. *Private communication.*

[156] J. Jones. *Private communication.*

[157] Y. Saveliev. *Private communication.*

[158] D. Grischkowsky, S. Keiding, M. Van Exter, and C. Fattinger. "Far-infrared time-domain spectroscopy with terahertz beams of dielectrics and semiconductors". In: *Journal of the Optical Society of America* 7.10 (1990), pp. 2006–2015.

[159] M. Naftaly and R. E. Miles. "Terahertz time-domain spectroscopy for material characterization". In: *Proceedings of the IEEE* 95.8 (2007), pp. 1658–1665.

[160] F. Ahr et al. "Narrowband terahertz generation with chirped-and-delayed laser pulses in periodically poled lithium niobate". In: *Optics Letters* 42.11 (2017), pp. 2118–2121.